



THE UNIVERSITY *of* EDINBURGH

This thesis has been submitted in fulfilment of the requirements for a postgraduate degree (e.g. PhD, MPhil, DClinPsychol) at the University of Edinburgh. Please note the following terms and conditions of use:

This work is protected by copyright and other intellectual property rights, which are retained by the thesis author, unless otherwise stated.

A copy can be downloaded for personal non-commercial research or study, without prior permission or charge.

This thesis cannot be reproduced or quoted extensively from without first obtaining permission in writing from the author.

The content must not be changed in any way or sold commercially in any format or medium without the formal permission of the author.

When referring to this work, full bibliographic details including the author, title, awarding institution and date of the thesis must be given.

In Situ Underwater Microwave Oil Spill and Oil Slick Thickness Sensor



Aliyu Bukar Dala

A thesis submitted in partial fulfilment of the requirements for
the degree of

DOCTOR OF PHILOSOPHY

The University of Edinburgh

March 2022

*To my beloved father
Who believed I could go further
When my feet stumbled
Raised me when I crumbled
Envisioned me at top of the plateau
You never got to see me grow
The clock stopped too early
Forever stuck at seven thirty*

Declaration of Originality

I hereby declare that this thesis was composed and originated entirely by myself, that the work contained herein is my own except where explicitly stated otherwise in the text, and that this work has not been submitted for any other degree or professional qualifications.

Aliyu B. Dala
March 2022
Edinburgh, UK

Acknowledgements

I would like to extend immense appreciation to my supervisor, Prof. Tughrul Arslan for his immeasurable guidance, support, encouragement, motivation and understanding. I am grateful for the environment he created for me to flourish as a PhD student and how he ensured I got all the assistance I needed.

My appreciation goes to my soulmate, Hakimat, for her understanding and support throughout my arduous PhD journey, to my son Abdallah for his patience and those warm hugs whenever I come back home and to my lavender, Kadeeja for her radiant smiles that gave me the strength to carry on.

I would like to thank the EWireless research group both past and present. I am grateful for all the support and camaraderie I got from them. Thank you Adewale, Godwin, Riza, Imran, Yichen, Xiaoyue, Amalina, Fengzhou, Rahmat, Minghui, Changjiang, Stefan, Mark, Yinhuan and Nazia. To my colleagues and friends in the School of Engineering and Scottish Microelectronics Centre at the University of Edinburgh, thank you for making the environment conducive for research and socialisation. I am indebted to the Petroleum Development Trust Fund, Nigeria for making this work possible.

I dedicate this work to my Father of blessed memory and my Mother. Thank you for your eternal support.

Lay Abstract

One of the most challenging regions of the planet to monitor is the underwater environment. Interestingly, Earth is a water planet with about 71 percent of its surface covered in water. Very vital resources abound the deep oceans such as marine life, oil and gas installations. Sometimes, accidents happen underwater with dire repercussions. In December of 2011, an oil spill occurred at the Bonga deep-water oil fields. Almost 2 million gallons of crude oil poured into the Atlantic Ocean, covering 185 km, killing marine lives and affecting no fewer than 1.5 million people and 350 coastal communities. About a year earlier, the worst oil spill in US history, the Deepwater Horizon oil spillage, resulted in over 130 million gallons of oil discharged into the Gulf of Mexico.

Several techniques have been used in sensing and monitoring the seas and oceans for oil spillage. One of the most popular methods is the use of synthetic aperture radar (SAR) mounted on satellites or aircraft to collect the information on the water surface. The data captured is analysed for possible oil spills. One of the demerits of this approach is that it has high latency, thus unfit for instances where real-time capabilities are required. It is also prone to falsely detecting the presence of oil spill. Another limitation of remote sensing techniques is their inability to precisely measure oil slick thickness. The oil slick thickness could determine the amount of oil discharged into the ocean during the spillage, therefore guiding oil spill countermeasures and legal cases. For this purpose, the in-situ methods are more reliable. Several techniques based on optical waves, capacitive and conductive sensing have been used. They all suffer from some limitations such as corrosion and blockage when they come in contact with the water medium. This work proposes the use of microwave sensing techniques for the first time in the detection of oil spill and the determination of oil slick thickness in seawater and freshwater. The novel sensor was able to detect when crude oil inclusions have been discharged into the water medium. A communication backbone was developed in the research to enable the sensor to wirelessly transmit the data obtained to the Internet for real-time monitoring.

Abstract

Nearly 30 percent of oil drilled globally is done offshore. Oil spillage offshore have far-reaching consequences on the environment, aquatic lives, and livelihoods as it was evident in the numerous accidents such as the Deepwater Horizon and Bonga oil spillages. Apart from detecting oil spillages, the determination of the oil slick thickness is very important. This is to enable the estimation of the volume and spread of oil discharged in oceans, seas and lakes. This information could guide the oil spill countermeasures and provide the basis for legal actions against the defaulting parties.

The viability of the use of radar in the detection of oil spill has already been established by airborne and space borne synthetic aperture radar (SAR). Notwithstanding, the high latency associated with SARs and its susceptibility of false positive and false negative detection of oil slick makes it vulnerable. It has also not been very successful in the determination of oil slick thickness. In situ methods such as the capacitive, conductive and optical based approaches have been used to detect as well as determine oil slick thickness. Some of these contact-based approaches are susceptible to corrosion, fouling and require several calibrations. Radio frequency (RF) signals in seawater suffer from attenuation and dispersion due to the high conductivity of the medium. Antennas, ideally matched to free space, suffer impedance mismatches when immersed in seawater.

In this thesis, we proposed the novel approach of using microwave techniques to detect oil spillage and determine oil slick thickness based on a contact-based in situ approach. The work began by undertaking an investigation into the properties of the North Sea water which was used as the primary transmission medium for the study. Subsequently, the research developed an ultrawideband antenna that radiated underwater, which was encapsulated in polydimethylsiloxane (PDMS). The antenna-sensor with a Faraday cage was used to develop a novel microwave oil spill sensor. A communication backbone was designed for the sensor using long range (LoRa) 868 MHz frequency based on a bespoke braid antenna buffered by oil impregnated papers to ameliorate against the influence of the seawater surface. Using a four layered RF switch controller and an antenna array consisting of four antenna-sensors, a novel microwave oil slick

thickness sensor was developed. The antenna-sensors were arranged in a cuboid fashion with antenna-sensor 3 and antenna-sensor 4 capable of detecting oil slick thickness at 23 mm and 46 mm using their transmission coefficient (S43) of -10 dB and -19 dB compared to that of the pure seawater respectively. For the 69 mm and 92 mm thickness, the transmission coefficient (S21) of antenna-sensor 1 and antenna-sensor 2 was used to determine these thicknesses with values of -13.5 dB and -24.14 dB with respect to that of pure seawater.

Table of Contents

Declaration of Originality	iii
Acknowledgements	iv
Lay Abstract	v
Abstract	vi
Table of Contents	viii
List of Figures	xii
List of Tables.....	xviii
Abbreviations and Acronyms.....	xix
Chapter 1	1
1.1 Research Motivation.....	1
1.2 Research Investigations	4
1.2.1 Design Challenges	4
1.2.2 Research Objectives.....	7
1.3 Original Contributions of Thesis	7
1.4 Simulation Package	8
1.5 Overview of the Thesis.....	9
1.6 Publications Arising from the Research.....	11
Chapter 2	13
2.1 Oil Spill Detection.....	13
2.2 Oil Slick Thickness Measurement.....	17
2.2.1 Remote Sensing Oil Slick Thickness Measurement.....	17
2.2.2 In Situ Oil Slick Thickness Measurement	18
2.3 Overview of In-situ Microwave Based Sensors for Oil Spill Detection and Oil Slick Thickness Measurement	33
2.4 Summary	34
Chapter 3	35
3.1 Maxwell's Equations	35
3.1.1 Time Harmonic Case	36
3.1.2 Waves Propagation in Lossless Media	37
3.1.3 Waves Propagation in Lossy Media	37

3.2 Seawater Analysis	38
3.2.1 Skin Depth	38
3.2.2 Debye's North Sea model	39
3.3 Investigation of North Seawater	40
3.3.1 CST Microwave Suite Simulation	40
3.3.2 Measurement of the relative Permittivity of North Seawater	40
3.4 Summary	44
Chapter 4	46
4.1 Requirement of Underwater Antenna Sensor	46
4.2 Design of Underwater Antenna	53
4.2.1 FCC Bandwidth Classification	56
4.2.2 Base Antenna Design	57
4.2.3 Trefoil Antenna Design	59
4.2.4 Trefoil Antenna Submerged in Water	65
4.2.5 Pulse Fidelity Factor	66
4.2.6 PDMS Buffer for Trefoil Underwater Antenna	68
4.2.7 Fabrication and Measurement Results	71
4.3 Summary	80
Chapter 5	82
5.1 Faraday Cage	82
5.1.1 Reflection Coefficients for Faraday Cage	84
5.1.2 Transmission Coefficients for Faraday Cage	84
5.2 Crude Oil Spill Simulation	85
5.3 Crude Oil Spill Measurement Setup	86
5.4 Crude Oil Spill Measurement	87
5.5 Reflection Coefficients for Oil Spill	88
5.5.1 70 mm Antenna Spacing	88
5.5.2 50 mm Antenna Spacing	89
5.6 Transmission Coefficients for Oil Spill	91
5.7 Summary	94
Chapter 6	96
6.1 Overview of Water Surface Communication	96
6.2 Antenna for Water Surface Communication using LoRa	99
6.2.1 Braid Antenna Design	100

6.2.2 Braid Antenna Simulations.....	102
6.2.3 Fabrication of Braid Antenna and Measurements	105
6.2.4 Oil Impregnated Buffer Design	108
6.3 VNA Experiments	111
6.4 Field Tests	112
6.4.1 Received Signal Strength Indicator (RSSI) Tests.....	112
6.4.2 Water Surface Antenna RSSI Tests	114
6.5 Summary	117
Chapter 7	119
7.1 System Architecture	119
7.1.1 Antenna Sensor System	121
7.1.2 RF Switching Controller Unit.....	124
7.1.3 Solar Power System.....	125
7.1.4 Android Application	125
7.2 VNA Characterisation of RF Switches	126
7.2.1 Single Pole Double Throw (SPDT) RF Switch	127
7.2.2 Single Pole Three Throw (SP3T) RF Switch	128
7.3 Novel RF Switching Circuit Development and Implementation	129
7.3.1 Circuit Diagram Design of Bespoke RF Switches	129
7.3.2 Four Layered RF Switch PCB Bespoke Design and Implementation...	130
7.4 Four Antenna Sensor Array Simulations.....	134
7.5 Dielectric Measurements	138
7.6 Oil Slick Thickness Measurement.....	140
7.6.1 Enclosure for the setup	140
7.6.2 Experimental Setup.....	141
7.6.3 Reflection Coefficients for Oil Slick Thickness Measurement	143
7.6.4 Transmission Coefficients for Oil Slick Thickness Measurement	145
7.7 Summary	147
Chapter 8	148
8.1 Conclusion.....	148
8.2 Suggestions for Future Work	150
8.2.1 Antenna Design	150
8.2.2 Antenna Array	151
8.2.3 RF Switching Circuit.....	151

8.2.4 Portable Standalone System	151
8.3 Final Comments	151
References	153
Appendices.....	163

List of Figures

Figure 2.1: Experimental settings for measuring oil slicks with different thicknesses (a) The overall experimental setting; (b) schematic showing side view of the box; (c) 2-D vertical view of the 12 plastic rings, with darker colours showing thicker oil [28].	19
Figure 2.2: (a) Model of proposed sensor (b) Optical ray model of the sensor [30].	20
Figure 2.3: Algorithm for Optical Measurement (b) Positioning for the transceivers [30].	21
Figure 2.4: Experimental Setup for Optical Measurement [30].	21
Figure 2.5: Schematic of Spectrometer [31].	22
Figure 2.6: Setup of LED-based spectrometer [31].	23
Figure 2.7: Test results for measurement of oil thickness [31].	23
Figure 2.8: Led-based spectrometer sensor in tank with diesel film [31].	24
Figure 2.9 Experimental setup of SD-OCT system for measuring. LS: laser source, DC: directional coupler, FC1 and FC2: fibre collimators, BS: beam splitter, GMS: galvanometer mirror system, SM: Spectrometer, L1 - L3: lenses, M1 and M2: mirrors, DG: diffraction grating, L-CCD: linear array charge coupled device, X-S: X-scanner, Y-S: Y-scanner [32].	24
Figure 2.10: Schematic for the glass cell for the measurement of oil slick thickness [32].	25
Figure 2.11: Volumetric structures and characteristics of oil slicks (width ~3.2 mm and length ~5.2 mm) (a) petroleum slick at B, (b) diesel slick at B (c) petroleum slick at A (d) diesel slick at A (e) petroleum slick at C (f): diesel slick at C [32].	26
Figure 2.12: Planar Capacitive measurement setup [33].	27
Figure 2.13: (a) capacitive sensor design (b) Enhanced sensor design with pins [35].	28
Figure 2.14: Sensor with waterproof enclosure (a) Front (b) Back [35].	28
Figure 2.15: Dipping Tests Experiment [35].	29
Figure 2.16: Block Diagram of the system [36].	30
Figure 2.17: System processing board [36].	30
Figure 2.18: Mechanical design of sensor [36].	31
Figure 2.19: Experimental setup for prototype in [36].	31
Figure 2.20: WM-OTS sampling floating emulsion. B):View of WM-OTS. C): High-resolution picture of the oil in the tube for which thickness was measured digitally at 80 μm . D): Area of sampling about 10 min before sample collection was performed [14].	32

Figure 3.1: Locations of seawater samples.	41
Figure 3.2: Experimental setup for dielectric measurement.	42
Figure 3.3: Relative permittivity for samples of seawater.	43
Figure 3.4: Tangential loss for experimental and Debye's seawater model.	44
Figure 4.1: Antenna encapsulated in a buffer layer	48
Figure 4.2: Antenna Performance in water with and without enclosure [57].	49
Figure 4.3: Flowchart of buffer synthesis procedure [57].	51
Figure 4.4: Measurement of relative permittivity of different selected liquid solutions [57].	52
Figure 4.5: Geometry of antenna design with buffer layer structure [63].	53
Figure 4.6: Experimental setup for underwater antenna [57].	53
Figure 4.7: Initial Base Antenna (a) Front (b) Back (c) Perspective.	57
Figure 4.8: Antenna characteristics for initial base antenna. (a) Reflection coefficient (b) Electric and magnetic field (c) Far field plot (d) XPD plot.	58
Figure 4.9: RAL Parametric Sweep (a) 5 mm (b) 10 mm (c) 15 mm (d) 20 mm (e) 25 mm.	59
Figure 4.10: Simulation plot for RAL length variation.	60
Figure 4.11: Patch Distance Variation from Circles. (a) 5.5 mm (b) 9.5 mm (c) 13.5 mm (d) 17.5 mm (e) 21.5 mm.	60
Figure 4.12: Simulation plot for trefoil minor circles distance variation.	61
Figure 4.13: Ground rectangular element length (GL) variation. (a) 4.6 mm (b) 9.6 mm (c) 14.6 mm (d) 19.6 mm.	62
Figure 4.14: Simulation plot for back parasitic rectangular element (GL) variation.	62
Figure 4.15: Simulated E-(XZ) and H-(XY) plane far-field radiation patterns at (a) 1.5 GHz with directivity of 2.07 dBi (b) 2 GHz with directivity of 2.46 dBi (c) 2.5 GHz with directivity of 3.04 dBi (d) 3 GHz with directivity of 3.73 dBi.	63
Figure 4.16: Cross polar discrimination (XPD) (a) 1.5 GHz (b) 2 GHz (c) 2.5 GHz (d) 3 GHz.	64
Figure 4.17: Surface Current (a) 1500 MHz (b) 2000 MHz (c) 2500 MHz (d) 3000 MHz.	65
Figure 4.18: Antenna immersed in water (a) Seawater (b) Freshwater.	65
Figure 4.19: Simulation plot for trefoil antenna submerged in seawater and freshwater.	66
Figure 4.20 : Simulated received near-field time-domain pulses radiated by the antenna-sensor at different angles in the H-plane	67
Figure 4.21: PDMS Buffer Encapsulation (a) Front (b) Back (c) Perspective.	69
Figure 4.22: PDMS Enclosed Antenna Immersed in Water (a) Freshwater (b) Seawater.	69
Figure 4.23: Simulation plot for PDMS thickness variation in seawater.	70

Figure 4.24: Simulation plot for PDMS thickness variation in freshwater.....	71
Figure 4.25: Fabricated trefoil antenna (a) Front (b) Back.	72
Figure 4.26: Reflection coefficient of measured two trefoil antennas vs simulated trefoil antenna.....	73
Figure 4.27: Mould for PDMS (a) 3D Model (b) 3D printed mould.	74
Figure 4.28: (a) Zeroing the scale (b) Weighing Dowsil 184 silicone elastomer base (c) Weighing Dowsil 184 silicone elastomer base & silicone curing agent.	76
Figure 4.29: (a) Magnetic mixing of Dow silicone solution (b) Degassing the mixed silicone solution.	76
Figure 4.30: PDMS encapsulated trefoil antenna.	77
Figure 4.31: Simulated and measured reflection coefficient of PDMS encapsulated antennas in free space.....	77
Figure 4.32: Experimental setup for underwater antenna tests.	78
Figure 4.33: KE5FX VNA utility software.....	79
Figure 4.34: Measured reflection coefficient of PDMS-encapsulated trefoil antenna in freshwater and seawater.	79
Figure 5.1: Antenna spacing	83
Figure 5.2: Oil spill sensing region (a) Antennas in acrylic in CST (b) Faraday cage in CST (c) Fabricated Faraday cage.....	83
Figure 5.3: Simulation plot showing reflection coefficient of different antenna-sensors spacing in freshwater.....	84
Figure 5.4: Simulation plot showing reflection coefficient of different antenna-sensors spacing in seawater.	84
Figure 5.5: Simulation plot showing transmission coefficient of different antenna-sensors spacing in freshwater.....	85
Figure 5.6: Simulation plot showing transmission coefficient of different antenna-sensors spacing in seawater.....	85
Figure 5.7: Experimental setup for the oil spill test for crude oil.	87
Figure 5.8: Plot showing reflection coefficient for oil spill using 70 mm antenna-sensors spacing.....	89
Figure 5.9: Plot showing reflection coefficient for oil spill using 50 mm antenna-sensors spacing.....	90
Figure 5.10: Plot showing reflection coefficient for oil spill using 15 mm antenna-sensors spacing.....	91
Figure 5.11: Plot showing transmission coefficient for oil spill using 70 mm antenna-sensors spacing.....	92
Figure 5.12: Plot showing transmission coefficient for oil spill using 50 mm antenna-sensors spacing.....	93
Figure 5.13: Plot showing transmission coefficient for oil spill using 15 mm antenna-sensors spacing.....	93

Figure 6.1: (a) BSN (b) IoT gateway.	100
Figure 6.2: Base Antenna (a) Front (b) Back (c) Perspective.	101
Figure 6.3: Braided Antenna Design; (a) 5 mm (b) 15 mm (c) 25 mm (d) 35 mm (e) Back.....	102
Figure 6.4: Reflection Coefficient of Braid antennas (with varied length).....	103
Figure 6.5: Optimal 35 mm antenna (a) Surface current (b) 3D far field radiation pattern (c) E-plane radiation pattern (d) H-plane radiation pattern.....	104
Figure 6.6: Parametric sweep of the width of the larger rectangular parasitic element on the back of the substrate	105
Figure 6.7: Picture of Fabricated Braided Antenna (a) Front (b) Back.	106
Figure 6.8: Off-the-Shelf Benchmark Antennas (a) Eightwood antenna (b) OC-LG antenna (c) Things Network gateway antenna.	107
Figure 6.9: S11 of Braided & benchmarking antennas.	108
Figure 6.10: Braid antenna enclosed in PLA container on a plastic foam buoy floating on water surface.	108
Figure 6.11: Braid antenna enclosed in an oil-impregnated barrier.....	109
Figure 6.12: Braid antenna inserted in an oil-impregnated paper buffer.	110
Figure 6.13: Oil-treated papers, barrier and braid antenna.	110
Figure 6.14: Antenna barrier inside enclosure with PCB of BSN.	111
Figure 6.15: Experimental setup for antenna measurements.	111
Figure 6.16: Measured reflection coefficients of antenna without buffer and antenna with buffer submerged in seawater.	112
Figure 6.17: Setup for the received signal strength indicator (RSSI) tests for receive and transmit antennas.	113
Figure 6.18: RSSI for antennas with respect to distance.	114
Figure 6.19: BSN deployed in the North Sea (a) with buffer (b) without buffer (c) Data relay node for RSSI tests.....	114
Figure 6.20: RSSI Tests for buffered and buffer-less braid antennas on surface water.	115
Figure 6.21: RSSI of submerged SN with buffered braid antenna.	116
Figure 7.1: System architecture diagram for the RF switched oil slick thickness sensor.	120
Figure 7.2: Sensor (a) Top layer (b) Bottom layer.....	122
Figure 7.3: Simulated E-(XZ) and H-(XY) plane far-field radiation patterns of sensor without reflector at (a) 1.5 GHz with directivity of 2.13 dBi (b) 2 GHz with directivity of 2.57 dBi (c) 2.5 GHz with directivity of 3.22 dBi (d) 3 GHz with directivity of 3.59.	123
Figure 7.4: Simulated E-(XZ) and H-(XY) plane far-field radiation patterns of sensor with reflector at (a) 1.5 GHz with directivity of 6.15 dBi (b) 2 GHz with directivity of	

6.09 dBi (c) 2.5 GHz with directivity of 6.82 dBi (d) 3 GHz with directivity of 7.4 dBi	124
Figure 7.5: Android App for controlling and selecting RF switches.	126
Figure 7.6: Representation of the RF switches' VNA evaluation setup.	126
Figure 7.7: Insertion losses of the SPDT.	127
Figure 7.8: Return losses of the SPDT.....	127
Figure 7.9: Insertion losses of the SP3T.	128
Figure 7.10: Return losses of the SP3T.....	128
Figure 7.11: Circuit diagram of customised RF switching system.	130
Figure 7.12: Four-layer PCB stack.	131
Figure 7.13: RF paths validation in CST.	132
Figure 7.14: Simulated reflection coefficient of RFC to RF1 path.....	132
Figure 7.15: Simulated transmission coefficient of RFC to RF1 path.....	133
Figure 7.16: Four layered PCB design (a) Top layer (b) Ground layer (c) Power layer (d) Bottom layer.	133
Figure 7.17: PCB controller for oil slick thickness measurement.	134
Figure 7.18: Four antenna-sensor array in cuboid configuration.	136
Figure 7.19: Simulation plot of transmission coefficient for different oil thickness. (a) Antenna-sensors 3 and 4 (b) Antenna-sensors 1 and 2.	138
Figure 7.20: Experimental setup for dielectric measurements.....	139
Figure 7.21: Dielectric measurement of HANACO oil and seawater.....	139
Figure 7.22: 3D model of enclosure (a) Perspective (b) Top cover.....	140
Figure 7.23: 3D Printed enclosure (a) Base (b) Perspective.	141
Figure 7.24: In situ microwave sensor for oil slick thickness measurement.	142
Figure 7.25: Top view of experimental setup for the oil slick thickness measurement.	142
Figure 7.26: Antenna-sensor 1 plot of measured reflection coefficient for 69 mm and 92 mm oil thickness.	143
Figure 7.27: Antenna-sensor 2 plot of measured reflection coefficient for 69 mm and 92 mm oil thickness.	144
Figure 7.28: Antenna-sensor 3 plot of measured reflection coefficient for 23 mm and 46 mm oil thickness.	144
Figure 7.29: Antenna-sensor 4 plot of measured reflection coefficient for 23 mm and 46 mm oil thickness.	145
Figure 7.30: Plot of measured transmission coefficient for oil thickness (a) 23 mm (b) 46 mm.	145
Figure 7.31: Plot of measured transmission coefficient for oil thickness (a) 69 mm (b) 92 mm.	146

List of Tables

Table 2.1: Test results for measurement of oil thickness [31].	23
Table 2.2: Benchmarking of oil slick thickness sensors	33
Table 3.1: Relative dielectric constants and conductivities for some media [45].	38
Table 4.1: Dielectric Properties of Seawater [54].	47
Table 4.2: Experimental configurations for medium and buffer [60].	49
Table 4.3: The Dimensions of the buffer enclosure [63].	53
Table 4.4: Classification for signals based on the bandwidth [69].	57
Table 4.5: Dimensions of initial base antenna.	58
Table 4.6: Dimensions of trefoil antenna.	63
Table 4.7 Fidelity Factor of antenna-sensor	67
Table 4.8: Buffer parameters.	68
Table 4.9: Properties of the PDMS phantom in CST.	70
Table 4.10: Parameter details for fabricated trefoil antenna.	72
Table 4.11: Properties of two-part base elastomer and curing agent [84].	75
Table 4.12: Comparison of Fabricated Antennas for Seawater Sensing Applications	80
Table 6.1: Dimensions of Base Antenna Parameters.	101
Table 6.2: Braid antenna fabrication details.	106
Table 6.3: Comparison of antennas for sea surface communication	117
Table 7.1: Four layered stack [126].	131

Abbreviations and Acronyms

ADIOS	Automated Data Inquiry for Oil Spill
AUV	Autonomous Underwater Vehicle
BOP	Blowout Preventer
BS	Beam Splitter
BSN	Buoyed Sensor Node
BW	Bandwidth
CAD	Computer-Aided Design
CASI	Compact Airborne Spectrographic Imagers
CCD	Charged-Coupled Device
CMOS	Complementary Metal Oxide Semiconductor
COTS	Commercial Off-The-Shelf
CPW	Coplanar Waveguide
CSS	Chirp Spread Spectrum
CST	Computer Simulation Technology
DG	Diffraction Grating
DWH	Deepwater Horizon
FCC	Federal Communications Commission
FLIR	Forward Looking Infrared
FPSO	Floating Production Storage And Offloading
GNOME	General NOAA Modelling Environment
GPIB	General Purpose Interface Bus
HANACO	Used Heavy Aromatic-Naphthenic Azeri Crude Oil
HB	Hyperband
pHEMT	Pseudomorphic High Electron Mobility Transistor
HF	High Frequency
IR	Infrared
ISM	Industrial Scientific And Medical
LDR	Light-Dependent Resistor

LIDAR	Light Detection And Ranging
LoRa	Long Range Communication
LoS	Line Of Sight
LPWA	Low Power Wide Area
LTE	Long Term Evolution
MLC	Maximum Likelihood Classification
MMIC	Monolithic Microwave Integrated Circuit
MWR	Microwave Radiometers
NB	Narrowband
NOAA	National Oceanic And Atmospheric Administration
NRDA	Natural Resource Damage Assessment
SDR	Software Defined Radio
SoC	System on Chip
WiMax	Worldwide interoperability for Microwave access
WiBro	Wireless Broadband

Chapter 1

Introduction

The background and motivation of this research for the use of microwave and radio frequency (RF) to detect oil spill and determine the oil slick thickness in seawater and freshwater, is presented in this chapter.

1.1 Research Motivation

Humans have been using crude oil in one form or the other for thousands of years. From the ancient Egyptians that used it to mummify their dead to the Babylonians that waterproofed their boats with it [1]. However, the real potential of crude oil was unleashed in the mid-19th Century. The modern history of the world is entwined with that of oil. The Industrial revolution, the invention of the automobile, the World Wars; were all powered by oil. It has been able to uplift countries from squalor to prosperity in an instance. We live in an oil world; we are surrounded by it. Oil is presently used to power our industries, automobiles, aviation, homes and offices. The derivatives of crude oil have permeated every sphere of our lives. From some of the plastics we use to some synthetic rubber, cosmetics, chemicals and lubricants; the importance of crude oil cannot be overemphasised [2].

Oil has an edge over other energy sources in that it is concentrated and could be easily transported over long distances. Sometimes, during these transportations, accidents do occur. Like the largest accidental oil spill in US history; BP's Deepwater Horizon's oil spill [3]. Oil spilled into the Gulf of Mexico from April to September 2010. This resulted in the loss of lives of 11 workers with 134 million gallons of oil spilled resulting in about 2,100 km of the U.S Gulf Coast covered in oil. BP was forced to pay \$ 65 Billion as settlement. The incident was as a result of the failure of the blowout preventer (BOP) [4] , which was connected to the riser for oil drilling from the well. The BOP was supposed to seal the oil well to prevent the spillage when the rig exploded but it failed to do so.

Around a year later, a similar incidence occurred off the coast in the Gulf of Guinea. The Bonga oil spill is one of the largest in Africa involving Shell Nigeria Exploration and Production Company's (SNEPCO) [5]. The pipeline connecting the well to the Float Production Storage and Offloading (FPSO) facility ruptured and oil was released into the sea. Around 40, 000 barrels gushed into the Atlantic covering an area of about 950 square kilometres [6]. Shell was fined \$3.6 Billion for the damage and the loss of livelihoods for the communities that depended on the area for their sustenance.

A robust monitoring system for oil spill detection would have been very useful in the early detection of the oil spill in both cases highlighted above and for most of the countless incidences of oil spills that have happened. The solutions that have been employed for monitoring of oil spills shall be discussed.

Several techniques have been used over the years for the detection of oil spillage. These methods could be broadly classified into two; active and passive remote sensing depending on whether the sensors emit signals (active) or if it relies on signals generated by the environment (passive).

The obvious limitation of the passive sensors is that it needs the perpetual presence of the source of illumination or signal to be able to remotely sense. For example, at night or in the absence of the sun, most passive sensors fail to detect changes in the environment except in the case of a thermal infrared.

The two most popular forms of active remote sensing are RADAR, which stands for radio detection and ranging, and LIDAR, light detection and ranging. RADAR sends out microwave or radio signals at a target and measures the reflected signals for detection. In the case of LIDAR, the emitter transmits light waves and receives the reflected signal using a collector to detect any changes.

Another important measurement apart from oil spill detection is the determination of the oil slick thickness to ascertain the extent of the oil spillage and the volume of oil discharged. These information are used for several reasons such as [7]:

1. determination of the size of oil spillage,
2. taking legal actions based on amount of oil discharged,

3. optimising oil spill countermeasures such as in situ burning and chemical dispersion,
4. understanding the physics of oil evaporation and oil spill spreading.

As stated by [7], the field of the oil slick thickness measurement is at a very early stage of development. Although several solutions have been proposed, very few are viable. Broadly, the oil slick thickness measurement could be classified into two; remote measurements and in situ measurements.

In this research, for the first time, a microwave based in situ oil spill sensor capable of oil spill detection and oil spill thickness determination was developed. The sensor comprised of four polydimethylsiloxane encapsulated antenna-sensor array with a bespoke RF switching circuit. The antenna-sensor array was specifically developed to operate in both seawater and freshwater with ultra-wideband characteristics. The encapsulation undertaken at the clean room facility of the University of Edinburgh, ensured that there was negligible impedance-mismatch between the antenna-sensor and the water medium.

None of the different methods deployed in prior art used the in situ scattering parameters from radio frequency antennas to determine oil spill or oil slick thickness. Radio frequency, unlike optical communication, is not obstructed by opaque objects and its fidelity is not degraded by introduction of light sources. And because the antenna-sensors are encapsulated by polydimethylsiloxane (PDMS), they are not prone to rusting like those deployed in conductive and capacitive contact-based method of oil spill detection and oil slick thickness measurements.

To enable real-time monitoring of the water medium, a water surface radio frequency long range (LoRa) telemetry subsystem was developed to publish the data obtained from the oil spill sensor continuously on the Internet. Although acoustic signals have greater advantages to RF signals underwater due to the attenuation and dispersion of the latter by the water medium, however, for water surface communication RF has the merit of higher bandwidth and lower latency.

1.2 Research Investigations

The overarching challenge of the research study is the investigation of the viability of the use of microwave techniques for the detection of oil spill and determination of oil slick thickness in the underwater environment. However, some secondary research challenges were developed in the process such as:

1. the investigation into the dielectric properties of the North Sea water,
2. the design and development of an ultra-wideband polydimethylsiloxane encapsulated antenna-sensors for underwater sensing,
3. the development of a bespoke RF switching circuit for the antenna-sensor array,
4. the design of LoRa water surface communication backbone.

1.2.1 Design Challenges

A. Dielectric Measurements of North Sea Water

The seawater, the primary propagation medium for this research, has higher salinity than freshwater. To guide the design and development of antennas and sensors for this research, a study was embarked upon to determine the dielectric properties of the seawater. The reflection, absorption and transmission of radio frequencies are governed by the dielectric properties [8].

Seawater samples were obtained in Newhaven, Portobello and Musselburgh. They were transported to the laboratory where the experiment was performed. The results obtained were compared with the Debye's model and the CST Microwave Studio model to establish a baseline for the research.

B. Underwater Antenna Design

For radar-based microwave oil spill detection and oil slick thickness measurement, a wideband antenna is desired to be able to operate in materials with diverse permittivity such as brine and crude oil, as well as for imaging purposes. One of the greatest challenges of RF antenna operations underwater is the mismatch between the antenna and the water medium which results in very high reflected signals. To ameliorate this,

a buffer layer has been employed around the antenna to serve as a matching medium between the antenna and water.

For the first time, this research investigated the use of polydimethylsiloxane (PDMS) to encapsulate a novel ultra-wideband trefoil antenna for underwater operation. The advantage of the PDMS technique of matching is that it can take the shape of the antenna just as the liquid buffers do, and it also has additional advantages of ruggedness and compactness compared to the liquid buffer. The resulting antenna-sensor was capable of ultra-wideband operations in both seawater and freshwater.

C. Performance Evaluation of Developed Underwater Microwave Sensors on the Detection of oil spill

After the antenna-sensors were fabricated, their performance was verified based on their ability to detect oil spill in both seawater and freshwater. Due to the high combustibility of crude oil, rapeseed oil was initially used as a proof-of-concept inclusion. A Faraday cage, which consisted of an acrylic container padded with copper foil to prevent electromagnetic interferences, was used as the sensing region for the two antenna-sensors. The S parameters for both antenna-sensors were used to evaluate the capability of the system to detect when the water medium had been adulterated by rapeseed inclusion.

Finally, a heavy aromatic-naphthenic Azeri crude oil was used for the experiment to validate the performance of the system to detect oil spill in both seawater and freshwater media. It is noteworthy that no far-field experiment was undertaken because the physics of electromagnetic wave propagation in water medium is different from that obtainable in free space and the antenna-sensors were radiating in the near-field regions.

D. Development of Telemetry System for Oil Sensor using LoRa Surface Communication

The microwave oil sensor operates on the water surface to be able to detect and measure oil slick thickness. Thus, for the sensor node to transmit its data in real-time, a telemetry system is required. A long range (LoRa) communication technique was considered due to its long distance and low power consumption. The availability of LoRa gateways that can relay the data to the Internet also made it attractive.

The influence of the water surface on radio frequency propagation was investigated to develop LoRa antenna capable of optimal transmission. An oil-impregnated paper buffer was developed to improve the performance of a novel braid antenna designed to operate at 868 MHz, which is Europe's industrial scientific and medical (ISM) band.

To validate the antenna's performance, it was benchmarked against some commercial off-the-shelf (COTS) LoRa antennas operating at the same frequencies. Afterwards, the sensor node with braid antenna, with buffer and that without buffer, were deployed in the field to compare their performances.

E. Compact RF Switching Circuit for Underwater Sensors

To enable the use of four antenna-sensor array, a switching circuit is required to select and operate each of the four antenna-sensors. Using two single pole double throw (SPDT) RF switches, a two-input, four-output compact RF switching circuit was developed. The switching circuit was controlled using a microcontroller and could be wirelessly activated using a Bluetooth and an android application.

To conform to regulations and to ensure optimal performance of the RF switch, it was developed on a four-layered PCB board. The two inner layers were used as ground and power by covering them with a copper pour at 0 V and 5 V respectively.

F. Performance Evaluation of Oil Slick Thickness Determination using Antenna-sensor Array

Using the RF switching circuit developed, four antenna-sensor array were able to be incorporated into a portable enclosure that was 3D printed purposely for this project. The four antenna-sensors were arranged in a cuboid fashion to enable it detect oil spillage and determine oil slick thickness. Two antenna-sensor pairs were placed so that they faced each other in a horizontal and vertical fashion respectively.

A transparent acrylic container was used with a tap at the bottom to discharge the mixtures as more crude oil was added to determine the capability of the system to measure the corresponding oil slick thickness. This was simplified since oil is less dense than water, thus it floats at the surface.

1.2.2 Research Objectives

The main objectives of this research are:

1. To investigate the use of remote and in situ techniques for the detection of oil spill and determination of oil slick thickness.
2. To investigate the propagation of electromagnetic waves in water medium and the dielectric properties of water.
3. To investigate antennas for underwater microwave communication and sensing.
4. To validate oil spill detection prototype in determining crude oil inclusion in unadulterated water.
5. To develop a water surface LoRa communication backbone for oil spill sensor's real-time capability.
6. To develop RF switching circuit to be integrated with the proposed antenna-sensor array.
7. To implement and evaluate antenna-sensor array for the measurement of oil slick thickness.

1.3 Original Contributions of Thesis

The research undertaken has come up with the following key contributions:

1. Ultra-wideband trefoil antenna and encapsulation of the antenna in PDMS for underwater microwave sensing.
2. Dielectric measurements of the North Sea water and comparison to Debye's and CST's model.
3. Water Surface communication backbone using novel LoRa antenna with oil-impregnated paper buffer.
4. Performance of the antenna-sensor in the detection of oil spill using microwave techniques.

5. Novel two-input, four-output RF switching circuit for antenna-sensor array.
6. Developing a novel in situ microwave sensor for the determination of oil slick thickness.

1.4 Simulation Package

There are several candidates for the high frequency antenna simulations with each having its advantage(s) and disadvantage(s) [9]. GdfidL Electromagnetic Field Simulator computes electromagnetic fields using single-node, multiple-core systems or clusters of such systems[10]. It is cheap and easy to use. However, it is only available on UNIX-based systems and the geometry tool is complex.

Ansys HFSS is a 3D electromagnetic simulation software for the design and simulation of high frequency products such as antennas, filters and printed circuit boards [11]. It is a powerful tool for frequency domain simulations and has a very rich list of boundary conditions. Some of its disadvantages are that its automatic mesh functionality is not always perfect and time domain and multiphysics capabilities were just recently added.

Comsol is a pioneer in multiphysics design. It is a general-purpose simulation software that is based on advanced numerical methods with multiphysics and single-physics modelling capabilities. It has a complete modelling workflow from geometry to postprocessing. It is also user-friendly [12]. Some of the shortcoming of Comsol are that the S parameter solver is not very convenient, the postprocessing capabilities is not fully developed, the port excitation mode description is inconvenient, and its geometry input is limited.

The advanced computational electromagnetics 3D parallel (ACE3P) is a comprehensive set of conformal, higher-order, parallel finite-element electromagnetic codes that is capable of multiphysics design in thermal, mechanical and electromagnetic simulations. It has high fidelity modelling, improved solution accuracy and speed [13]. However, it is very complex to use, not commercial and has very limited technical support.

CST Microwave Studio is a high-performance 3D electromagnetic (EM) analysis software package used for the design and optimisation of EM components and systems such as antennas, filters, printed circuit boards, cables, chips, connectors, biomedical and optical structures. Although the tetrahedral mesh was introduced relatively recently and its eigenmode solvers are slow, it offers several advantages. It has very powerful time domain and frequency domain solvers compared to the rest. These solvers can perform hybrid simulations offering the flexibility to analyse multiple components that make up whole systems in an efficient and straightforward way. It can be combined with other SIMULIA products for multiphysics and integrated electronics simulations. CST allows EM simulation to be integrated into the design flow and drives the development process from the earliest stages [14]. CST is user-friendly with rapidly evolving capabilities. It has excellent technical support, community and documentations. These were some of the reasons CST Microwave Studio was selected as the EM simulation package of choice for this research.

1.5 Overview of the Thesis

The thesis is organised into eight chapters as follows:

Chapter 1: Introduction

This chapter presents the background and motivation to carry out the research. The research objectives and design challenges encountered during the research are highlighted. A brief introduction of some remote sensing and in situ methods used for underwater oil spill detection and oil slick measurement are presented.

Chapter 2: Overview

This chapter presents the literature review on oil spill detection and oil slick thickness measurements. In this chapter, the state of the art for the detection and determination of oil slick measurement are presented. Their principles of operations were thoroughly investigated. An in-situ microwave oil sensor is presented that comprised of the proposed PDMS-encapsulated antenna-sensor with RF switching circuit developed in this thesis.

Chapter 3: Propagation of Electromagnetic Waves in Water

This chapter investigates the transmission medium using the foundational Maxwell's equation and extending it to the propagation of electromagnetic waves in a lossy medium such as seawater. Subsequently, the mathematical models were validated using experimental data obtained from three samples of seawater acquired in three different locations. The relative permittivity and loss tangent were discussed.

Chapter 4: Underwater Antenna-Sensor Design and Fabrication

This chapter presents the design and development of underwater antenna-sensor for microwave oil spill detection and oil slick thickness measurement. The chapter started by establishing the requirements of an underwater antenna before proceeding to design a trefoil antenna and encapsulating it in PDMS for underwater application. The antenna-sensor was submerged in both seawater and freshwater and the measured results were compared to results obtained with the simulations. The bandwidths improvements were discussed with respect to the Federal Communications Commission (FCC) standards.

Chapter 5: Microwave Oil Spill Detection Prototype

In this chapter, a microwave oil spill sensor was developed using the antenna-sensor fabricated in chapter 4. Three antenna-spacing of 15 mm, 50 mm and 70 mm were selected. The oil spill sensing region comprised of a 3D printed polylactic acid (PLA) container padded with copper foil. Due to the high combustibility of crude oil, the experiment began with rapeseed oil that had similar dielectric constant with the former. Afterwards, the experiment proceeded with caution using heavy aromatic-naphthenic Azeri crude oil. The experiment was done in both seawater and freshwater.

Chapter 6: Communication Backbone for Oil Spill Telemetry System

In this chapter, a design and implementation of a water surface radio frequency communication backbone for the telemetry system of the in-situ microwave oil spill sensor was undertaken. Emphasis was placed on the design, fabrication, testing and implementation of a novel braid antenna capable of both submerged and water surface communication at 868 MHz LoRa range of frequency. An oil-impregnated paper buffer region was incorporated around the braid antenna. It was shown that the

introduction of this barrier had substantially improved the performance of the degraded antenna when placed on and in water.

Chapter 7: In Situ Microwave Oil Spill Detection and Oil Slick Thickness Measurement Sensor

In this chapter, a novel compact RF switching circuit was developed on a four-layer PCB board. It was integrated with an array comprising of four antenna-sensors to detect oil spill and determine oil slick thickness. The work began with evaluating SPDT and single pole three throw (SP3T) evaluation boards before adopting two SPDT switches in a two-input, four-output configuration. An enclosure for the setup was 3D printed based on the dimensions determined from the CST simulations. Crude oil was used as an inclusion in a seawater medium. Oil floats on water due to its lower density. This allowed the developed sensing system to determine the oil slick thickness using the orientation of the antenna-sensor array.

Chapter 8: Conclusion and Future Work

This chapter concludes the research studies conducted and described in this thesis. Contributions of this thesis are re-highlighted and further research based on the developed in situ microwave oil spill detection and oil slick thickness sensor are suggested for future work.

1.6 Publications Arising from the Research

During this research, the following journals and conference papers have been published and submitted:

Journal papers:

1. A. Dala and T. Arslan, "Design, Implementation, and Measurement Procedure of Underwater and Water Surface Antenna for LoRa Communication", *Sensors*, vol. 21, no. 4, Art. no. 4, Jan. 2021, doi: 10.3390/s21041337.
2. A. Dala and T. Arslan, "In Situ Microwave Sensors and Switching Circuit for Oil Spill Thickness Measurement," in *IEEE Sensors Journal*. (Accepted for publication)

3. A. Dala and T. Arslan, “In-situ remote sensor for the detection of oil spill in seawater and freshwater using microwave techniques,” in *Elsevier Measurement: Sensors*. (Journal Submitted, Under Review)
4. A. Dala and T. Arslan, “Compact Wideband Trefoil Antenna for Underwater Microwave Applications,” in *IEEE Transactions on Antennas and Propagation*. (Journal Submitted, Under Review)

Conference papers:

1. A. Dala, M. S. R. Bashri, and T. Arslan, ‘Investigation into the Properties of the North Seawater for Radio Frequency Propagation’, p. 72 (5 pp.)-72 (5 pp.), Jan. 2018, doi: 10.1049/cp.2018.1680.
2. A. Dala, T. Arslan, and I. Saied, ‘Design of a Triangular Slotted Parasitic Yagi-Uda Antenna for Underwater Linear Sensor Network’, in *2019 Conference on Microwave Techniques (COMITE)*, Apr. 2019, pp. 1–4. doi: 10.1109/COMITE.2019.8733431.
3. A. Dala, A. Adetomi, G. Enemali, and T. Arslan, ‘RR4DSN: Reconfigurable Receiver for Deepwater Sensor Nodes’, in *2018 NASA/ESA Conference on Adaptive Hardware and Systems (AHS)*, Aug. 2018, pp. 280–284. doi: 10.1109/AHS.2018.8541455.

Chapter 2

Overview

In this chapter, a comprehensive review on the current oil spill detection and oil slick thickness measurement systems is presented. For oil spill detection, currently radar is one of the most popular techniques that is deployed. There are three main configurations of radar which are side-looking airborne radar (SLAR), synthetic aperture radar (SAR) and a third less used type, ship-borne radar. Each has its advantages and demerits. SLAR, is cheaper and mostly used in airborne systems such as an aircraft. The ship-borne radar is used on ships offering a range of 3 to 80 kilometres depending on the antenna height. SAR has wider coverage and offers better resolution. It is often used on satellites for remote sensing. SAR is an active remote sensing technique that involves mounting radar on a straight-line moving platform, which could be an airplane or a space-borne system like satellite. However, SARs have weaknesses with respect to inflexibility based on time and location. It is affected by high latency with respect to oil spill detection and it is not efficient in continuous tracking of oil spillage.

The demerits of the satellite SARs are more pronounced for the measurement of oil slick thickness. In this regard, several in situ technologies have found greater application success such as the capacitive, conductive and optical based methods. However, the capacitive and conductive methods are prone to rusting when used in contact with the water medium. The optical methods can be affected by opaqueness of the oil and introduction of external light sources. Radio frequencies are more robust in that regards.

2.1 Oil Spill Detection

For marine or ocean remote sensing, there are distinctly two modes of oil spill detection: water surface and underwater remote sensing [15]. The first and most frequently deployed is the water surface remote sensing. Numerous types of passive and active

remote sensing methods deploy techniques such as visible spectrum, infrared, near infrared, ultraviolet and microwave. The latter is the most popular method.

SAR has wider coverage and offers better resolution. This radar is directed at an area of interest to produce fine-resolution images in 3 dimensions or 2 dimensions. Like any imaging radar, an electromagnetic signal travelling at the speed of light targets a surface. The signals are reflected from the surface as a backscatter which is recorded, as well as its time delay. The SAR image is developed using the strength of the backscatter and its time delay [16]. This technique has been extensively used in the detection of oil spill in marine and coastal areas. Some of the popular operational satellite SAR include RADARSAT, Sentinel-1, Kompsat-5, TerraSAR-X and TecSAR.

In [17], SAR was used for the detection of marine oil spill over the Indian Ocean using four oil spill events as case studies. An improved methodology using S-1 SAR satellite data at speed between 3 to 9 m/s for all events were utilised. Varying atmospheric conditions and influence of wind currents on oil spill spreads and degradation were investigated. The oil spills trajectory production was modelled using General National Oceanic and Atmospheric Administration (NOAA) operational modelling environment (GNOME) model. The oil spill weathering processes were modelled using automated data inquiry for oil spill (ADIOS). A maximum oil spill movement of 33 kilometres from the source of the spill was observed and the evaporation of the crude oil was observed to be high. The study concluded stating the cost effectiveness of the SAR based oil spill detection technique.

SAR and underwater gliders were used in combination to detect oil seeps in the lower Congo basin [18]. One SAR image of the site was captured at least after every 12 hours for a period of 21 days. Two concomitant underwater gliders were fitted with fluorescence sensors and the results obtained from them were compared with those from the SAR images. 80 recurring oil seeping sites were identified using SAR. Six out of those sites were investigated using the underwater gliders. Consequently, vertical pipes of hydrocarbon fluids detected by the gliders corresponded to the images obtained from the SAR.

In [19], the weakness of the satellite SAR with respect to its inflexibility based on time and location were highlighted. It is one of the most used methods of oil spill

detection, however, it suffers from long latency based on when the oil spill occurs and the time when a satellite can send an image on the site and its inability to continually track the spillage. Thus, they proposed the use of an airborne L-band, low noise, high resolution uninhabited aerial vehicle SAR (UAVSAR) for oil spill response. It was able to get several more images in an hour compared to the satellite SAR. Notwithstanding, the limitations of the UAVSAR were identified in the study. Being a science instrument and not meant for urgent response platform, there is the need for oil spill response community to develop and deploy airborne SARs in the form of a large aircraft capable of long-range communications or smaller aircrafts for targeted area of coverage. This would make the airborne SAR more expensive than the satellite SAR because the response community do not invest in the satellite SAR expeditions.

To mitigate against the weaknesses of the satellite SAR, a proof-of-concept model for the use of multiple sensors including satellite SAR, in-situ measurements and multispectral imaging for the detection of oil emulsions was put forward in [20]. The challenges and pitfalls of oil spill detection by imaging using imaging radar was reviewed in [21], where the difficulty of discriminating between radar signatures of oil films and biogenic slicks were highlighted. These often led to misleading results obtained for the oil spill detection. With satellite SAR, the preponderance of false positives for oil spills that are misinterpreted and false negative where a detection occurs when nothing exists inspired [22] to adopt the use of an in-situ autonomous system for the detection of oil spill. The proposed system termed ARIEL consisted of a drone and an unmanned surface vehicle (USV). Both systems worked in a collaborative fashion with oil detection sensors installed in each of them. The drone, the first layer, was installed with a visible and a thermal camera package. It was used to eliminate false negatives. The second layer, the USV, was fitted with a fluorosensor. It validated all cases reported by the drone and detected unnoticed cases. The ARIEL system aimed to reduce the cost associated with deploying manpower in cases of false negatives or positive and the corresponding human risks. However, the configuration of this system makes it expensive and the cost of maintaining a system like this could become exceedingly high.

In [23], the Progetto pilota Inquinamento Marino da Idro-carburi project (PRIMI) was combined with a forecasting and observation modules responsible for the oil spill detection based on SAR and LIDAR, to detect oil spill and forecast the oil spill displacement after the detection. The forecasting module was based on Lagrangian numerical circulation models. The in-situ models were based on simulation. Several oil spills were detected using the observation modules. These spills were verified in situ using the forecasting modules. In this study, a case for further work to combine the satellite models and a realistic in situ data to refine the PRIMI data was made.

The underwater oil spill remote sensing also involves the use of both passive and active sensors [15]. Some of these techniques are used in the detection of oil in the water column or at the bottom of the sea. One of such techniques employs the use of ultrasonic signals to detect oil spill based on the difference in the acoustic profile of water and oil at the bottom of the sea. Laser fluorosensors have been used for the detection of oil spill up to 2 meters in the water column. It does this by detecting the aromatic compounds found in oil. Chemical analysis comprising of spectrometry or fluorometry have been used to also detect oil in water. The use of camera for the detection of oil has also been employed.

The detection of oil spill with respect to thermal infrared (IR) depends on the temperature difference between the emulsified oil and the surrounding water. During daytime, the sun heats up the water surface, however, the high viscosity of the emulsified oil means that internal convection is restricted. Thus, the emulsified oil layer does not lose heat to the underlying water surface and therefore is warmer. These changes however disappear at night except in the few circumstances that the air temperature is substantially warmer than the water surface temperature. Here in, lies the limitations of this technique [24].

A spill oil point-of-testing device (SOPD) was developed in [25] for on-site fluorescence monitoring of oil concentrations. SOPD adopts a multi-mega pixel approach which can detect oil spill even in the presence of environmental noise caused by dust and other impurities. This has superior performance compared to photodetectors that are commonly used in existing instrumentation that rely on single-pixel

detection. It uses light-emitting diodes (LEDs) as excitation source and a complementary metal oxide semiconductor (CMOS) image sensor as a detector.

2.2 Oil Slick Thickness Measurement

Apart from the detection of oil spillage, another important measurement is the determination of the oil slick thickness to ascertain the extent of the oil spillage and the volume of oil discharged. These information have many uses such as for legal action for oil discharged, determination of the effectiveness of oil spill countermeasures, optimisation of oil spill countermeasures, determination of the rate of spread of the discharge, studying the physics of the oil spill spread and evaporation [7].

As an example, the Deepwater Horizon (DWH) oil spill accident resulted in oil slick covering over 149,000 square km off the Gulf of Mexico [26]. The oil spill countermeasures involved pumping 1.8 million gallons of dispersants, emulsifying the oil and enabling easier metabolism by bacteria. The severity of the impact was determined by the natural resource damage assessment (NRDA) trustees by conducting comprehensive toxicity testing program that involved accurately determining the oil slick thickness to ascertain the volume of discharge [27].

As stated by [7], the field of the oil slick thickness measurement is at a very early stage of development. Although several solutions have been proposed, very few are viable. Broadly, the oil slick thickness measurement could be classified into two; remote measurements and in situ measurements. The work shall delve into some of the promising prior arts in both areas of oil slick thickness measurements.

2.2.1 Remote Sensing Oil Slick Thickness Measurement

For oil spill detection, one of the most widely used technique is remote sensing which involves the detection and measurement of the physical properties of the water surface through satellite or aircraft by using emitted and reflected radiation from sensors[28]. These sensors operate by detecting the properties of the sea surface modified by the presence of the oil. The passive sensors used in remote sensing such as ultraviolet (UV), thermal infrared (IR), forward looking infrared (FLIR) and compact airborne

spectrographic imagers (CASI) are not able to penetrate rain, haze, fog or cloud cover [29]. This severely limits their real-time capabilities. Although microwave radiometers (MWR) are often not affected by these limitations and it can provide the oil slick thickness, it is unable to do so for emulsified oil. Under the right conditions, thermal IR can identify relatively thick oil spill. RADAR can penetrate cloud and fog, no matter the time of the day, however, it is less effective.

Thick and thin oil slick were determined in [30] using a multi-source image processing system capable of processing optical, SAR and polarimetric SAR (PolSAR) data. As a case study, an oil seep detected by National Aeronautics and Space Administration's (NASA) uninhabited aerial vehicle synthetic aperture radar (UAVSAR) in the Gulf of Mexico was used.

Oil slick volume was estimated by combining airborne hyperspectral and pool experiment data in [31]. Two HySpex spectral cameras mounted on an aircraft captured the data during a clean-up exercise in the North Sea in 2015. The same cameras were used to capture the data at the pool experiment. The results obtained from the experiments allowed for accurate detection of oil slick and differentiation of thin and thick pixels within the slick. The oil spill thickness was determined in [32] by using sunglint, which is a phenomenon whereby sunlight is reflected from the surface of water at the exact instance a satellite sensor views it [33].

2.2.2 In Situ Oil Slick Thickness Measurement

The accuracy and resolution of the oil slick thickness measurement provided by remote sensing is very low, thus the need for in situ measurements. For in situ measurements, the sensors for the determination of oil slick thickness are usually placed locally in the environment that needs to be measured. This could be contact or non-contact based, depending on if the sensor is submerged in the water body or not, respectively. Several techniques have been used for the in situ oil slick thickness measurements such as thermal IR, conductivity, capacitance and optical methods.

A. Thermal Infrared

In [34], thermal infrared camera was used to determine the oil slick thickness. The setup for the experiment could be seen in Figure 2.1. Two tanks with volume of $45 \times 35 \times 40$

cm were filled with clear and turbid water. Twelve small plastic rings with diameter of 8.3 cm were placed in both the clear and turbid water tank. Using a pipette, different volumes of crude oil were added to the twelve rings. A Testo 890-2 thermal infrared imager placed at about 1 meter above the water surface was used to obtain the brightness temperature of all the oil slicks as well as that of the oil-free water. It was discovered that the optimal time for the oil slick thickness measurement was around local noon, followed by midnight. The worst time for the oil slick thickness measurements were the period before sunrise and after sunset. This work was extended to quantify oil slick thickness on ocean surfaces in [35].

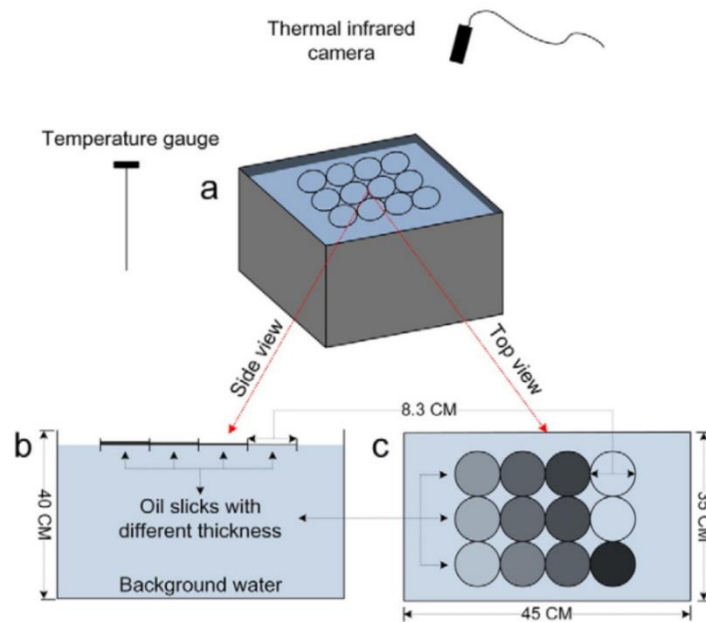


Figure 2.1: Experimental settings for measuring oil slicks with different thicknesses (a) The overall experimental setting; (b) schematic showing side view of the box; (c) 2-D vertical view of the 12 plastic rings, with darker colours showing thicker oil [28].

B. Optical-Based Method

The use of optical fibre-based antennas in conjunction with image processing techniques were used to detect oil slick thickness in [36]. The system proposed consisted of two optical fibres that were used as a transmitter and a receiver. The schematic of the setup could be seen in Figure 2.2 (a). The operation of this system could be explained using Figure 2.2 (b). The transmitter, excited by a light source, transmits the signal incident at 45 degrees that impinges the boundary of the oil and

water with some of the signal refracted and other part of it reflected or scattered. The receiver probe captures this latter signal with the light intensities signifying different oil thickness or concentration. The physics of propagation of the signal in the medium is governed by Snell's law given in (2.1).

$$n_a \sin(\theta_a) = n_1 \sin(\theta_1) = n_b \sin(\theta_b) \quad (2.1)$$

where n_a , n_1 , and n_b are the incident index of the water, incident index of oil and refracted index of air. θ_a , θ_1 and θ_b are the incident angle of the probe, oil reflection angle and refraction angles respectively.

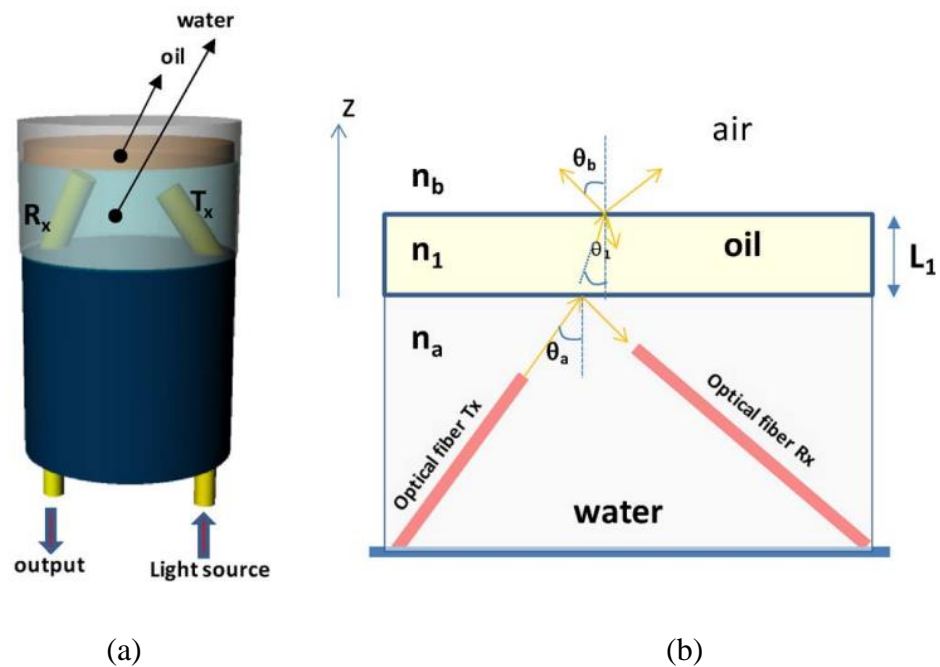


Figure 2.2: (a) Model of proposed sensor (b) Optical ray model of the sensor [30].

The algorithm used for the oil thickness detection could be seen in Figure 2.3 (a). The correct and wrong positioning of the sensor could be seen in Figure 2.3 (b). If the sensor is not in the correct position, it is shaken to ensure it is. If the right position is achieved, the measurement would then be undertaken. This is one of the weaknesses of the system which would require intervention whenever the position of the oil sensor is wrong. The fidelity of the received signal is reduced by the introduction of light and when the visibility of the transmitted signal has been obscured by opaque liquids such as crude oil.

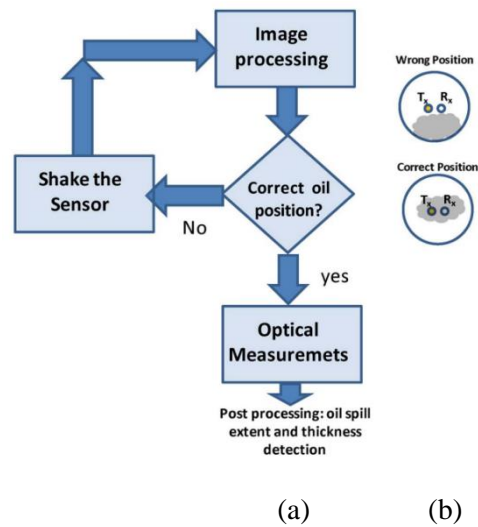


Figure 2.3: Algorithm for Optical Measurement (b) Positioning for the transceivers [30].

The experimental setup for the system could be seen in Figure 2.4 with the different components highlighted. The lighted sensor was empty and was later loaded with liquids. As part of the experiment, Agip 7004 and Toyota LV 75 oil with viscosities of 13.2 and 4.1 at 100 °C were used.

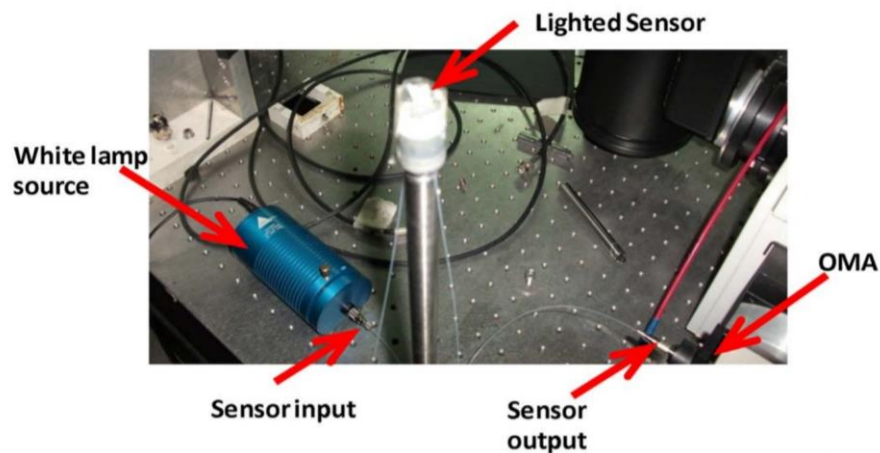


Figure 2.4: Experimental Setup for Optical Measurement [30].

It was observed that the sensor had higher sensitivity for the Agip oil, because it had smaller refractive index even though it had higher viscosity compared to the total sample.

A led-based spectrometer was developed in [37] to measure oil slick thickness of thin oil sheens floating on water. The oil thickness was determined based on the light

absorption analysis. This prototype targeted very thin oil thickness in the range of 100 μm to 3000 μm only under diverse environmental and liquid conditions. The proposed system was comprised of an upper part, the light sensor, which was positioned above the water surface and a lower part, the light emitter, which was submerged underwater and was responsible for emitting light on the bottom layer of the oil sheen. The schematic could be seen in Figure 2.5.

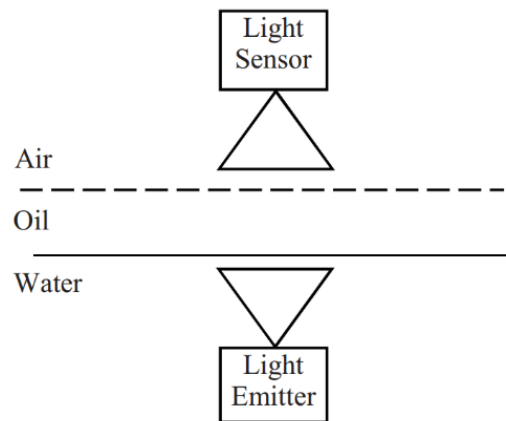


Figure 2.5: Schematic of Spectrometer [31].

An Atmega328P microcontroller was used to perform analysis on the light absorbed to determine the oil thickness. The light emitter comprised of red, orange, yellow, green and blue LEDs working in the visible spectrum of 400 nm to 750 nm, a single infrared (IR) operating at 940 nm and two ultraviolet (UV) LEDs operating at wavelengths of 385 nm and 395 nm respectively. The light sensor was made of TSL230BR light-to-frequency converter chip for measuring light intensity. The initial experimental setup could be seen in Figure 2.6.

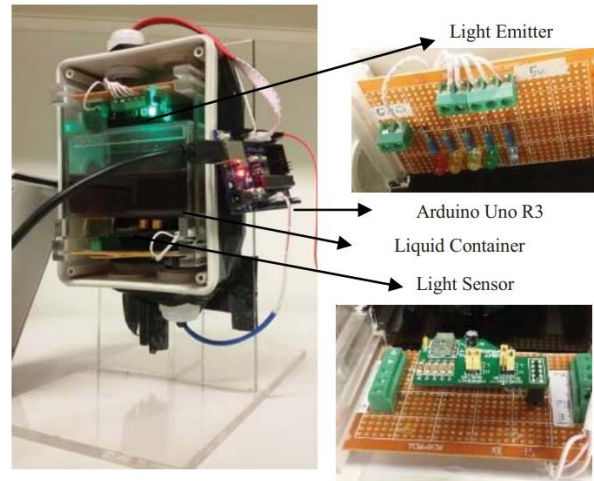


Figure 2.6: Setup of LED-based spectrometer [31].

The results obtained for various oil thickness could be seen in Table 2.1 and Figure 2.7.

Table 2.1: Test results for measurement of oil thickness [31].

Test No.	Actual Thick. (μm)	Avg. Meas. Thick. (μm)	Abs. Error (μm)	S.D.	Sample Size	Sample Duration
1	500	1422.79	922.79	954.35	63	02:06
2	1000	1485.94	485.94	863.82	65	02:08
3	1000	1544.56	544.56	1288.49	48	01:34
4	2000	1882.72	117.28	1043.50	87	02:52
5	2000	2162.05	162.05	815.72	91	03:00
6	3000	2745.70	254.3	395.76	105	03:30
		Avg.	414.48		Avg.	02:31

It could be observed that the absolute error between the actual thickness and the average measured thickness increased as the oil thickness decreased.

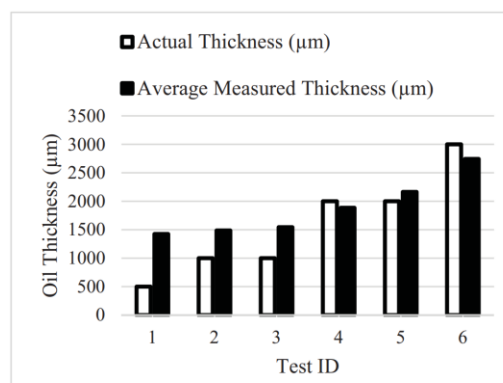


Figure 2.7: Test results for measurement of oil thickness [31].

At 500 μm , the absolute error was almost 1000 μm . It was impossible to establish oil thickness below 500 μm . This was noted in the work to be a consequence of the irregular distribution in the oil film as it could be seen in Figure 2.8.



Figure 2.8: Led-based spectrometer sensor in tank with diesel film [31].

It was further observed that the capabilities of the sensor were further degraded when dealing with opaque liquids such as fresh Hoops crude oil. The oil-fouling of the light sensor lenses contributed to the inaccuracy of the sensor especially at very thin oil thickness.

A spectral domain optical coherence tomography (SD-OCT) was used for the first time in [38] to obtain 3-D structure and superficial characteristics of oil slicks on water. It employed single-pixel optical intensity for high accuracy reconstruction of the oil slick thickness. The schematic diagram is shown in Figure 2.9.

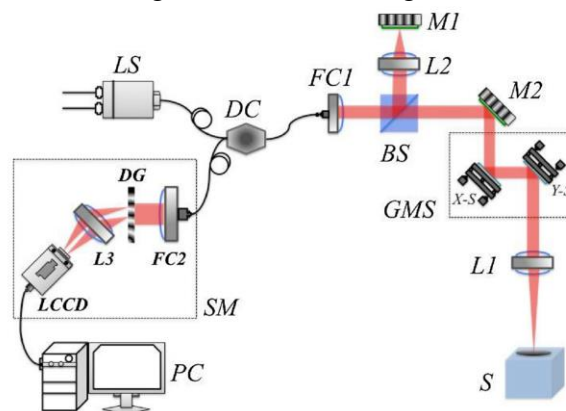


Figure 2.9 Experimental setup of SD-OCT system for measuring. LS: laser source, DC: directional coupler, FC1 and FC2: fibre collimators, BS: beam splitter, GMS: galvanometer mirror system, SM: Spectrometer, L1 - L3: lenses, M1 and M2: mirrors, DG: diffraction grating, L-CDD: linear array charge coupled device, X-S: X-scanner, Y-S: Y-scanner [32].

A continuous-wave laser with a centre wavelength of 1300 nm at 10 mW output power was used as the light source. The output laser was divided into the reference arm and sample arm by the non-polarising beam-splitter (BS) with a ratio of 50/50. The achromatic lens (L1) and galvanometer scanner (GM) in the sample arm focused and scanned the laser beam. The achromatic lens (L2) focused the reference beam and a gold-coated mirror (M) reflected the beam. The directional coupler (DC) recombined and interfered the back-reflected laser beams from the reference and sample arms before transmitting the combined signal to the spectrometer (SM). Here, the fibre collimator (FC2) collimated the laser beam and dispersed it on the diffraction grating (DG) and then using the achromatic lens (L3), it was focused on the linear charged-coupled device (L-CCD) camera.

Diesel and petroleum were used in the experiment. Since diesel is a clean oil and petroleum is a heavy oil, their diffusion area and thickness would vary. A glass cell which floats on the seawater was used as a detecting area for the diesel and petroleum. A schematic of the experimental setup could be seen in Figure 2.10.

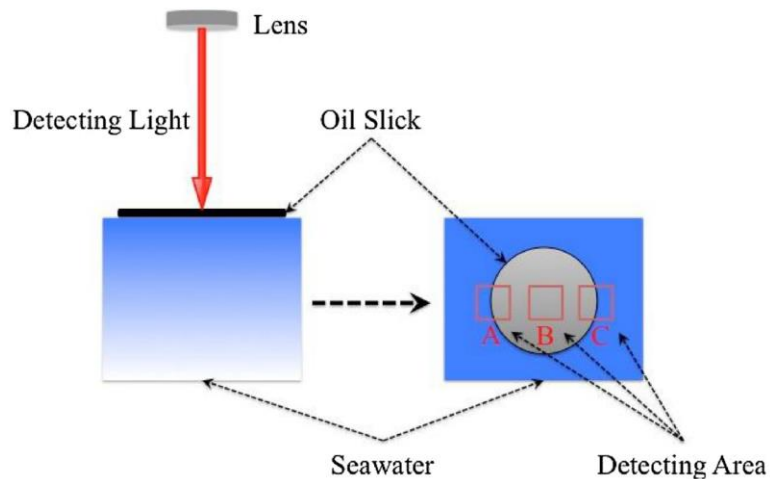


Figure 2.10: Schematic for the glass cell for the measurement of oil slick thickness [32].

The samples were placed outdoors for 15 minutes to allow the oil slick to fully diffuse on the water surface. The imaging region of diesel slick was $2.65\text{ mm} \times 2.69\text{ mm}$ while that of petroleum was $2.17\text{ mm} \times 2.65\text{ mm}$. The volumetric structures and surface characteristics of the oil slick on water surface could be seen in Figure 2.11. In Figure 2.11 (a) and (b) the entire volumetric structures of oil slicks in the central region

(B of Figure 2.10) can be seen. The diesel slick represented by the white arrows at $27 \pm 5.5 \mu\text{m}$ was thicker than that of petroleum at $15 \pm 5.5 \mu\text{m}$ represented by the yellow arrows.

Figure 2.11 (c) and (d) represent the volumetric structures of the petroleum and diesel in the left border (A) of Figure 2.10 respectively. The thickness of the slick for the petroleum and diesel were $19 \pm 5.5 \mu\text{m}$ and $31 \pm 5.5 \mu\text{m}$ respectively. For the right boarder (C) of Figure 2.10, the thickness for the petroleum and diesel slick were $21 \pm 5.5 \mu\text{m}$ and $35 \pm 5.5 \mu\text{m}$ as shown in Figure 2.11 (e) and (f) respectively.

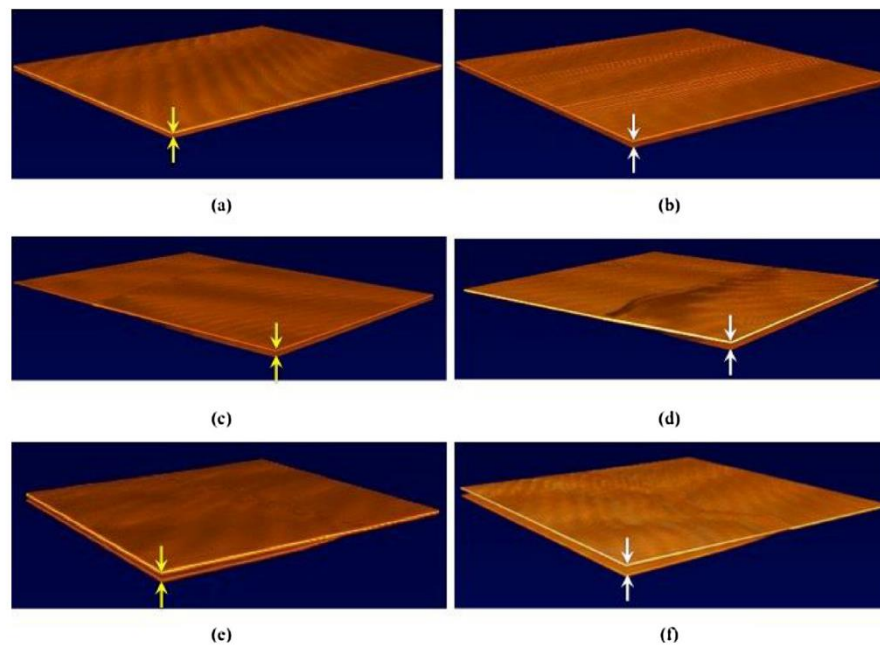


Figure 2.11: Volumetric structures and characteristics of oil slicks (width $\sim 3.2 \text{ mm}$ and length $\sim 5.2 \text{ mm}$) (a) petroleum slick at B, (b) diesel slick at B (c) petroleum slick at A (d) diesel slick at A (e) petroleum slick at C (f): diesel slick at C [32].

C. Capacitive-Based Methods

In [39], a liquid-level gauge was developed. It was made up of two parallel planar electrodes, a capacitance-controlled oscillator and a microcontroller. The electrodes were four metres long. One of the electrodes, E_0 , as shown in Figure 2.12 was long while the other was divided into several segments.

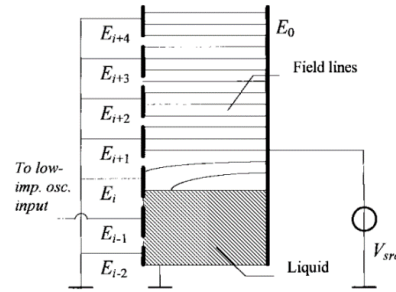


Figure 2.12: Planar Capacitive measurement setup [33].

The capacitances were connected to the ground, the low-impedance measurement-system input or the low-impedance voltage source. The level of the liquid (l) could be ascertained by determining the interface segment, i , that had the value between the capacitance in air (C_{i+1}) and capacitance in the liquid (C_{i-1}). Consequently, the capacitance of the interface segment (C_i) can be interpolated to find the interface position (p) using (2.2).

$$p = l \times \left(\frac{C_i - C_{i+1}}{C_{i-1} - C_{i+1}} + i \right) \quad (2.2)$$

A noncontact capacitance-type level sensing probe was used in [40] to determine liquid levels. In [41], a capacitive contact-based instrument was developed to ameliorate the factors militating against contact-based sensors such as oil fouling, adding, drift with time and dependence on constant calibration. The system only required initial calibration. The sensor was designed as an array of conductive electrodes built on a PCB represented by the diagram in Figure 2.13 (a). The change in the dielectric property of the material surrounding the electrodes results in a change in the measured capacitance and thus it was used to determine if the electrodes were in air, oil or water. By determining the instantaneous interface location of each fluid, the data required for the estimation of the oil slick thickness was obtained.

The sensor was designed to work with differential measurements rather than absolute measurement to eliminate the need for any static calibration formula. The sensing electrodes, connection tracks, anti-fouling pin and the PCB are shown as w , x , y and z respectively in Figure 2.13 (b).

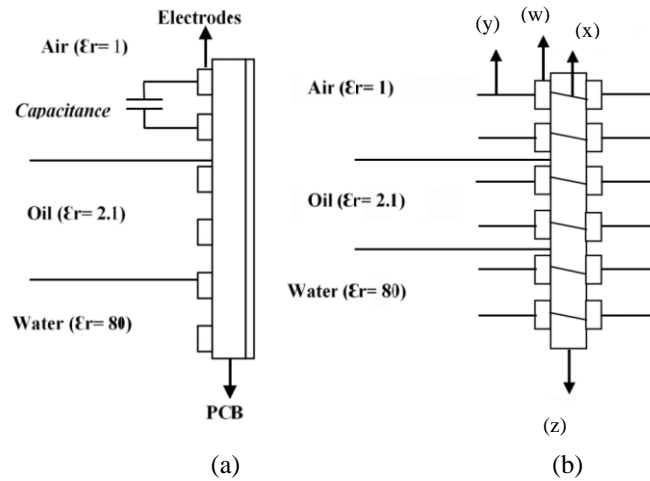


Figure 2.13: (a) capacitive sensor design (b) Enhanced sensor design with pins [35].

The sensor board could be seen in Figure 2.14. It was developed using a four layered board with the two inner layers serving as the connection tracks. The forty-eight conducting electrodes were designed on the two surface layers.

To determine a relative percentage difference (RD), in both static and dynamic conditions, (2.3) was used.

$$RD[i](\%) = \frac{|Current[i] - Calibration[i]|}{Calibration[i]} \times 100 \quad (2.3)$$

where i is the electrode index, *Calibration* is the obtained voltage when the sensor is completely dry, and *Current* is the instantaneous measured voltage.

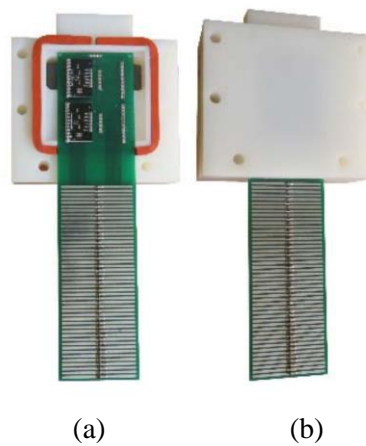


Figure 2.14: Sensor with waterproof enclosure (a) Front (b) Back [35].

Indoor laboratory tests were performed where several quantities of different types of oil were poured in a glass containing water. These oils were diesel, weathered hoops, Hydrocal 300 and Calsol 8240. Each oil was discharged to create eight different oil slick thickness from 3.175 mm to 76.2 mm. To calculate the amount of oil required to achieve certain oil thickness, (2.4) was used.

$$T = V \times \frac{10^{-3}}{A} \quad (2.4)$$

where A is the area of the container measured in m^2 , T is the thickness of oil measured in millimetres and V is the volume of the oil measured in millilitres. The sensor submerged in water with an oil slick during the laboratory test could be seen in Figure 2.15.

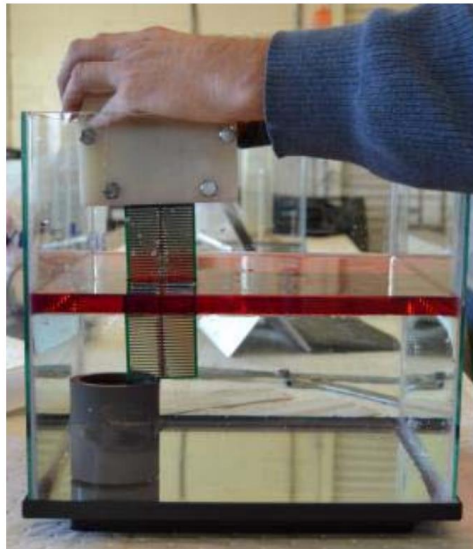


Figure 2.15: Dipping Tests Experiment [35].

D. Hybrids Optical and Conductive-Based Method

Both conductivity and optical measurement methods were used for the determination of oil slick thickness in [42]. They employed the independent use of light sensor array and a conductivity array. The block diagram of the sensor could be seen in Figure 2.16. The processing board for the sensor comprising of the plugs for both the LED and conductivity connectors could be seen in Figure 2.17.

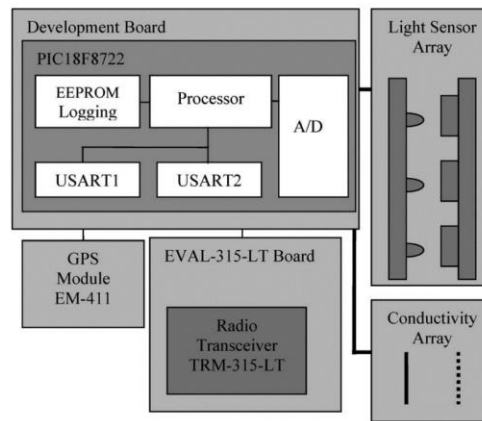


Figure 2.16: Block Diagram of the system [36].

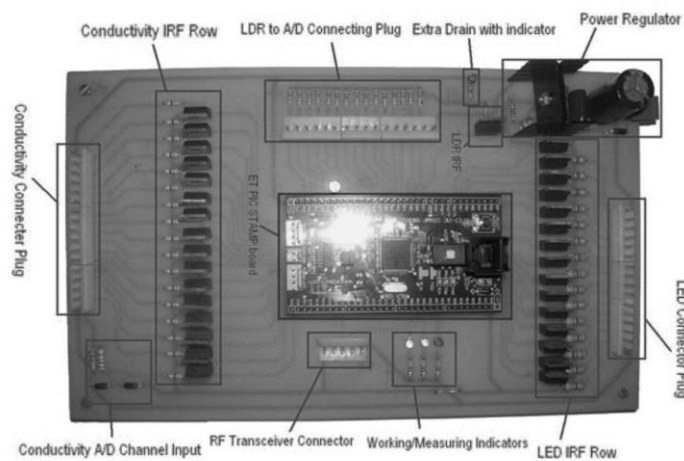


Figure 2.17: System processing board [36].

The light sensor array consisted of an optical colour sensor based on the physics of the variation of the properties and intensity of light propagating through certain medium. Blue LEDs were used as the source of light because of their ability to exhibit very low absorption in water [43] and high absorption in oil [44].

Light-dependent resistor (LDR), capable of detection of blue light in the narrow range between 440 and 490 nm was used as the receiver. The longitudinal arrays of the LED-LDR pair could be seen in Figure 2.18 (a) with the interior shown in Figure 2.18 (b). The LDR resistance is low when the blue light passes through water and it is high when passing through oil. Thus, this was used to determine the oil slick thickness.

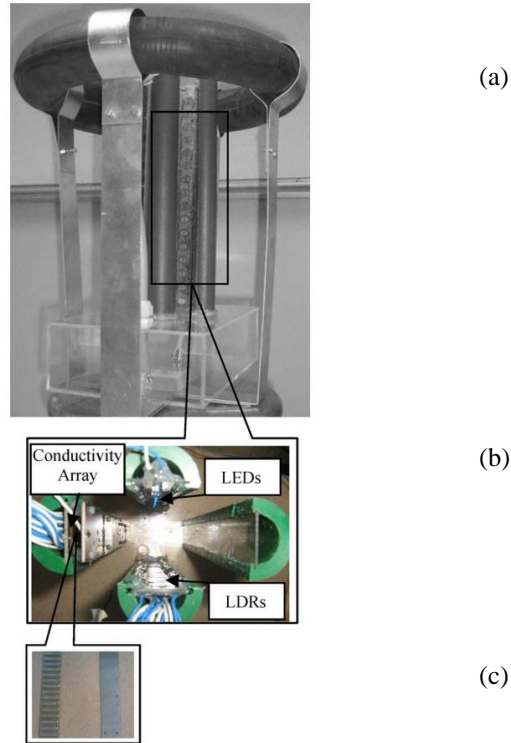


Figure 2.18: Mechanical design of sensor [36].

The conductivity array is a passive sensor that operates on the principle of the varying conductivity of aqueous liquids. The presence of salt in seawater makes it highly conductive while oil has low electric conductivity. Thus, the electric current passing through seawater is high while that passing through oil is low. Just like in the LED-LDR pair, two plates were used in the longitudinal array of conductive metals. These could be seen in Figure 2.18 (c). The experimental setup with the sensor immersed in seawater and an oil slick at the surface could be seen in Figure 2.19.

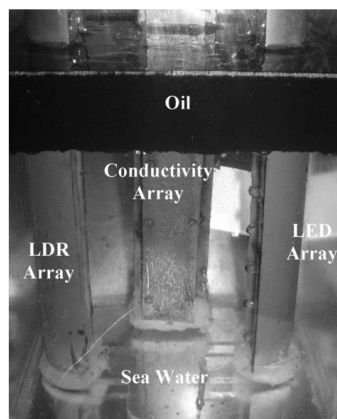


Figure 2.19: Experimental setup for prototype in [36].

E. In Situ Automated Water Mapping Oil Thickness Sampler (WM-OTS)

To validate the data obtained from the optical satellite based on maximum likelihood classification (MLC) supervised procedure, three different in situ oil thickness measurement techniques were considered in [20]; the use of absorbent pads, which were suitable for thin layered oils up to a few hundred micrometres thick; the use of dip plates which depends on the level of emulsification for its performance; the use of an automated water mapping oil thickness sampler (WM-OTS) capable of measuring oil thickness from 5µm to several centimetres. WM-OTS was finally selected for the measurement due to its consistency and broad range of operation. Image of WM-OTS can be seen in panel (A) and (B) of Figure 2.20 respectively. The oil inside a tube could be seen in panel (C) and the area of spill sampling could be seen in panel (D) of Figure 2.20.

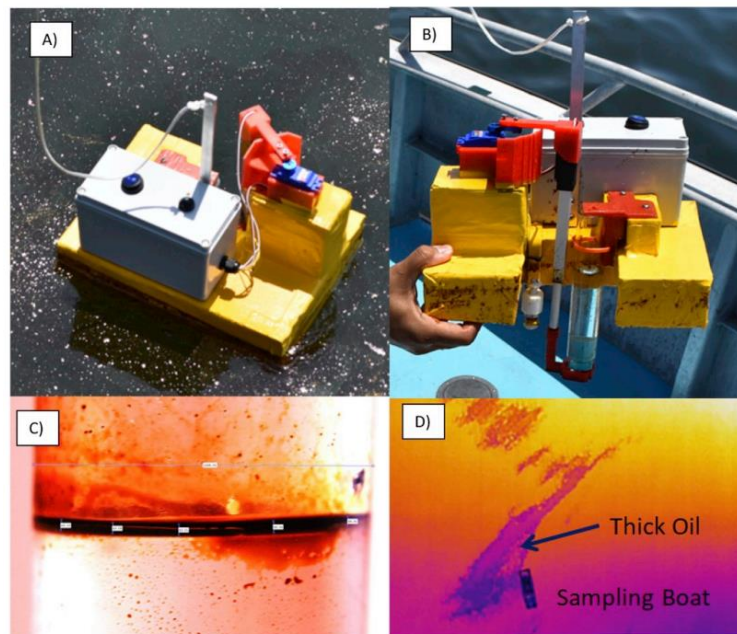


Figure 2.20: WM-OTS sampling floating emulsion. B):View of WM-OTS. C): High-resolution picture of the oil in the tube for which thickness was measured digitally at 80 µm. D): Area of sampling about 10 min before sample collection was performed [14].

Table 2.2 shows the comparison between the different in situ oil spill sensors, highlighting their merits and demerits.

Table 2.2: Benchmarking of oil slick thickness sensors

Technology	Sensitivity (mm)	Maximum Thickness (mm)	Rust-Free	Optical Interference
Microwave (This work)	0.5	100	Yes	No
Capacitive [41]	3.175	76.2	No	No
Thermal [35]	0.4	4	Yes	No
Led-based Spectrometer [37]	0.1	0.5	Yes	Yes
Spectral Domain Optical Coherence Tomography (SD-OCT) [38]	0.0022	0.0264	Yes	Yes
WM-OST [20]	0.005	0.320	Yes	No

2.3 Overview of In-situ Microwave Based Sensors for Oil Spill Detection and Oil Slick Thickness Measurement

To the best of the author’s knowledge, this is the first time that a contact-based in situ microwave technique shall be used in the detection of oil spill as well as the determination of oil slick thickness in the underwater environment. The author believes this is a pioneer work in the niche of in situ oil spill detection and oil slick thickness measurement using microwave sensing.

The use of the antenna-sensor makes this possible by transmission and reception of microwave signal. The principle of operation of the oil spill detection is based on the initial calibration of the system done by capturing the S parameters of the unadulterated water medium and the continual measurement of the medium for any change in the dielectric property that would result in a change in the transmission and reflection coefficients.

The determination of oil slick thickness using the microwave approach is possible by the cuboid configuration of the four antenna-sensor array with each pair having more differentiability with respect to the transmission coefficients at certain volume of submersion of the antenna-sensor by the oil inclusion. A novel RF switching circuit was developed to operate the four antenna-sensors.

The seawater has high relative permittivity of around 74 unlike that of the unit value for free space. And it is saline and thus highly conductive, thus disperses and attenuates radio frequencies. This presents challenges to underwater microwave sensors and limits their range of operation to the radiating near field regions.

2.4 Summary

This chapter provides a comprehensive overview of current underwater oil spill detection and oil slick thickness measurement systems. Oil spill detection systems were first discussed with emphasis to remote sensing based on satellite and airborne SAR. Their limitations were highlighted based on latency and real-time capabilities as well as the costs of deployment and operation with respect to the airborne SAR.

The weaknesses of the SAR in oil slick thickness measurement were explained. The need for an in situ approach to both oil spill detection and oil slick thickness measurement were presented. Different in situ methods used as oil sensors were reviewed. Most of them were contact based. The merits and demerits of those systems were discussed. None of the systems reviewed used radio frequencies. Finally, an overview of the in situ microwave sensor for oil spill detection and oil slick measurements using antenna-sensor array and switching circuits were discussed. The next chapter shall investigate the propagation of electromagnetic waves in seawater and undertake experiments to determine its relative permittivity and loss tangent.

Chapter 3

Propagation of Electromagnetic Waves in Water

Radio frequencies (RF) suffer from absorption, attenuation and dispersion in seawater due to high conductivity, permittivity and salinity of the medium. Notwithstanding, use of RF for underwater application is viable. RF offers the advantage of low latency and high bandwidth compared to acoustic signals. It is also harmless to marine lives.

However, to optimally utilize RF in seawater, some investigations into the properties of the medium must be performed. In this chapter, a look at the foundational Maxwell's equations and how they relate to the lossy seawater transmission medium was done.

Three seawater samples were obtained from Musselburgh, Newhaven and Portobello. Some tests were performed on the samples using the 8753C vector network analyser (VNA) and 85070E dielectric probe kit. The relative permittivity and tangential loss obtained were compared with that of Computer Simulation Technology (CST) Microwave Studio and Debye's model. The Debye's model for the North Sea was used to validate the experimental values.

The dielectric constant and the loss tangent would be useful in designing, modelling and optimizing an RF antenna-sensor targeting seawater.

3.1 Maxwell's Equations

In this section, a brief look at Maxwell's differential equations and their implications on wave propagation both in lossless and lossy media were undertaken. The behaviours of electromagnetic fields depend on fundamental differential equations put forth by Maxwell in 1865. They are presented in (3.1 – 3.4) [45].

$$\nabla \times \bar{H} = \frac{\partial \bar{D}}{\partial t} + \bar{J} \quad (3.1)$$

$$\nabla \times \bar{E} = - \frac{\partial \bar{B}}{\partial t} \quad (3.2)$$

$$\nabla \cdot \bar{D} = \rho \quad (3.3)$$

$$\nabla \cdot \bar{B} = 0. \quad (3.4)$$

where \bar{H} is the magnetic field vector in amperes/meter, \bar{E} is the electric field vector in volts/meter, \bar{D} is the electric displacement vector in coulombs/meter², \bar{B} is the magnetic flux density vector in webers/meter², \bar{J} is the current density vector in amperes/meter², and ρ is the volume charge density in coulombs/meter³.

3.1.1 Time Harmonic Case

It is sufficient to investigate waves at a single frequency because the behaviour of a wave as a function of time can be expressed as a superposition of waves at different frequencies through Fourier transform. The wave at a single frequency is termed time harmonic and can be described by the real part of a phasor field in (3.5) [45].

$$\bar{E}(\bar{r}, t) = \text{Re}[\bar{E}_{ph}(\bar{r}) e^{j\omega t}] \quad (3.5)$$

where $\bar{E}(\bar{r}, t)$, the vector field, is a real function of position \bar{r} and time t . $\bar{E}_{ph}(\bar{r})$ is the phasor field.

Rewriting the Maxwell's equations in (3.1-3.4) with respect to the time harmonic case yields (3.6 – 3.9) [45].

$$\nabla \times \bar{H}(\bar{r}) = j\omega \bar{D}(\bar{r}) + \bar{J}(\bar{r}) + \bar{J}_s(\bar{r}) \quad (3.6)$$

$$\nabla \times \bar{E}(\bar{r}) = -j\omega \bar{B}(\bar{r}) \quad (3.7)$$

$$\nabla \cdot \bar{D}(\bar{r}) = \rho + \rho_s \quad (3.8)$$

$$\nabla \cdot \bar{B}(\bar{r}) = 0 \quad (3.9)$$

where \bar{J}_s and ρ_s are the source currents and source charges respectively. It is important to note that in the time harmonic case, \bar{J} and ρ are the induced current density and the induced charge density, respectively,

3.1.2 Waves Propagation in Lossless Media

The characteristics of the transmission medium determines the relationships among \bar{D} , \bar{E} , \bar{B} , \bar{H} , and \bar{J} . An isotropic medium is one in which the constitutive parameters \bar{D} and \bar{E} , and \bar{B} and \bar{H} , do not depend on the direction of \bar{E} and \bar{H} .

For a linear, passive and lossless isotropic medium where \bar{J} is equal to zero, (3.10) and (3.11) were derived [45].

$$\bar{D} = \epsilon \bar{E} \quad (3.10)$$

$$\bar{B} = \mu \bar{H} \quad (3.11)$$

where ϵ is the dielectric constant in farads/meter, μ is the permeability in henries/meter. The dielectric constant and permeability for free space, represented as ϵ_0 and μ_0 are given in (3.12) and (3.13) respectively.

$$\epsilon_0 = 8.854 \times 10^{-12} \simeq \frac{10^{-9}}{36\pi} F/m \quad (3.12)$$

$$\mu_0 = 4\pi \times 10^{-7} H/m \quad (3.13)$$

The relative dielectric constant ϵ_r , and relative permeability μ_r for the lossless medium are stated in (3.14) and (3.15) respectively [45].

$$\mu_r = \frac{\mu}{\mu_0} \quad (3.14)$$

$$\epsilon_r = \frac{\epsilon}{\epsilon_0} \quad (3.15)$$

3.1.3 Waves Propagation in Lossy Media

In a lossy medium such as seawater, the current density \bar{J} is not zero but directly proportional to the electric field \bar{E} , in a relationship governed by Ohm's law given in (3.16).

$$\bar{J} = \sigma \bar{E} \quad (3.16)$$

where σ is the conductivity of the medium given in siemens/meter. Maxwell's equation in (3.6) can be rewritten as (3.17) with respect to frequencies up to microwave, where conductivity is real and independent of frequency.

$$\begin{aligned} \nabla \times \bar{H} &= j\omega\epsilon\bar{E} + \sigma\bar{E} + \bar{J}_s \\ &= j\omega\epsilon_c\bar{E} + \bar{J}_s, \end{aligned} \quad (3.17)$$

where ϵ_c is the complex dielectric constant given in (3.18) [45].

$$\epsilon_c = \epsilon - j(\sigma/\omega) \quad (3.18)$$

The conductivity term $\sigma\vec{E}$ in (3.17) is absorbed into the dielectric constant as the imaginary part. The relative complex dielectric constant, loss tangent and complex index of refraction (n) are given by (3.19), (3.20) and (3.21) respectively.

$$\epsilon_r = \frac{\epsilon_c}{\epsilon_0} = \frac{\epsilon}{\epsilon_0} - j\frac{\sigma}{\omega\epsilon_0} = \epsilon' - j\epsilon'' \quad (3.19)$$

$$\tan \delta = \frac{\epsilon''}{\epsilon'}, \quad (3.20)$$

$$n = (\epsilon_r)^{1/2} = n' - jn'' \quad (3.21)$$

where ϵ' , the relative permittivity, is the real part of the complex permittivity and ϵ'' , the dielectric loss factor, is the complex part.

The permeability of most materials, such as seawater, is the same with that of free space. Table 3.1 shows some examples of relative dielectric constants and conductivity of some media at low frequencies.

Table 3.1: Relative dielectric constants and conductivities for some media [45].

Medium	Relative dielectric constant, ϵ	Conductivity, σ (S/m)
Wet earth	10	10^{-3}
Dry earth	5	10^{-5}
Freshwater	81	10^{-3}
Seawater	81	4
Copper	1	5.8×10^7
Silver	1	6.17×10^7
Brass	1	1.57×10^7

3.2 Seawater Analysis

3.2.1 Skin Depth

One of the most important theories for understanding how waves propagate in a conductive medium is the skin depth. The seawater has high relative permittivity which results in corresponding high conductance. This produces losses as the waves propagate through the seawater. The extent to which the wave could propagate before its initial

value dropping to about 37% is known as the skin depth or depth of penetration, δ . It is given by (3.22) [46];

$$\delta = \frac{1}{\alpha} = \frac{1}{\omega \sqrt{\frac{\mu\epsilon}{2} \left(1 + \frac{\sigma^2}{\omega^2\epsilon^2} - 1\right)}} \quad (3.22)$$

where ω is the angular frequency.

Because seawater is a good conductor, (3.22) becomes (3.23).

$$\delta = \frac{1}{\alpha} \cong \sqrt{\frac{2}{\omega\mu\sigma}} = \sqrt{\frac{1}{\pi f \mu\sigma}} \quad (3.23)$$

Water is a diamagnetic material; thus, it has a unit permeability. This implies that the skin depth for seawater depends on the frequency and conductivity. Thus, at higher frequency, the distance travelled by electromagnetic waves in seawater reduces significantly.

The other parameter upon which the penetration depth depends on is the conductivity, σ . This is related to the permittivity and loss tangent, $\tan\delta$ by (3.24).

$$\tan\delta = \frac{\sigma}{\alpha\epsilon'} \quad (3.24)$$

The loss tangent is defined as the losses a radio signal incurs as it passes through a medium [47].

3.2.2 Debye's North Sea model

The radio frequency dependence of dielectric medium was investigated by [48]. The polarization of the dielectric consist of the induced and orientation components [49]. A modified version of the Debye's equation is given in (3.25),(3.26) and (3.27) [50], [51].

$$\epsilon = \epsilon' - j\epsilon'' \quad (3.25)$$

where

$$\epsilon' = \epsilon_{ir} + \frac{\epsilon_s - \epsilon_{ir}}{1 + (\omega t_r)^{2(1-\alpha)}} \quad (3.26)$$

$$\epsilon'' = \left(\frac{\epsilon_s - \epsilon_{ir}}{1 + (\omega t_r)^{2(1-\alpha)}} \cdot (\omega t_r)^{(1-\alpha)} \right) + \frac{\sigma_s}{\omega\epsilon_0} \quad (3.27)$$

ϵ_s and ϵ_{ir} are the seawater static permittivity and dielectric permittivity high-frequency limit respectively, ϵ_0 is the permittivity of free space, σ_s and t_r are the ionic conductivity and relaxation time of seawater, α is the distribution of relaxation time.

As stated in [51], the seawater model of $\epsilon_{ir} = 4.9$ and $\alpha = 0$, describes the Debye's equation. Both the salinity and temperature for the Debye's model were kept at a constant value. The salinity for the North Sea water was selected as 34 [52] and the temperature was taken as 22^oC.

3.3 Investigation of North Seawater

3.3.1 CST Microwave Suite Simulation

One of the most important tools for modelling, designing and optimising antennas is the CST microwave suite. It was used extensively in the simulations performed throughout this research, to design and validate the performances of antennas in free space, encapsulated by buffer and when submerged in seawater and freshwater. The relative permittivity of the seawater phantom in CST was compared with the measured and Debye's model.

3.3.2 Measurement of the relative Permittivity of North Seawater

A. Obtaining the seawater samples

Samples of seawater were obtained from three locations around the North Sea. These locations; Musselburgh, Portobello and Newhaven, can be seen marked in red stars in Figure 3.1. It is noteworthy to state that the samples were obtained from the coastal areas. The labelled samples were then transported to the laboratory where the test for the relative permittivity and tangential loss were performed.



Figure 3.1: Locations of seawater samples.

B. Experimental Setup

- To begin, the experimental kit was set up as shown in Figure 3.2. The Agilent Connection Expert was launched to verify that the computer could communicate with the HP 8753C vector network analyser (VNA) through the general purpose interface bus (GPIB).
- The next step was to run the 85070 software that controls the 8753C network Analyser. In the prompt, 8753C network Analyser was selected as the instrument type, and its address was chosen as 16, while the address of the standard instrument control library (SICL) GPIB card was selected as 0.
- Under “Calibration”, the “Configure cal” was selected. The probe type was the “High temperature”. “Refresh standard type” was “Air” and the deionised water temperature was measured to be 22°C. The “Calibration type” was specified as “Air/short/water”. The high temperature dielectric probe was first suspended in air and the air calibration was performed. Subsequently, a short rod was connected to the probe and the short calibration was done. Finally, the probe was immersed in deionised water and the water calibration was undertaken.
- The frequency was set to sweep from 1 MHz to 3 GHz with the linear sweep option

- “Perform Cal” was then selected, and the high temperature probe was left in open air. Next, a shorting block was connected to the probe. Finally, the probe was inserted in the deionised water, which was at a temperature of 22⁰C.
- The measurements for the different samples of the seawater were performed and the results were saved. The results were also displayed on the VNA in the form of a polar plot

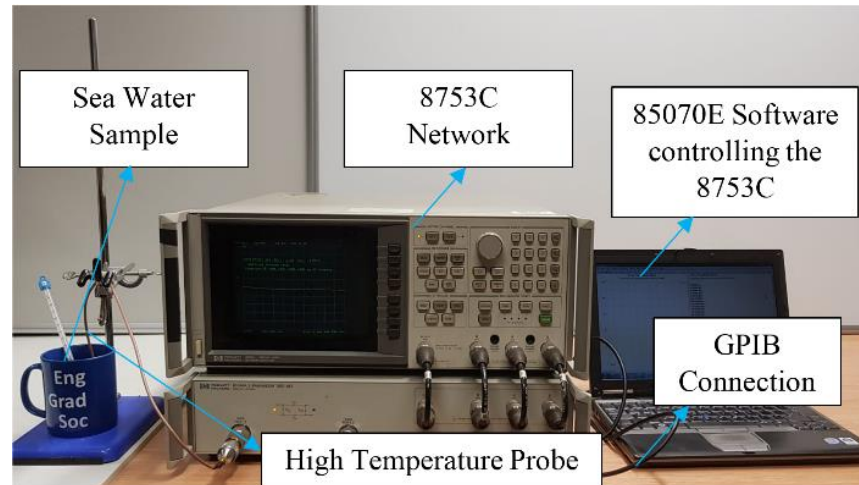


Figure 3.2: Experimental setup for dielectric measurement.

C. Comparison of frequency variation with the properties of seawater

The relative permittivity of a medium such as seawater is frequency dependent. The rate at which a radio wave attenuates in a seawater is a function of the dielectric constant of the medium[49]. Several works have tried to model the behaviour of electromagnetic waves in seawater propagation using realistic mathematical models [49], [50], [53] but very few have undertaken physical experiments.

The seawater channel is multipath and time varying; therefore, there is no fit all solutions for all the oceans. These results were obtained for the North Sea where the sensor node is going to be deployed for testing. The results for the three specific locations; Musselburgh, Newhaven and Portobello as well as the CST and Debye’s models are shown in Figure 3.3.

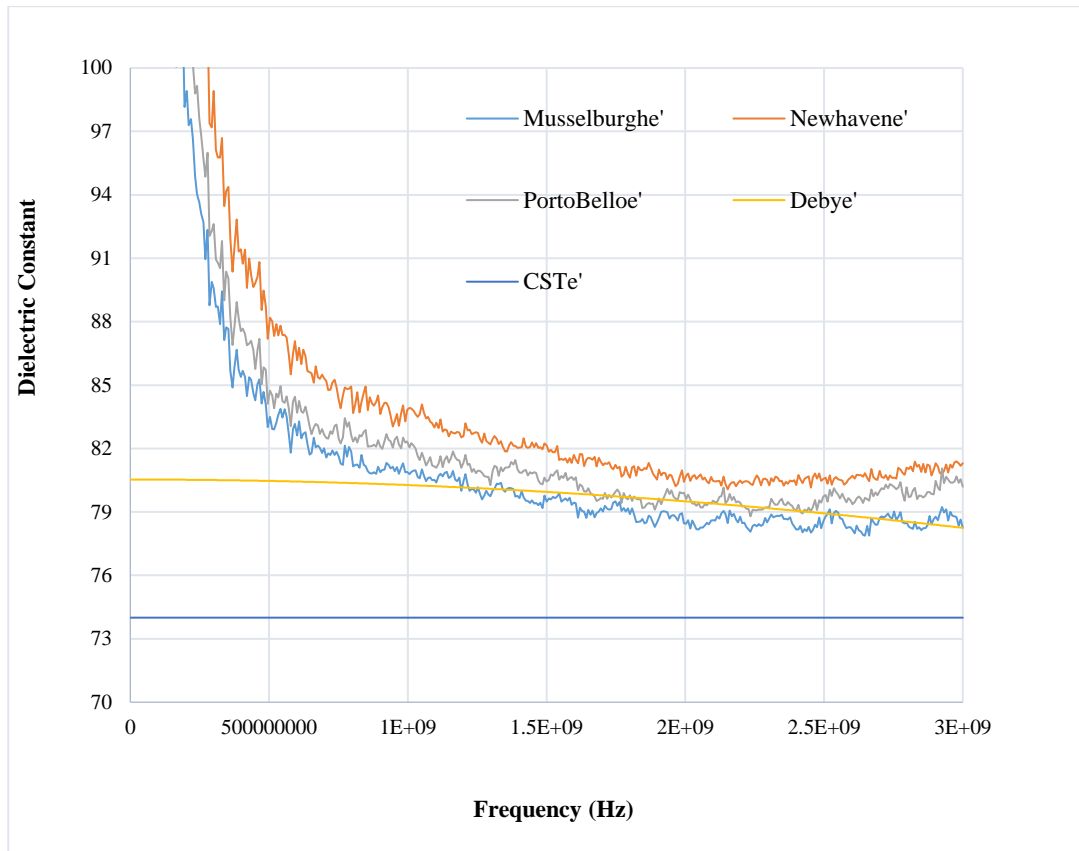


Figure 3.3: Relative permittivity for samples of seawater.

It is noteworthy that the dielectric constant for the different water samples of the seawater fluctuates between 78 to 84 at frequencies beyond 1 GHz. The Debye's model cuts through an average value for the three samples beyond the 1 GHz frequency. The CST model has a flat permittivity of 74 across all frequencies. The targeted frequency of operation for the oil spill sensor node is between 500 MHz and 3 GHz. This range has a considerable value of relative permittivity.

To appreciate the implication this would have in the frequency of transmission, it would be useful to investigate the conductivity model of the seawater medium using the average value of the experimental result and Debye's model. The CST's flat value for the dielectric constant does not make it an eligible candidate for the comparison.

The loss tangent is the measure of losses that an electromagnetic wave suffers as it passes through a medium. It was given in (3.20).

Figure 3.4 shows the tangential loss for the North Sea using the experimental and Debye's models. The lower the tangential loss, the lower the dispersion and attenuation of the signal. Based on the experimental data and the Debye's model, the value of the tangential loss significantly decreased between 500 MHz to about 3000 MHz. This range lies within the frequency of operation of both the antenna-sensor (500 MHz to 3000 MHz) and the communication backbone LoRa antenna (868 MHz). The lower tangential loss within this region signifies lower signal losses which would be beneficial to the proposed systems.

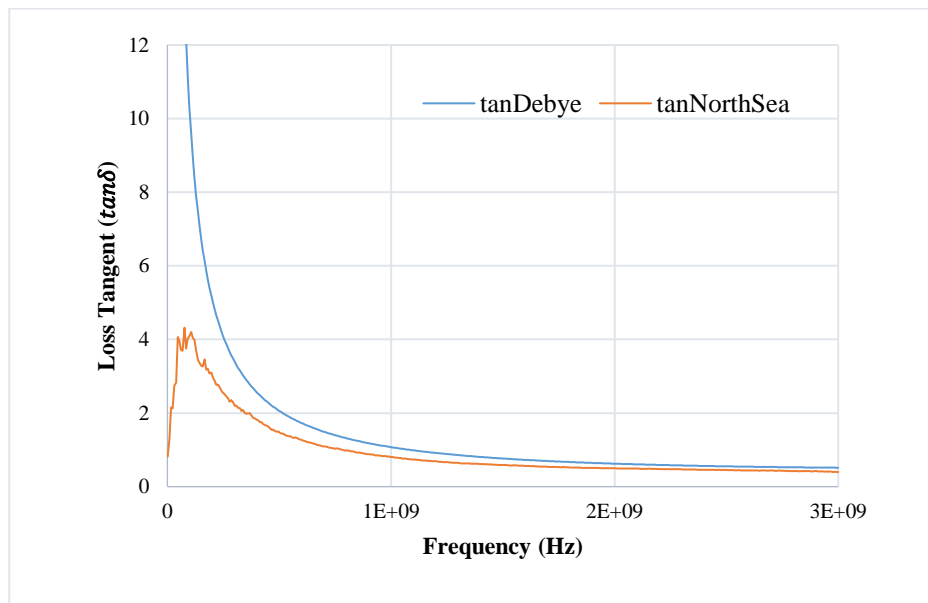


Figure 3.4: Tangential loss for experimental and Debye's seawater model.

3.4 Summary

This chapter discussed the investigation of the properties of the North seawater using experimental data and mathematical models. The use of radio frequency for underwater application has been proven to be viable. To successfully utilize RF, it was important that some of the relevant properties of the North Sea water were investigated. Samples of the North Sea water were obtained from three different locations. Their relative permittivity and loss tangents were determined using the high temperature dielectric probe and the 8753C vector network analyser.

The Debye's mathematical was determined for North Sea and it was used to validate the experimental values. It was determined that the flat value of relative permittivity for seawater in CST at 74 was impractical for all frequencies. The loss tangent of the experimental and Debye's models were compared. It was found that the target resonant frequency of 500 MHz and 3 GHz has a lower tangential loss compared to the lower ranges of frequencies. The next chapter shall undertake the design of an underwater antenna-sensor to be used for oil spill sensing and oil slick thickness determination in seawater.

Chapter 4

Underwater Antenna Sensor Design and Fabrication

The fundamental subsystem in the in situ microwave oil spill detection and oil slick thickness determination sensor is the antenna. Thus, great emphasis must be placed on its performance and efficiency. Mono-static switching is applied in this research which demands that the same antenna can transmit and receive signals. This chapter describes the requirement of designing an antenna-sensor for underwater application and subsequently developing a trefoil antenna and encapsulating it in PDMS for radiation in both seawater and freshwater. Some of the design considerations of the antenna-sensor requires the antenna to be able to operate underwater, to have high cross polar discrimination (XPD) to reject signals from orthogonally placed antennas, compactness and ruggedness. Thus, a low-profile antenna is essential for the antenna-sensor. Low-profile antennas would minimise the dimensions of the buffer layer required for the antenna-sensor. These requirements exclude high-profile antennas such as Vivaldi, loop, aperture, and log periodic antennas while making planar monopole antennas more attractive as a candidate for the antenna-sensor.

4.1 Requirement of Underwater Antenna Sensor

A plethora of resources and activities such as marine life, oil and gas installations, shipwrecks, explorations and search and survey abound underwater. Almost three-quarter of the world is covered in water. Thus, sensing, monitoring and observing the underwater environment is of paramount importance.

Due to the varying and contrasting values of the dielectric properties of the freshwater, seawater, oil, gas and brine, the candidate antenna should be capable of operating over diverse relative permittivity shown in Table 4.1 [54].

Table 4.1: Dielectric Properties of Seawater [54].

Material	Gas	Oil	Brine	Water
ϵ_r	1-j0	2.2-j0.1	50-j40	70-j10

A wideband antenna characteristic would be essential for optimal performance over these ranges of materials most especially in order to be able to adapt an imaging or detection algorithm for a radar based microwave sensing such as confocal delay and sum (CDAS) [55], for a subsequent imaging and determination of oil slick thickness.

Another essential characteristic of the antenna would be compactness. This quality is readily offered by patch antennas that exhibit good performances at relatively smaller dimensions. They are also lightweight, easy to fabricate, cheap and could also be adapted to be used in any shape. These attributes make this antenna a very suitable option.

Techniques like acoustics and wired communication have found more success underwater compared to radio frequencies despite its ubiquity in terrestrial applications. The militating factors to the poor performance of radio frequency systems underwater are the attenuation in the propagating radio waves and the profound mismatch between the antenna and the transmission medium.

There have been numerous methods put forth in the literature to ameliorate these conditions. An example is by covering the antenna with a matching material such as in [56] where a monopole antenna for an autonomous underwater vehicle (AUV) was coated with resin of dielectric constant 2.65.

Another popular method is by using a buffer layer around the antenna to provide impedance matching between the antenna and the medium. In this method, the antenna is encapsulated in another medium, as seen in Figure 4.1 before it is immersed in the water medium.

In [57], seawater was the transmission medium with 3.5% salinity and relative permittivity of $\epsilon = 79 + i32$. A helical antenna operating at a resonant frequency of 50 MHz was used as the radiating structure. It was enclosed by substantial insulating layer of deionised water. This was to minimise reactive near-field losses and to enable

minimal matching structure for electromagnetic wave propagation in the seawater transmission medium. Deionised water was selected as the impedance-matching liquid because it has similar real part of relative permittivity as seawater with much smaller conductivity ($\epsilon = 81 + i6.42$) [58].

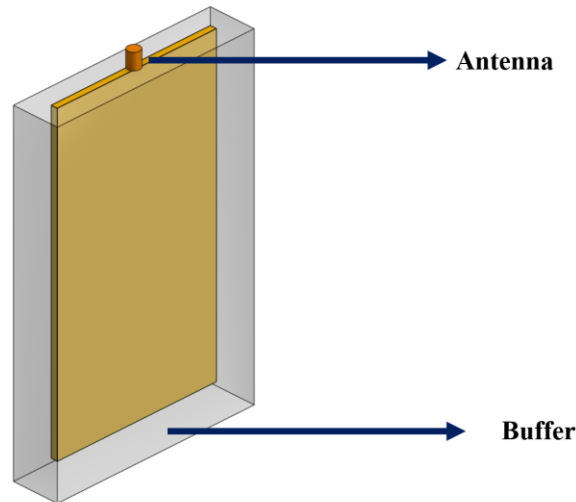


Figure 4.1: Antenna encapsulated in a buffer layer

The matching enclosure enables the approximate reduction of antenna size by a factor of 9 with respect to the free space dimensions. It also improves electromagnetic energy coupling to the surrounding seawater transmission medium [59]. These inadvertently reduced ohmic losses that resulted from submerging the antenna in water with high salinity.

As shown in Figure 4.2, laboratory testing of the antenna performance in brackish water (salt water with 0.5 % salinity) at 2.45 GHz clearly showed the superior performance of an antenna enclosed in an impedance-matching liquid like the deionised water to conventional methods that do not use impedance-matching enclosures [57].

Air gaps were absent in both configurations. The transmitter-receiver pairs that employed the impedance-matching enclosures outperformed those that do not by approximately 20 dB when both were immersed in brackish water. The tuning was further refined using a network analyser and by immersing the antennas in a gallon containing deionised water.

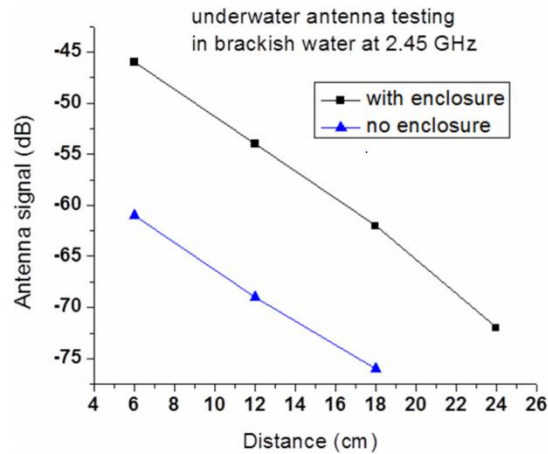


Figure 4.2: Antenna Performance in water with and without enclosure [57].

In [60] the underwater experiment was undertaken under three configurations as it could be seen from Table 4.2. Both the reflection parameters as well as the transmission coefficients were obtained. In type-a, the propagation medium and both buffer layers were filled with tap water. Type-b had seawater as the material for the propagation layer as well as the two impedance-matching buffer layers. For type-c, the propagation layer was seawater while the buffer layers were filled with tap water.

Table 4.2: Experimental configurations for medium and buffer [60].

Type	Configurations		
	Buffer layer (L)	Propagation layer	Buffer layer (R)
a	Tap water	Tap water	Tap water
b	Seawater	Seawater	Seawater
c	Tap water	Seawater	Tap water

The antennas were operated at a frequency of 40 MHz. When both the propagation layer and buffer layers were empty, no signal was received due to the high cut-off. However, when the whole tank was filled with tap water as is the case with type-a, the cut off becomes lower, thus received signals could be observed. The cut off reduces further when the tank was filled with seawater (type-b), however no received signal was observed. This is because of approximately 220 dB attenuation of the high frequency (HF) signals from the salt water. An outstanding result was obtained from type-c where the buffer layers were filled with tap water and the propagation layer was filled with seawater. The performance was similar to type-a, although it was 20 dB better in performance to the type-a configuration at 40 MHz. This clearly illustrated the need for impedance-matching of the antennas to achieve good performance.

In [61], a 2 x 4 tapered slot antenna (TSA) antenna array for underwater application was proposed. The design and fabrication of the array started with a single unit. The antenna array fabricated had ultra-wideband (UWB) characteristics, however, there was no practical deployment of the antenna in the underwater environment.

In [62], [63], UWB microstrip antenna contained in a liquid buffer layer was designed and fabricated. The buffer layer functioned as a container for the antenna and a matching layer between the antenna and the transmission medium (freshwater). The relative permittivity of the buffer layer ϵ_{rb} was determined using the geometric average of the relative permittivity between air, ϵ_{ra} and freshwater, ϵ_{rf} as it could be seen in (4.1). The optimal ϵ_{rb} was found to be 8.85.

$$\epsilon_{rb} = \sqrt[2]{\epsilon_{ra} \cdot \epsilon_{rf}} \quad (4.1)$$

The buffer layer thickness was determined by the radiating near field region equation shown in (4.2).

$$R \leq \frac{2D^2}{\lambda} \quad (4.2)$$

where R is the boundary of near field region, D is the maximum linear dimension of the antenna, λ is the wavelength that can be calculated from (4.3).

$$\lambda = \frac{c/n}{f} \quad (4.3)$$

where c is the speed of light, n is the refractive index of the medium and f is the operating frequency of the antenna.

An acrylic material with the same dimension as the buffer was made to serve as the buffer layer container. Liquids were chosen as the buffer layer materials because of the ease to synthesise and tune its parameters to match the simulated value of ϵ_{rb} . They also have the advantage of taking the shape of the container. The candidate liquid solution would be diluted with distilled water until the optimal ϵ_{rb} was achieved. Figure 4.3 shows a flowchart used to develop the buffer.

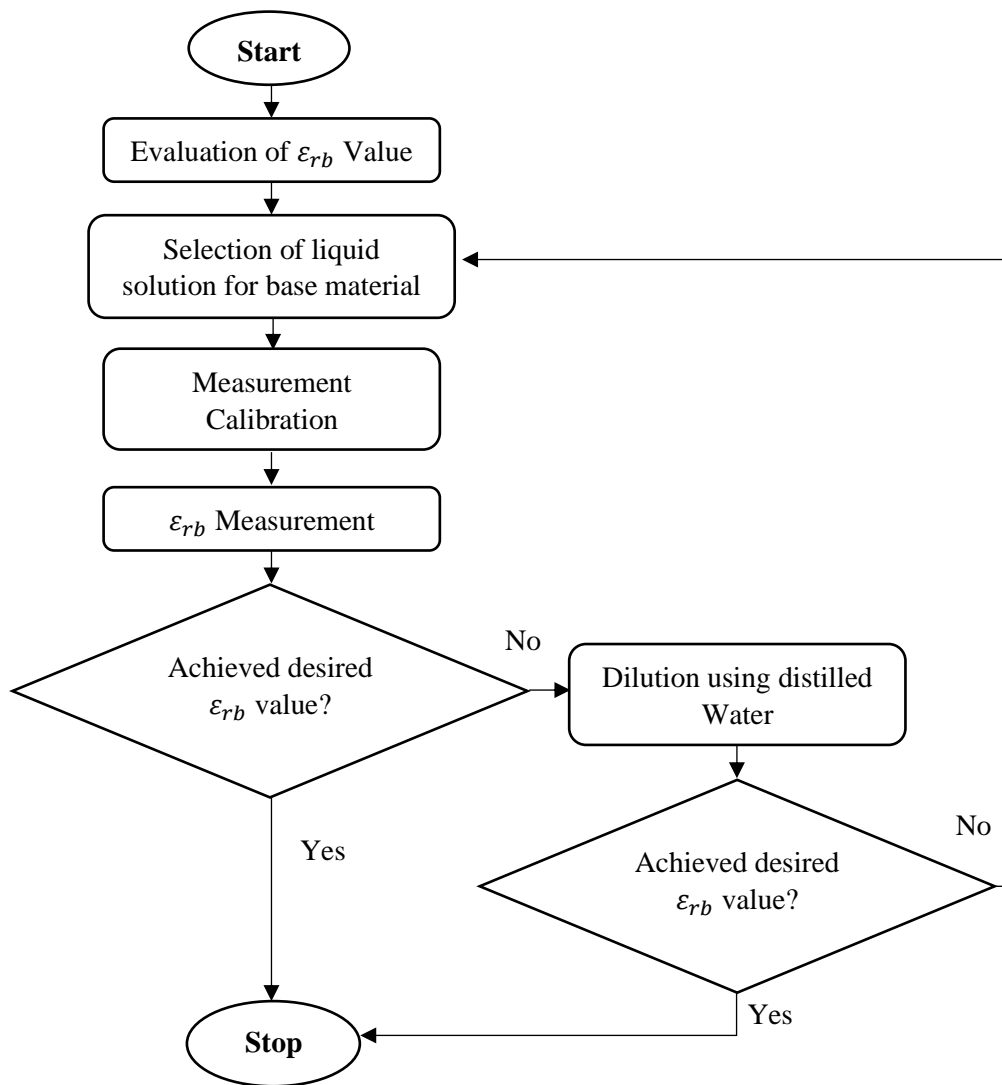


Figure 4.3: Flowchart of buffer synthesis procedure [57].

Using a dielectric probe connected with Keysight’s PNA-Network Analyser (N5232A), several liquid solutions were tested. Their performances could be seen in Figure 4.3. Among the solutions, the superior performance was exhibited by methyl acetate, CH_3COOH . It produced a solution closest to the calculated value of ϵ_{rb} (8.85) at 6.65 operating at a frequency of 340 MHz. To achieve the value of ϵ_{rb} at 8.85, several ratios of mixtures between methyl acetate and distilled water were performed. A ratio of 6:1 was determined to be optimal as it could be seen in Figure 4.4.

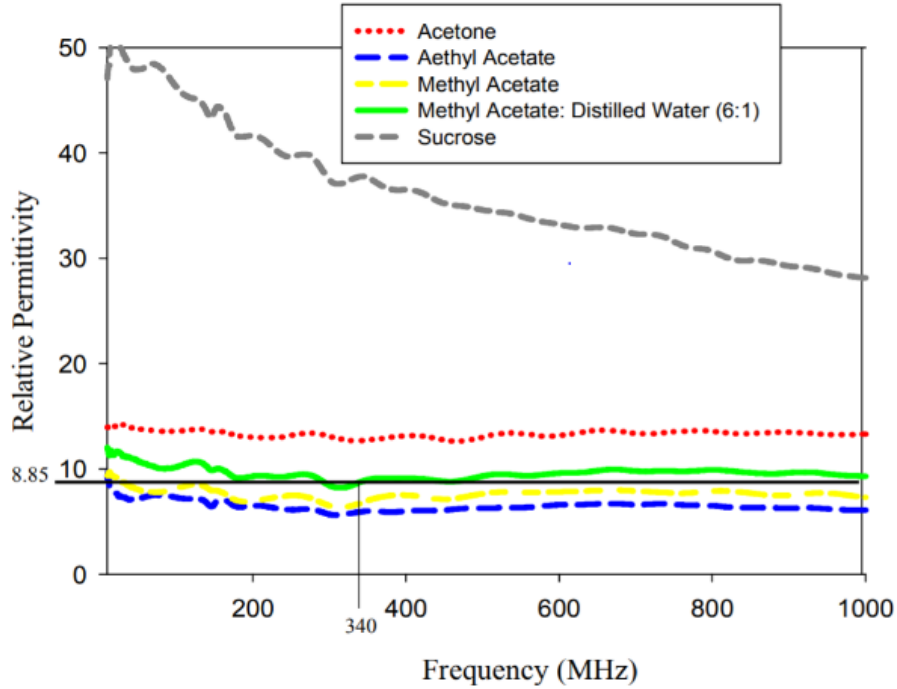


Figure 4.4: Measurement of relative permittivity of different selected liquid solutions [57].

The buffer dimensions were determined using the base antenna dimensions as well as the near-radiating field region equation in (4.2) [63]. The dimensions could be seen in Figure 4.5 and Table 4.3. The experimental setup could be seen in Figure 4.6 below.

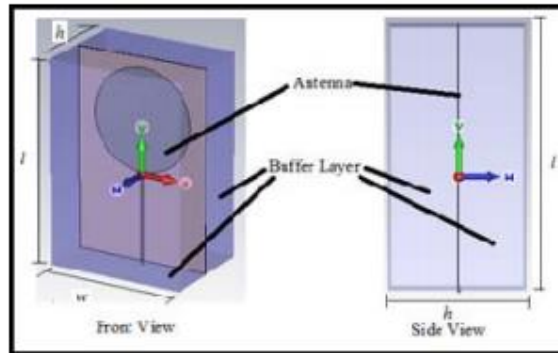


Figure 4.5: Geometry of antenna design with buffer layer structure [63].

Table 4.3: The Dimensions of the buffer enclosure [63].

Parameter	Dimension (mm)
Width, w	250
Length, l	370
Thickness, h	257.6

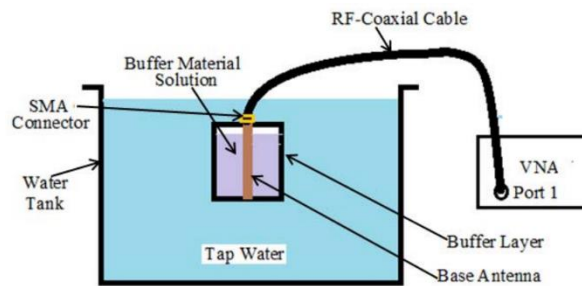


Figure 4.6: Experimental setup for underwater antenna [57].

4.2 Design of Underwater Antenna

Based on the requirements put forth for the antenna-sensor in section 4.1, a planar monopole antenna was selected as the base antenna. Its low-profile, ruggedness, compactness, high XPD, ultra-wideband capabilities with negligible distortions and

ease of adopting it for underwater environment by encapsulating it in a low-profile buffer makes it the candidate for the antenna-sensor.

There is a plethora of antennas as candidates for the choice antenna such as dipole, spiral, Yagi-Uda, monopole and Vivaldi antennas. However, as reported in the literature, monopole antennas offer superior advantages of wideband, lightweight, simplicity and ability to transmit and receive signals with minimal distortions [64] [55], [65].

Different configurations of printed monopole antennas exist [65]; printed square monopole antenna (PSMA), printed rectangular monopole antenna (PRMA), printed circular monopole antenna (PCMA), printed elliptical monopole antenna (PEMA) , printed triangular monopole antenna (PTMA) and printed hexagonal monopole antenna (PHMA). Each of these have different feed positions. They could be fed by coplanar waveguide (CPW) or 50-ohm feedline. The optimal width of the ground plane was established as 10 mm.

The standard equation derived for a cylindrical antenna could be modified in order to determine the lower-edge frequency, f_{low} , for generalised monopole antennas[65]. The formula given in (4.4) was adopted from a planar cylindrical configuration by equating the height of the patch of a planar monopole antenna, L in cm, to that of a cylindrical monopole antenna.

$$f_{low} = \frac{c}{\lambda} = \frac{7.2}{(L + r + p)} \text{ GHz} \quad (4.4)$$

where r in cm is the effective radius of the equivalent cylindrical antenna, p is the length of the 50 Ω feedline in cm. The printed circuit monopole antenna has a dielectric substrate unlike the planar disc monopole antenna which (4.4) was derived for. Thus, a further modification would have to be carried out to accommodate the relative permittivity of the printed circuit design on f_{low} . This could be seen in (4.5).

$$f_{low} = \frac{c}{\lambda} = \frac{7.2}{\{(L + r + p) \times k\}} \text{ GHz} \quad (4.5)$$

where k is equal to $\sqrt{\epsilon_r}$. ϵ_r is the relative permittivity of the substrate used in the printed circuit board for the antenna.

There are two critical parameters in the design of a monopole antenna which are the shape and size of the feedline and the radiating patch [66]. The initial design was decided using the PCMA with a 50Ω coplanar waveguide (CPW) feedline. CPW is one of the best options for transmission lines due to its simplicity, quasi-TEM mode propagation, fabrication ease and ease of shunt and series mounting of active and passive electronic devices [55], [66] [67].

The radius of the design A , was taken as 1.2 cm. With this, the value of L and r can be calculated appropriately using (4.6) and (4.7) respectively [65].

$$L = 2A \quad (4.6)$$

$$r = \frac{A}{4} \quad (4.7)$$

The effective dielectric constant ϵ_{eff} , phase velocity v_{ph} and characteristic impedance Z_0 of a transmission line can be determined by using quasi-static approximation as given in (4.8),(4.9) and (4.10) respectively [66].

$$\epsilon_{eff} = \frac{C}{C_0} \quad (4.8)$$

$$v_{ph} = \frac{c}{\sqrt{\epsilon_{eff}}} \quad (4.9)$$

$$Z_0 = \frac{1}{Cv_{ph}} \quad (4.10)$$

where c , C and C_0 are the speed of light in free space, line capacitance of the transmission line and the line capacitance of the transmission line when no dielectrics exists, respectively.

To calculate the values of the effective phase velocity and characteristic impedance of the CPW transmission lines, equations (4.8) and (4.9) were substituted into (4.10) to yield (4.11).

$$Z_0^{CPW} = \frac{30\pi}{\sqrt{\epsilon_{eff}^{CPW}}} \frac{K(k)}{K(k')} \quad \Omega \quad (4.11)$$

where k and k' are given by the (4.12) and (4.13).

$$k = \frac{a}{b} \tag{4.12}$$

$$k' = \sqrt{(1 - k^2)} \tag{4.13}$$

And K is the complete elliptical integral of the first kind shown in (4.14).

$$\epsilon_{eff}^{CPW} = 1 + \frac{1}{2}(\epsilon_r - 1) \frac{K(k) K(k_1')}{K(k') K(k_1)} \tag{4.14}$$

where k_1 could be determined using (4.15).

$$k_1 = \sinh.(\pi a / 2h) / \sinh.(\pi b / 2h) \tag{4.15}$$

FR-4 was used for this antenna because of its affordability, availability and negligible losses associated with its frequency of operation which is below the upper limit of the S-band [68]. The FR-4 substrate that had a dielectric constant of 4.3, loss tangent of 0.01, thickness of 1.6 mm and a copper patch of thickness 0.035 mm. The initial lower-edge frequency was determined using (4.5), (4.6) and (4.7) to be 739 MHz.

4.2.1 FCC Bandwidth Classification

Based on the Federal Communications Commission (FCC), the fractional bandwidth, B_F , for an antenna could be calculated using (4.16) [69].

$$B_F = \frac{B}{f_c} = 2 \frac{f_h - f_l}{f_h + f_l} \tag{4.16}$$

where f_h and f_l are the high and low frequency limits, f_c is the center frequency and B is the bandwidth. The several classifications of bandwidth based on the fractional bandwidth (B_F) and band ratio (b_r) could be seen in Table 4.4.

Table 4.4: Classification for signals based on the bandwidth [69].

Band Type		Fractional Bandwidth	Band Ratio
Radar/Communications	Electromagnetic Interference	$B_F = 2 \frac{f_h - f_l}{f_h + f_l}$	$b_r = \frac{f_h}{f_l}$
Narrowband (NB)	Hypoband (NB)	$0.00 < B_F \leq 0.01$	$0.00 < b_r \leq 1.01$
Wideband (WB)	Mesoband (MB)	$0.01 < B_F \leq 0.25$	$1.01 < b_r \leq 1.29$
Ultra-Wideband (UWB)	Sub-Hyperband (SHB)	$0.25 < B_F \leq 1.50$	$1.29 < b_r \leq 7.00$
	Hyperband (HB)	$1.50 < B_F \leq 2.00$	$7.00 < b_r < \infty$

4.2.2 Base Antenna Design

Using Computer Simulation Technology (CST) Microwave Studio, the base antenna was designed in accordance with the calculations of the parameters obtained. The initial base antenna design could be seen in Figure 4.7. The detailed calculated dimensions for the antenna could be seen in Table 4.5.

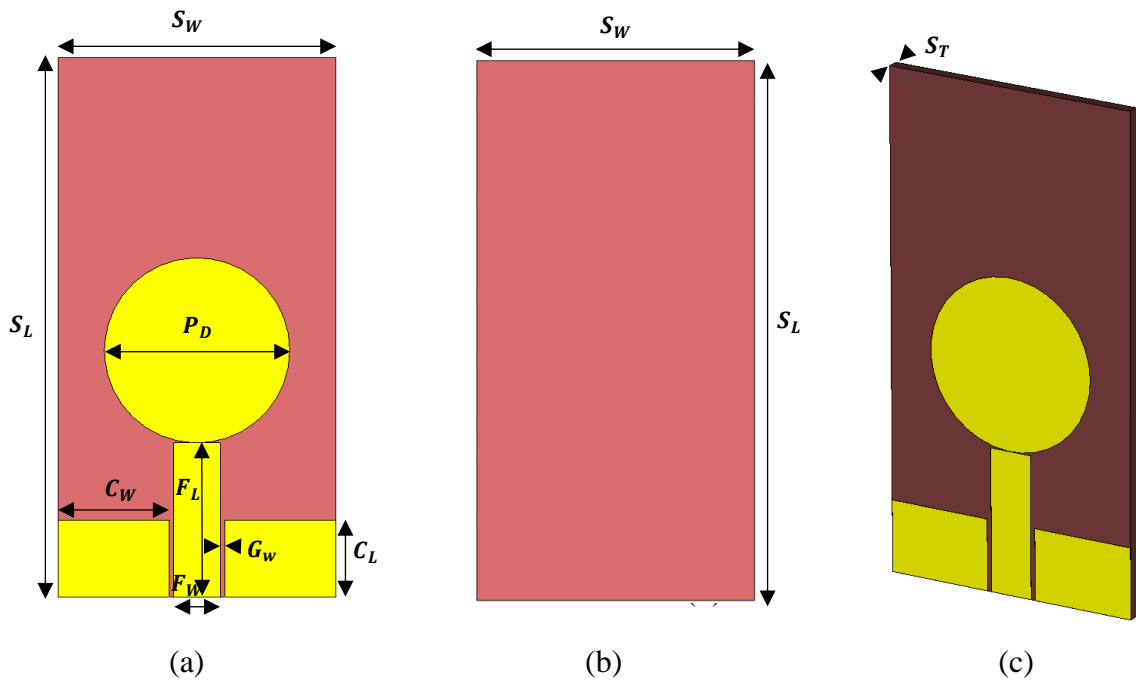


Figure 4.7: Initial Base Antenna (a) Front (b) Back (c) Perspective.

Table 4.5: Dimensions of initial base antenna.

Antenna Parameters	Symbol	Dimensions (mm)
Substrate Length	S_L	70
Substrate Width	S_W	36
Substrate Thickness	S_T	1.6
Antenna Patch Diameter	P_D	24
Feedline Length	F_L	20
Feedline Width	F_W	6
CPW Gap	G_W	0.59
CPW Length	C_L	10
CPW Width	C_W	14.41
Copper Thickness	Tcu	0.035

The antenna characteristics obtained from the initial base antenna simulation in CST could be seen in Figure 4.8.

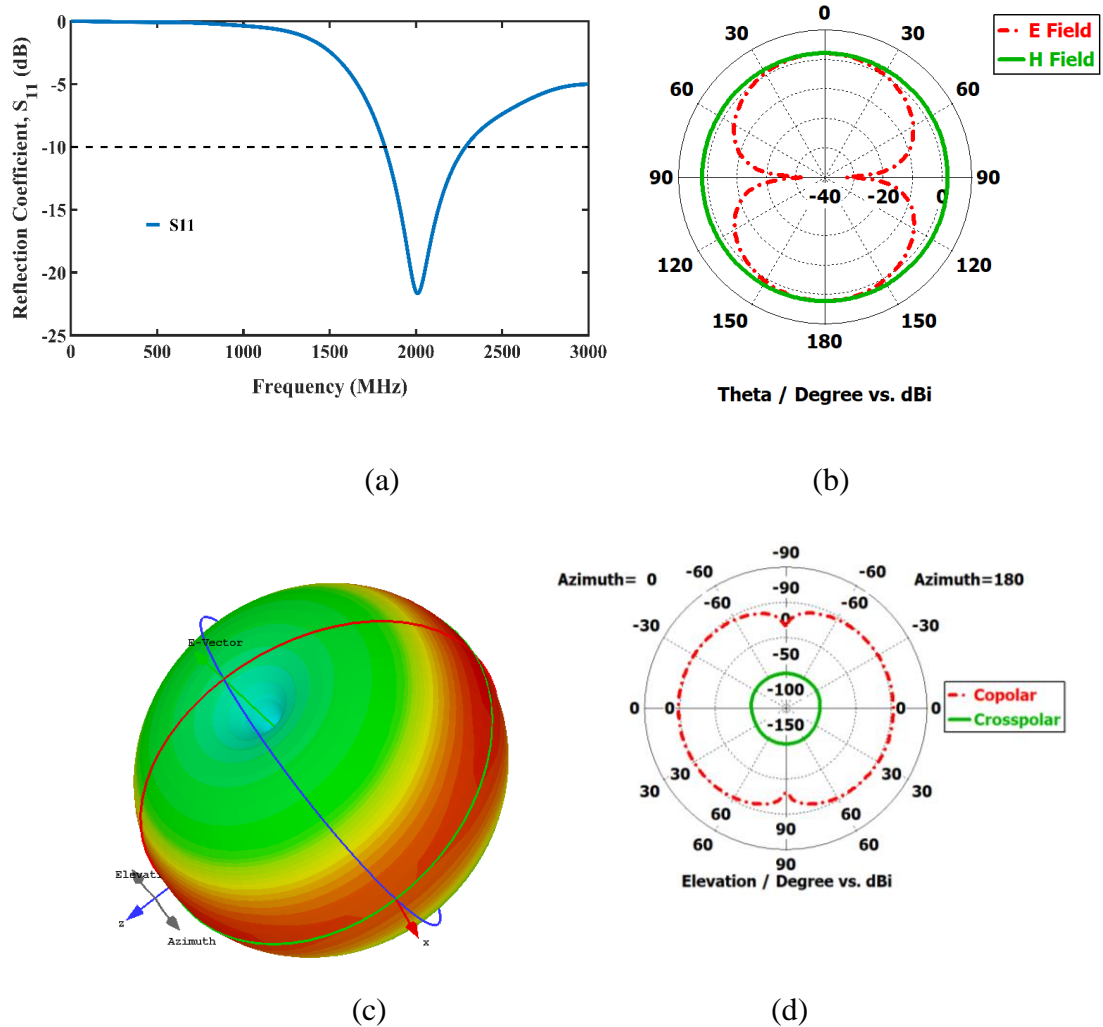


Figure 4.8: Antenna characteristics for initial base antenna. (a) Reflection coefficient (b) Electric and magnetic field (c) Far field plot (d) XPD plot.

From the S11 parameter shown in Figure 4.8 (a), the 467 MHz bandwidth spanned 1820 MHz to 2287 MHz resulting in 0.227 fractional bandwidth. This does not lie in the UWB region. Thus, there is a need to improve the bandwidth characteristics of the antenna.

The initial antenna exhibited an omnidirectional radiation characteristic as it could be seen in Figure 4.8 (b) and (c) with a gain of 2.08 dBi. The Cross Polar Discrimination (XPD) for the antenna, the ratio between the co polar and its orthogonal cross polar component as it could be seen in Figure 4.8 (d), was 102 dBi. This very high XPD gain demonstrates that the antenna has correspondingly high selectivity in the presence of orthogonally aligned antennas.

4.2.3 Trefoil Antenna Design

Both seawater and freshwater have very high relative permittivity while some of the materials sensed in the water medium have low dielectric constant such as crude oil. And often for imaging purposes, a wideband antenna characteristics are desired [70], [71] and [72]. Thus, the work proceeded to transform the bandwidth of the base antenna to that with ultra-wideband capabilities.

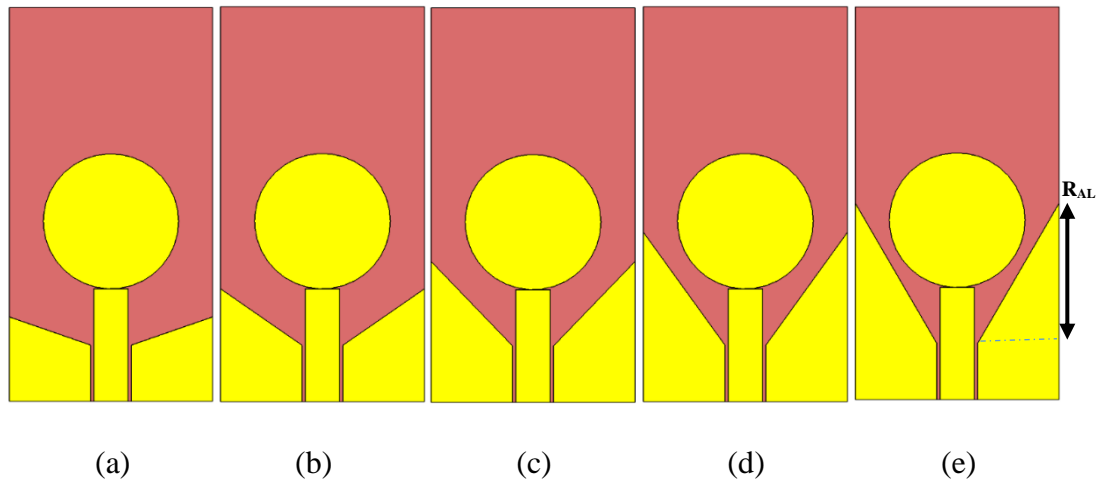


Figure 4.9: R_{AL} Parametric Sweep (a) 5 mm (b) 10 mm (c) 15 mm (d) 20 mm (e) 25 mm.

Different methods have been used to achieve this wide bandwidth characteristics. One of the methods as reported by [55], [73] involves tapering the CPW. Others

involved introducing slots on the patch and elements on the back of the substrate [74], [75], [76].

A right triangular taper element was introduced to the CPW of the base antenna. The height of the triangular element, R_{AL} , was varied as it could be seen in Figure 4.9.

The optimal value of R_{AL} , resulting in the best reflection coefficient (S_{11}) response was ascertained as it could be seen in Figure 4.10. There is obviously a deterioration in the bandwidth as the height increased.

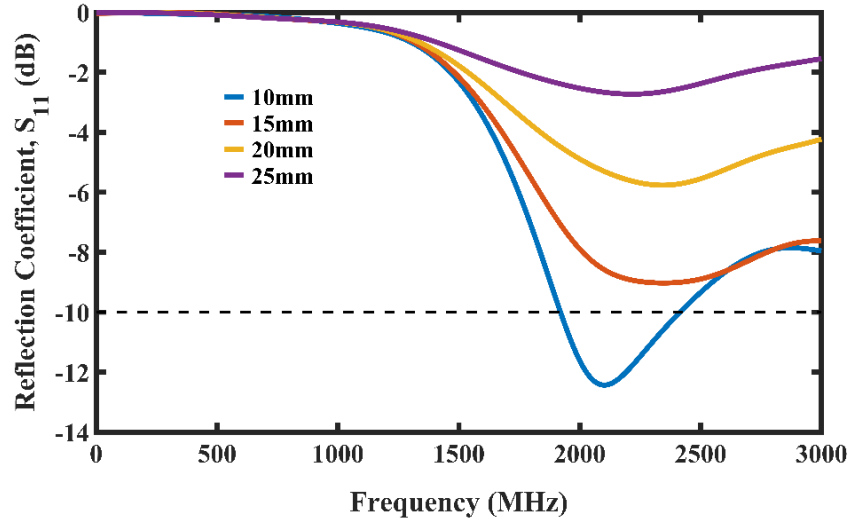


Figure 4.10: Simulation plot for RAL length variation.

To further enhance the the wideband characteristics, two circular elements were added on the patch to form a trefoil design.

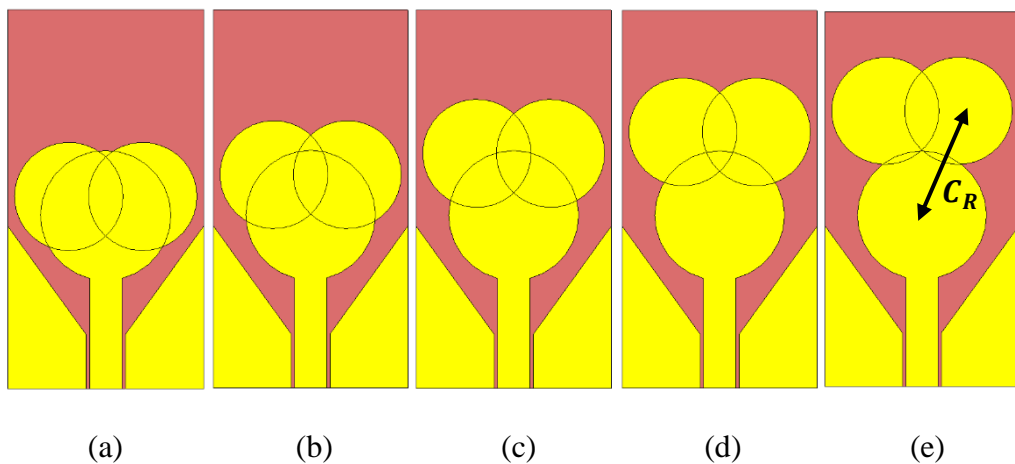


Figure 4.11: Patch Distance Variation from Circles. (a) 5.5 mm (b) 9.5 mm (c) 13.5 mm (d) 17.5 mm (e) 21.5 mm.

The value of R_{AL} was fixed at 20 mm. The distance from the center of the circular patch and the center of the two circular elements (C_R) were varied using a parametric sweep. This could be seen in Figure 4.11. The response of the reflection coefficients were recorded.

The reflection coefficients obtained from the optimisation parametric sweep on the position of the two circles from the center of the circular patch could be seen in Figure 4.12. A substantial improvement in the bandwidth at a distance of 17.5 mm and 21.5 mm corresponding to 0.489 and 0.576 fractional bandwidth respectively, were achieved.

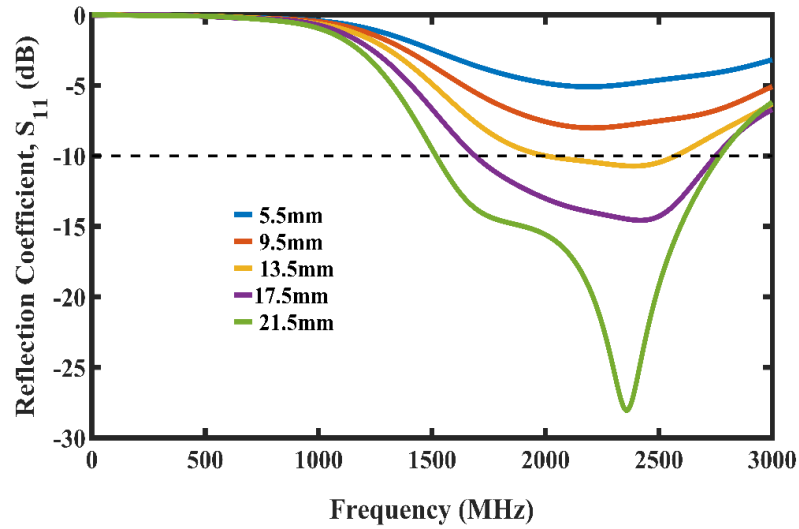


Figure 4.12: Simulation plot for trefoil minor circles distance variation.

To improve the bandwidth further, a parasitic rectangular element was added on the back of the substrate as it could be seen in Figure 4.13. The optimal value of the width of the parasitic element (G_W) was determined to be 16 mm and length of the element, (G_L) was varied using a parametric sweep in CST.

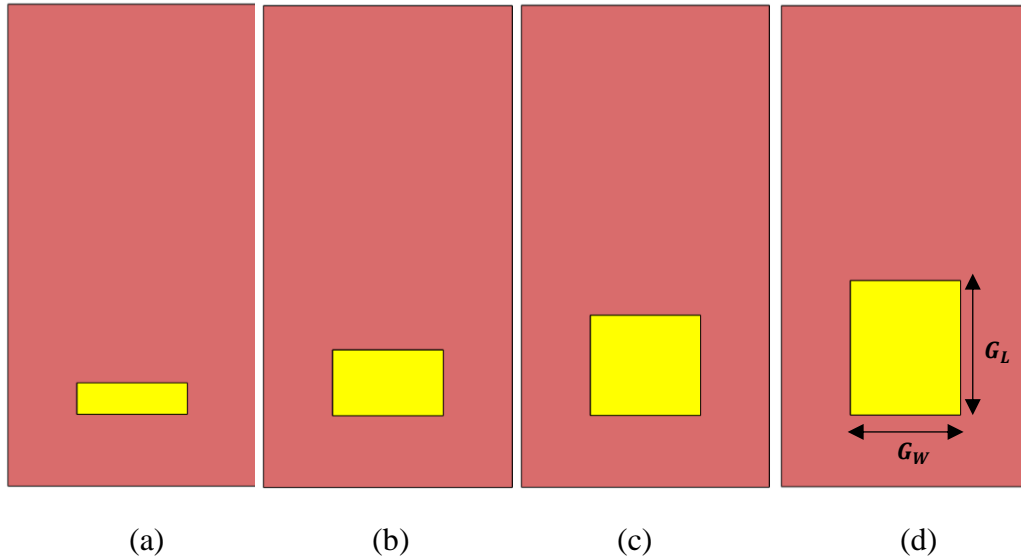


Figure 4.13: Ground rectangular element length (G_L) variation. (a) 4.6 mm (b) 9.6 mm (c) 14.6 mm (d) 19.6 mm.

The reflection coefficients obtained from introducing a rectangular parasitic element introduced at the back of the substrate and varying its dimensions could be seen in Figure 4.14. The optimal bandwidth was attained with G_L equal to 9.6 mm. This resulted in 0.694 fractional bandwidth signifying an ultra-wideband characteristics.

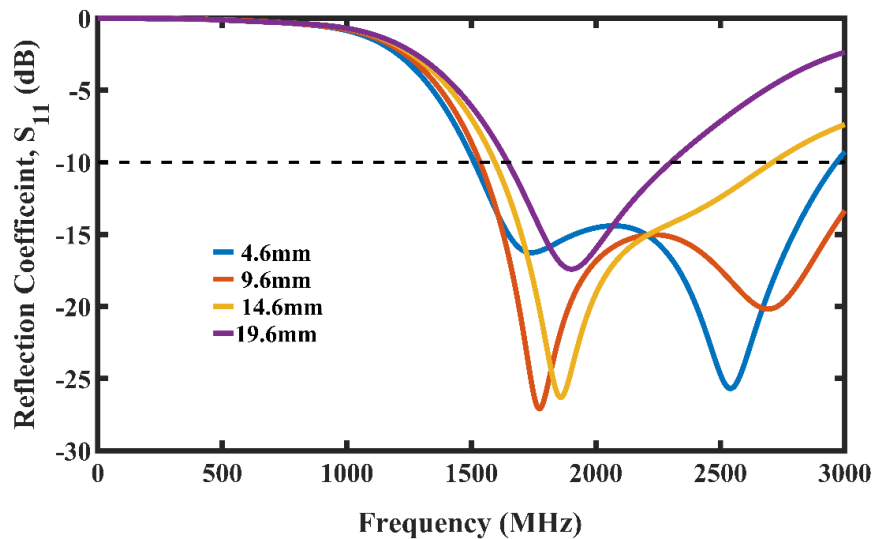


Figure 4.14: Simulation plot for back parasitic rectangular element (G_L) variation.

The dimensions of the final trefoil antenna could be seen in Table 4.6. The substrate dimensions were 1.6 mm, 70 mm and 36 mm for the thickness, length and width

respectively. The copper thickness was 35 micrometres and the patch radius was 24 mm. The two circular elements added to the patch were 10 mm in radius.

Table 4.6: Dimensions of trefoil antenna.

Antenna Parameters	Symbol	Dimensions (mm)
Substrate Length	S_L	70
Substrate Width	S_W	36
Substrate Thickness	S_T	1.6
Antenna Patch Radius	C_R	24
Circular Element Radius	C_{rE}	10
Distance of Patch & Circles	C_C	17.5
Feedline Length	F_L	20
Feedline Width	F_W	6
CPW Gap	G_{pw}	0.59
CPW Length	C_L	30
CPW Width	C_W	14.41
Taper Height	R_{AL}	20
Copper Thickness	T_{cu}	0.035

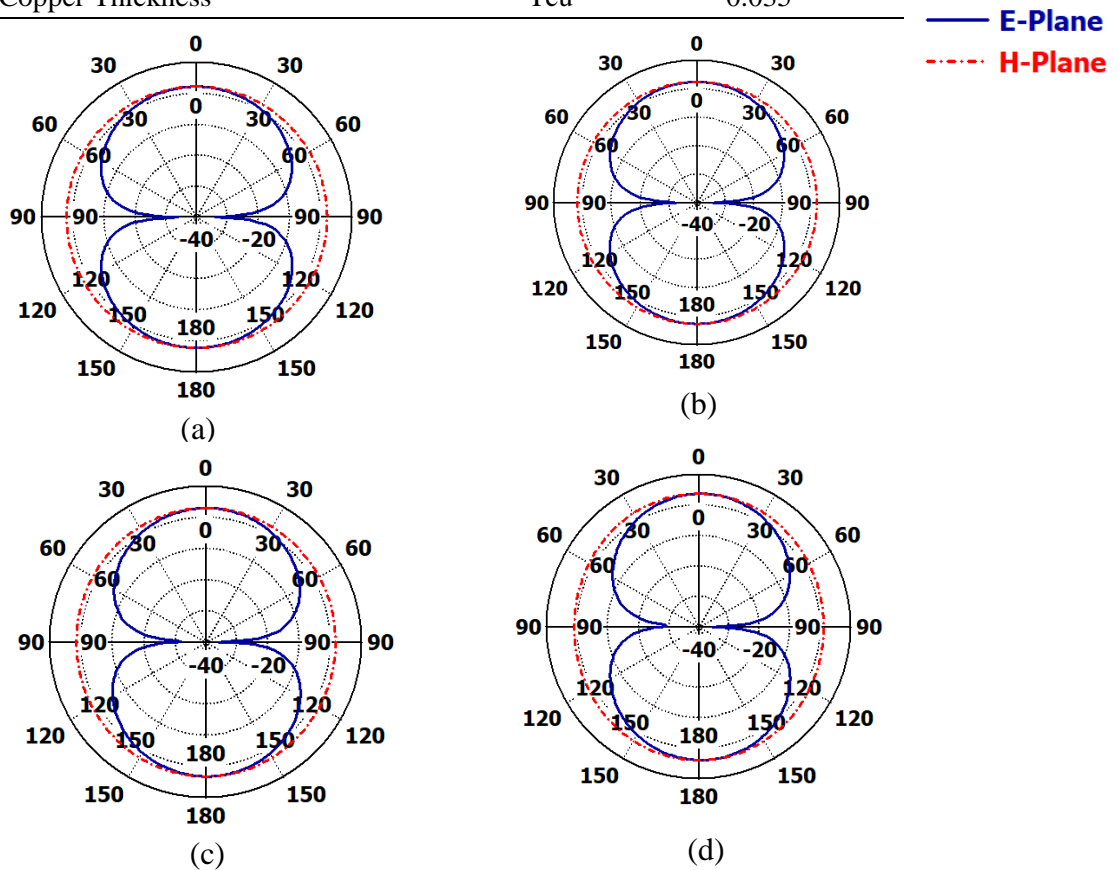


Figure 4.15: Simulated E-(XZ) and H-(XY) plane far-field radiation patterns at (a) 1.5 GHz with directivity of 2.07 dBi (b) 2 GHz with directivity of 2.46 dBi (c) 2.5 GHz with directivity of 3.04 dBi (d) 3 GHz with directivity of 3.73 dBi.

From Figure 4.15, it could be seen that the radiation pattern on the H-plane, which falls on the X-Z plane, across all frequencies was omnidirectional while that on the E-plane, which falls on the Y-Z plane, is bidirectional. The directivity improved from 2.07 dBi at 1.5 GHz to 3.73 dBi at 3 GHz.

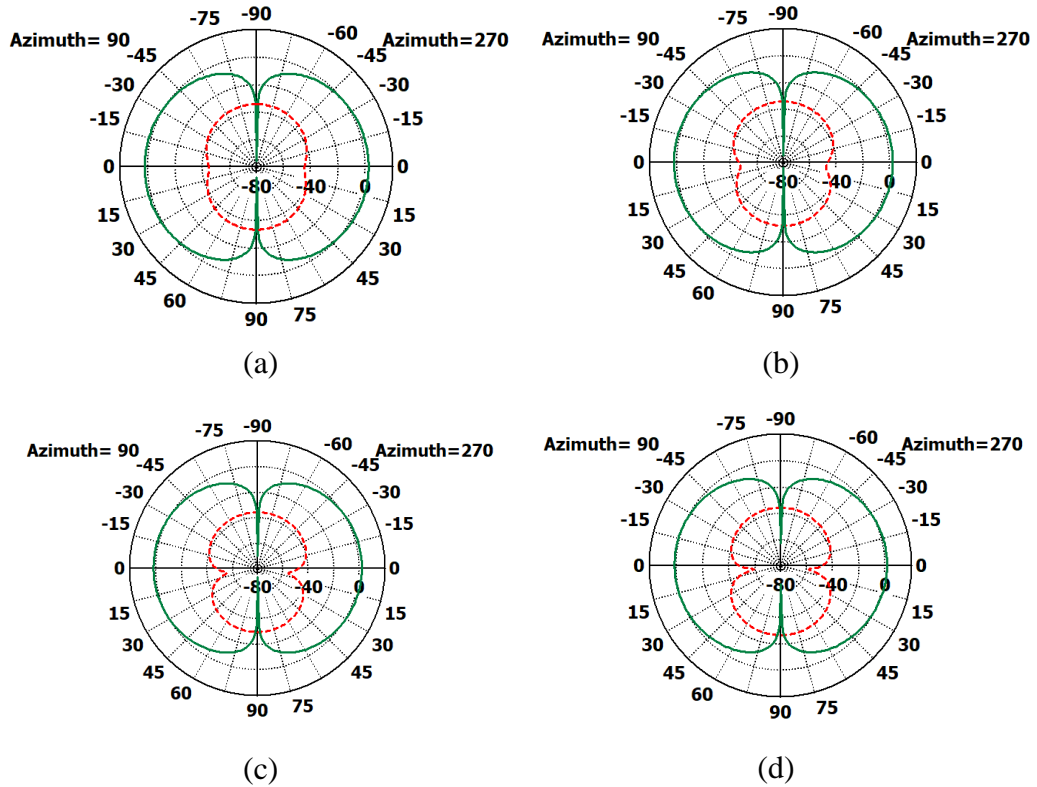


Figure 4.16: Cross polar discrimination (XPD) (a) 1.5 GHz (b) 2 GHz (c) 2.5 GHz (d) 3 GHz.

The XPD for the Trefoil antenna, could be seen in Figure 4.16 for the four frequencies. Although the XPD had degraded below the initial antenna designed, it is still above the recommended 30 dB range for all four frequencies of interest [77].

The surface current distributions for the frequencies of interests could be seen in Figure 4.17. At 1500 MHz, the currents were concentrated on the feedline, on edges of the trefoil patch and the tapered CPW as well as on the boundary of the rectangular element on the back of the substrate as it could be seen in Figure 4.17 (a). At 2000 MHz, the current had spread covering a wide area of the trefoil patch with its sudden reduction on the boundary of the rectangular element on the back of the substrate as it could be seen in Figure 4.17 (b). The current spread increased on the trefoil at 2.5 GHz

as well as on the rectangular element on the back as it could be seen in Figure 4.17 (c). Figure 4.17 (d) showed the maximum current distribution for the antenna at 3000 MHz.

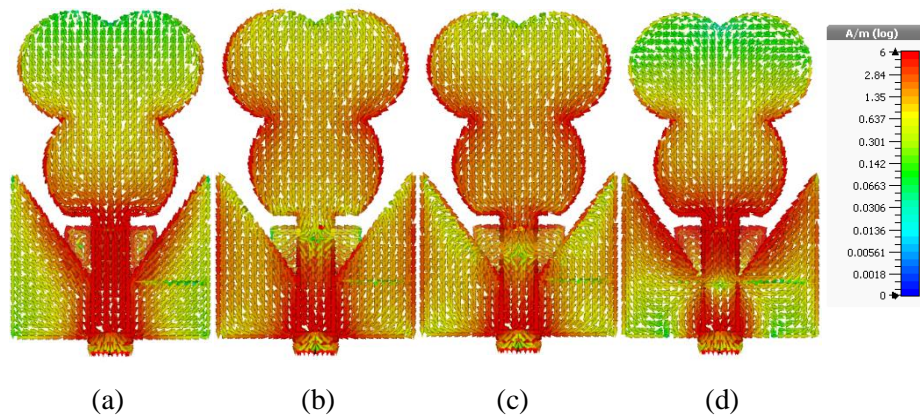


Figure 4.17: Surface Current (a) 1500 MHz (b) 2000 MHz (c) 2500 MHz (d) 3000 MHz.

4.2.4 Trefoil Antenna Submerged in Water

The designed trefoil antenna is targeted to radiate underwater. Thus, it is imperative that the antenna is optimised for underwater operations. Using the CST environment, the final trefoil antenna was immersed in seawater and freshwater phantom as it could be seen in Figure 4.18 (a) and Figure 4.18 (b) respectively.

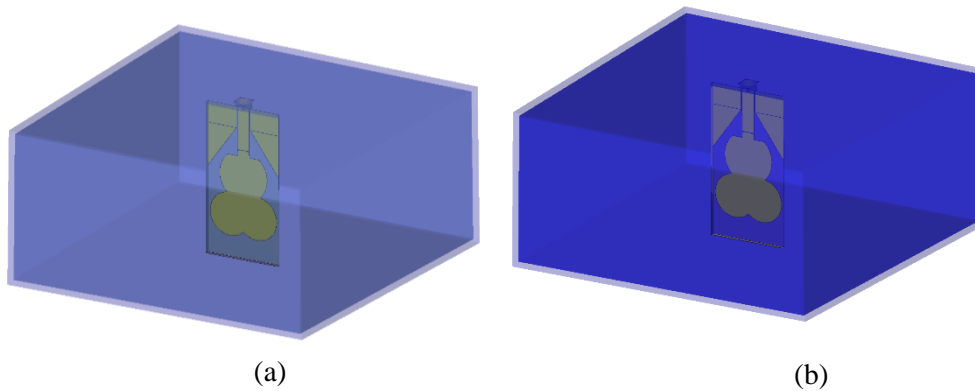


Figure 4.18: Antenna immersed in water (a) Seawater (b) Freshwater.

Predictably, the reflection coefficient of the antenna deteriorated adversely when it was immersed in both media. This was due to the mismatch between the antenna (that was originally designed and optimised for free space application) and the water media.

Thus, most of the power was transferred back to the port of the antenna and only a negligible power was transmitted. There was no -10 dB bandwidth along the whole span of the bandwidth as it could be seen in Figure 4.19. Notwithstanding, it could be seen that the antenna had slightly better performance in freshwater compared to seawater due to the high salinity of the latter that contributed to higher dispersion and attenuation of the RF signal.

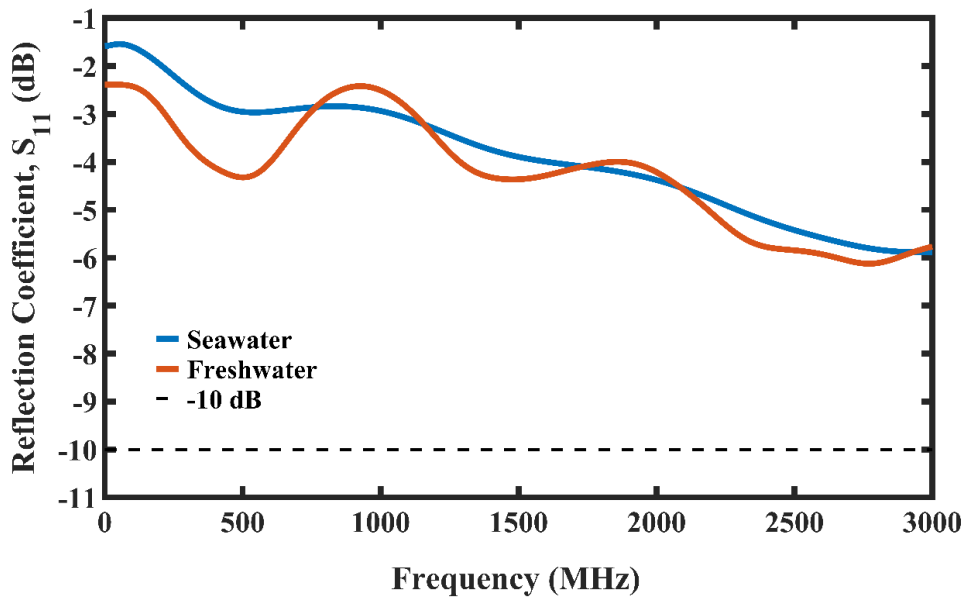


Figure 4.19: Simulation plot for trefoil antenna submerged in seawater and freshwater.

4.2.5 Pulse Fidelity Factor

The developed antenna-sensors would be operating in the near-field region with ultrawideband characteristics. Narrowband antennas are less immune to distortions compared to UWB antennas. UWB has wider band and therefore the possibility of different transmission behaviour within different bandwidth range. Thus, a very important characteristics of UWB antennas is the pulse fidelity factor. It provides the measure of the similarity between the output waveform of an ideal signal to the actual received waveform. The fidelity factor has a maximum and minimum distortion values of 0 and 1 respectively, introduced by the antenna. The fidelity factor, F , can be determined using (4.17) [78].

$$F = \max \int_{-\infty}^{+\infty} r(t) \times S_r(t + \tau) dt \quad (4.17)$$

where $r(t)$ and $S_r(t)$ are the normalised ideal received pulse and actual received pulse for the links.

Four electric probes were placed at an equidistance of 40mm from the antenna-sensor with angle of 0° , 90° , 180° and 270° degrees respectively. Figure 4.20 shows the computed time-domain responses received by the probes surrounding the antenna-sensors.

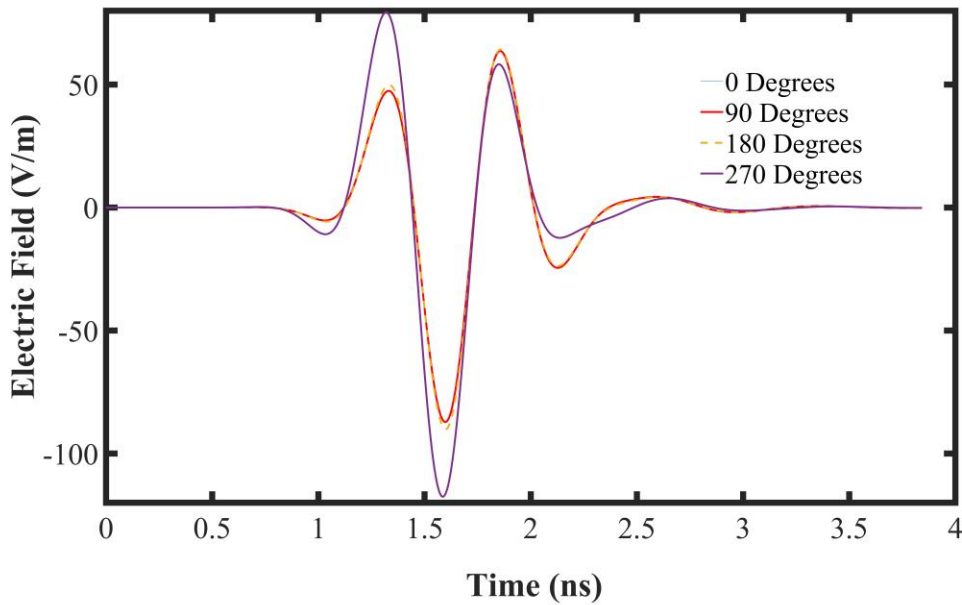


Figure 4.20 : Simulated received near-field time-domain pulses radiated by the antenna-sensor at different angles in the H-plane

The Fidelity Factor for the four angles could be seen in Table 4.7. It could be seen that all the angles exhibited very high fidelity factor with the least at 90° having a value of 0.9685. This shows that the antenna-sensors can transmit and receive signals with very minimal distortions to the original signal in all angles.

Table 4.7 Fidelity Factor of antenna-sensor

Angle (Degrees)	Fidelity Factor
0°	0.9713
90°	0.9685
180°	0.9997
270°	0.9713

4.2.6 PDMS Buffer for Trefoil Underwater Antenna

In this section, a buffer region was introduced to enclose the trefoil antenna and ameliorate the degradation of the antenna performance when it was immersed in water as seen in section 4.2.4.

The need arises to be able to match the antenna with the water medium to achieve maximum power transfer. As shown in section 4.1, buffers have been used to achieve this. However, based on our extensive search of the literature, this is the first time that polydimethylsiloxane (PDMS) is used as a buffer for an underwater antenna. It has several advantages over liquid buffers in the form of robustness, rigidity and applicability. It shares similar advantage as liquid enclosures as it could also take whatever shape required before it is cured.

PDMS also has the advantage of lightweight, ease of controlling the dielectric and magnetic properties [79]. It has extremely high flexibility, heat resistance, chemical stability and water resistance [80]. PDMS has been found to be a suitable choice in the development of radio frequency components because it has a relatively low loss in the microwave region [81], [82]. Compared to other polymers, PDMS is easier to prepare[83].

The initial thickness of the buffer layer was determined by the radiating near field region equation in (4.2) and it was found to be 60 mm at a frequency of 1.38 GHz. The initial buffer dimensions could be seen in Table 4.8. The trefoil antenna, totally enclosed in the PDMS, could be seen in Figure 4.21.

Table 4.8: Buffer parameters.

Buffer Parameters	Symbol	Dimensions (mm)
Buffer Length	B_L	76
Buffer Width	B_W	42
Buffer Thickness	B_T	60

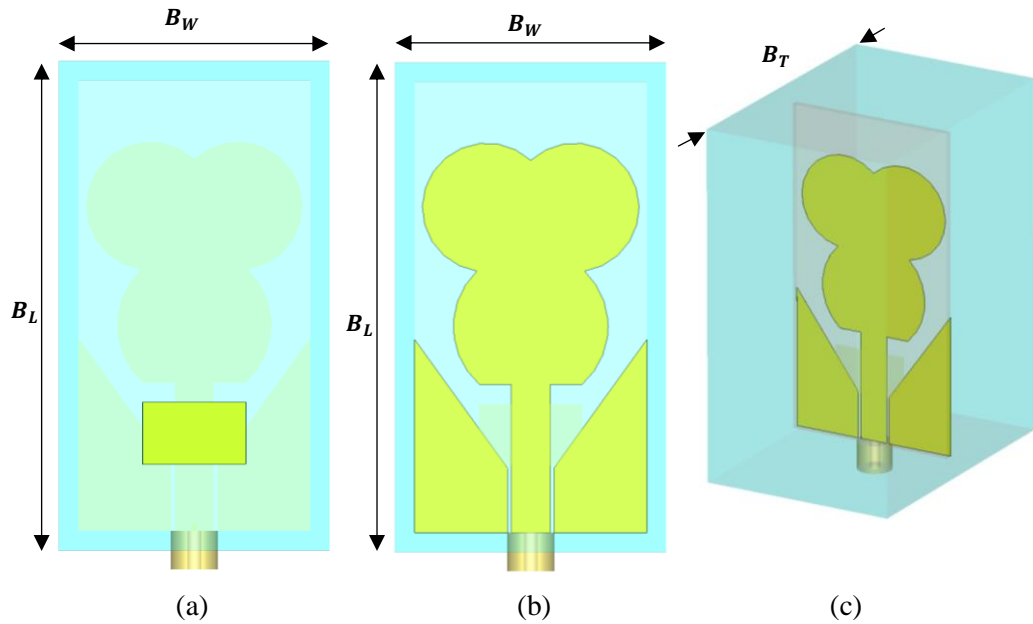


Figure 4.21: PDMS Buffer Encapsulation (a) Front (b) Back (c) Perspective.

The PDMS enclosed antenna was then immersed in freshwater and seawater as it could be seen in Figure 4.22 (a) and Figure 4.22 (b) respectively. A simulation of the PDMS encapsulated antenna was undertaken to provide a benchmark for the subsequent dimensions and measurements of the fabricated trefoil antenna encapsulated in PDMS. Parametric sweeps were performed where the buffer thickness was varied in CST using arbitrary points of 10 mm, 20 mm, 40 mm, 60 mm and 80 mm for both seawater and freshwater media. The properties of the PDMS buffer material used in the simulation could be seen in Table 4.9.

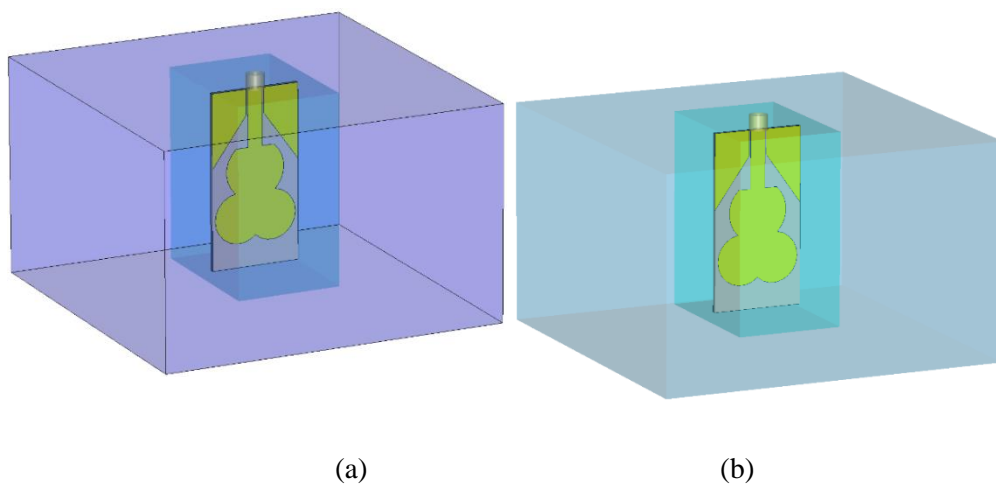


Figure 4.22: PDMS Enclosed Antenna Immersed in Water (a) Freshwater (b) Seawater.

Table 4.9: Properties of the PDMS phantom in CST.

PDMS Properties	Values
Relative Permittivity	2.5
Permeability	1
Electric Conductivity	$2.5e^{-14}[S/m]$
Material Density	$0.97[kg/m^3]$
Thermal Conductivity	$0.15[W/K/m]$
Heat Capacity	$1.4kJ/K/kg]$
Diffusivity	$0.000110457[m^2/s]$
Young’s Modulus	$615[kN/mm^3]$
Poisson’s Ratio	0.475

The results obtained from varying the thickness of the PDMS encapsulating the trefoil antenna after it has been submerged in water could be seen in Figure 4.23 and Figure 4.24 for seawater and freshwater respectively. It is interesting to note that in both cases when the PDMS-encapsulated trefoil antenna was submerged in seawater and freshwater, the maximum bandwidths were achieved at a PDMS buffer thickness of 10 mm. The fractional bandwidth, B_F , in both media were in the UWB range. However, it could be seen that the fractional bandwidth for the freshwater at 0.92 was higher than that obtained in seawater which was 0.81.

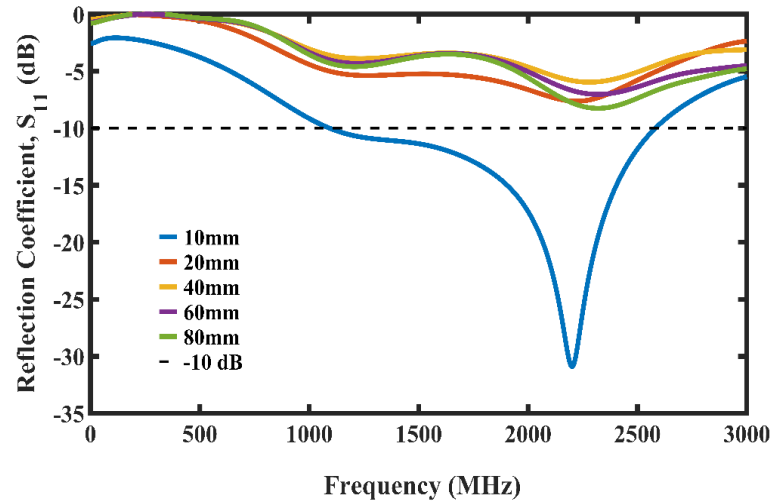


Figure 4.23: Simulation plot for PDMS thickness variation in seawater.

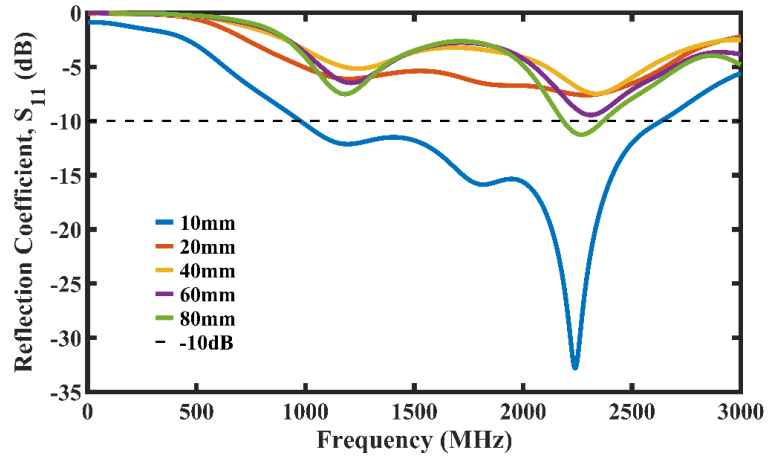


Figure 4.24: Simulation plot for PDMS thickness variation in freshwater.

4.2.7 Fabrication and Measurement Results

To validate the design and simulations results for the underwater trefoil antenna, the work proceeded to fabricate and measure the antenna as well as the PDMS-encapsulated antenna.

A. Trefoil Antenna

The Trefoil antenna designed in section 4.2.3 was manufactured as it could be seen in Figure 4.25. The antenna was fabricated on an FR-4 substrate from PCBWay with a dimension of 70.5 mm by 36.5 mm by 1.6 mm. A 50 Ohm SMA connector was soldered unto the antenna.

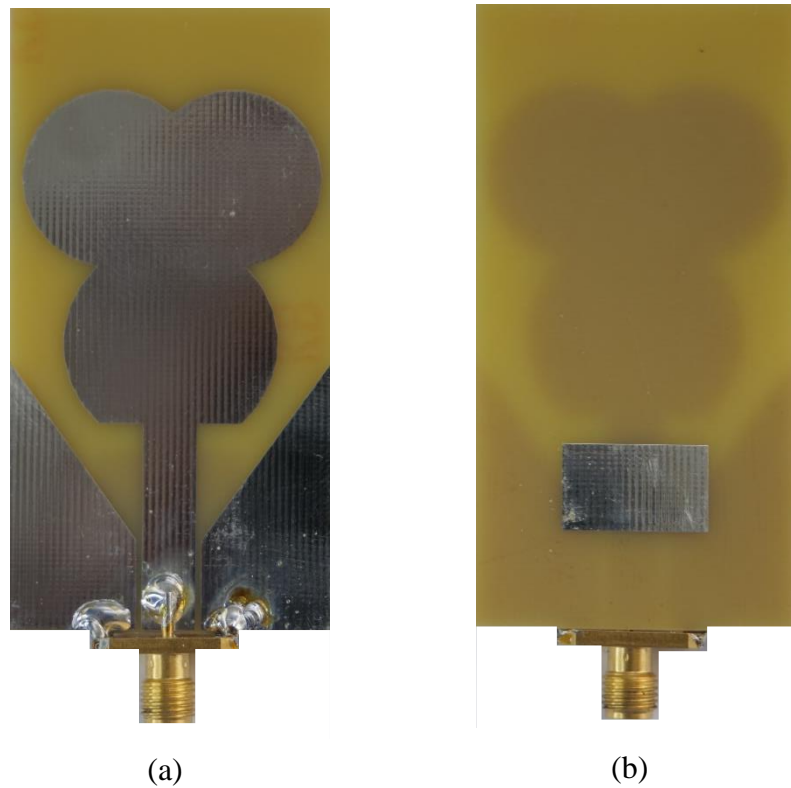


Figure 4.25: Fabricated trefoil antenna (a) Front (b) Back.

The detailed parameters used in the fabrication of the trefoil antenna could be seen in Table 4.10. Using a HP 8753 VNA, VNA utility software and PC, the reflection coefficients of the antennas were obtained.

Table 4.10: Parameter details for fabricated trefoil antenna.

Product Details	Parameters
Board Types	Single Pieces
Size	70.5 mm x 36.5 mm
Layer	2
Thickness	1.6 mm
Silkscreen	None
Surface Finish	HASL with lead
Via Process	Tenting vias
Material	FR-4: TG130
Minimum Track/Spacing	6/6 mil
Solder Mask	None
HASL to ENIG	No
Finished Copper	1 oz Cu

The reflection coefficient measurements obtained for two of the fabricated trefoil antennas could be seen in Figure 4.26. They were compared with the result obtained for the simulation of the antenna in CST.

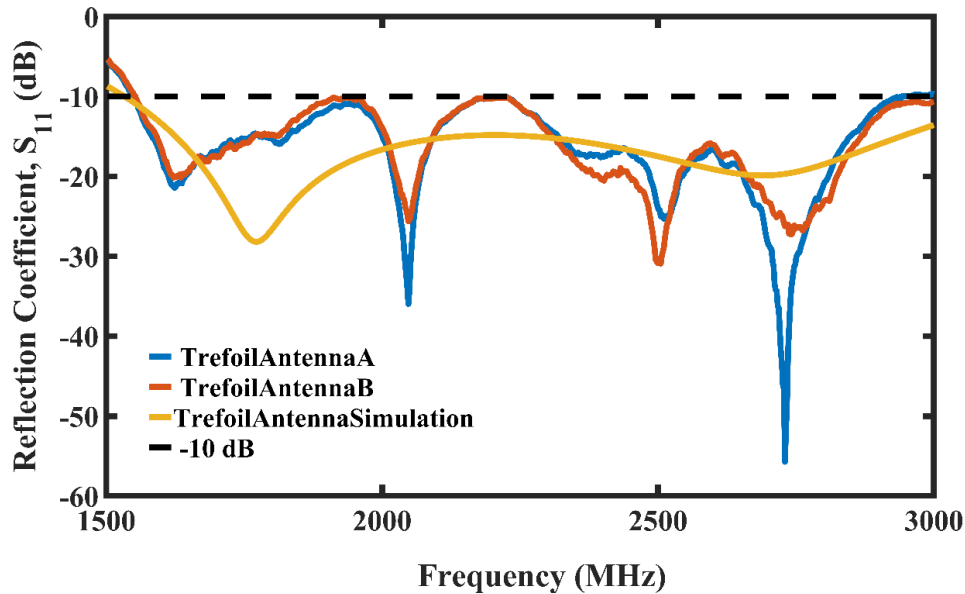


Figure 4.26: Reflection coefficient of measured two trefoil antennas vs simulated trefoil antenna.

It could be seen that the measured result of the reflection coefficients of the two antennas conformed to the simulated results. The -10 dB of the simulated Trefoil antenna began at 1545 MHz and exceeded 3000 MHz while the measurement of the two fabricated antennas began at 1550 MHz and extended to 3000 MHz with a resultant fractional bandwidth of 0.640. Both the simulated and measured antennas exhibited UWB characteristics.

The CST simulations were based on optimal test environment without noise such as thermal, flicker and white noise resulting from the electronics or interferences. However, in the real world, these noises exist. Sometimes, even the movement of the cables could introduce noise into the system. The effects of these noises could be seen as oscillations in the measured results of the S parameters.

B. PDMS Mould

To encapsulate the trefoil antenna with a PDMS, a mould is required. A PDMS mould was designed using a 3D model software based on the PDMS dimensions from the

simulations in section 4.2.5. The mould was 3D printed using polyactic acid (PLA). An image of the 3D model and the final 3D printed moulds could be seen in Figure 4.27 (a) and Figure 4.27 (b) respectively.

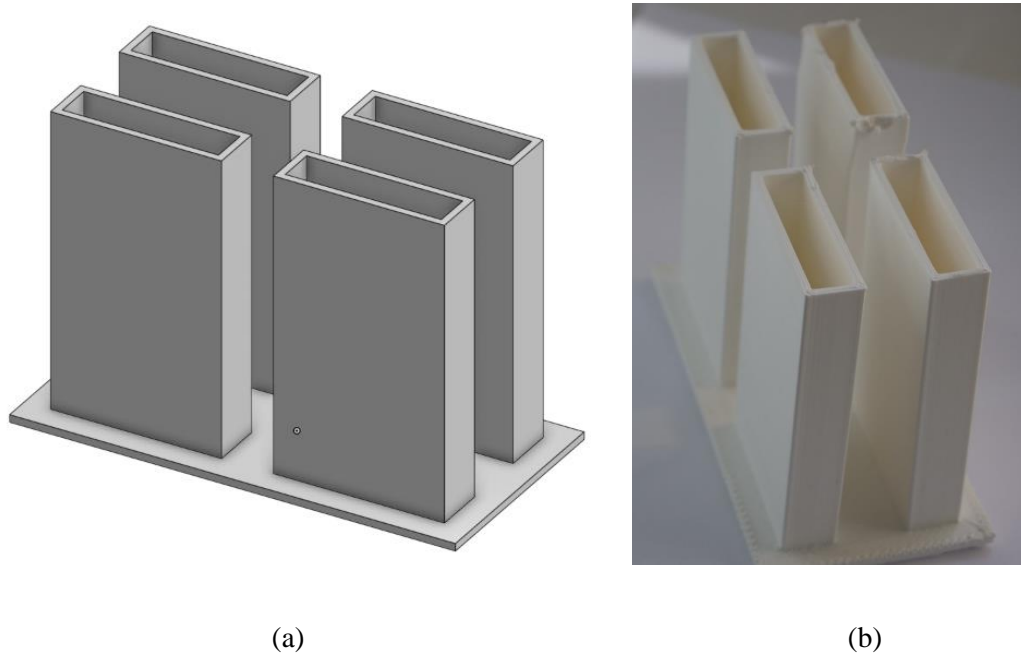


Figure 4.27: Mould for PDMS (a) 3D Model (b) 3D printed mould.

C. PDMS Fabrication

The Dow silicone 10 to 1 encapsulant, supplied as two-part liquids were used for the PDMS encapsulation [84]. The properties of the two-part base elastomer and curing agent could be seen in Table 4.11.

Table 4.11: Properties of two-part base elastomer and curing agent [84].

Property	Unit	Result
Viscosity (Base)	cP	5100
	Pa-sec	5.1
Viscosity (Mixed)	cP	3500
	Pa-sec	3.5
Thermal Conductivity	btu/hr ft °F	0.15
	W/m °K	0.27
Specific Gravity (Cured)		1.03
Working Time at 25°C (Pot Life-Hours)	Hours	1.5
Cure Time at 25°C	Hours	48
Heat Cure Time at 100°C	Minutes	35
Heat Cure Time at 125°C	Minutes	20
Heat Cure Time at 150°C	Minutes	10
Durometer Shore		43
Dielectric Strength	Volts/mil	500
	kV/mm	19
Volume Resistivity	Ohm*cm	2.9E+14
Dissipation Factor at 100 Hz		0.00257
Dissipation Factor at 100 kHz		0.00133
Dielectric Constant at 100 Hz		2.72
Dielectric Constant at 100 kHz		2.68
Linear CTE (by DMA)	Ppm/°C	340
Tensile Strength	PSI	980
	MPa	6.7
	Kg/cm ²	69
Refractive Index	@589 nm	1.4118
Refractive Index	@632.8 nm	1.4225
Refractive Index	@1321 nm	1.4028
Refractive Index	@1554 nm	1.3997
UL RTI Rating	°C	150

The PDMS encapsulation of the antenna was performed in the University of Edinburgh's clean room facility at the Scottish Microelectronics Centre. Initially, the weight of the container was zeroed on the scale as seen from Figure 4.28 (a). Subsequently, the silicone elastomer base was poured into the container. The weight of the silicone elastomer base was recorded as it could be seen in Figure 4.28 (b) to be 155.4 g. The silicone curing agent was added using the ratio of 10:1 between the base and the curing agent respectively. This resulted in a solution of 170.7 g as seen in Figure 4.28 (c).

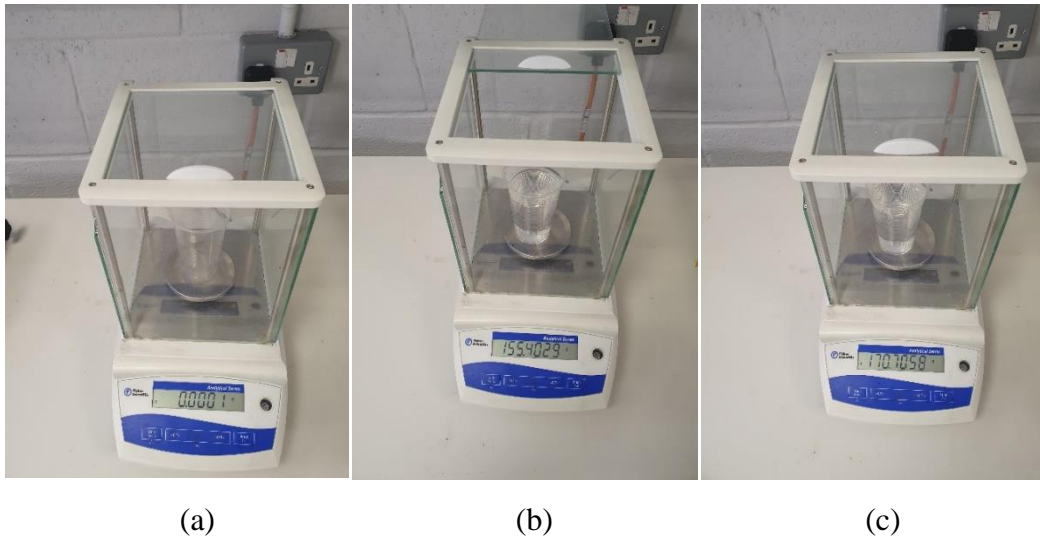


Figure 4.28: (a) Zeroing the scale (b) Weighing Dowsil 184 silicone elastomer base (c) Weighing Dowsil 184 silicone elastomer base & silicone curing agent.

The next stage of the process was the mixing of the solution. It was allowed to thoroughly mix for 15 minutes using an automatic magnetic mixer as it could be seen in Figure 4.29 (a). Some air bubbles were formed because of the mixing. These are unwanted because they could create air traps around the antenna and may affect the final antenna performance. Thus, there is a need to de-air or degas the mixture. The degassing was done with a vacuum pump and a desiccator as it could be seen in Figure 4.29 (b). The degassing process was allowed to run for two hours.

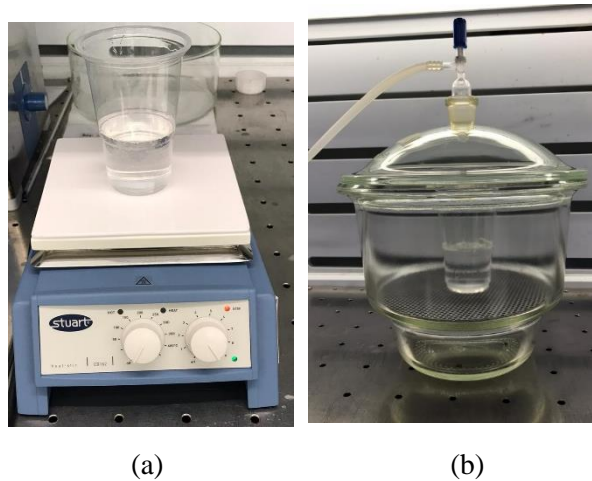


Figure 4.29: (a) Magnetic mixing of Dow silicone solution (b) Degassing the mixed silicone solution.

The final process was the curing of the solution. The antennas were then placed in the moulds and the degassed mixture was poured into the moulds. From Table 4.10, using a heat cure at 100°C, the curing time is 35 minutes. This period reduces to 10 minutes at a temperature of 150°C. However, since we were using a PLA mould, we had to resort to curing at a room temperature of 25°C which required two complete days. The final PDMS encapsulated antennas could be seen in Figure 4.30.

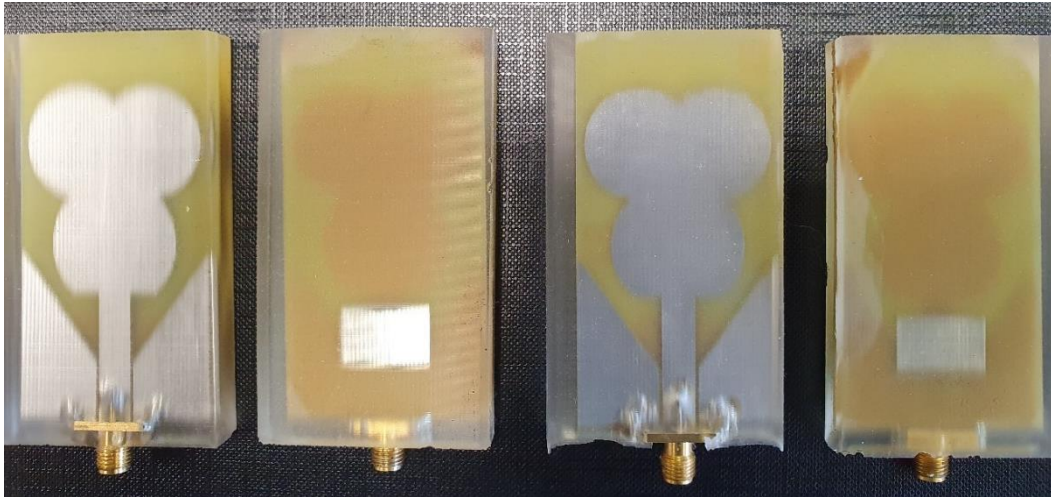


Figure 4.30: PDMS encapsulated trefoil antenna.

The reflection coefficients of two PDMS-encapsulated trefoil antennas were measured in free space. Figure 4.31 shows both the measured and simulated results.

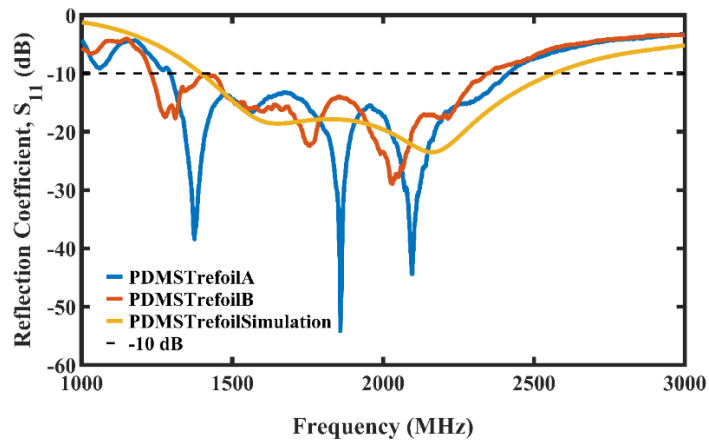


Figure 4.31: Simulated and measured reflection coefficient of PDMS encapsulated antennas in free space.

It could be seen that the simulated reflection coefficient conformed to the measured results from the two antennas except for a slight shift of frequencies. The measured PDMS-encapsulated trefoil antenna A had a fractional bandwidth of 0.61, PDMS-encapsulated trefoil antenna B had a fractional bandwidth of 0.63 and the simulation PDMS-encapsulated antenna's fractional bandwidth was 0.60. The PDMS-encapsulated antenna, also called the antenna-sensor, targets the underwater environment, not free space, therefore no far field tests were undertaken. Additionally, the antennas shall be operating in the near-field regions.

D. PDMS-Encapsulated Trefoil Antenna in Seawater and Freshwater

The PDMS-encapsulated antenna was immersed in water as it could be seen in the experimental setup shown in Figure 4.32. Using an open, short and load studs, a one-port calibration was performed on the HP 8753 VNA. The frequency of interests was selected from 300 KHz to 3000 MHz with 1601 points for smooth representation of both the transmission and reflection coefficients. These settings conformed to the simulation settings in CST used for this design.



Figure 4.32: Experimental setup for underwater antenna tests.

The S-parameters were captured using the KE5FX VNA utility software on the computer as it could be seen in Figure 4.33. This was done for the antenna submerged in both seawater and freshwater.

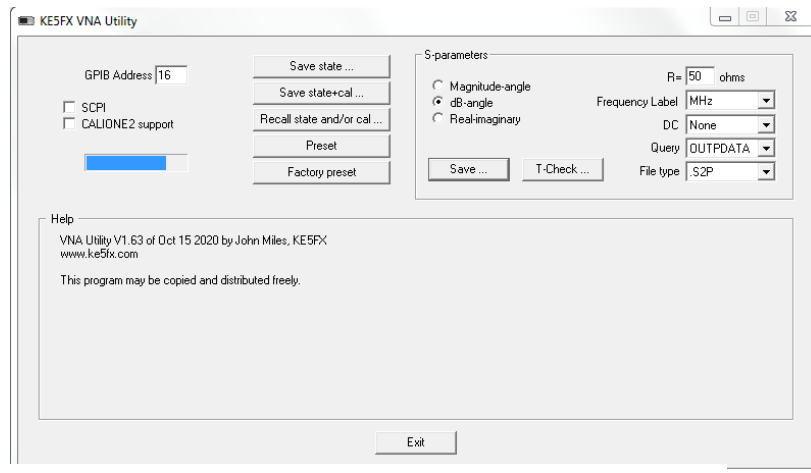


Figure 4.33: KE5FX VNA utility software.

Using the experimental setup, the reflection coefficients of the PDMS-encapsulated trefoil antenna in both seawater and freshwater were obtained as shown in Figure 4.34. The fractional bandwidth of the antenna was found to be 1.024 and 0.951 for the freshwater and seawater media respectively. These values show that the antenna exhibited ultra-wideband performance characteristics when submerged in both media.

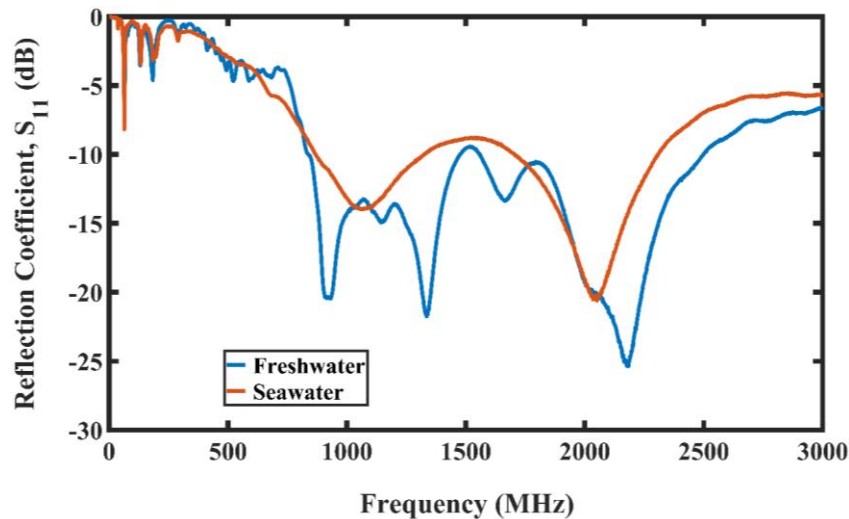


Figure 4.34: Measured reflection coefficient of PDMS-encapsulated trefoil antenna in freshwater and seawater.

From Table 4.12, it could be seen that the novel PDMS-encapsulated trefoil antenna design radiates underwater with UWB characteristics unlike the other antennas. It also has anti-rust capabilities because it was encapsulated in PDMS. This is very important because the antenna would be immersed in seawater. Seawater reacts with copper or metals, which most antennas are made from, resulting in oxidation and rust. These would have adverse effects on the antenna performance.

Table 4.12: Comparison of Fabricated Antennas for Seawater Sensing Applications

Antenna	UWB Fractional Bandwidth	Encapsulation Type	Anti-rust
Trefoil Antenna (This work)	0.951	PDMS	Yes
Ref [85]	N/A	Deionised Water	No
Ref [86]	N/A	None	No
Ref [60]	N/A	Tap Water	No
Ref [87]	N/A	None	No

4.3 Summary

In this chapter, ultra-wideband PDMS-encapsulated trefoil antennas for sensing and imaging application in both seawater and freshwater were designed, developed and fabricated.

The antenna design began with a microstrip printed circular monopole antenna (PCMA) with a coplanar waveguide (CPW). The initial base antenna had a fractional bandwidth of 0.227. A right-angled triangle taper on the CPW was introduced which resulted in a slight improvement in the B_F by just 0.001.

However, when the trefoil design was implemented by adding two minor circles to the patch antenna, the B_F improved substantially to UWB region at 0.581 fractional bandwidth. Adding the rectangular parasitic element to the back of the substrate in the final trefoil antenna design resulted in an ultra-wideband characteristic in the region of 0.694 B_F . The trefoil antenna was fabricated on FR-4 substrate and the free space

reflection coefficient measurements were performed. A B_F of 0.64 was obtained which was just slightly below the simulated result.

However, when the final trefoil antenna was submerged in seawater and freshwater without a buffer in CST, no fractional bandwidth was obtained due to the impedance mismatch between the antenna and the media. Introduction of a 10 mm PDMS buffer in CST resulted in a substantial improvement of the B_F up to 0.81 and 0.92 for the seawater and freshwater respectively.

With this simulated validation, a PDMS-encapsulation for the antenna based on the simulated dimensions using Dow silicone 10 to 1 encapsulant, supplied as two-part liquids were performed. Some moulds were designed and 3D printed. The antennas were inserted into the middle of the moulds and the degassed mixture of the elastomer and curing agent were poured into the mould. The mixture was allowed to cure for 48 hours and thereafter the measurements of the reflection coefficients for the PDMS-encapsulated antennas were performed. The measured B_F of the encapsulated trefoil antenna in both seawater and freshwater, had the best performances with respect to all measurements in terms of the fractional bandwidth. The antenna-sensor had UWB fractional bandwidths in seawater and freshwater with values of 0.951 and 1.024 respectively.

The next chapter shall employ the use of the antenna-sensor developed in this chapter, for developing an in situ microwave oil spill detection prototype in a transmitter-receiver pair configuration targeting seawater and freshwater media.

Chapter 5

Microwave Oil Spill Detection Prototype

In this chapter, a prototype of oil spill detection sensor made from the antenna-sensor designed in the previous chapter was developed. A Faraday cage was manufactured for the experiment consisting of a 3D printed PLA container padded by copper foil. The spacing of the two antenna-sensor were determined and separation distances of 15 mm, 50 mm and 70 mm were selected. The simulations result for the oil spill were validated experimentally beginning with rapeseed oil as a proof-of-concept before proceeding to use heavy aromatic-naphthenic Azeri crude oil as an inclusion in both the seawater and freshwater medium. The experiment with the rapeseed oil can be found in APPENDIX A. The 15 mm, 50 mm and 70 mm antenna spacing with freshwater medium and heavy aromatic-naphthenic Azeri crude oil as an inclusion can be found in APPENDIX B.

In this chapter, only the experiment with seawater medium and the heavy aromatic-naphthenic Azeri crude oil as an inclusion shall be discussed.

5.1 Faraday Cage

Two antenna-sensors were placed inside an acrylic container of 2 mm thickness in the CST environment. The container was filled with water phantom at 20 degrees Celsius. The distance between the antennas were varied and the reflection coefficients were observed. The distances of interests were 15 mm, 20 mm, 40 mm, 60 mm, 70 mm and 80 mm. A schematic of the antenna-sensor spacing could be seen in Figure 5.1.

A Faraday cage, used to eliminate interference from external electromagnetic waves as shown in [88],[89] and [90] was developed in CST by covering the acrylic container with copper.

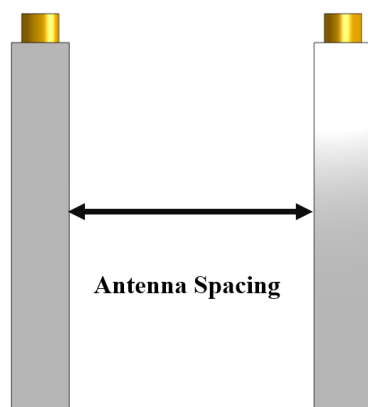


Figure 5.1: Antenna spacing

The CST model of the acrylic container and the simulated and fabricated Faraday cages could be seen in Figure 5.2 (a), (b) and (c) respectively for the 70 mm antenna spacing with all of them filled with water.

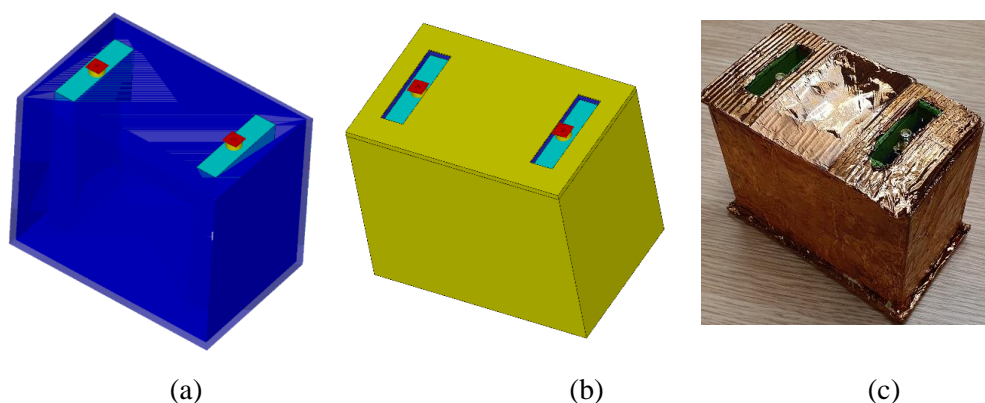


Figure 5.2: Oil spill sensing region (a) Antennas in acrylic in CST (b) Faraday cage in CST (c) Fabricated Faraday cage.

For simplicity, this work shall be looking at only the reflection coefficients (S_{11}) of the transmitting antenna and the forward transmission coefficients (S_{21}) of transmitting antenna to the receiving antenna. This is because the performances of both antennas were similar, thus both the forward and reverse transmission coefficients were the same.

5.1.1 Reflection Coefficients for Faraday Cage

The simulation results for the reflection coefficients of the PDMS-encapsulated trefoil antennas placed in the Faraday cage and filled with water with the distance between the antennas varied could be seen in Figure 5.3 and Figure 5.4 for freshwater and seawater respectively.

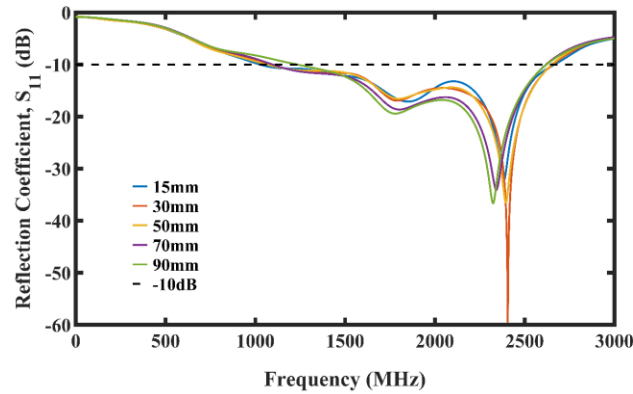


Figure 5.3: Simulation plot showing reflection coefficient of different antenna-sensors spacing in freshwater.

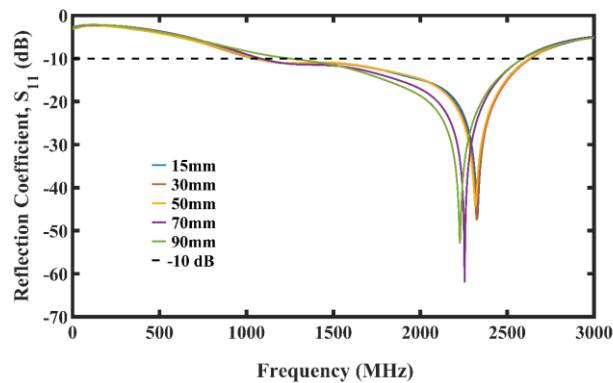


Figure 5.4: Simulation plot showing reflection coefficient of different antenna-sensors spacing in seawater.

5.1.2 Transmission Coefficients for Faraday Cage

The corresponding transmission coefficients for the two antenna-sensors when submerged in freshwater and seawater could be seen in Figure 5.5 and Figure 5.6 respectively.

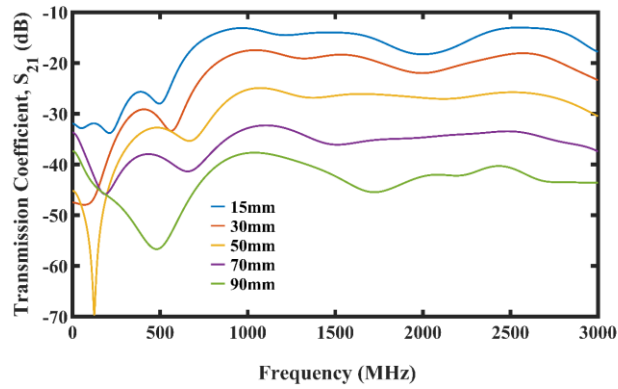


Figure 5.5: Simulation plot showing transmission coefficient of different antenna-sensors spacing in freshwater.

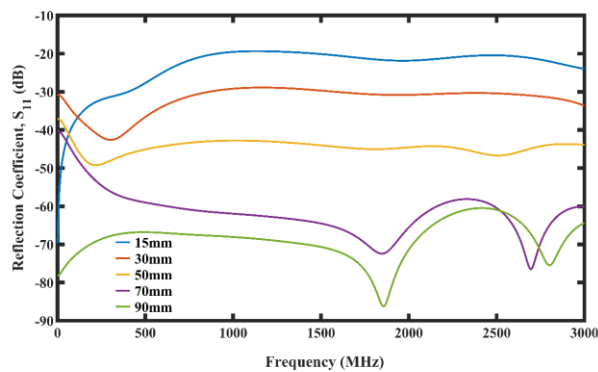


Figure 5.6: Simulation plot showing transmission coefficient of different antenna-sensors spacing in seawater.

Based on the results from Figure 5.3, Figure 5.4, Figure 5.5 and Figure 5.6, the work adopted the antenna distance of 15 mm, 50 mm and 70 mm for the oil spill simulation and experiments.

5.2 Crude Oil Spill Simulation

To have a proof of concept for the oil spill detection prototype, the three selected Faraday cage experimental setups for antenna-sensor spacing of 15 mm, 50 mm and 70 mm were filled with a medium with variable relative permittivity in CST. For each of

the antenna-sensor distance, the relative permittivity property of the medium was varied to mimic that of the oil spill.

When oil spill occurs, water combines with oil and the dielectric property of the medium changes. This change is what shall be detected to establish the occurrence of oil spillage. The relative permittivity was varied from that of unadulterated freshwater to seawater and subsequently it was reduced until a dielectric constant of crude oil was attained.

5.3 Crude Oil Spill Measurement Setup

With the water as the medium and the crude oil or rapeseed oil as inclusions, two-phase Tinga-Voss-Blossey (2-TVB) mixture model suitable for materials that have multiple confocal ellipsoidal structures that mix poorly with each other, could be used to estimate the dielectric properties of the resulting mixtures [91]. The quasi-two-phase model of the complex relative permittivity of the mixtures has been adopted for both freshwater and seawater given by (5.1).

$$\epsilon_{mixture} = \epsilon_{medium} + \frac{3v_{oil}\epsilon_{medium}(\epsilon_{oil} - \epsilon_{medium})}{2\epsilon_{medium} + \epsilon_{oil} - v_{oil}(\epsilon_{oil} - \epsilon_{medium})} \quad (5.1)$$

where ϵ is the complex permittivity, v is the volume fraction, ϵ_{medium} is the complex permittivity of the freshwater or seawater host medium and ϵ_{oil} is the complex permittivity of the inclusion (rapeseed oil or crude oil).

The oil spill experiments were performed using seawater as the transmission. The oil spill experimental setup can be seen in Figure 5.7. A two full port calibration was done on the 8753 Vector Network Analyser (VNA) using the open, short and load studs. The frequency span was chosen to be 2999.7 MHz, with a start frequency of 0.3 MHz and stop frequency of 3000 MHz. The number of points were selected to be 1601 to get very accurate plots. The power was set at -10 dBm. After the calibration, the two ports of the 8753 VNA were connected to the two antenna-sensors. The transmitting antenna-sensor was connected to port 1 while the receiving antenna-sensor was connected to port 2.

The S Parameters of the PDMS encapsulated trefoil antennas were obtained in seawater to verify their performances. The performances shall be compared with those obtained from the simulation. The oil spill experiments were performed using the 70 mm, 50 mm and 15 mm antenna-sensor spacing Faraday cage setups.



Figure 5.7: Experimental setup for the oil spill test for crude oil.

5.4 Crude Oil Spill Measurement

Crude oil is highly combustible [92]. Thus, the experiment began with a non-volatile liquid that is not as inflammable as crude oil to provide a proof of concept for the microwave oil spill detection prototype. Rapeseed oil was chosen because it has a relative permittivity similar to crude oil [93]. Rapeseed oil has a dielectric constant of around 2.93 while crude oil has a relative permittivity of 2.2 to 2.4 [94]. The methods and results obtained for the rapeseed oil experiment could be found in APPENDIX A.

After successfully developing a proof of concept using the rapeseed oil, the work proceeded with caution to experiment using crude oil as inclusion in seawater and

freshwater media. Heavy aromatic-naphthenic Azeri crude oil (HANACO) was used as an inclusion for the experiment.

The two antennas were placed in the Faraday cage. A 650 ml volume of water was then poured into the Faraday cage. The S parameters for the unadulterated seawater were obtained using KE5FX VNA Utility software on the PC that was connected to the 8753 VNA. Subsequently, 10 ml of the HANACO was added to the seawater medium and the S Parameters were measured for the new mixture. 10 ml of the HANACO crude oil were continuously added to the solution until a maximum of 100 ml of the HANACO crude oil was added to the seawater medium. The S Parameters were continuously measured for each added HANACO inclusion. These were done for all the three Faraday cage setups with antenna-sensor spacing of 15 mm, 50 mm and 70 mm in seawater. For the experimental results of the freshwater medium and HANACO crude oil inclusions, please refer to APPENDIX B.

5.5 Reflection Coefficients for Oil Spill

The reflection coefficients obtained for both the simulation and measured results would be discussed in this section. The measured results are represented as bold lines while the simulated results are exhibited in dashed lines.

Changes can be observed in the reflection coefficient of all the antenna-sensors in the three setups. This was due to changes in the dielectric constant of the seawater that resulted from the introduction of HANACO crude oil which had a substantially lower relative permittivity compared to the former.

5.5.1 70 mm Antenna Spacing

It could be seen from Figure 5.8 that noticeable divergences in the reflection coefficients from that of pure seawater began at around 500 MHz for the 70 mm spaced antenna-sensors in both the simulation and measured results. For the simulation, the changes extended to around 3000 MHz while that for the measured S11 extended to around 2000 MHz.

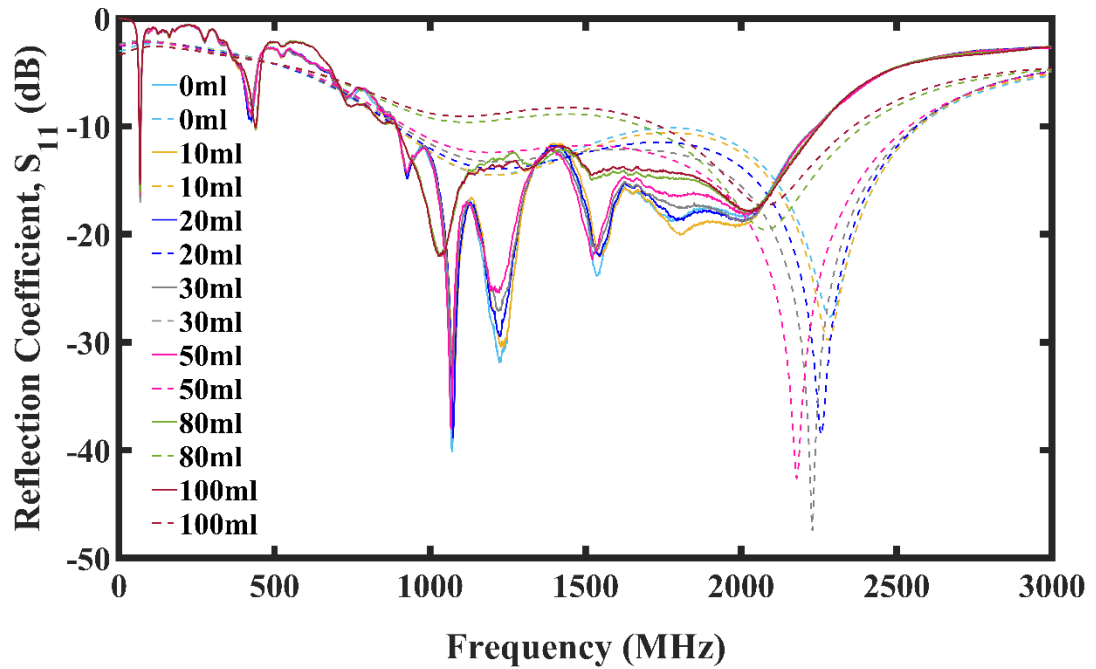


Figure 5.8: Plot showing reflection coefficient for oil spill using 70 mm antenna-sensors spacing.

5.5.2 50 mm Antenna Spacing

It could be seen from Figure 5.9 that noticeable divergences in the reflection coefficients from that of pure seawater began at around 873 MHz for the 50 mm spaced antenna-sensors in the simulation results. These divergences could be seen from 1000 MHz in the measured S_{11} . The S_{11} for the simulation and measured results extended to 2990 MHz and 2000 MHz respectively.

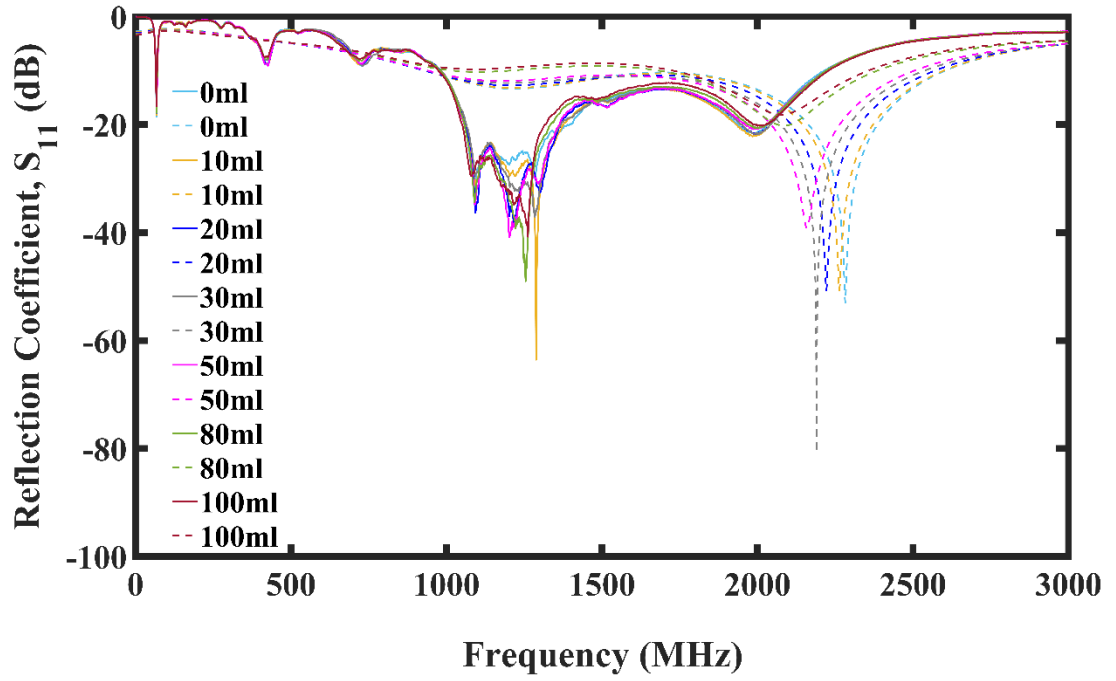


Figure 5.9: Plot showing reflection coefficient for oil spill using 50 mm antenna-sensors spacing

For antenna-sensors in the 15 mm setup, the changes in the measured reflection coefficient spanned from 750 MHz to 2500 MHz, as shown in Figure 5.10. For the simulations, the changes for the antenna-sensors spanned from 800 MHz to 2900 MHz.

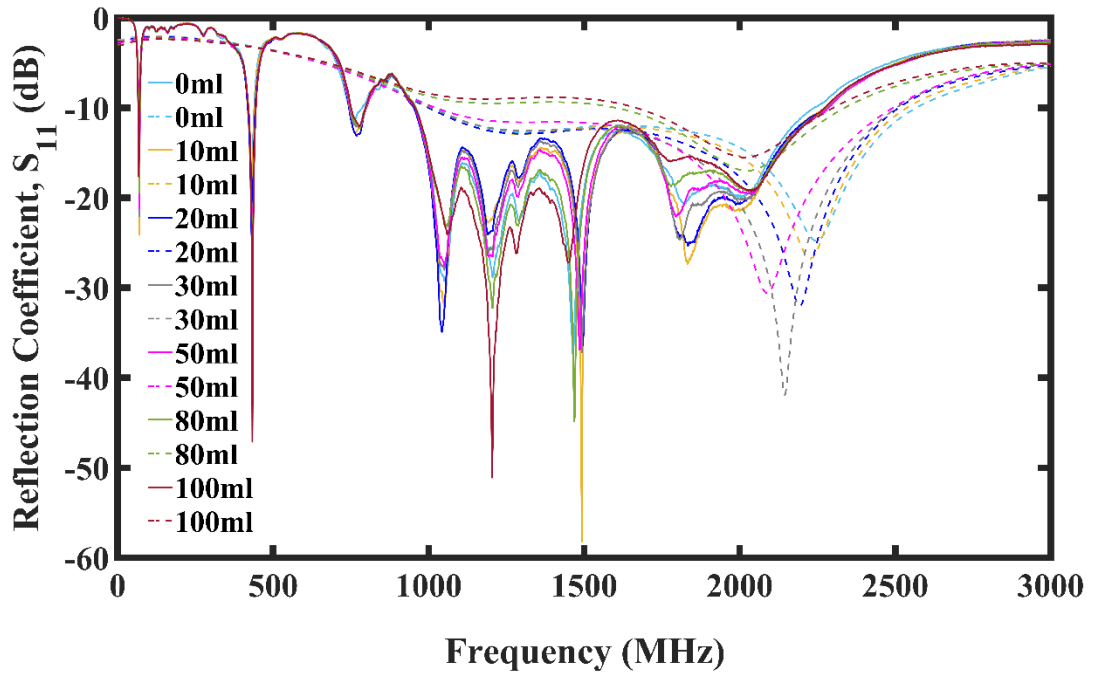


Figure 5.10: Plot showing reflection coefficient for oil spill using 15 mm antenna-sensors spacing

These changes in the reflection coefficients and corresponding shifts in frequency, and consequently bandwidth, is due to a change in the dielectric constant of the water transmission medium because of the inclusion of HANACO crude oil.

5.6 Transmission Coefficients for Oil Spill

The transmission coefficients obtained for both the simulation and measured results would be discussed in this section. The measured results are represented as bold lines while the simulated results are exhibited in dashed lines.

The transmission coefficients could be seen from Figure 5.11, Figure 5.12, and Figure 5.13 for the 70mm, 50mm and 15mm antenna-sensors spaced Faraday cage setups respectively. The forward transmission coefficient (S_{21}) and the reverse transmission coefficient (S_{12}) were obtained for the three setups. Because these values were similar for the same setup, only the forward transmission coefficient shall be considered. For clarity, only the S_{21} for the pure seawater host medium and the mixture

with HANACO oil inclusions of 10 ml, 50 ml, 80 ml and 100 ml are shown in all the three setups.

As it could be seen from Figure 5.11, for the 70mm setup, there was no noticeable difference between the pure seawater and adulterated seawater at 10 ml and 50 ml. However, the difference in the S_{21} is obvious between the three states and the HANACO adulteration at 100 ml

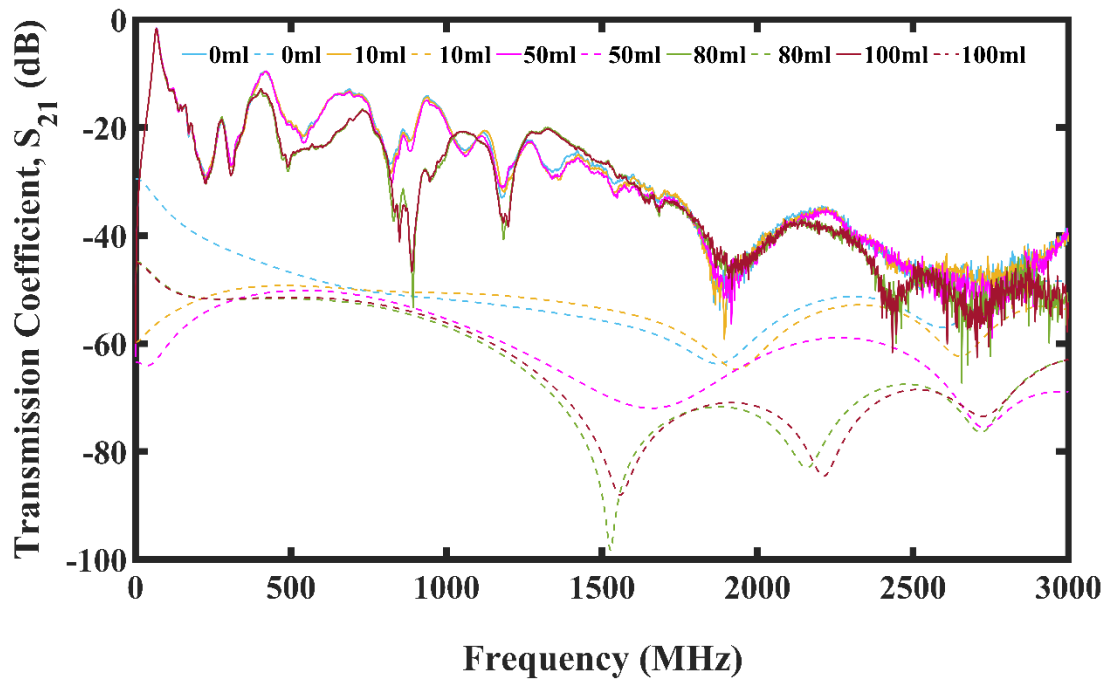


Figure 5.11: Plot showing transmission coefficient for oil spill using 70 mm antenna-sensors spacing.

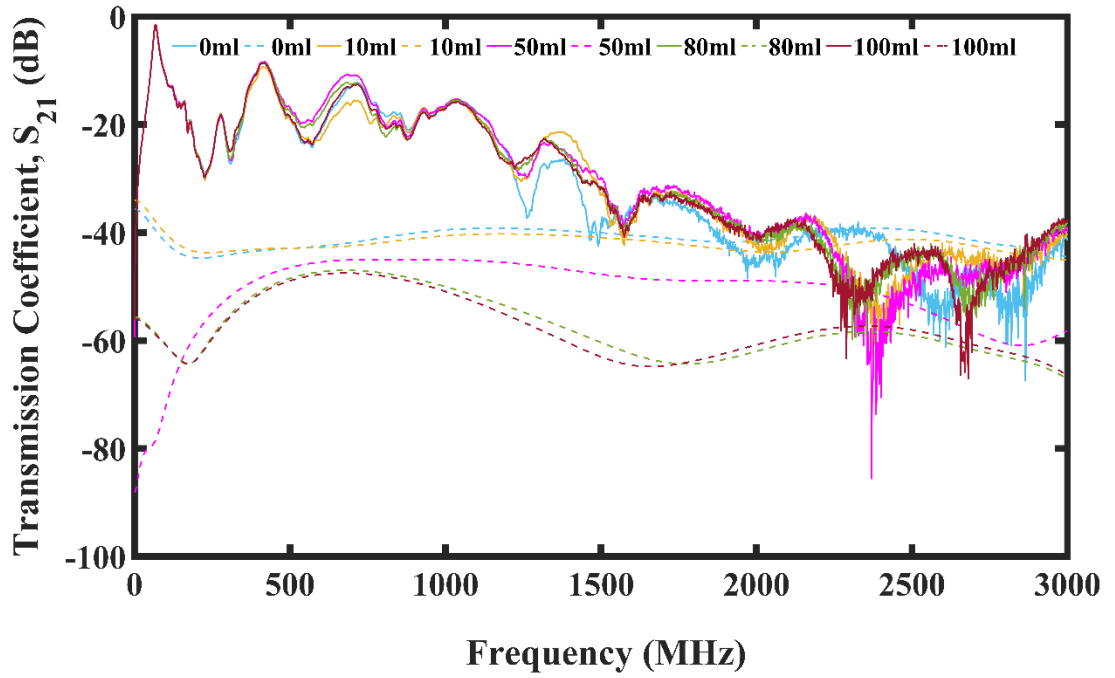


Figure 5.12: Plot showing transmission coefficient for oil spill using 50 mm antenna-sensors spacing.

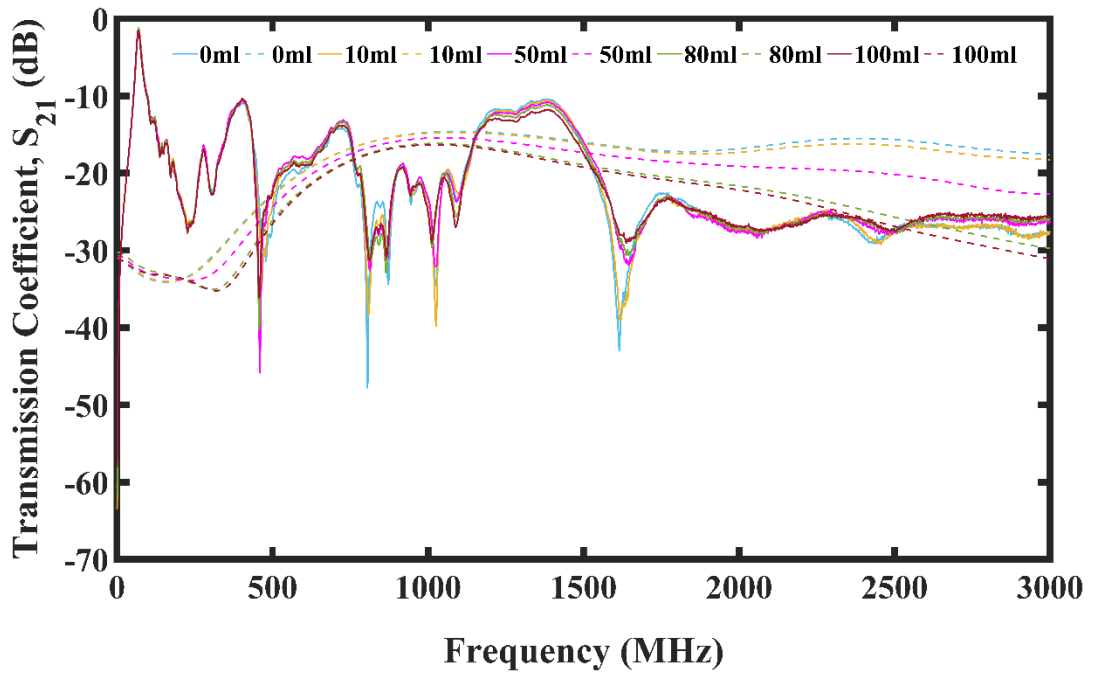


Figure 5.13: Plot showing transmission coefficient for oil spill using 15 mm antenna-sensors spacing.

It could be seen that the value of the transmission coefficients reduces with increasing oil spillage and frequency. Based on the simulation and measured results, the transmission coefficients for the antennas separated by 15 mm had the highest values due to the proximities of the antenna-sensors. The result of the 50 mm setup shows noticeable differences in all three adulteration states in both simulation and measurements. Finally, for the 15 mm antenna-sensors spacing, the variation in the S21 was the most minimal. This may be partly due to the reason that the antenna-sensors were spaced too close together. Notwithstanding, all the transmission coefficients in all cases decreased with frequency due to the high lossy nature of seawater. The difference in the simulation and measured results are as a result of noises and other imperfections in the experimental setups.

The S11 of the three antenna-sensor spacings could be used for the detection of oil spill. However, based on the S21, 70 mm antenna spacing exhibited the superior performance with the least performance shown by 15 mm antenna spacing setup.

5.7 Summary

In this chapter, a novel in-situ oil spill monitoring device capable of the detection of oil spillage in both seawater and freshwater was designed and developed. The device comprised of two novel PDMS-encapsulated ultra-wideband underwater microwave trefoil antennas enclosed in a Faraday cage.

Using the reflection and transmission coefficients simulation results, antenna-sensors spacing of 15mm, 50mm and 70mm were selected to develop the Faraday cage setups for the oil spill sensing experiment. The use of the Faraday cage was to eliminate electromagnetic interference that may affect the fidelity of the results. This was done by covering the acrylic container with a copper foil.

The work was able to validate the capability of the device for oil spill detection by developing a customised medium in CST with a variable dielectric constant. The relative permittivity was varied between that of fresh water at 78, seawater at 74 and down to that of oil at 2.33. The antenna-sensors were able to detect those changes both

using the reflection and transmission coefficients. These formed the basis for the experiment.

Due to the high combustibility of crude oil, the work used rapeseed oil to provide a proof-of-concept of the detection capability of the device before proceeding with the heavy aromatic-naphthenic Azeri crude oil for the oil spill experiment in freshwater and seawater. The baseline of the pure freshwater and seawater at 0 ml adulterations were registered and then the crude oil inclusions were continually added to the water medium for all three antenna-sensors spacing until 100 ml of the HANACO had been added.

The reflection coefficients obtained showed variations in the responses in relation to those of the unadulterated seawater medium. The 70mm setup's S11 for the inclusions were observed to start varying from that of the unadulterated seawater from 500 MHz to 2000 MHz. Difference in relative permittivity was observed at 10 ml crude oil and increased at 50 ml and 100 ml. For the 50mm setup, noticeable difference in the reflection coefficient could be seen from 800 MHz to 2500 MHz. For 15 mm setup, it was from 750 MHz to 2500 MHz. The transmission coefficients for the 70 mm and 50 mm setups had better variation compared to the 15 mm setups.

In the next chapter, a long range (LoRa) water surface communication backbone enabling real-time application for the microwave oil spill sensor using a novel 868 MHz braid antenna shall be discussed.

Chapter 6

Communication Backbone for Oil Spill Sensor Telemetry System

In this chapter, a novel design, fabrication, measurement, and implementation of an antenna with dual ability of short underwater and water surface long range (LoRa) communication at ISM band of 868 MHz was undertaken. This was to provide a telemetry system for the in-situ microwave oil spill detection and oil slick measurement sensor operating at the water surface and when submerged underwater. This enables the microwave sensor to have real-time data transmission capabilities.

A novel braid antenna was developed operating at LoRa's 868 MHz band. It was observed that the antenna's performance deteriorated underwater, resulting in a non-existent -10 dB effective bandwidth between 668 MHz and 1068 MHz. The introduction of an oil-impregnated paper buffer around the antenna resulted in an effective 400 MHz bandwidth within the same frequency span. The antenna was benchmarked using some commercial off-the-shelf (COTS) LoRa antennas operating at 868 MHz.

6.1 Overview of Water Surface Communication

Different communication methods exist. Both wired and wireless approaches for the propagation of signals underwater have been deployed. These includes acoustics [95], radio frequency (RF) [96], optical waves [97] and wired communication [98]. The underwater communication medium, unlike the terrestrial free space, has high permittivity and conductivity. These characteristics make acoustic signals better suited for long range underwater communication. However, the inherent high latency and low bandwidth of acoustics makes it unattractive for high bandwidth and real-time applications. Because acoustics operate in the hearing range of some marine life, it is injurious to them [99].

The RF signals are less successful for underwater communication because of its high attenuation and consequently limited range of transmission. However, for terrestrial applications, RF transmissions are more advantageous compared to acoustic signals because of its lower latency and higher bandwidth [100], [101]. Thus, from the water surface to any terrestrial base station, the RF is better suited for the transmission of data.

The candidates for this RF communication backbone can be broadly classified as short range or long range. Technologies such as Bluetooth, WiFi and Zigbee can be grouped into the former. These would not be useful in Internet of Things (IoT) applications that requires to send low bandwidth sensor data over long distances. For these, the low power wide area (LPWA) communication technologies are more suited. The two contending candidates for this technology are the narrowband IoT (NB-IoT) and the long range (LoRa). The NB-IoT was set up by the 3rd Generation Partnership Project (3GPP). It is part of the Long Term Evolution (LTE) standard but has been stripped of some of its features such as handover, carrier aggregation, and dual connectivity to simplify it. It uses the quadrature phase shift keying (QPSK) modulation scheme and operates in the licensed band of LTE [102].

LoRa operates in the unlicensed bands below 1 GHz. It employs the chirp spread spectrum modulation (CSS) which enables it to have the long great link budget. NB-IoT boasts of better quality of service (QoS), reliability and range. However, LoRa is unlicensed, thus cheaper and has better performances with respect to battery management and capacity [102], which are essential capabilities for a wireless sensor. This work adopted LoRa technology because of these advantages it offers.

The work shall review the state of the art in this field. It shall explore the different long range sensor node communication systems that were developed using the LPWA technology and review the designs that are capable of both water surface and underwater communication considering the effects of the water surface and underwater environment on the antenna performance.

Off-the-shelf components were used to assemble a low cost unmanned surface vehicle to collect parametric data of rivers, lakes or seas in [103]. The data collected

were transmitted using LoRa to a cloud infrastructure. Arduino UNO was used for the data acquisition and processing. A Libelium SX1272 LoRa module was used for data transmission.

In [104], the reliability of LoRa in estuary flooding scenario was investigated using two experimental setup. One was built so that all communication was done on land, to serve as a basis for comparison, while the other was deployed in a river estuary to study the effects of the water surface and the changing water levels on the propagated signal. The antenna heights and distances of the LoRa node with the gateway were investigated. The study concluded that reliability of the LoRa communication depended on the height of the LoRa nodes and consequently the tidal levels.

The old first generation sailing monitoring systems based on 3G technology was replaced by LoRa low power wide area network in [105]. This was due to the former's limitations with respect to coverage and high power consumption. The experiment verified that an increase in the spreading factor (SF) or a decrease in bandwidth (BW) increases the over-the-air transmission time.

The influence of water surface on the radiation pattern of a spiral antenna operating in the S-, C-, X- and Ku-bands was investigated by [106]. A model of the spiral antenna was developed in CST Microwave Suite and the seawater was modelled by placing a perfect electric conductor (PEC) material under the antenna perpendicular to its aperture. The simulation was performed from 2 to 18 GHz. Different scenarios were adopted for the simulation. The first did not involve a water surface. Subsequently, the antenna was raised to a height of 1, 3.5 and 15 m. The study concluded that it was advantageous to raise the antenna as high as possible from the water surface to maintain the fidelity of the received signal.

A log-periodic antenna for long range communication was simulated in [107] for seawater quality monitoring. The antenna was simulated at 36 cm above the seawater surface. The seawater surface was found in this study to improve the matching of the antenna. In [108], a bowtie antenna was implemented for underwater communication using 433 MHz frequency range. The antenna was designed based on a previous work by [109]. Initially, the antenna was designed to resonate at 433 MHz in air with a return

loss of around -10 dB. A 1.6 mm printed circuit board with a copper thickness of 35.6 mm and FR-4 glass-reinforced epoxy laminate was used for the design of the antenna. A 0.30 cubic meter volume was used to simulate the water surface. The work in [108] performed lab tests for the submerged sensor nodes and subsequently deployed the sensor nodes in a canal where the maximum distance achieved was 7 meters and 5 meters for baud rates of 1.2 kbps and 25 kbps respectively.

The design, measurement, and implementation of both a sensor node that transmits data and an IoT gateway that receives this data and publishes it on the Internet was undertaken in this work. The antenna is an integral part of any wireless sensor, thus a novel approach to the design and implementation of a braid antenna using an oil-impregnated paper buffer to improve the performance of the antenna underwater and on water surface operating at 868 MHz frequency range shall be presented. The 868 MHz band is the authorised industrial scientific and medical (ISM) band in Europe.

6.2 Antenna for Water Surface Communication using

LoRa

The system comprises of a buoyed sensor node (BSN) that sends water surface temperature and a terrestrial IoT gateway that receives this data and publishes it on the Internet. The BSN was placed on a buoy and deployed on seawater to measure the water surface temperature and send the data to the terrestrial IoT gateway.

The system architecture for the BSN and IoT gateway could be seen in Figure 6.1 (a) and Figure 6.1 (b) respectively. The systems were both solar powered by a 6V 2W solar panels. An Atmega328P microcontroller controls the operation of the temperature sensor as well as the RFM95 LoRa module. The realtime clock, Ds3231, enabled the microcontroller to go to sleep and wake up to preserve energy which is of paramount importance in wireless sensor node operations.

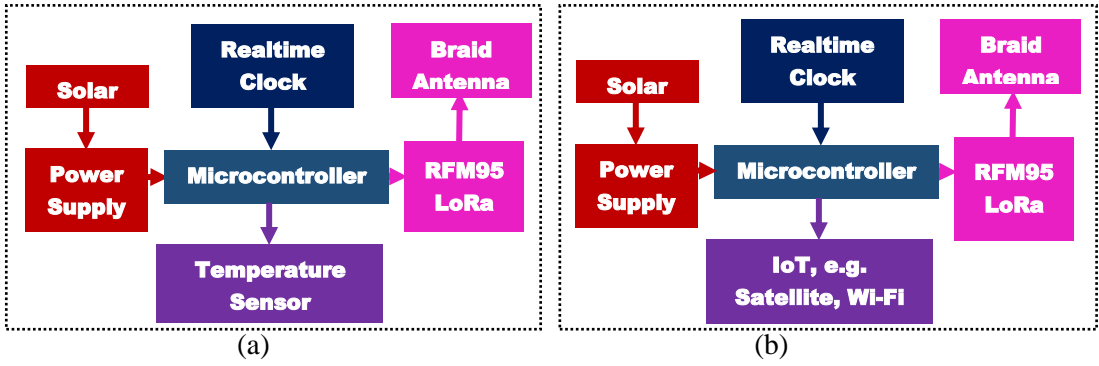


Figure 6.1: (a) BSN (b) IoT gateway.

6.2.1 Braid Antenna Design

The initial design was a printed triangular monopole antenna (PTMA) [110]. It has a triangular patch with a coplanar waveguide (CPW). It does not have a ground plane on the bottom of the FR-4 substrate. The dimensions of the antenna were determined by equating the lower frequency, f_L of the PTMA and its dimensions as it could be seen in (6.1).

$$f_L = \frac{c}{\lambda} = \frac{7.2}{\{(L+r+p) \times k\}} \text{GHz} \quad (6.1)$$

where L & r are the height of the planar monopole antenna and the effective radius of the equivalent monopole antenna respectively. p is the length of the 50Ω feed line of the antenna. All these dimensions are in cm. k can be determined from $\sqrt{\epsilon_{ff}}$. ϵ_{ff} is the relative permittivity of the FR-4 substrate used for the patch antenna design in this work.

To determine both L and r , the side length T of the antenna were used in (6.2) and (6.3) respectively.

$$L = \frac{\sqrt{3}}{2} T \quad (6.2)$$

$$r = \frac{T}{4\pi} \quad (6.3)$$

Using equations (6.1-6.3) the dimensions obtained for the base antenna could be seen in Figure 6.2 and Table 6.1.

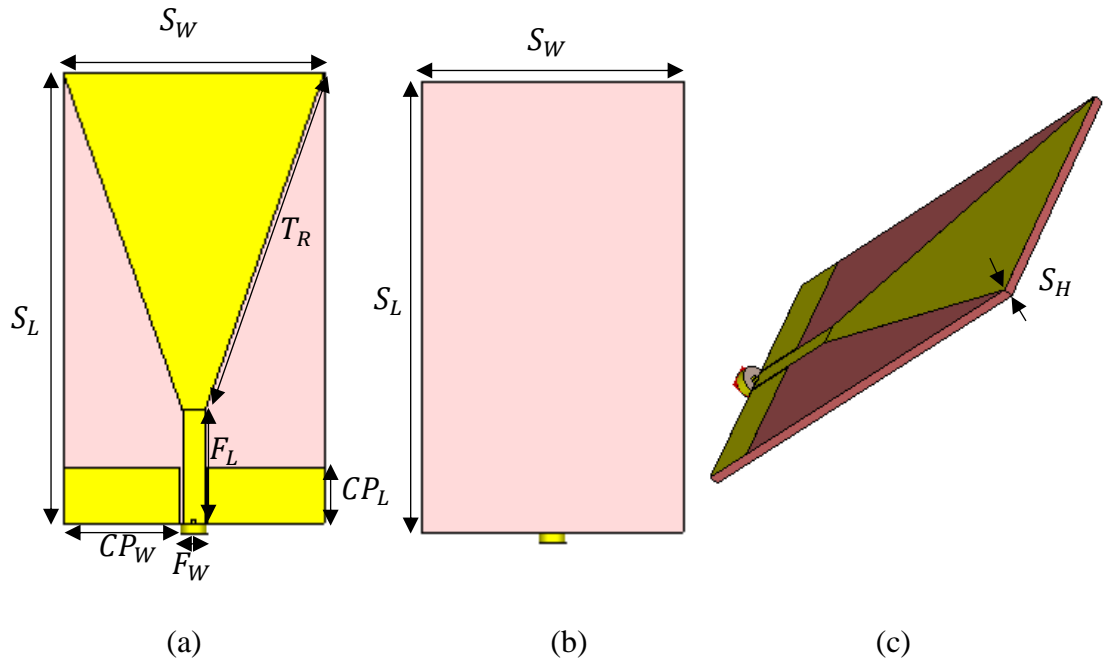


Figure 6.2: Base Antenna (a) Front (b) Back (c) Perspective.

Table 6.1: Dimensions of Base Antenna Parameters.

Parameter	Symbol	Dimension (mm)
Substrate Length	S_L	120
Substrate Width	S_W	70
Substrate Thickness	S_H	2.4
Feed Length	F_L	30
Feed Width	F_W	6
CPW Length	CP_L	15
CPW Width	CP_W	31.41
Triangular Side Length	T_R	95.52

6.2.2 Braid Antenna Simulations

The buoy sensor node and the LoRaWAN Gateway operate at 868 MHz ISM band. Thus, the designed antenna must be able to resonate or operate at this frequency. To achieve this frequency of operation on the base PTMA design, some modifications were made to it. A scalene triangle was added to the CPW and 11 braid slots of 1 mm were introduced on the triangular patch antenna. A rectangular element was introduced from the top end of the braided patch and its length was varied from 5 mm to 35 mm at a step of 10 mm. A representation of these could be seen from Figure 6.3 (a-d). Two rectangular elements were introduced to the back plane of the substrate as it could be seen in Figure 6.3 (e).

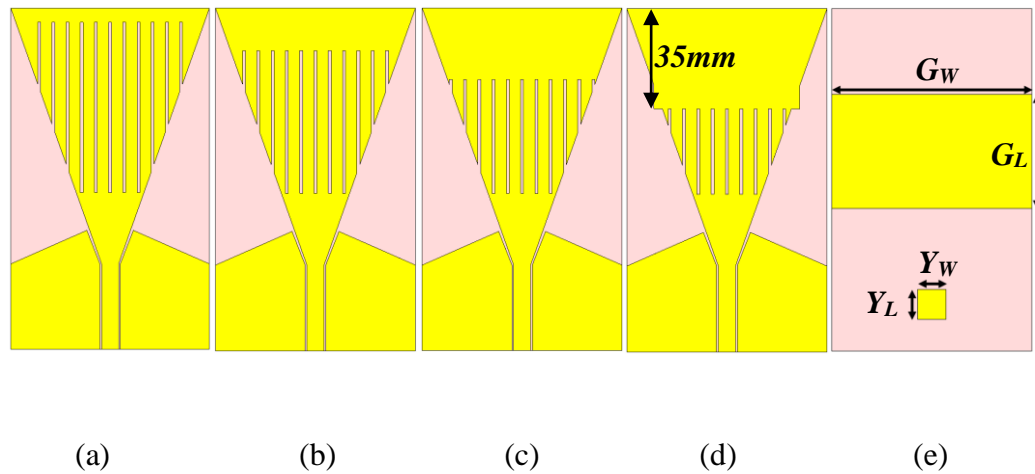


Figure 6.3: Braided Antenna Design; (a) 5 mm (b) 15 mm (c) 25 mm (d) 35 mm (e) Back.

The base antenna, as it could be seen from Figure 6.4 was resonant at 733 MHz. The 122 MHz bandwidth spanned from 680 MHz to 802 MHz. The results from introducing the braid slots, scalene triangular element to the CPW, the two rectangular elements on the bottom plane of the substrate and varying the rectangular length from 5mm to 35 mm, could be seen in Figure 6.4. This resulted in an upward translation of the resonant frequency. The bandwidth for the 35 mm connector was resonant at 867 MHz and spans from 777 MHz to 1016 MHz resulting in a 239 MHz bandwidth.

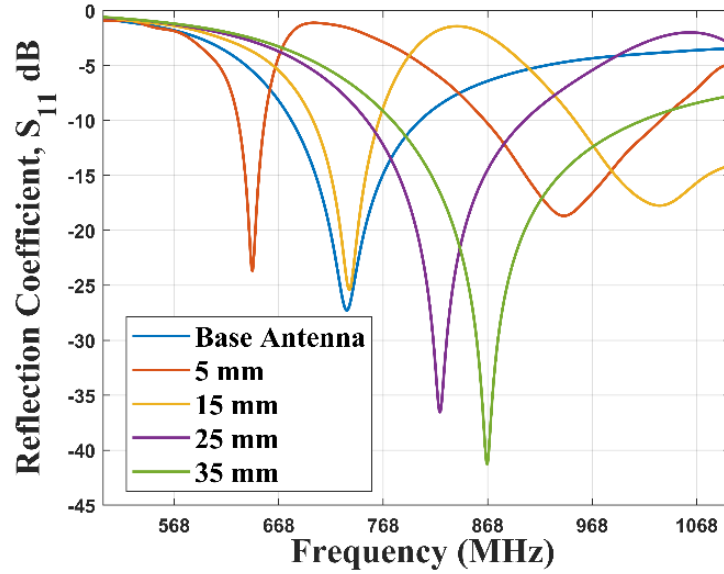


Figure 6.4: Reflection Coefficient of Braid antennas (with varied length).

Some of the 35 mm connector Braid antenna characteristics could be seen in Figure 6.5. The surface current could be seen from Figure 6.5 (a) to be distributed along the slots introduced in the antenna in the form of braids and along the feedline. The antenna has an omnidirectional far field radiation pattern as it could be seen in Figure 6.5 (b) which would enable the antenna to communicate with other sensor nodes in all directions. The antenna has a gain of 2.11 dB. The antenna also exhibited omnidirectional radiation properties in the H plane as it could be seen in Figure 6.5 (d) and a bidirectional radiation pattern in the E plane shown in Figure 6.5 (c).

Based on [111] and results from parametric sweeps, the relationship between the dimensions of the parasitic elements on the back of the substrate seen in Figure 6.3 (e) and the lower frequency (L_{flow}) could be seen in (6.4).

$$L_{flow} = 0.875G_w + 0.9G_L + 0.1Y_w + 0.25Y_L \quad (6.4)$$

where G_w and G_L are the width and length of the larger rectangular parasitic element and Y_w and Y_L are the width and length of the smaller rectangular element.

As it could be seen, the larger rectangular parasitic element has greater influence on the frequency compared to the smaller element. The parametric sweep for the

former's width, G_w , while keeping G_L, Y_w, Y_L at 40 mm, 10 mm and 10.4 mm respectively could be seen in Figure 6.6.

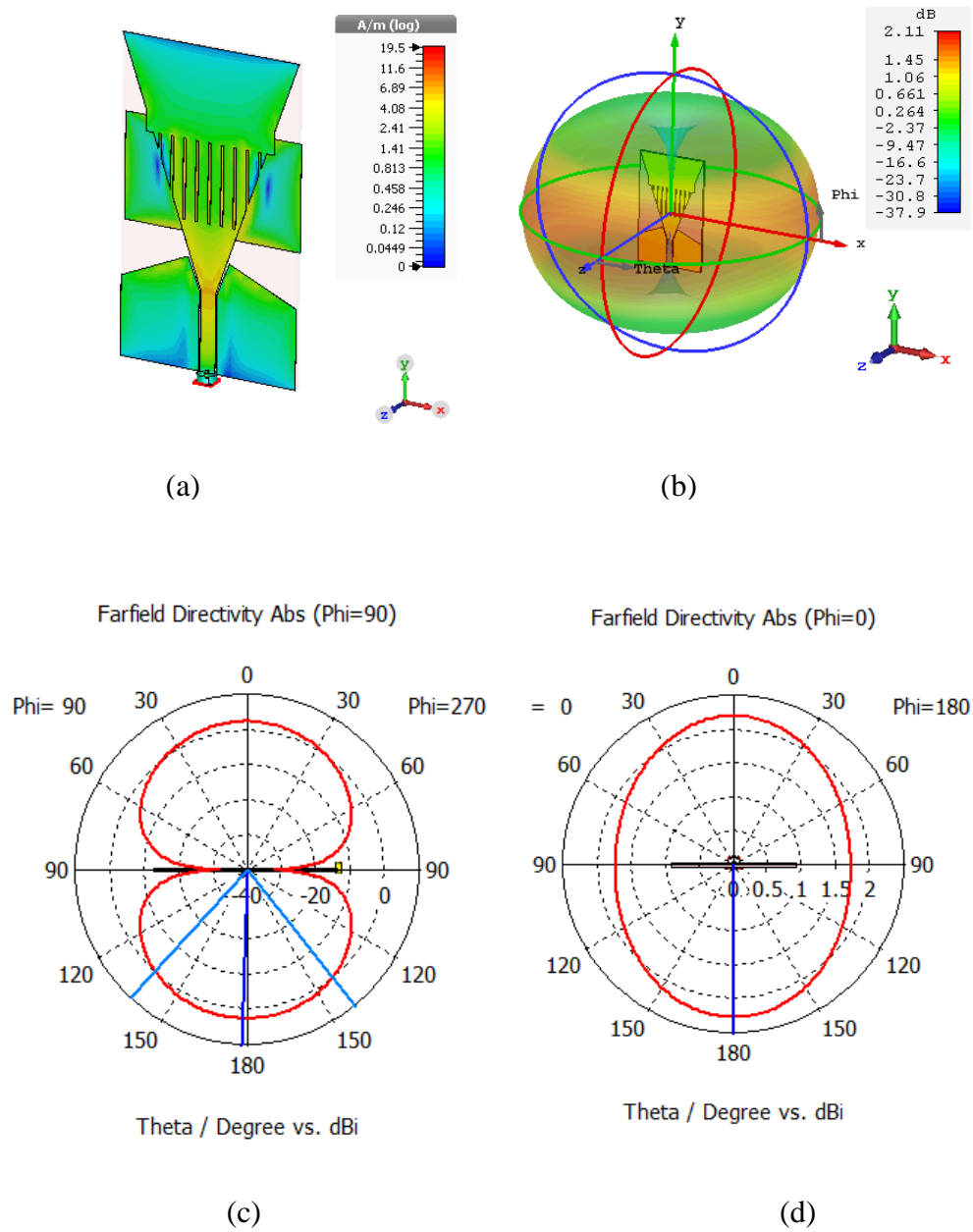


Figure 6.5: Optimal 35 mm antenna (a) Surface current (b) 3D far field radiation pattern (c) E-plane radiation pattern (d) H-plane radiation pattern.

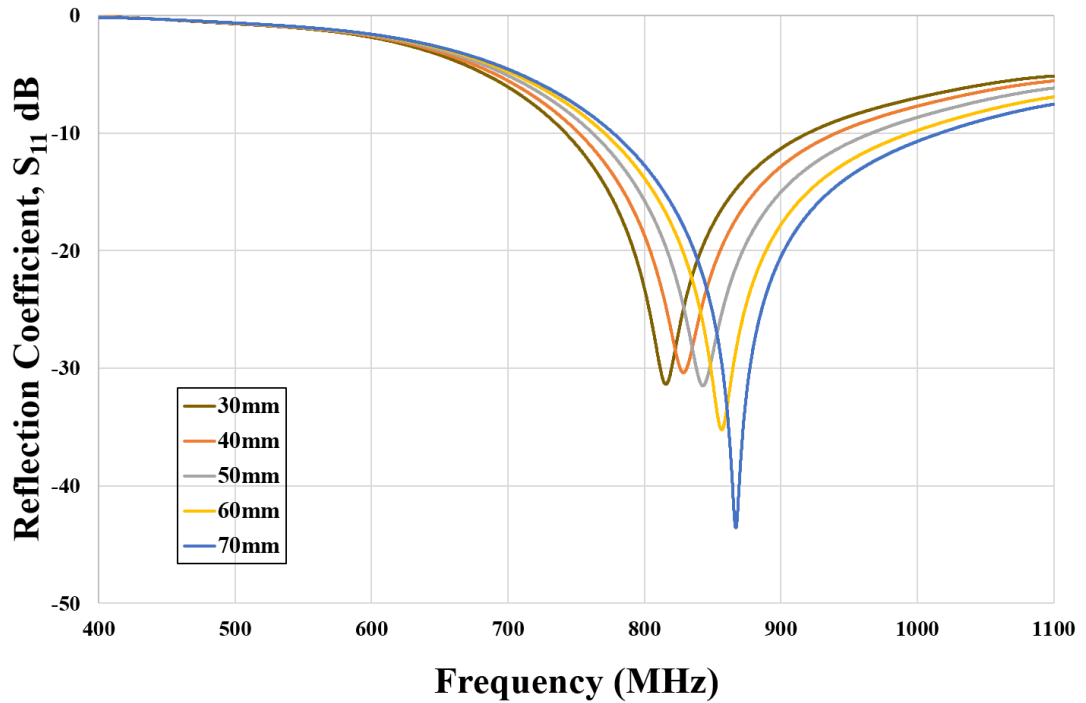


Figure 6.6: Parametric sweep of the width of the larger rectangular parasitic element on the back of the substrate

6.2.3 Fabrication of Braid Antenna and Measurements

The Braid antenna with 35 mm connector was chosen due to its superior performance and was fabricated. The antenna was fabricated by Eurocircuits based on the parameters given in Table 6.2. The front and back of the fabricated Braid antenna could be seen in Figure 6.7 (a) and Figure 6.7 (b) respectively.

Table 6.2: Braid antenna fabrication details.

Product Details	Parameters
Panel Length	120.5
Panel Width	70.5
Board Thickness	2.4
Base Material	FR-4 Improved
Soldermask	None
Layers	2
Copper Thickness	35 micrometres

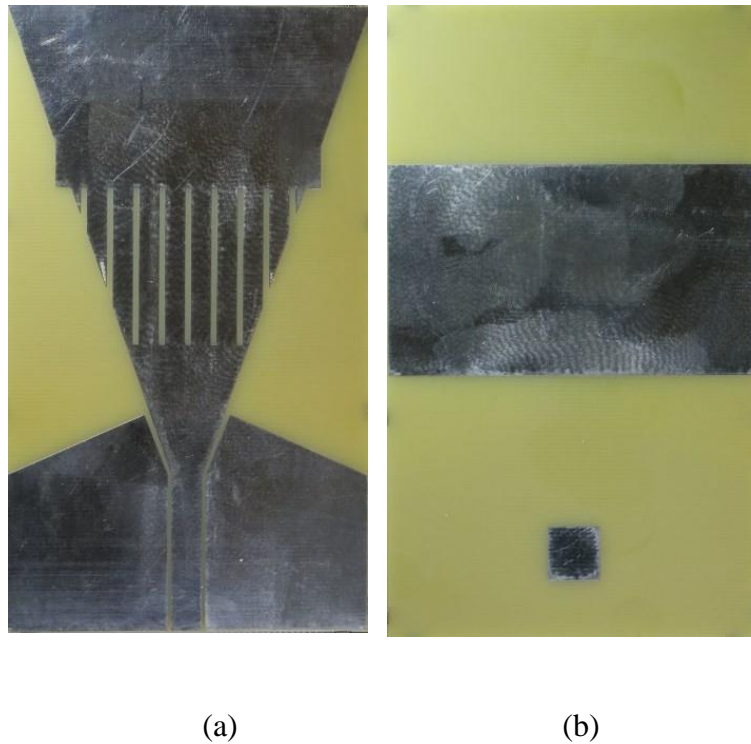


Figure 6.7: Picture of Fabricated Braided Antenna (a) Front (b) Back.

To determine and benchmark the performance of the fabricated Braid antennas, three LoRa antennas were used; an Eightwood antenna, OC-LG antenna from Linx Technologies and The Things Network (TTN) LoRa gateway antenna, shown in Figure 6.8 (a), Figure 6.8 (b) and Figure 6.8 (c) respectively.

The antennas' reflection coefficients (S11) were measured using a PC that was connected to a HP 8753 vector network analyser (VNA) via a general purpose interface

bus (GPIB). The VNA has a dynamic range of 100 dB with frequency range of 300 kHz to 3 GHz. A 3.5 mm calibration sets were used to prepare the 50 ohm ports of the VNA for the measurements. The frequency was swept from 668 MHz to 1068 MHz with the centre frequency at 868 MHz, corresponding to the Europe’s ISM band. The source power was selected at -10 dBm.



Figure 6.8: Off-the-Shelf Benchmark Antennas (a) Eightwood antenna (b) OC-LG antenna (c) Things Network gateway antenna.

The results for the benchmarking measurements could be seen in Figure 6.9. The -10 dB bandwidth for the OC-LG antennas were resonant at 740 MHz which spanned from 723 MHz to 754 MHz resulting in a bandwidth of 31 MHz. Eightwood A Antenna had a bandwidth span of 81 MHz starting from 871 MHz to 952 MHz. Eightwood B had a bandwidth that began at 871 MHz and ended at 964 MHz spanning a bandwidth of 93 MHz.

The fabricated Braid A antenna had a bandwidth of 176 MHz, that started from 842 MHz and ended at 1018 MHz. It had a centre frequency of 930 MHz. The Braid B antenna had similar performance with the Braid A antenna. It had a -10 dB bandwidth of 168 MHz that started from 842 MHz and ended at 1010 MHz.

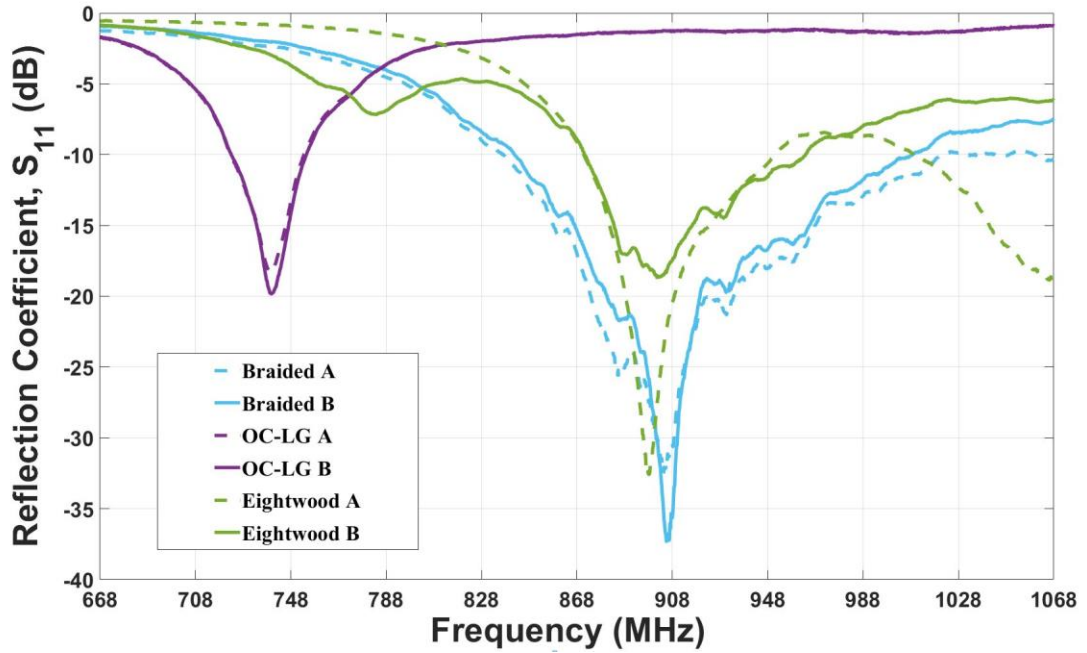


Figure 6.9: S11 of Braided & benchmarking antennas.

6.2.4 Oil Impregnated Buffer Design

In this section, the novel antenna design for the water surface is presented. It begins with the buffer-less design and proceeded to the buffer design.

A. Buffer-less Design

The BSN enclosure was constructed in CST and the antenna was embedded inside it. A picture of this could be seen in Figure 6.10.

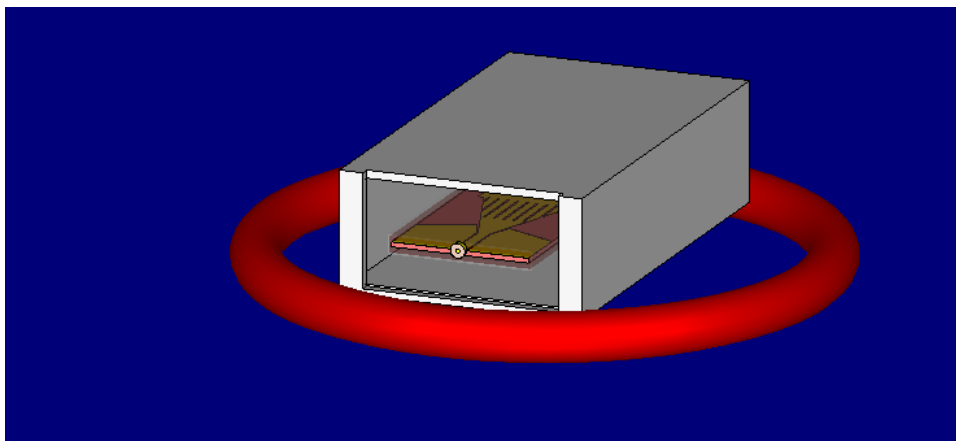


Figure 6.10: Braid antenna enclosed in PLA container on a plastic foam buoy floating on water surface.

The enclosure was then placed on a torus with the characteristics of a polyethylene plastic foam, representing the buoy. A water environment was modelled, and the BSN as well as the enclosure was placed on the water phantom. A simulation of these models resulted in a degradation of the reflection coefficient performance of the braid antenna.

B. Buffer Design

To ameliorate the degradation of the S11 performance, a hollow barrier was constructed around the antenna using PLA with a thickness of 1 mm. The width and length of the barrier were 74 mm and 122 mm respectively. The barrier, which could be seen in Figure 6.11 was then filled with oil impregnated paper, so that the antenna was placed in the middle of these treated papers. A parametric sweep with respect to the barrier thickness was performed to determine the optimal thickness for the best S11. Four Buffer thickness were used in the parametric sweep: 10 mm, 20 mm, 35 mm and 45 mm.

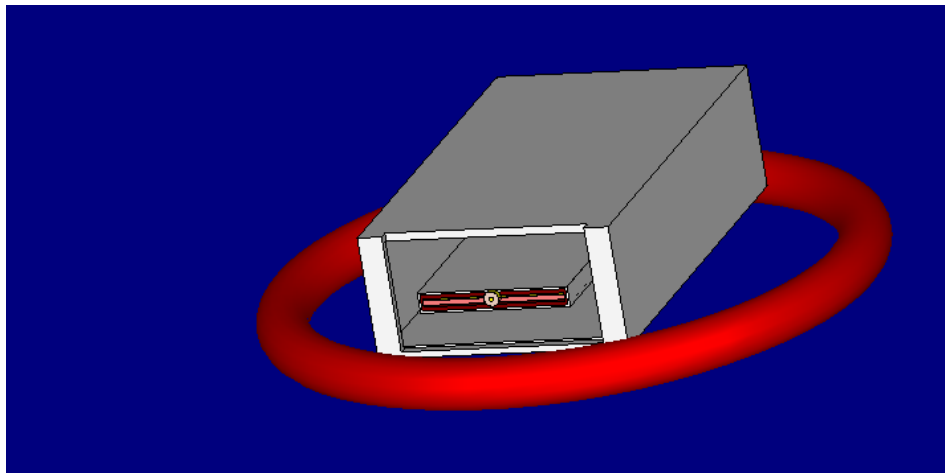


Figure 6.11: Braid antenna enclosed in an oil-impregnated barrier.

Figure 6.12 shows the reflection coefficient of the antenna enclosed in the PLA container, placed on the buoy which was in turn deployed in water. The figure also shows the results obtained by introducing a barrier with oil impregnated paper around the antenna and varying the buffer thickness from 10 mm to 45 mm. The antenna without the buffer does not have a -10 dB bandwidth as it could be observed. The optimal bandwidth was attained with the 10 mm thick buffer.

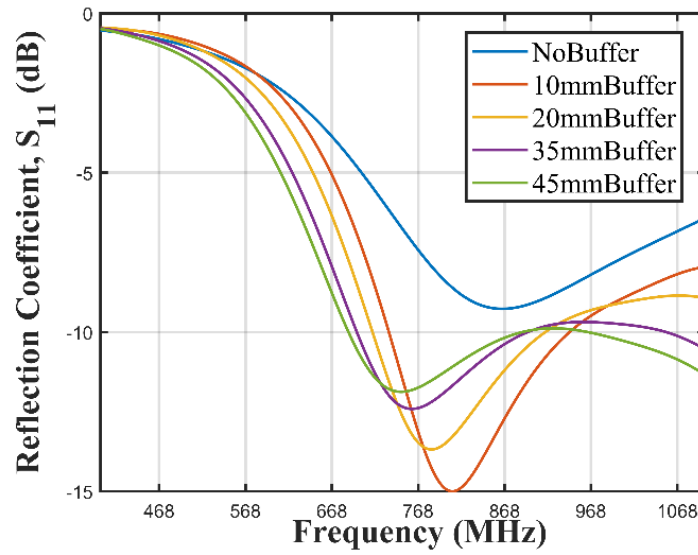


Figure 6.12: Braid antenna inserted in an oil-impregnated paper buffer.

The buffer at 10 mm thickness was 3D printed using PLA. Thirty papers were cut into a width of 36 mm and length of 120 mm so that they could fit into the fabricated barrier. These papers were then treated with oil as it could be seen in Figure 6.13.



Figure 6.13: Oil-treated papers, barrier and braid antenna.

The antenna was placed inside the barrier and the oil treated papers were used to sandwich the antenna. The antenna was then connected to the RFM95 LoRa transceiver in the BSN enclosure as it could be seen in Figure 6.14.

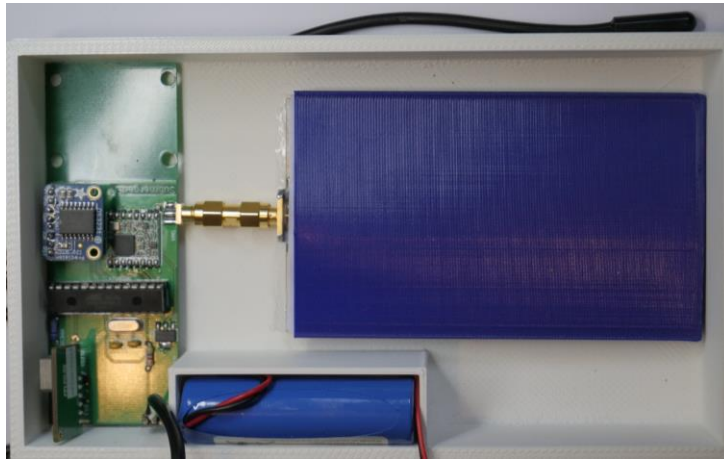


Figure 6.14: Antenna barrier inside enclosure with PCB of BSN.

6.3 VNA Experiments

The antenna with the oil-impregnated paper buffer and the one without the barrier were examined. The experimental set up for this could be seen in Figure 6.15. It consisted of a VNA with an SMA-to-SMA coaxial cable connecting the antenna to the VNA through port 1 of the VNA. The results were captured using a software on the PC.



Figure 6.15: Experimental setup for antenna measurements.

The results for the buffered and barrier-less antenna could be seen in Figure 6.16. This could be seen to conform to the results obtained from the simulation. The barrier-less antenna had no effective -10 dB bandwidth over the 400 MHz span of frequency around the 868 MHz LoRa centre frequency. The antenna with the buffer had better performance with a -10 dB bandwidth spanning the bandwidth of interest.

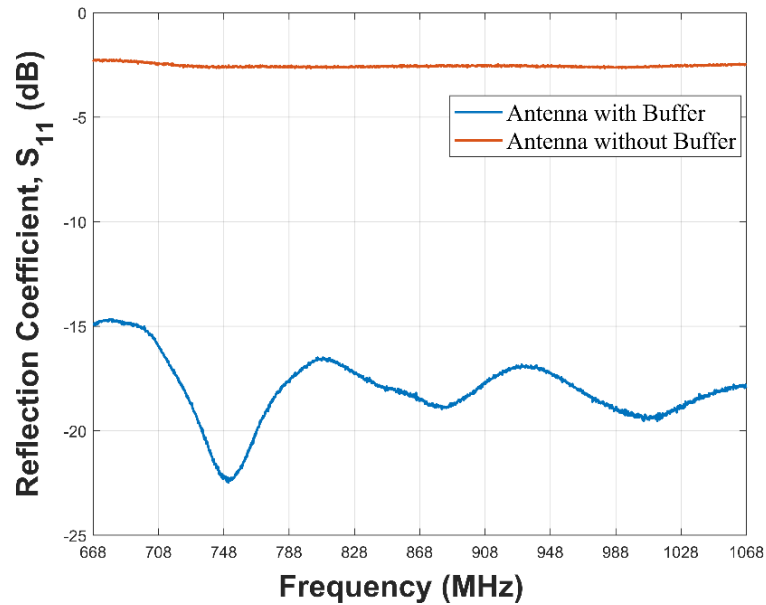


Figure 6.16: Measured reflection coefficients of antenna without buffer and antenna with buffer submerged in seawater.

6.4 Field Tests

To validate the operation of the developed braid antenna, a field test was performed using RFM95 LoRa transceivers to determine the received signal strength indicator (RSSI) on land and on the water surface. The Eightwood antennas were selected because they exhibited better -10 dB bandwidth performance compared to the OC-LG antennas as it could be seen in Figure 6.9.

6.4.1 Received Signal Strength Indicator (RSSI) Tests

The braid antenna and Eightwood antenna were used for the received signal strength indicator tests. RFM95 LoRa module was used as the transceiver for transmitting and receiving the signal. An Atmega328 was used as the microcontroller responsible

for processing the captured signal. The setup for the field tests with the transmitter and receiver could be seen in Figure 6.17.

The antennas were mounted on a tripod using a support platform that was 3D printed. The transmitting LoRa node was equipped with a temperature sensor. The receiving antenna had an organic LED-emitting diode (OLED) display that printed out the received temperature as well as the RSSI of the received signal. Both the transmitter and receiver were ensured to have a clear Line of Sight (LoS) to minimise both destructive and constructive interference that may result from obstacles. The transmitter was fixed at a spot while the receiver was moved at a space of 20 meters.



Figure 6.17: Setup for the received signal strength indicator (RSSI) tests for receive and transmit antennas.

The RSSI results obtained for both the Braid and Eightwood antennas could be seen in Figure 6.18 over 300 meters. The braid antenna could be seen to have better RSSI values over all the measured distance.

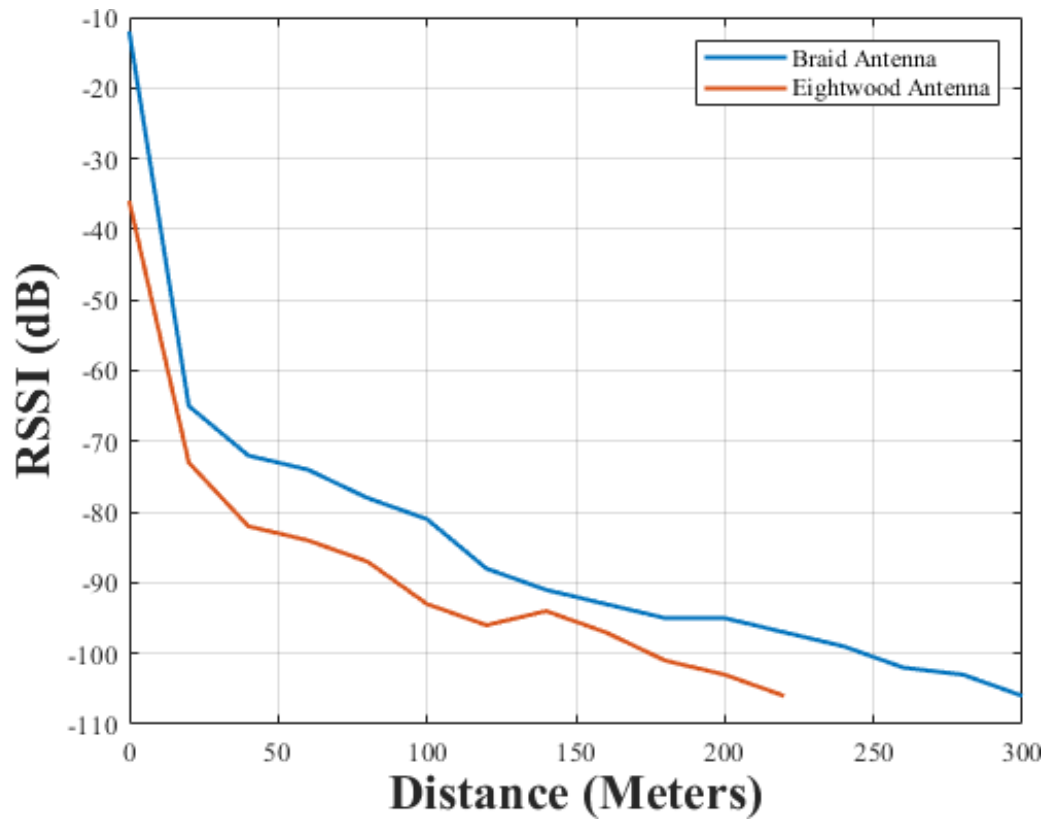


Figure 6.18: RSSI for antennas with respect to distance.

6.4.2 Water Surface Antenna RSSI Tests

The system integrated solar powered BSN and IoT gateway could be seen in Figure 6.18. The first image, shown in Figure 6.19 (a) had the oil treated paper barrier while the other one in Figure 6.19 (b) did not have a buffer around the antenna.

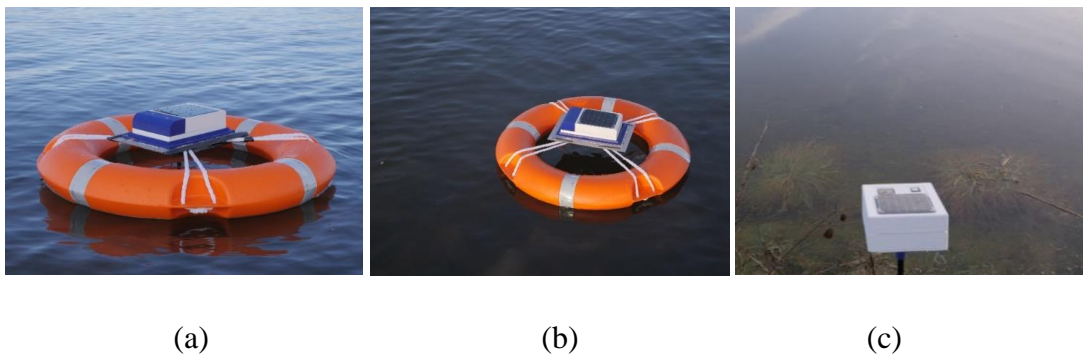


Figure 6.19: BSN deployed in the North Sea (a) with buffer (b) without buffer (c) Data relay node for RSSI tests.

This was to enable the RSSI test to determine and compare the performances of the two different system setups. The temperature data obtained from the BSNs were transmitted to the IoT LoRa gateway shown in Figure 6.19 (c). All the three systems were waterproofed to protect them against water from the waves and rain.

The RSSI results for the BSN with the buffer and the other without a buffer could be seen in Figure 6.20. The RSSI of the water surface communication for the BSN without the buffer could be seen to be worse than the one with the buffer. At 80 meters, no signal was received from the BSN without the buffer. The one with the barrier had an extended reception up to 160 meters.

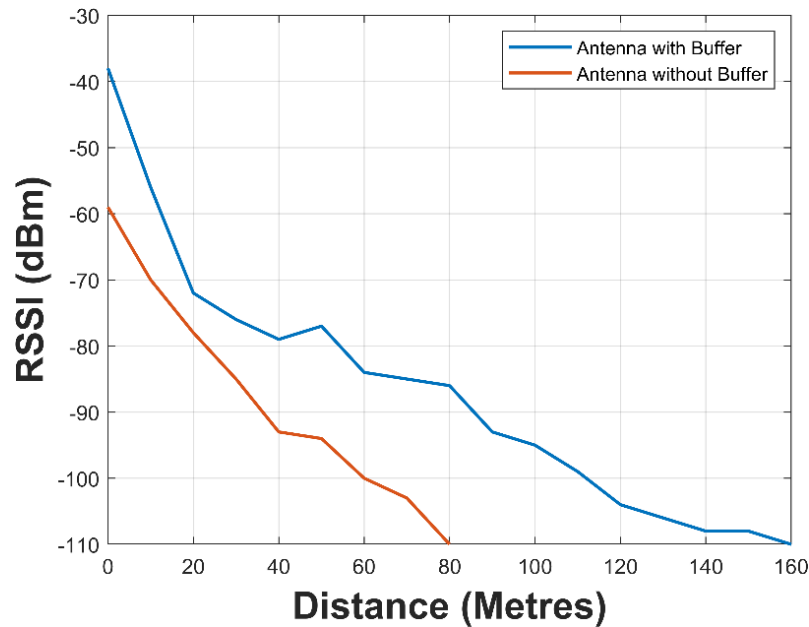


Figure 6.20: RSSI Tests for buffered and buffer-less braid antennas on surface water.

The tests for the RSSI of both the BSN with the buffered antenna and the one without the barrier were undertaken at Edinburgh. Subsequently, the buffered sensor node was waterproofed and submerged inside a pond. The readings for the RSSIs at different distances were obtained until the submerged BSN was out of range.

The outcome of this experiment could be seen in Figure 6.21. The maximum distance attained was six (6) meters with an RSSI of -110 dBm. The range of operation

of this wireless sensor could be increased by placing sensor nodes at this distance to relay the sensor data in a multi-hop fashion underwater.

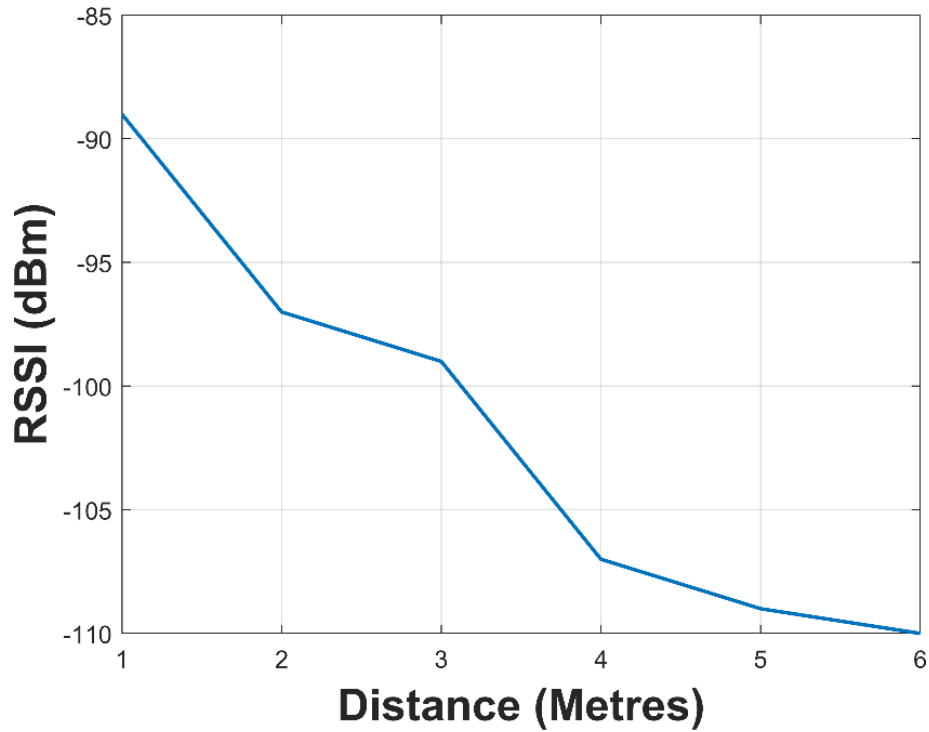


Figure 6.21: RSSI of submerged SN with buffered braid antenna.

A comparison of the braid antenna buffered by the oil impregnated paper buffer compared with some state-of-the-art antennas could be seen in Table 6.3. The braid antenna operates in the ISM LoRa band for the United Kingdom which makes it ideal for this application. Its long range achieved on water surface communication and considerable communication distance when submerged makes it attractive for use in the telemetry system for the microwave oil spill sensors

Table 6.3: Comparison of antennas for sea surface communication

Antenna	Centre Frequency (MHz)	Buffer	Bandwidth in Free space	Bandwidth for Submerged	Range on Water Surface (m)	Range when Submerged (m)
Braid Antenna	906	Oil Impregnated Paper	176 MHz	400 MHz	160	6
OC-LG	740	N/A	31 MHz	N/A	N/A	N/A
Eightwood	900	N/A	93 MHz	N/A	N/A	N/A
Ref [108]	443	N/A	N/A	Tap Water	N/A	7
Ref [85]	2400	Deionised Water	N/A	None	3.8	0.054

6.5 Summary

In this chapter, a design and implementation of a water surface radio frequency communication backbone for the telemetry system of the in-situ microwave oil spill sensor was undertaken. A novel design, fabrication, measurement, and implementation of an antenna with dual ability of underwater and water surface LoRa communication at 868 MHz was developed. The antenna was incorporated into a sensor node that was capable of transmitting sensor data using RF communication underwater and over water surface to a gateway node that publishes the data on the Internet.

Initially, the base antenna was designed and simulated. However, its centre frequency was 733 MHz and had a frequency span from 608 MHz to 802 MHz. This did not fall within Europe's ISM band of 868 MHz which the LoRa in United Kingdom operates at. By introducing braid slots to the patch antenna and a scalene triangle on the CPW, the performance of the antenna was improved. A connector length of 35 mm on the antenna patch yielded optimal performance with respect to the S11.

The antenna had an omnidirectional radiation pattern which allowed the BSN to communicate with any other sensor node or gateway in every direction at the expense of directionality which would have yielded higher gain. The novel Braid antenna was fabricated and the measured result showed it radiated in the 868 MHz frequency of interest compared to the other antennas that were used for the benchmarking.

The Braid antenna pair and the pair of the best performing antenna among the COTS antennas, the Eightwood antenna, underwent a received signal strength indicator test. The results obtained showed that the Braid antenna exhibited better RSSI performance to the Eightwood antennas with respect to distance.

The reflection coefficient of the Braid antenna deteriorated when it was enclosed in a PLA enclosure, fixed to a buoy, and placed on a seawater surface. The degradation worsened when the BSN was submerged in water. This was obviously because of mismatch resulting from introduction of the underwater environment. However, when the Braid antenna was sandwiched between two bunches of oil-impregnated papers, the performance improved immensely.

A received signal strength indicator tests were performed on both variants of the BSNs in the North Sea. The BSN with buffered antenna sustained a communication link of over 160 meters from the gateway node while the barrier-less antenna was only capable of a communication range of 80 meters. The BSN with the buffered antenna was able to attain a communication range of 6 meters with an RSSI of -110 dBm when submerged in water.

The next chapter culminates in the design and development of an in situ microwave sensor for the detection as well as the determination of oil slick thickness.

Chapter 7

In Situ Microwave Oil Spill Detection and Oil Slick Thickness Measurement Sensor

In this chapter, in situ microwave sensor for the detection of oil spill and oil slick thickness measurement was developed. It was made from the antenna-sensors developed in chapter 4. The measurement of oil slick thickness, although at an early stage, has immense applications in determining the extent and quantity of crude oil accidentally discharged in oceans.

To use the antenna-sensor array, a novel four-layer RF switching PCB was developed for the microwave sensor. The bespoke RF switching circuit comprised of two single pole double throw (SPDT) switches. Each of the Gallium Arsenide (GaAs) pHEMT HMC849ALP4CE SPDT switches had their two output RF ports connected to two antenna-sensors and their input RF port connected to a port of the VNA.

An android application was developed on a smartphone to select each of the antenna-sensors for the oil slick thickness measurements. Simulation results formed the basis for the dimensions and orientation of the sensors in a 3D printed enclosure for the final experiment.

Crude oil has lower density than salted seawater, therefore, it floats on the surface. This enabled the four antenna-sensor array to establish the oil thickness using radio frequency. The simulated and measured transmission coefficients showed the capability of the antenna-sensors and switching circuit to determine the oil slick thickness using in situ microwave approach.

7.1 System Architecture

The PDMS-encapsulated antenna-sensors were arranged in an array for oil spill detection and oil slick thickness determination. The near-field sensing region of the oil

slick thickness measurement, whether in a container or in the sea, has cuboid geometry with the oil slick floating at the surface and the seawater at the bottom. Thus, the choice for the cuboid orientation of the antenna-sensors. Four antenna-sensors are sufficient for the measurement of the oil slick thickness. However, increasing the number of antenna-sensors to eight or more, although would increase the complexity and cost of the system, it may improve the sensitivity of the oil slick thickness sensor.

To operate the four antenna-sensors using the two ports on the 8753 VNA, an RF switching circuit based upon commercial off-the-shelf (COTS) components was developed. The schematic for the complete initial setup could be seen in Figure 7.1 which comprised of the RF switches, microcontroller, Bluetooth, 8753 VNA, Smartphone and a PC.

The two RF switches used were two single pole double throw (SPDT) non-reflective Gallium Arsenide (GaAs), pseudomorphic high electron mobility transistor (pHEMT), HMC849ALP4CE with ultra-wideband operating frequency of DC to 6 GHz [112]. A single pole three throw (SP3T) non-reflective GaAs, monolithic microwave integrated circuit (MMIC) having a wideband bandwidth that spanned from DC to 3.5 GHz [113] was also used for the initial design.

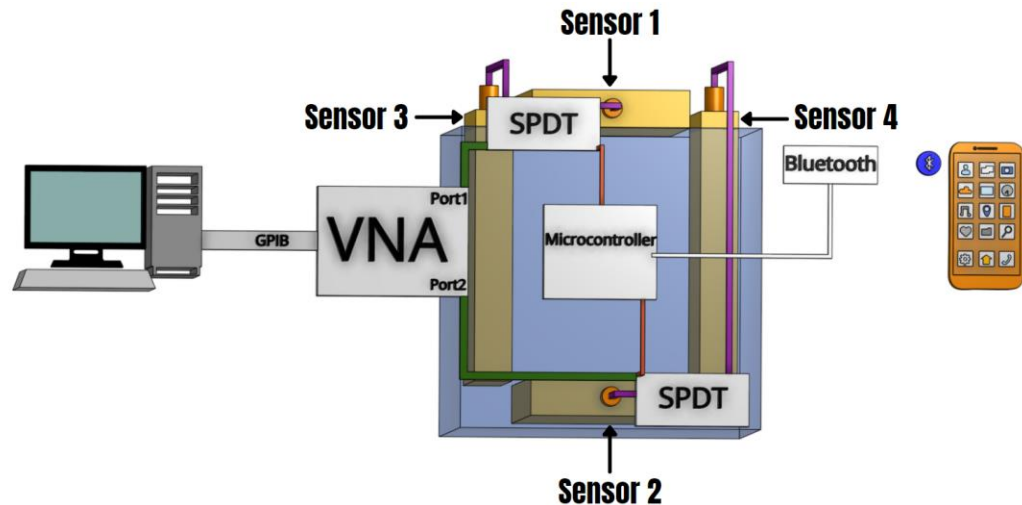


Figure 7.1: System architecture diagram for the RF switched oil slick thickness sensor.

The start frequency of interest is DC to an end frequency of 3 GHz, which falls within the operating frequencies of both switches.

To control these RF Switch evaluation boards, a controller unit comprising primarily of Atmega328P microcontroller [114] was used. This device was low powered and operates with a bias voltage of +5V which is the same with the bias voltage used by both RF switches. Each RF switch has only two control lines to select a particular RF path, making them simple to operate by the microcontroller. A two layered PCB was developed for the microcontroller to control the RF switches with LEDs as indicators for each port selected. Subsequently, the RF switch evaluation boards were replaced by their surface mount devices (SMD) equivalent on a four-layered PCB board that contained all the electronic components for the oil sensor.

To provide wireless connection between the microcontroller and a smartphone to operate the RF switches, a HC-06 Bluetooth module was used for the project. Although there is a preponderance of several wireless technology available, the Bluetooth has one of the lowest power consumption and ease of application. An android application was developed and installed to operate the switches on the smartphone.

The RF switches' inputs were connected to each of the ports on the VNA. The VNA was connected to the PC using a general purpose interface bus (GPIB). The VNA had an operating frequency of DC to 3 GHz. The operation provided by the android application enabled both the transmission and reflection coefficients to be obtained in a mono-static and multi-static switching configurations on the VNA.

7.1.1 Antenna Sensor System

The antenna-sensor was the PDMS-encapsulated trefoil antenna developed in chapter 4. To increase the gain and make the antenna unidirectional, a copper foil was introduced on the bottom layer of the PDMS, as it was done in [115],[116],[117] and [118]. This was developed in CST and optimised. Images of the top and bottom layers of the PDMS-encapsulated antenna-sensor could be seen in Figure 7.2 (a) and Figure 7.2 (b) respectively.

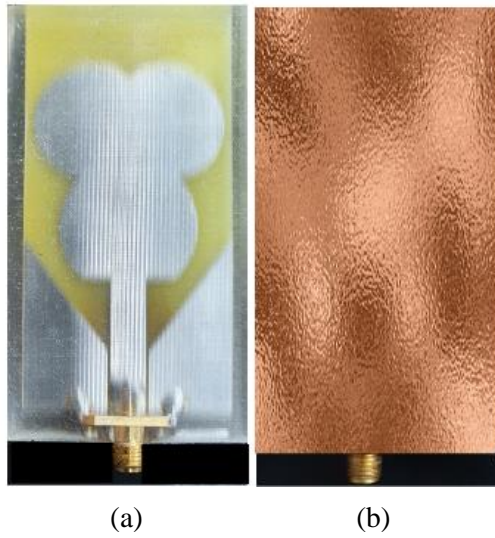


Figure 7.2: Sensor (a) Top layer (b) Bottom layer.

From Figure 7.3, the antenna-sensor without the copper reflector, at the frequencies of interest, could be seen to have a bidirectional radiation pattern on the E-plane and omnidirectional pattern on the H-plane. The lowest and highest directivities were attained at 1.5 GHz and 3 GHz corresponding to 2.13 dBi and 3.59 dBi respectively. The directivity, and gain increased with frequencies.

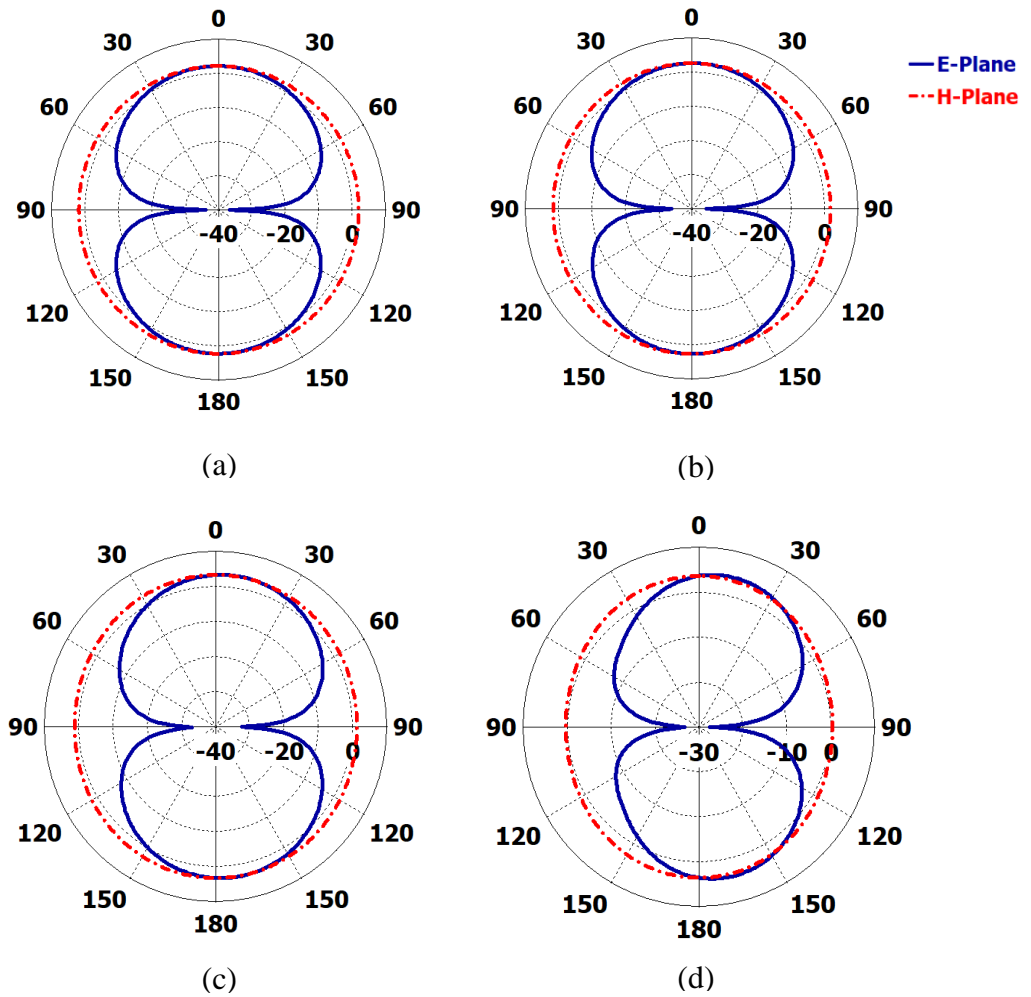


Figure 7.3: Simulated E-(XZ) and H-(XY) plane far-field radiation patterns of sensor without reflector at (a) 1.5 GHz with directivity of 2.13 dBi (b) 2 GHz with directivity of 2.57 dBi (c) 2.5 GHz with directivity of 3.22 dBi (d) 3 GHz with directivity of 3.59.

The introduction of the reflector on the bottom of the PDMS layer could be seen to transform the antenna into a unidirectional radiation pattern in both the E-plane and H-plane. This had drastic effects on the directivity increasing it from 2.13 dBi to 6.15 dBi at 1.5 GHz and from 3.59 dBi to 7.4 dBi at 3 GHz. The simulated far-field radiation patterns could be seen in Figure 7.4.

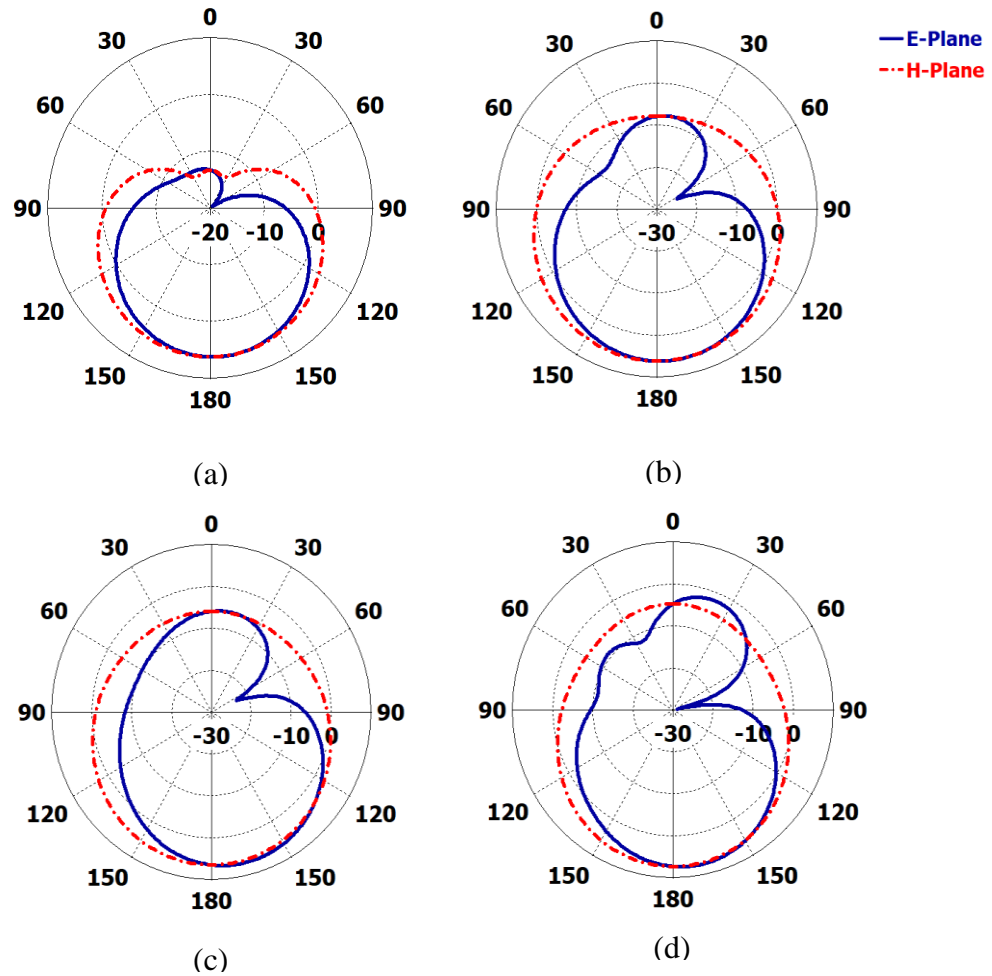


Figure 7.4: Simulated E-(XZ) and H-(XY) plane far-field radiation patterns of sensor with reflector at (a) 1.5 GHz with directivity of 6.15 dBi (b) 2 GHz with directivity of 6.09 dBi (c) 2.5 GHz with directivity of 6.82 dBi (d) 3 GHz with directivity of 7.4 dBi.

7.1.2 RF Switching Controller Unit

The control of the RF switches and LED indicators was handled by a CMOS 8-bit Atmega328P microcontroller [119]. It is low powered and based on the advanced AVR reduced instruction set computer (RISC) architecture. The wireless connection between the microcontroller and the android app was provided by the HC-06 Bluetooth module based on the CSR BC04 Bluetooth technology. The wireless transceiver has external 8M bit flash with 2.4 GHz antenna [120].

The experimental setup is made up of four antenna-sensors. However, the HP5783 Vector Network Analyser (VNA) has only two ports: Port 1 and Port 2. To operate all

the antenna-sensors, RF Switches are required. Each of the two antenna-sensors pair shall be connected to each of the RF switches. This is also very useful when the number of antennas in the array is increased. A HMC849ALP4CE single pole double throw (SPDT) switch was used on one of the ports. It is a high isolation non-reflective GaAs, pHEMT SPDT with operating frequency of DC to 6 GHz [112]. A HMC245AQS16E single pole three throw (SP3T) switch has three output ports (RF1, RF2 and RF3) was connected to the other port of the VNA. For this project, only the two output ports of the SP3T (RF1 and RF2) were used to connect the two antenna-sensors [113]. The last one (RF3) could be used to provide reference for a portable VNA. Both switches were convenient for this work's frequency of operation of DC to 3 GHz.

7.1.3 Solar Power System

The in situ microwave oil spill sensor would operate remotely on the water surface, thus there is a need to have sustainable energy source to power it. For this purpose, a solar panel [121], lithium-ion battery [122] and its charger [123] and non-isolated DC/DC converter step-up power supply [124] were used.

7.1.4 Android Application

To control and select the relevant antenna-sensors and switches, an android app was developed using MIT App Inventor as it could be seen Figure 7.5. The microcontroller was programmed to enable the HC-06 module to determine the reflection and transmission coefficients. The app was capable of both mono-static and multi-static switching configurations.



Figure 7.5: Android App for controlling and selecting RF switches.

7.2 VNA Characterisation of RF Switches

To ascertain a baseline and provide a validation of the performances of the RF switches on the development boards, the insertion and return losses for the RF ports on each of the evaluation boards were undertaken. The schematic of the setup for the characterisation of the RF switches could be seen in Figure 7.6.

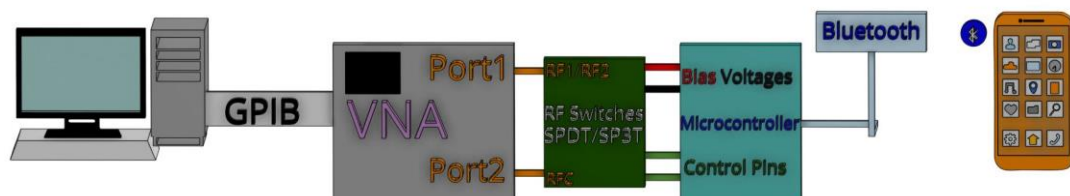


Figure 7.6: Representation of the RF switches' VNA evaluation setup.

A full two-port calibration was performed on the HP8753 VNA using the load, short, open and thru studs. The frequency of operation was set from 0.3 MHz to 3000 MHz with 1601 points. The RF input pin, RFC, was connected to the port 2 of the VNA and the RF output port of interest, which could be RF1, RF2 or RF3, was connected to the port 1 of the VNA. The VNA was connected to the PC using GPIB. A software on the PC was used to capture the S Parameters of the switches. To select the appropriate

RF path, the microcontroller was programmed using the truth tables in section 7.1.4. The Bluetooth and android application enabled the wireless selections.

7.2.1 Single Pole Double Throw (SPDT) RF Switch

The insertion loss and return loss from DC up to 3 GHz, obtained for the SPDT HMC849ALP4CE valuation board, could be seen in Figure 7.7 and Figure 7.8 respectively. The insertion loss had a maximum value of around -0.89 dB and a minimum value of -1.48 dB for both RF1 and RF2 ports. The return loss for the same board shows excellent performance too with values of up to -29 dB. All these results conform with those exhibited in the datasheet of the evaluation board in [112].

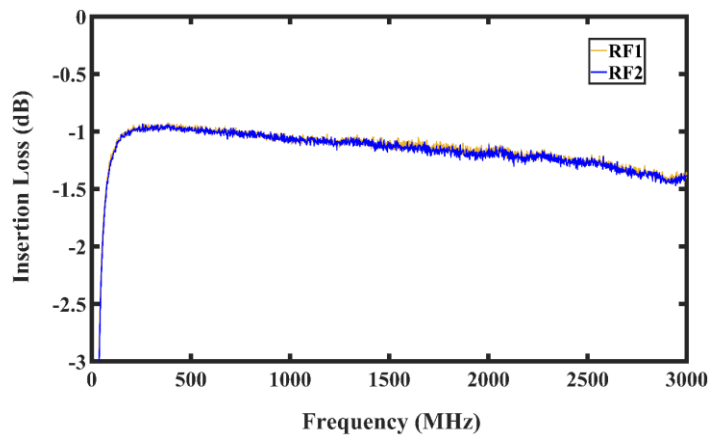


Figure 7.7: Insertion losses of the SPDT.

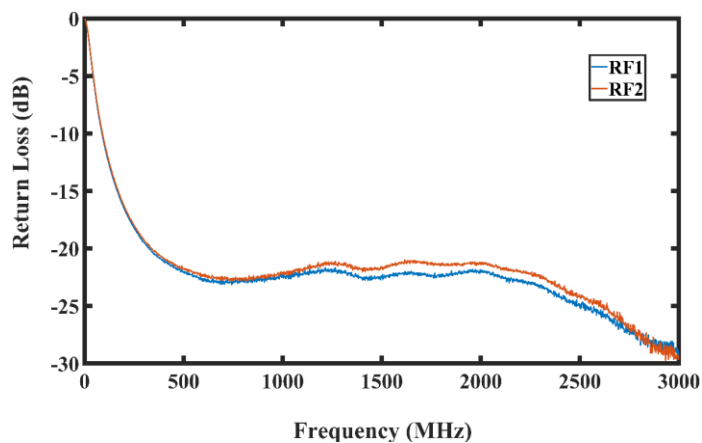


Figure 7.8: Return losses of the SPDT.

7.2.2 Single Pole Three Throw (SP3T) RF Switch

The insertion loss of the HMC245AQS16E SP3T evaluation board could be seen in Figure 7.9. Although its performance was less than the SPDT, it was however around -2 dB at its worst, which was just around -0.2 dB below the one obtained from the datasheet in [113]. The return loss had comparable performance to the SPDT switch as it could be seen in Figure 7.10.

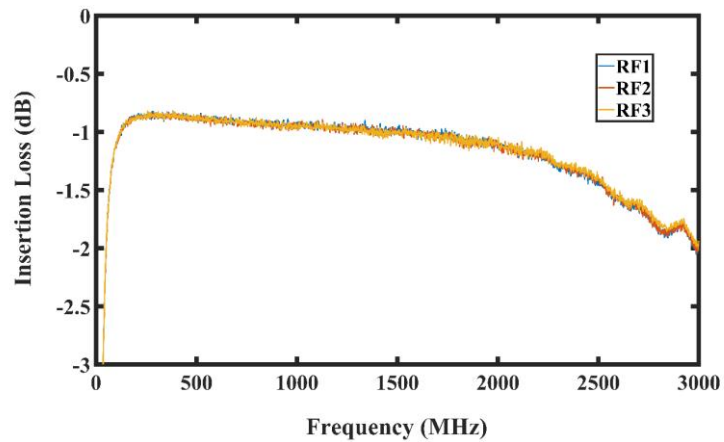


Figure 7.9: Insertion losses of the SP3T.

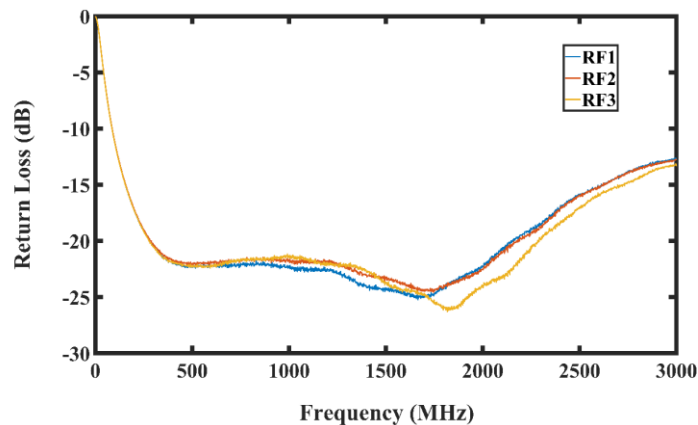


Figure 7.10: Return losses of the SP3T.

These outstanding performances of both RF switches by the VNA provided a baseline and validation to the efficiencies of the switches. This was to ensure that

unwanted degradation or noises are not cascade to the final RF antenna-sensors because of imperfections from the VNA or the RF switches themselves.

7.3 Novel RF Switching Circuit Development and Implementation

With the successful implementation of the RF switching using the COTS, the project proceeded with the replacement of the evaluation boards and other components, to design and develop a novel bespoke PCB for the final experiment. The reasons for this were to make the final microwave sensor more compact and reliable and to prepare the integration of the sensor with an ultra-wideband system on chip (SoC) transceiver system or software defined radio, capable of replacing the cumbersome VNA.

7.3.1 Circuit Diagram Design of Bespoke RF Switches

Using a schematic software, the circuit for the RF switch was designed as it could be seen in Figure 7.11. The circuit comprised of all the components used for the VNA characterisation of the switches with the notable inclusion of two HMC849ALP4CE SPDT RF switches. The SP3T switch was replaced with an SPDT for simplicity of the design and because the SPDT offers outstanding performances in the frequency range of interest. A 100pF 0402 SMD capacitor was connected to each of the RF paths to provide blocking function against the DC signals and the outputs of the capacitors were terminated by a 50 Ohm SMA connector.

The Vctl and the EN of the first RF switch, SPDTA, were connected to PB1 and PB2 of the microcontroller respectively. For the second SPDTB, the Vctl and EN were connected to the PB3 and PB4 of the Atmega328P.

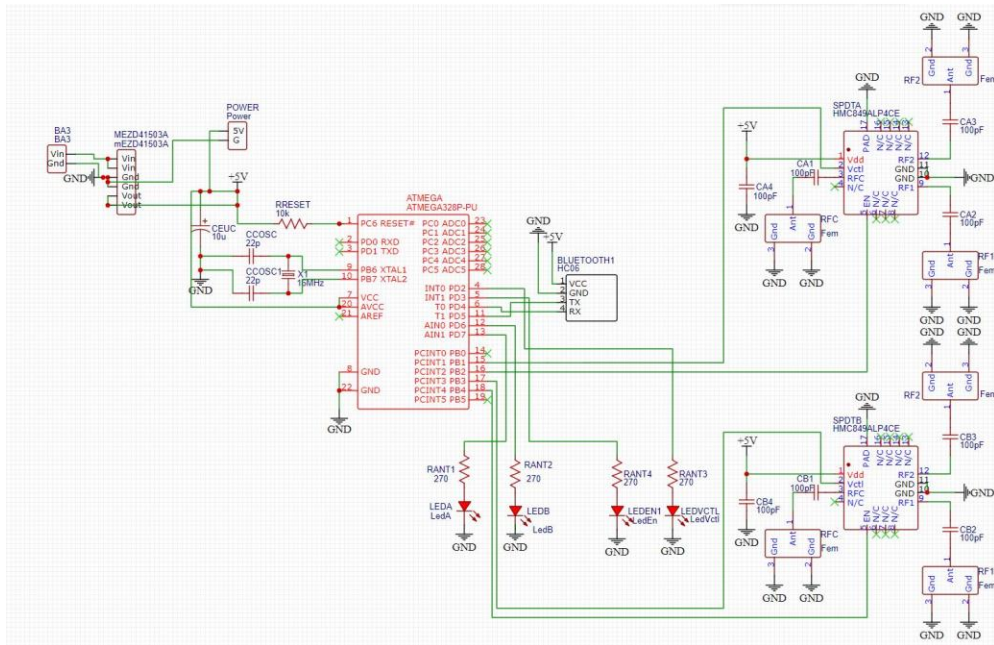


Figure 7.11: Circuit diagram of customised RF switching system.

7.3.2 Four Layered RF Switch PCB Bespoke Design and Implementation

A. Design Considerations of Four Layered PCB

Most countries have enacted regulations on the amount of RF emissions that are permissible from an electronic device. And because PCBs usually accommodates DC components, introducing RF devices could have devastating implications on the performances of the system. Thus, the need for optimal PCB design cannot be overemphasised. One of the efficient methods of a robust RF PCB design is the use of multilayers [125]. For a four-layered board, a typical configuration could be seen in Table 7.1 [126]. Each of the layers are made up of copper as it could be seen and the top and inner layer 2 were separated with a prerog, which is a dielectric insulant. The same insulant was used between the inner layer 3 and bottom layer.

Table 7.1: Four layered stack [126].

Layer	Material Type	Thickness	
Top Layer1	Copper	0.035 mm	
Prepreg	7628*1	0.2 mm	
Inner Layer2	Copper	0.0175 mm	1.1mm (with copper core)
Core	Core	1.065 mm	
Inner Layer3	Copper	0.0175 mm	
Prepreg	7628*1	0.2 mm	
Bottom Layer4	Copper	0.035 mm	

For this project, the four-layered PCB approach, seen in Figure 7.12, was adopted. The top layer was used for RF and DC signals, the second was used as the ground, the third layer was reserved for the +5V bias voltage and the fourth layer was dedicated for the RF and DC signals.



Figure 7.12: Four-layer PCB stack.

B. PCB Validation of RF Paths in CST

As recommended in [112], CST was used to validate the PCB design of the RF paths. The RF Solutions’ 50 Ω straight PCB mount, subminiature A connector (SMA) [127] was used on the four-layered board. The SMA is suitable for board thickness of 1.2 mm to 1.6 mm. The overall thickness of the four layered board was 1.57 mm which made it suitable. It had a maximum frequency capability of up to 18 GHz which was appropriate for the antenna-sensors and SPDT switches.

The impedance calculator in [126] was used to determine the thickness of the RF trace at 50 Ohms which was 300 micrometres. Using a trace width of 0.3 mm, the RF paths on the PCB board in CST was designed. The layers were stacked with respect to the design specifications. The SMA ground was connected to the ground layer via a cylindrical copper element.

For simplicity, only the input RF (RFC) to RF1 path was modelled in CST as it could be seen in Figure 7.13. This was because the RFC to RF2 path was similar to the RFC to RF1 path.

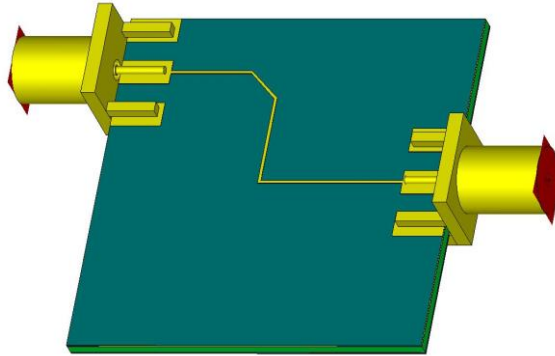


Figure 7.13: RF paths validation in CST.

The reflection coefficient obtained for the RFC to RF1 path in CST could be seen in Figure 7.14. It could be seen that the value of S_{11} was well below -10 dB for the 3 GHz bandwidth.

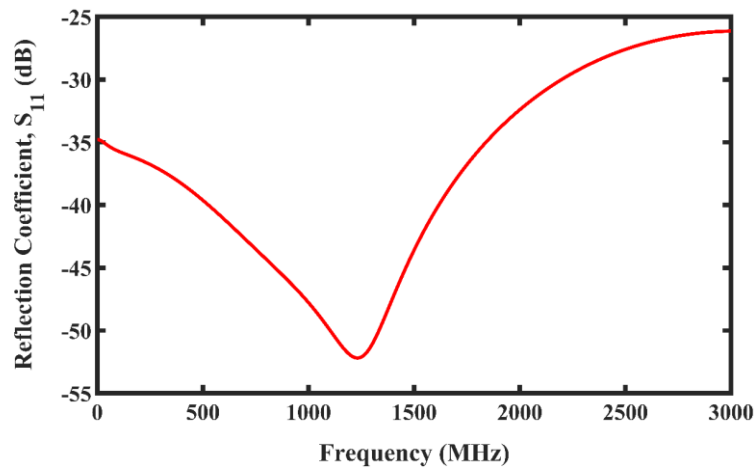


Figure 7.14: Simulated reflection coefficient of RFC to RF1 path.

The transmission coefficient obtained also exhibited outstanding performance below -1 dB for the frequency range of 0 MHz to 3000 MHz as it could be seen in Figure 7.15. Therefore, the trace width thickness and routing configurations were applied to the PCB design.

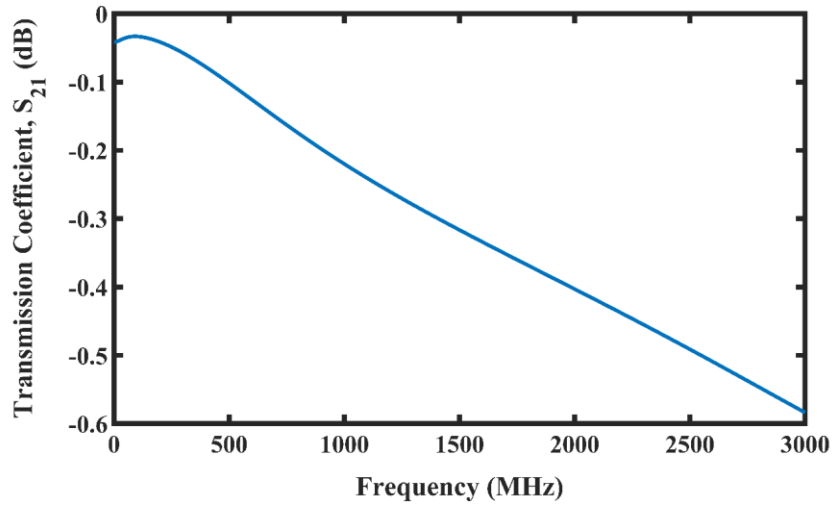


Figure 7.15: Simulated transmission coefficient of RFC to RF1 path.

C. PCB Implementation of RF Switches

The circuit diagram developed in section 7.3.1 was transformed into the four layered PCB shown in Figure 7.16.

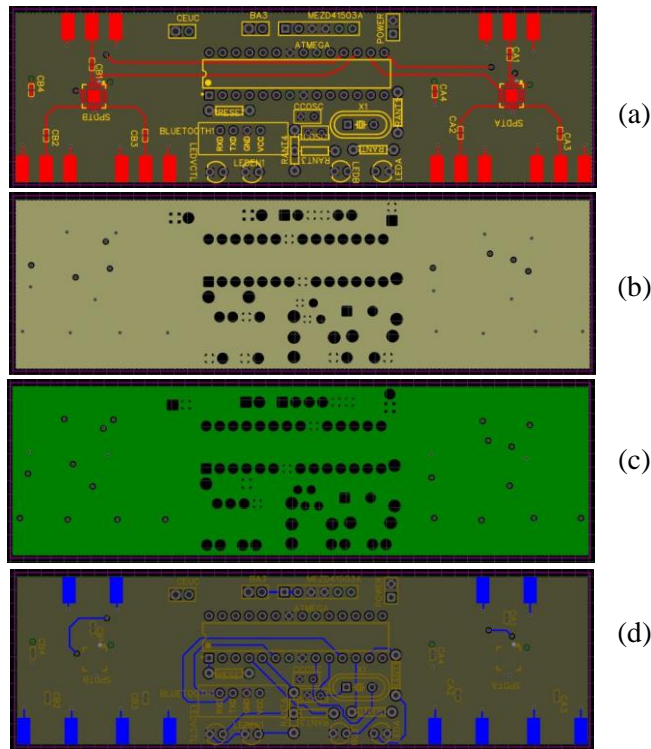


Figure 7.16: Four layered PCB design (a) Top layer (b) Ground layer (c) Power layer (d) Bottom layer.

The optimised CST RF paths were transferred to the four-layer PCB. The Atmega328P microcontroller could be at the middle of the board with its accompanying components such as the crystals oscillator, capacitors and the Bluetooth module. The two SPDT RF switches occupied the two ends of the top layer PCB as shown in Figure 7.16 (a). These was done to further minimise the electromagnetic interference on the RF path from the DC components. With the calculated 0.3 millimetres for the RF trace width, the RF paths were designed on the top layer. The trace width for the traces for the other parts of the circuit including the Atmega328P was 254 micrometres.

A copper pour was applied to the ground layer and the power layer with respect to 0 V and +5V as shown in Figure 7.16 (b) and Figure 7.16 (c) respectively. The fourth layer, Figure 7.16 (d), was used as an RF and signal layer for the microcontroller and other DC components.

The four-layered bespoke PCBs were fabricated using Eurocircuits, for the controller circuit that comprised of the Atmega328P microcontroller, two SPDT switches ICs and HC-06 Bluetooth as it could be seen in Figure 7.17, in preparation for the oil slick thickness measurement experiment.



Figure 7.17: PCB controller for oil slick thickness measurement.

7.4 Four Antenna Sensor Array Simulations

Oil has lower density compared to seawater. Thus, when oil spill occurs, the oil floats on the seawater surface in a macroscopic phase. Using Young's equation, the surface tension of the oil-water interfaces (γ_{ow}) could be ascertained as shown in (7.1) [128].

$$\gamma_{ow} = \frac{\gamma_{oa} \cos \theta_o - \gamma_{wa} \cos \theta_w}{\cos \theta_{ow}} \quad (7.1)$$

where θ_{ow} , θ_o , θ_w are the contact angles of oil droplet in water, oil-air and water-air interfaces respectively. γ_{oa} and γ_{wa} are the surface tensions of the oil–air and water–air interfaces respectively.

As oil is added to water, the oil layer increases correspondingly. Thus, antenna-sensor 1 and antenna-sensor 2 were placed at 80 mm apart to monitor the oil thickness vertically as it could be seen in Figure 7.26. Antenna-sensor 3 and antenna-sensor 4 were placed 74 mm apart to monitor the change horizontally. The simulation was performed from 0.3 MHz to 3000 MHz with 1601 points.

Both the horizontal and vertical distances between the four antenna-sensors lie within the Fresnel region given by (7.2) [129].

$$R_{NF} \leq \frac{2D^2}{\lambda} \quad (7.2)$$

where R_{NF} is the radiating near field, D is the maximum antenna length and λ is the wavelength.

The complex relative permittivity of liquids is dependent on frequency and can be represented by (7.3).

$$\epsilon(\omega) = \epsilon'(\omega) - j\epsilon''(\omega) \quad (7.3)$$

where the real part, ϵ' , is the relative permittivity and the imaginary part, ϵ'' , is the dielectric loss factor.

The loss tangent, which is the losses experienced by an electromagnetic wave as it transverse a medium, is given by (7.4) [130].

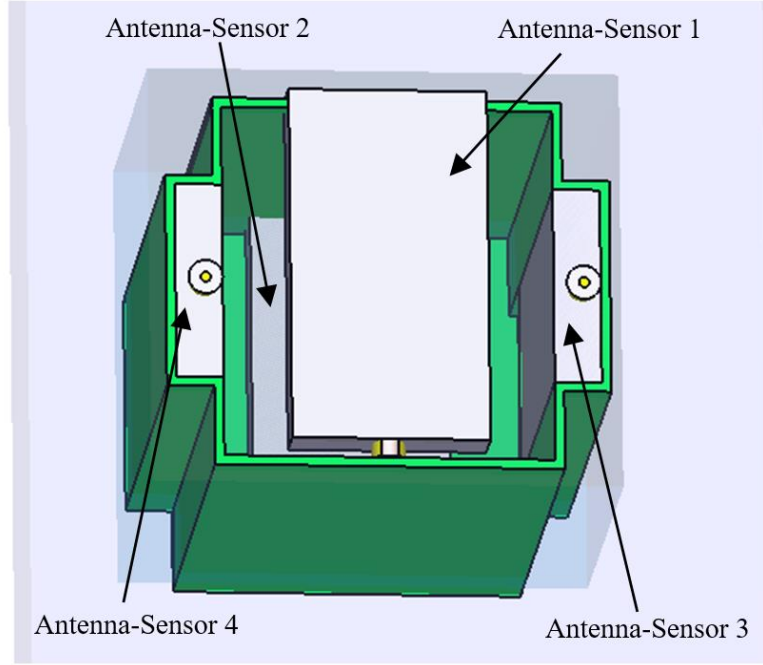


Figure 7.18: Four antenna-sensor array in cuboid configuration.

$$\tan(\delta) = \frac{\epsilon''}{\epsilon'} \quad (7.4)$$

Weiner theory presented the complex dielectric constant for both upper and lower two-phase composite given in (7.5) and (7.6) respectively [131].

$$\epsilon_{.wl} = \left(\frac{f_1}{\epsilon_1} + \frac{f_2}{\epsilon_2} \right)^{-1} \quad (7.5)$$

$$\epsilon_{.wu} = f_1 \epsilon_1 + f_2 \epsilon_2 \quad (7.6)$$

where f_1 and f_2 are the filling factors of liquid 1 and 2, ϵ_1 and ϵ_2 are the dielectric constant of liquid 1 and 2 respectively.

The complex permittivity can be related to the volume of the two mixtures (V_1 and V_2) using the Lichtenecker's equation shown in (7.7) [132].

$$\epsilon_{ref} = \exp \left[V_1 \log \epsilon_{.wl} + V_2 \log \epsilon_{.wu} \right] \quad (7.7)$$

Using the complex permittivity, the transmission coefficient could be obtained by (7.8) [133].

$$S_{21} = \frac{2n}{2n \cos(\beta nl) + j(1 + n^2) \sin(\beta nl)} \quad (7.8)$$

where l is the thickness of the sample under test, β is the phase constant and n is the complex refractive index. $n = \sqrt{\mu_r \epsilon_{ref}}$ and μ_r is the magnetic permeability which is unity for non-magnetic materials. $\beta = 2\pi/\lambda$, where λ is the wavelength.

The setup for the oil spill experiment was developed in CST as it could be seen in Figure. 7.18. The medium comprised of a top and bottom layer containing a heavy aromatic-naphthenic Azeri crude oil (HANACO) phantom and seawater respectively. Oil floats on water due to its lower density compared to the highly saline seawater. The crude oil layer was varied to represent increase in the thickness of the oil slick.

The transmission coefficients of the vertically placed antenna-sensor 3 and antenna-sensor 4 (S43) and horizontally placed antenna-sensor 1 and antenna-sensor 2 (S21), for inclusion of crude oil at 23 mm, 46 mm, 57.5 mm, 69 mm, 80.5 mm, 92 mm and 103.5 mm slick thickness compared to that of pure seawater could be seen in Figure 7.19 (a) and (b) respectively. The *mean ± standard deviation* of the S43 of pure seawater was -88.7264 ± 19.2041 . As the crude oil inclusion increased, it could be seen that the transmission coefficient improved due to the decrease in the relative permittivity of the new mixed medium.

The difference in average values of S43 across the frequency of interest from 0.3 MHz to 3000 MHz for the crude oil slick thickness at 23 mm and 46 mm compared to the S43 of seawater were -21 dB and -42.1 dB respectively.

However, the S43 for oil slick thickness at 57.5 mm, 69 mm, 80.5 mm, 92 mm and 103.5 mm compared to that of seawater were -69.6 dB, -68.75 dB, -67.9 dB and -67.45 dB respectively.

These values show that the antenna-sensors 3 and 4 could detect the oil slick thickness at both 23 mm and 46 mm, however, a difficulty arises with the 57.5 mm, 69 mm, 80.5 mm, 92 mm and 103.5 mm oil slick thickness. The difference of the S43 between these values were less than -2.5 dB.

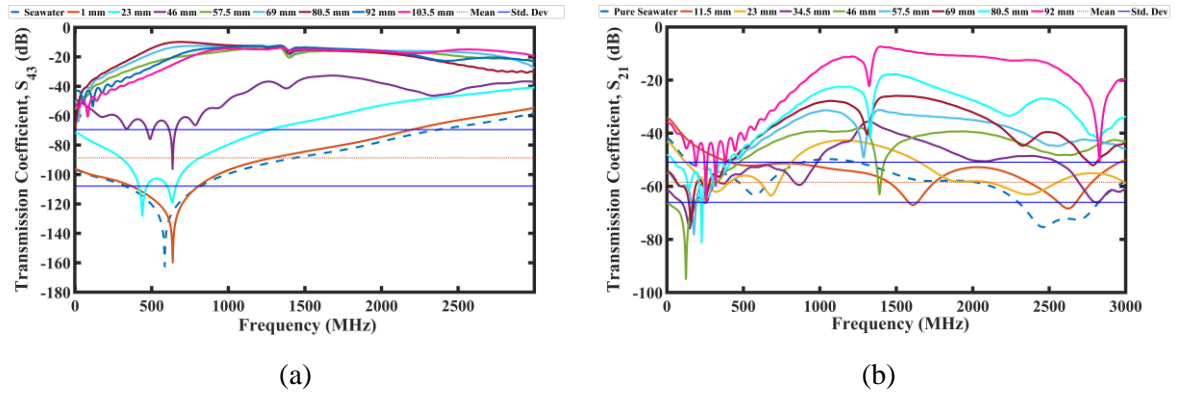


Figure 7.19: Simulation plot of transmission coefficient for different oil thickness. (a) Antenna-sensors 3 and 4 (b) Antenna-sensors 1 and 2.

When the crude oil slick thickness increased to 69 mm and 92 mm, the best responses were captured by the horizontally placed antenna-sensors 1 and 2 as it could be seen in Figure 7.19 (b). The *mean ± standard deviation* of the S_{21} of pure seawater captured by these antenna-sensors was -58.48 ± 7.57 . As the crude oil thickness increased from 69 mm to 92, a marked improvement could be seen from the figure. The differences in the average values of S_{21} of the oil slick thickness at 69 mm and 92 mm compared to that of seawater were -19.33 dB and -36.78 dB respectively for the frequency range of interest.

Thus, antenna-sensors 1 and 2 were able to clearly differentiate between the responses at 69 mm and 92 mm oil slick thickness unlike antenna-sensors 3 and 4. Therefore, by combining the two transmission coefficients, S_{21} and S_{43} , the system could distinctively detect the thickness of the oil slick from 0 mm, 23 mm, 46 mm, 69 mm and 92 mm.

7.5 Dielectric Measurements

Dielectric measurements of the complex permittivity of both seawater and HANACO were performed using Keysight's 85070 high temperature probe connected to a HP 8753 VNA. The VNA was connected to a computer via National Instrument's GPIB-USB-HS. The complete set up for the measurement could be seen in Figure 7.20 with

the high temperature probe immersed in the medium. The measurements were obtained from 1 GHz to 3 GHz at 25°C.

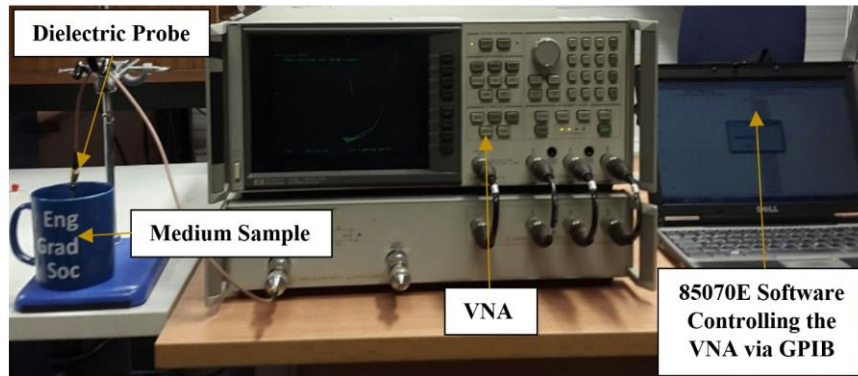


Figure 7.20: Experimental setup for dielectric measurements

The complex permittivity of the seawater and HANACO were measured, and the results obtained could be seen in Figure 7.21. The average of the real part, the relative permittivity of oil and seawater, across the whole frequencies is 2.4 and 79 respectively. At 1.8 GHz, the real part of the relative permittivity of the HANACO and seawater were 2.3 and 77 respectively.

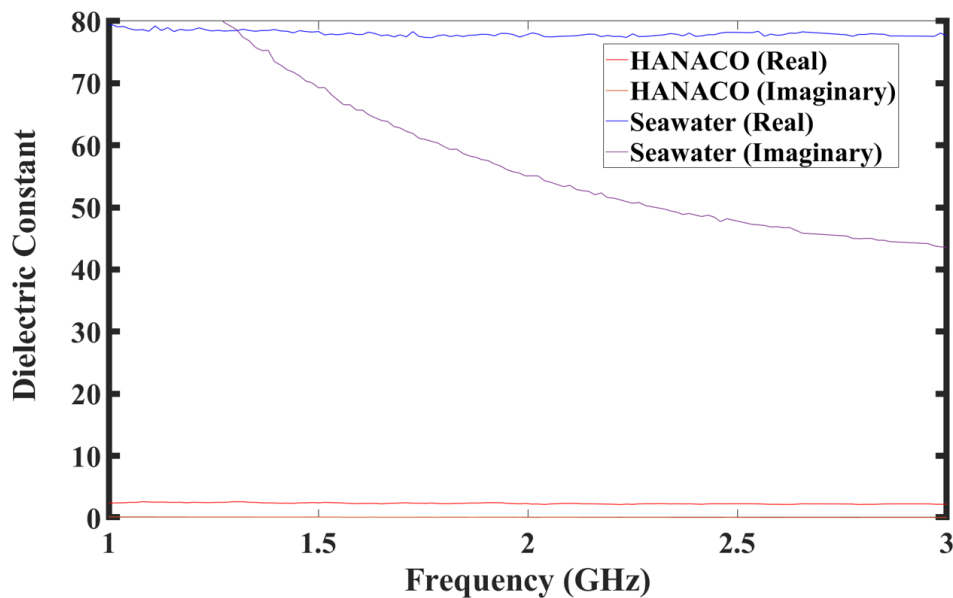


Figure 7.21: Dielectric measurement of HANACO oil and seawater

7.6 Oil Slick Thickness Measurement

With the insights gained from the simulations results in CST, the research proceeded to validate the findings experimentally.

7.6.1 Enclosure for the setup

For the final experiment, an enclosure was required to house the antenna-sensors in the orientation that was simulated in CST microwave studio. To accomplish that, the enclosure was designed in Onshape, a 3D computer-aided design (CAD) tool. This could be seen in Figure 7.22. The dimensions of the antenna-sensors support in the enclosure were ported from the CST so that the same vertical separation of 80 mm between antenna-sensor 1 and antenna-sensor 2 and also the horizontal separation distance of 74 mm between antenna-sensor 3 and antenna-sensor 4 were maintained. The cover, with the solar panel holes can be seen in Figure 7.22 (b).

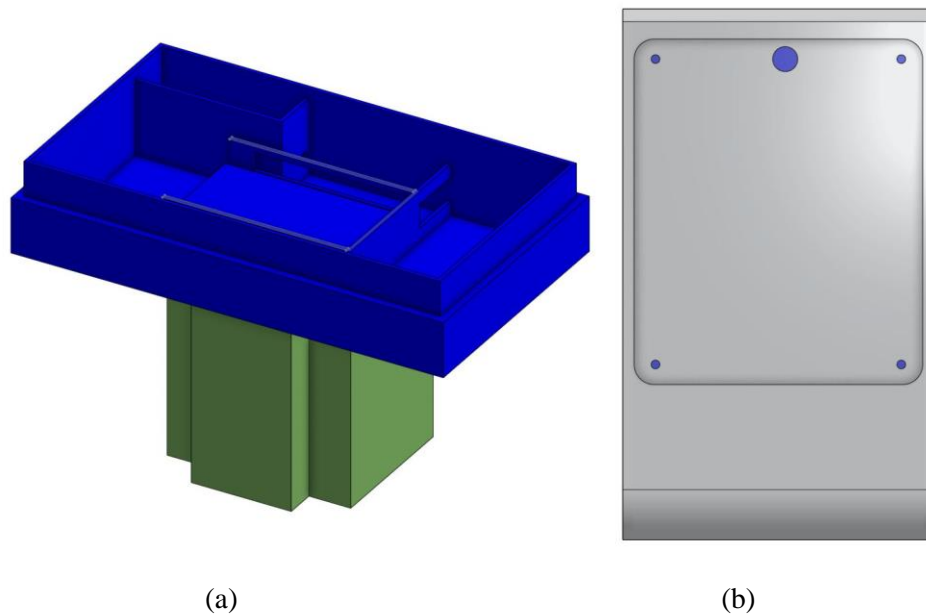


Figure 7.22: 3D model of enclosure (a) Perspective (b) Top cover.

After the 3D modelling, the enclosures were 3D printed using PLA. The images of the base housing the three antennas-sensors (antennas-sensor 2, antennas-sensor 3 and

antennas-sensor 4) could be seen in Figure 7.23 (a). The complete enclosure with the solar panel mounted could be seen in Figure 7.23 (b).

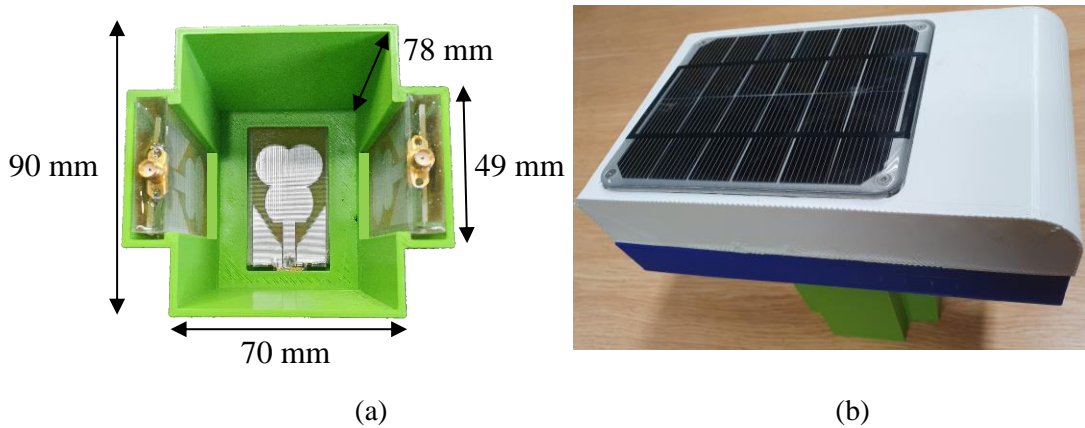


Figure 7.23: 3D Printed enclosure (a) Base (b) Perspective.

7.6.2 Experimental Setup

The complete setup for the oil spill detection and oil slick thickness determination could be seen in Figure 7.24. Port 1 of the VNA was connected to the RFC of SPDTA and port 2 of the VNA was connected to the RFC of the SPDTB as shown in Figure 7.25. Each of the SPDT switches have two antennas connected to it in a vertical and horizontal orientation. The high XPD value of the antenna-sensors ensure that there is negligible mutual coupling between adjacent antenna-sensors. As it could be seen, SPDTA was connected to antenna-sensors 1 and 3 while SPDTB was connected to antenna-sensors 2 and 3.

A full-2 port calibration was performed on the VNA using a 3.5 mm calibration kit. The number of points were selected to be 1601 with an input power of -10 dBm and a frequency range of 0.3 MHz to 3000 MHz. The reflection calibrations were done on each port using the open, short and load studs. A thru was connected and transmission calibrations were undertaken as well.

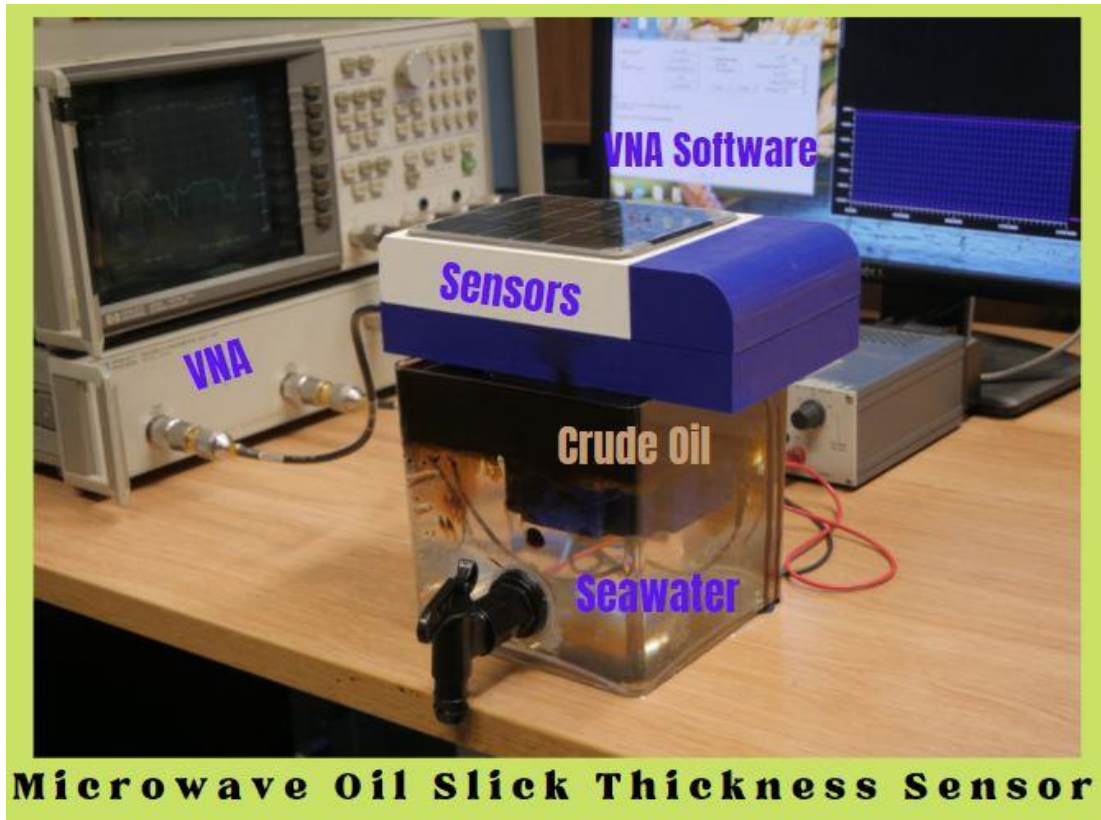


Figure 7.24: In situ microwave sensor for oil slick thickness measurement.

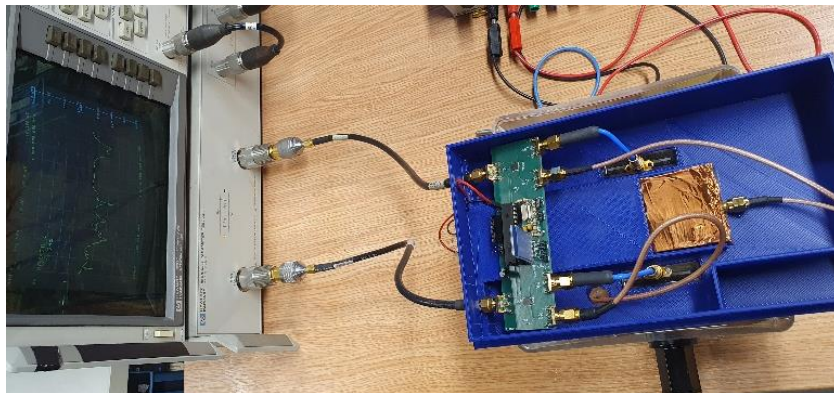


Figure 7.25: Top view of experimental setup for the oil slick thickness measurement.

The transparent water container was initially filled with seawater at 3,375 cubic centimetres. The S parameters for all the antennas in the setup was captured by the KE5FX VNA utility software on the PC that was connected to the VNA using the GPIB, to provide the baseline for the pure seawater. Using the tap at the base of the container,

520 cubic centimetre cube of water was drained from the container. Crude oil at the same discharged volume was introduced to take the container to the starting volume while ensuring the crude oil mixed vigorously with the seawater medium. The oil floats to the surface as it could be seen in the setup in Figure 7.24. This is because crude oil has lower density compared to seawater that has high salinity [134]. The thickness of oil slick was measured at 23 mm. The same process of discharging the medium at 520 cubic centimetres and reintroducing the same volume of crude oil was repeated until all the antenna-sensors in the setup were completely submerged in crude oil at 92 mm oil slick thickness. The S parameters captured for the 0 mm, 23 mm, 46 mm, 69 mm and 92 mm oil slick thickness shall be discussed.

7.6.3 Reflection Coefficients for Oil Slick Thickness Measurement

The reflection coefficient for the setup could be seen in Figure 7.26 and Figure 7.27, for antenna-sensor 1 (S11) and antenna-sensor 2 (S22) respectively. For the 69 mm and 92 mm oil slick thickness, the changes in the S11 and S22 is obvious from the figures. The *mean ± standard deviation* of the S11 and S22 for the pure seawater for antenna-sensor 1 and antenna-sensor 2 were -9.54767 ± 5.624276 and -13.6076 ± 5.9741 respectively.

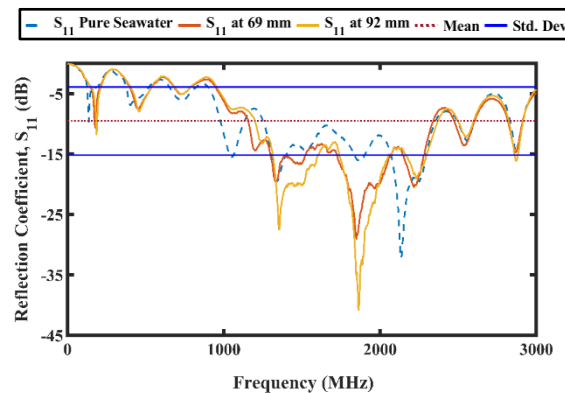


Figure 7.26: Antenna-sensor 1 plot of measured reflection coefficient for 69 mm and 92 mm oil thickness.

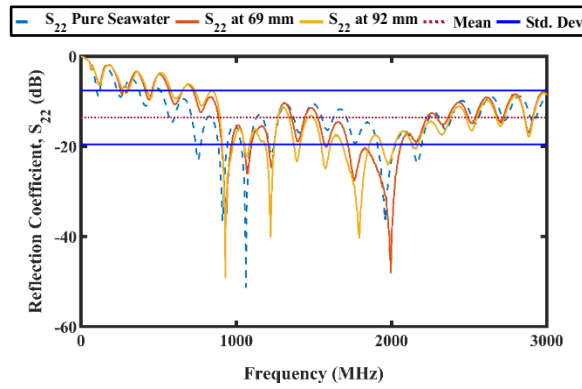


Figure 7.27: Antenna-sensor 2 plot of measured reflection coefficient for 69 mm and 92 mm oil thickness.

The reflection coefficient for antenna-sensors 3 (S33) and antenna-sensors 4 (S44) could be seen in Figure 7.28 and Figure 7.29 respectively. The S33 and S44 responses, as the oil slick thicknesses of 23 mm and 46 mm were introduced to the pure seawater medium, could be seen in the figures. The *mean* \pm *standard deviation* of the S33 and S44 for the pure seawater for antenna-sensor 3 and antenna-sensor 4 were -10.7489 ± 6.0125 and -12.0417 ± 5.9507 respectively.

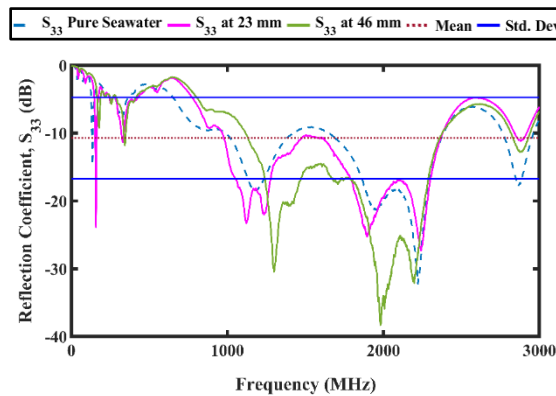


Figure 7.28: Antenna-sensor 3 plot of measured reflection coefficient for 23 mm and 46 mm oil thickness.

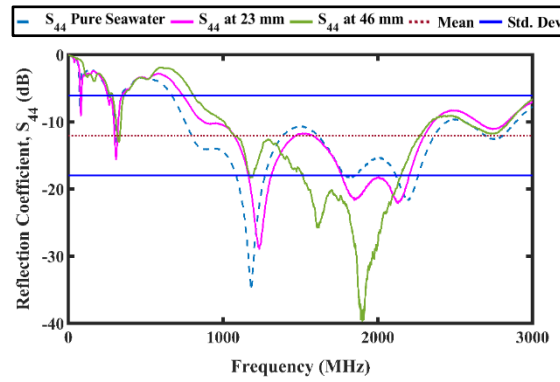


Figure 7.29: Antenna-sensor 4 plot of measured reflection coefficient for 23 mm and 46 mm oil thickness.

7.6.4 Transmission Coefficients for Oil Slick Thickness Measurement

The transmission coefficients for antenna-sensor 3 and antenna-sensor 4 (S43) could be seen in Figure 7.30 (a) and Figure 7.30 (b) for the 23 mm and 46 mm oil slick thicknesses respectively. The *mean ± standard deviation* of the S43 for pure seawater was -48.638 ± 13.888 . When the oil slick thickness was at 23 mm and 46 mm, the *mean ± standard deviation* of the S43 for the new media increased to -38.9872 ± 10.21724 and -29.6345 ± 9.9981 respectively.

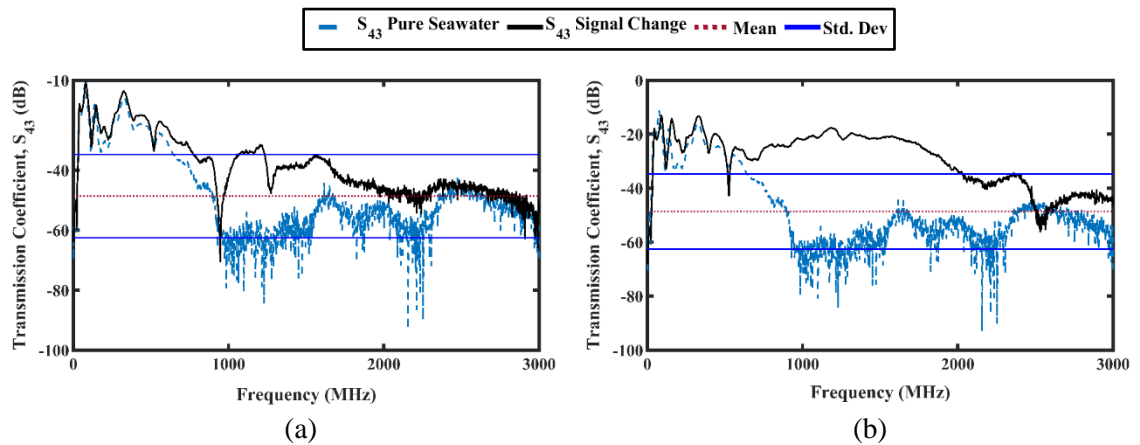


Figure 7.30: Plot of measured transmission coefficient for oil thickness (a) 23 mm (b) 46 mm.

The change in the dielectric constant of the seawater medium by introduction of crude oil at much lower dielectric constant, resulted in improvement of the transmission

coefficients' response indicating oil spillage and detecting its thickness. This validates the results obtained from the simulation plots. The difference in the average values of the S₂₁ of the pure seawater and those at 23 mm and 46 mm oil slick thicknesses were -10 dB and -19 dB respectively exhibiting high differentiability of oil slick thickness by the system.

The transmission coefficients for antenna-sensor 1 and antenna-sensor 2 (S₂₁) could be seen in Figure 7.31 (a) and Figure 7.31 (b) for the 69 mm and 92 mm oil slick thicknesses respectively. The *mean ± standard deviation* of the S₂₁ for the pure seawater was -56.9 ± 9.218 while that of the new medium with 69 mm and 92 mm oil slick thicknesses were -43.85 ± 7.0692 and -32.76 ± 7.0524 respectively. This was also in agreement with results obtained from the simulation plots. As the crude oil inclusion was added to the medium, the S₂₁ improved at 69 mm. At 92 mm oil slick thickness, the S₂₁ was further ameliorated. The difference in the average values of the S₂₁ of the pure seawater and those at 69 mm and 92 mm oil slick thicknesses were -13.5 dB and -24.14 dB respectively exhibiting high differentiability of oil slick thickness by the system.

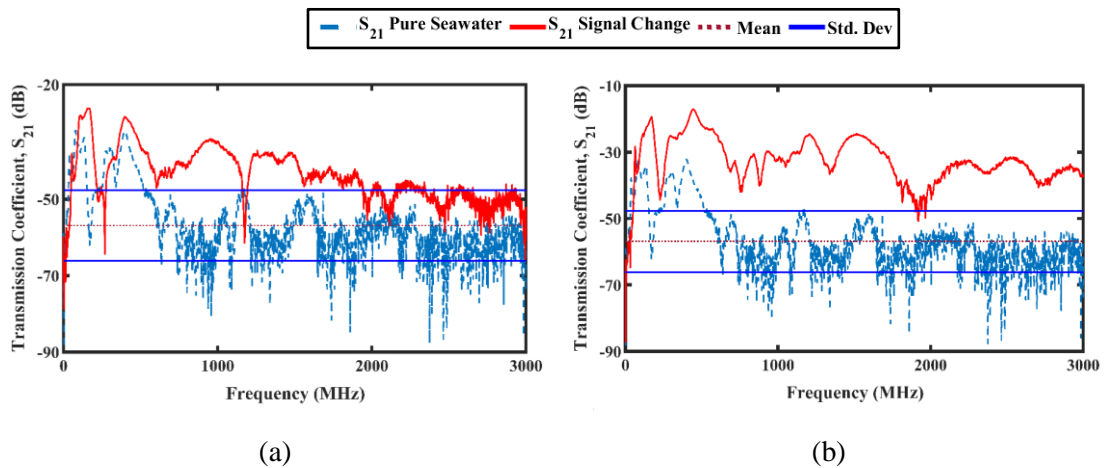


Figure 7.31: Plot of measured transmission coefficient for oil thickness (a) 69 mm (b) 92 mm.

Although noticeable changes could be observed from the reflection coefficients when HANACO oil was introduced to the medium, thus proving its ability to detect oil spillage, however, for the determination of oil slick thickness, the work found that the

transmission coefficients were more reliable based on both simulation and measurement results.

7.7 Summary

In this chapter, a novel compact RF switching circuit was developed and connected with four antenna-sensors to determine the thicknesses of oil slicks. The RF switches were characterised with respect to their insertion and return loss to ensure that noises and interferences were not cascaded to the antenna-sensor array.

The RF switch was developed on a four-layer PCB with the inner layers filled with copper pour to represent the ground and power layer. The RF paths were first designed in CST and validated before the dimensions and orientations were ported to the final PCB design. An Atmega328P microcontroller controlled the operation of the switch and a Bluetooth module enabled each of the antenna-sensor to be selected in a mono-static and multi-static configuration.

The developed sensor was able to show that oil slick thickness could be measured using in situ microwave approach. Noticeable changes were observed from the reflection coefficients when oil was introduced to the medium, thus the ability to detect oil spillage. However, for the determination of oil slick thickness, it was found that the transmission coefficients were more reliable based on both simulation and measurement results. Oil slick thickness of 0 mm, 23 mm, 46 mm, 69 mm and 92 mm were distinctively identified using the S21 and S43.

This work forms the foundation for future work on the determination of oil slick thickness using microwave sensors. The next chapter summarises and concludes the work undertaken in this thesis.

Chapter 8

Conclusion and Future Work

The overarching aim of this thesis is to provide the foundational basis of using microwave sensing techniques in the detection of oil spill and measurement of oil slick thickness offshore. This was achieved through investigating the properties of the seawater, developing underwater antenna-sensors and deploying them as prototypes that detected oil spill and measured the oil slick thickness. Rapeseed oil and crude oil were used as inclusions in both seawater and freshwater media. The transmission coefficients of the antenna-sensors were used to differentiate oil slick thickness from 0 mm to 92 mm. This chapter summarises and concludes the research undertaken in this thesis, highlighting the contributions made and suggestions on possible directions for future work.

8.1 Conclusion

Oil spill detection and oil slick determination are two important parameters for the oil and gas industries as well as other stakeholders such as the government, environmentalists and the larger society. This is because oil spill has devastating consequences on the environment, climate change, people living in the coastal areas of the affected sites and the marine flora and fauna. To prevent accidental and intentional discharge into the environment, it is important that the defaulting parties are penalised based on the quantity of oil discharge. The oil slick thickness could assist in providing this estimation. The information could also be used for planning the oil spill countermeasures. The in situ oil slick thickness measurement is at its early stage with techniques such as capacitive, optical, thermal infrared and conductive methods deployed. This was the first attempt at using contact-based in situ microwave technique for underwater sensing of crude oil.

The overarching aim of this thesis was to provide a proof of concept of using microwave in the detection of oil spill and determination of oil slick thickness. Thus, a microwave

oil spill and oil slick thickness measurement sensors were designed, developed and implemented in this research.

In the first stage of this research, the properties of seawater were investigated using mathematical models and dielectric measurements of seawater samples obtained in the North Sea. This probed the properties of the seawater such as its relative permittivity, dielectric loss factor and loss tangent. This was important because the research targeted the North Sea water as its primary transmission medium.

The second stage of this study developed an underwater antenna-sensor that was designed from a trefoil antenna encapsulated in polydimethylsiloxane (PDMS). This enabled the antenna to achieve impedance matching and radiate in the water medium. The dimensions of the PDMS were optimised using CST Microwave Studio simulations before it was developed in the clean room facility at the University of Edinburgh.

The antenna-sensors manufactured were used to develop an in situ microwave oil spill detection prototype in the third stage of this study. It consisted of two antenna-sensors separated by a distance inside a Faraday cage. The experiment was performed with heavy aromatic-naphthenic Azeri crude oil as an inclusion and seawater as the host medium. The crude oil was continuously added to the seawater and both the reflection and transmission coefficients were repeatedly capture.

To enable the in-situ microwave sensor to have real-time capabilities, a telemetry system using 868 MHz long range (LoRa) communication was developed in the fourth stage of this work. LoRa offered the advantages of low power consumption and long-range communication. The seawater surface, where the oil spill sensor operates, affects transmissions at radio frequencies. An antenna was developed to mitigate against such effects. The base antenna consisted of a novel braid antenna buffered by oil-impregnated papers. Fields tests for the antenna both on the water surface and underwater was undertaken.

The final stage of this research presents the development of the in-situ microwave sensor for oil spill detection and oil slick thickness measurement underwater. An array of the antenna-sensors developed in stage 2 were used in this stage. The back of the

PDMS encapsulated antenna-sensors were padded with copper foils to make their radiation unidirectional. A novel four-layered PCB RF switching circuit was developed to connect the four antenna-sensors to the two ports of the VNA. The bespoke RF switching circuits' controller consisted of two single pole double throw (SPDT) RF switches, Atmega328P microcontroller, Bluetooth module, light-emitting diodes (LEDs) and power supply. The orientation and dimensions of the antenna-sensors were first simulated in CST which provided the parameters for the 3D printed enclosures for the oil slick thickness measurements. Heavy aromatic-naphthenic Azeri crude oil was used as the inclusion while seawater was used as the medium for the oil slick thickness measurement. Oil is less dense than the salty seawater, so it floated at the surface. Using the cuboid placement of the four antenna-sensor array, the prototype was used to successfully determine oil slick thickness at 0 mm, 23 mm, 46 mm, 69 mm and 92 mm.

The in-situ microwave oil spill detection and oil slick thickness measurement sensor prototype developed in this study provided very insightful and transformative results as reported in this thesis. This sensor could be extended for use in the detection of some impurities in the underwater environment. Suggestion for achieving a portable, more compact and efficient standalone system in the future are highlighted in the next section.

8.2 Suggestions for Future Work

Although the research work performed and discussed in this thesis was able to show a proof-of-concept for the use of in-situ microwave antennas in the detection of oil spill and determination of oil slick thickness, more experiments and upgrades are required to make the sensor commercially ready and viable to be used as a portable system. Some of the suggestions for future work are highlighted as follows:

8.2.1 Antenna Design

An integral part of the microwave oil spill sensor is the antenna. Thus, an improvement in the antenna design with respect to directivity, gain and efficiency shall have a direct impact on the overall efficiency of the system. The antenna-sensor should be made

unidirectional without the addition of the copper foil at the back of the PDMS. A reduction in the dimensions of the antenna could also have a subsequent reduction in the size of the PDMS buffer and the overall system.

8.2.2 Antenna Array

The reduction in the dimension of the antenna-sensor could enable more antenna-sensors to be incorporated in the array. This may improve the efficiency of the microwave sensor and probably enable it to measure thinner oil slicks. However, the antenna-sensors' cross polar discrimination should be considered during the design, simulation and measurement.

8.2.3 RF Switching Circuit

A novel four-layered, two-input, four-output RF switch was developed for this research. With increase in the number of antenna-sensors in the array, there would be a requirement for RF switches that can handle the operations of those antenna-sensors. A consideration should be made on increasing the layers of the PCB to six (6) or more to increase the compactness and efficiency of the developed RF switching circuit. RF switches with higher number of RF output ports should be considered as well.

8.2.4 Portable Standalone System

To deploy the in situ microwave in the field, the VNA has to be replaced with a system on chip (SoC) or a device that is capable of characterising the water transmission medium with respect to the scattering parameters. A good candidate for this would be a software defined radio such as LimeSDR that has been used to develop portable VNAs. It could be used with a raspberry Pi 4 that has a USB 3.0 capabilities to drive the SDR and control the selection of the antenna-sensors attached to the RF switches.

8.3 Final Comments

The use of in situ microwave sensing technique in the detection of oil spill and determination of oil slick thickness has several merits over capacitive, conductive and

optical based approaches such as robustness, anti-rust, anti-fouling and non-interference by external light sources. The in situ microwave oil spill sensor could in conjunction with remote sensing techniques such as satellite and airborne SARs, provide more ubiquitous and real-time capabilities. The microwave sensor would find greater application in areas close to the exploration sites such as the risers or pipes that connect to the floating production storage and offloading (FPSO), which are two of the sites vulnerable to oil spillage as was the case with the Deepwater Horizon and Bonga oil spillages. The presence of the microwave oil spill sensors would be able to alert the authorities in real-time if there was a case of oil spillage and may help reduce the catastrophe that oil spill does to the environment, marine life and livelihoods of the people that live around those areas.

References

- [1] Nirbachita. R. Progga, ‘The ancient use of oil’, *The Business Standard*, Jul. 31, 2020. <https://www.tbsnews.net/feature/panorama/ancient-use-oil-114025> (accessed Oct. 14, 2021).
- [2] ‘Use of oil - U.S. Energy Information Administration (EIA)’. <https://www.eia.gov/energyexplained/oil-and-petroleum-products/use-of-oil.php> (accessed Jul. 22, 2021).
- [3] ‘9 of the Biggest Oil Spills in History’, *Encyclopedia Britannica*. <https://www.britannica.com/list/9-of-the-biggest-oil-spills-in-history> (accessed Jul. 22, 2021).
- [4] Z. Liu and Y. Liu, ‘A Bayesian network based method for reliability analysis of subsea blowout preventer control system’, *J. Loss Prev. Process Ind.*, vol. 59, pp. 44–53, May 2019, doi: 10.1016/j.jlp.2019.03.004.
- [5] ‘Shell liable to \$3.6 billion fine over Bonga oil spill, Nigerian court rules’. <https://www.premiumtimesng.com/news/headlines/273177-shell-liable-to-3-6-billion-fine-over-bonga-oil-spill-nigerian-court-rules.html> (accessed Jul. 22, 2021).
- [6] ‘Shell faces \$5 billion fine over Nigeria Bonga oil spill’, *Reuters*, Jul. 17, 2012. Accessed: Jul. 22, 2021. [Online]. Available: <https://www.reuters.com/article/us-shell-nigeria-fine-idUSBRE86G0X020120717>
- [7] M. Fingas, ‘The Challenges of Remotely Measuring Oil Slick Thickness’, *Remote Sens.*, vol. 10, no. 2, Art. no. 2, Feb. 2018, doi: 10.3390/rs10020319.
- [8] C. Gabriel, S. Gabriel, and E. Corthout, ‘The dielectric properties of biological tissues: I. Literature survey’, *Phys. Med. Biol.*, vol. 41, no. 11, pp. 2231–2249, Nov. 1996, doi: 10.1088/0031-9155/41/11/001.
- [9] A. Grudiev, ‘Simulation packages and Review of Codes’, p. 28.
- [10] W. Bruns, ‘The Gdfidl Electromagnetic Field Simulator’, <http://www.gdfidl.de/>. <http://www.gdfidl.de/> (accessed Feb. 20, 2022).
- [11] ‘Ansys HFSS | 3D High Frequency Simulation Software’. <https://www.ansys.com/en-gb/products/electronics/ansys-hfss> (accessed Feb. 20, 2022).
- [12] ‘COMSOL: Multiphysics Software for Optimizing Designs’, *COMSOL*. <https://www.comsol.com/> (accessed Feb. 20, 2022).
- [13] ‘ACE3P CW18 Accelerator Code Workshop’, *ACE3P CW18 Accelerator Code Workshop*. <https://conf.slac.stanford.edu/cw18/> (accessed Feb. 20, 2022).
- [14] krn5, ‘CST Studio Suite 3D EM simulation and analysis software’. <https://www.3ds.com/products-services/simulia/products/cst-studio-suite/> (accessed Feb. 20, 2022).
- [15] M. Fingas and C. E. Brown, ‘A Review of Oil Spill Remote Sensing’, *Sensors*, vol. 18, no. 1, Art. no. 1, Jan. 2018, doi: 10.3390/s18010091.
- [16] ‘Overview | Get to Know SAR’, *NASA-ISRO SAR Mission (NISAR)*. <https://nisar.jpl.nasa.gov/mission/get-to-know-sar/overview> (accessed Jul. 22, 2021).

- [17] S. Naz, M. F. Iqbal, I. Mahmood, and M. Allam, 'Marine oil spill detection using Synthetic Aperture Radar over Indian Ocean', *Mar. Pollut. Bull.*, vol. 162, p. 111921, Jan. 2021, doi: 10.1016/j.marpolbul.2020.111921.
- [18] D. Dhont, R. Jatiault, and P. Lattes, 'Combined Use of SAR and Underwater Gliders for Oil Seeps Detection', in *IGARSS 2019 - 2019 IEEE International Geoscience and Remote Sensing Symposium*, Jul. 2019, pp. 7865–7868. doi: 10.1109/IGARSS.2019.8898602.
- [19] C. E. Jones and B. Holt, 'Experimental L-Band Airborne SAR for Oil Spill Response at Sea and in Coastal Waters', *Sensors*, vol. 18, no. 2, Art. no. 2, Feb. 2018, doi: 10.3390/s18020641.
- [20] O. Garcia-Pineda *et al.*, 'Classification of oil spill by thicknesses using multiple remote sensors', *Remote Sens. Environ.*, vol. 236, p. 111421, Jan. 2020, doi: 10.1016/j.rse.2019.111421.
- [21] W. Alpers, B. Holt, and K. Zeng, 'Oil spill detection by imaging radars: Challenges and pitfalls', *Remote Sens. Environ.*, vol. 201, pp. 133–147, Nov. 2017, doi: 10.1016/j.rse.2017.09.002.
- [22] M. Andreotti *et al.*, 'ARIEL: An Autonomous Robotic System for Oil Spill Detection', presented at the Offshore Technology Conference, May 2020. doi: 10.4043/30894-MS.
- [23] A. Pisano *et al.*, 'An oceanographic survey for oil spill monitoring and model forecasting validation using remote sensing and in situ data in the Mediterranean Sea', *Deep Sea Res. Part II Top. Stud. Oceanogr.*, vol. 133, pp. 132–145, Nov. 2016, doi: 10.1016/j.dsr2.2016.02.013.
- [24] J. Svejkovsky, A. Lewis, J. Muskat, J. H. S. Andersen, S. Benz, and O. Garcia-Pineda, 'Rebuttal to published article "Review of oil spill remote sensing" by M. Fingas and C. Brown', *Mar. Pollut. Bull.*, vol. 93, no. 1, pp. 294–297, Apr. 2015, doi: 10.1016/j.marpolbul.2015.01.005.
- [25] D. Seo, S. Oh, S. Shin, M. Lee, Y. Hwang, and S. Seo, 'Smartphone compatible on-site fluorescence analyzer for spilled crude oil based on CMOS image sensor', *Sens. Actuators B Chem.*, vol. 289, pp. 93–99, Jun. 2019, doi: 10.1016/j.snb.2019.03.086.
- [26] R. Pallardy, 'Deepwater Horizon oil spill | Summary, Effects, Cause, Clean Up, & Facts', *Encyclopedia Britannica*, 2010. <https://www.britannica.com/event/Deepwater-Horizon-oil-spill> (accessed Oct. 06, 2021).
- [27] S. Cheemalapati, H. Forth, H. Wang, K. Konnaiyan, J. Morris, and A. Pyayt, 'Measurement of thickness of highly inhomogeneous crude oil slicks', 2017. <https://www.osapublishing.org/ao/ViewMedia.cfm?uri=ao-56-11-E72&seq=0&guid=3185ca36-f940-44ef-8e8d-f79883da8694&html=true> (accessed Oct. 06, 2021).
- [28] G. Suir, K. Suir, and S. Sapkota, 'Use of remote sensing to detect and predict aquatic nuisance vegetation growth in coastal Louisiana: summary of findings', Environmental Laboratory (U.S.), Apr. 2018. doi: 10.21079/11681/26649.
- [29] ITOPF, 'Aerial Observation of Marine Oil Spills'. Impact PR & Design Limited, Canterbury. [Online]. Available: https://www.itopf.org/fileadmin/uploads/itopf/data/Documents/TIPS_TAPS_new/TIP_1_Aerial_Observation_of_Marine_Oil_Spills.pdf

-
- [30] P. C. Genovez, C. E. Jones, S. J. S. Sant'Anna, and C. C. Freitas, 'Oil Slick Characterization Using a Statistical Region-Based Classifier Applied to UAVSAR Data', *J. Mar. Sci. Eng.*, vol. 7, no. 2, Art. no. 2, Feb. 2019, doi: 10.3390/jmse7020036.
- [31] R. Laure, V.-R. Françoise, and M. Véronique, 'Oil Slick Volume Estimation from Combined Use of Airborne Hyperspectral and Pool Experiment Data', in *IGARSS 2019 - 2019 IEEE International Geoscience and Remote Sensing Symposium*, Jul. 2019, pp. 5776–5779. doi: 10.1109/IGARSS.2019.8899057.
- [32] S. He and H. Dong, 'Simultaneous estimation of the refractive index and thickness of marine oil slick from the degree of linear polarization of the sun-glint reflection', *Prog. Electromagn. Res.*, vol. 163, pp. 133–142, Jan. 2018, doi: 10.2528/PIER18092601.
- [33] 'The Science of Sunlint', Sep. 11, 2014. <https://earthobservatory.nasa.gov/images/84333/the-science-of-sunglint> (accessed Oct. 06, 2021).
- [34] Y. Lu, W. Zhan, and C. Hu, 'Detecting and quantifying oil slick thickness by thermal remote sensing: A ground-based experiment', *Remote Sens. Environ.*, vol. 181, pp. 207–217, Aug. 2016, doi: 10.1016/j.rse.2016.04.007.
- [35] J. Jiao, Y. Lu, C. Hu, J. Shi, S. Sun, and Y. Liu, 'Quantifying ocean surface oil thickness using thermal remote sensing', *Remote Sens. Environ.*, vol. 261, p. 112513, Aug. 2021, doi: 10.1016/j.rse.2021.112513.
- [36] A. Massaro, A. Lay-Ekuakille, D. Caratelli, I. Palamara, and F. C. Morabito, 'Optical Performance Evaluation of Oil Spill Detection Methods: Thickness and Extent', *IEEE Trans. Instrum. Meas.*, vol. 61, no. 12, pp. 3332–3339, Dec. 2012, doi: 10.1109/TIM.2012.2210336.
- [37] M. Saleh, G. Oueidat, M. Ghamlouch, I. H. Elhadj, and D. Asmar, 'LED-based Spectrometer for In Situ Oil Slick Thickness Measurement', in *2018 IEEE International Multidisciplinary Conference on Engineering Technology (IMCET)*, Nov. 2018, pp. 1–6. doi: 10.1109/IMCET.2018.8603042.
- [38] F. Yan *et al.*, 'Thickness measurement and three-dimensional structure imaging of oil slick on water by optical coherence tomography', *Optik*, vol. 180, pp. 1036–1042, Feb. 2019, doi: 10.1016/j.ijleo.2018.11.147.
- [39] F. N. Toth, G. C. M. Meijer, and M. van der Lee, 'A planar capacitive precision gauge for liquid-level and leakage detection', *IEEE Trans. Instrum. Meas.*, vol. 46, no. 2, pp. 644–646, Apr. 1997, doi: 10.1109/19.572052.
- [40] S. C. Bera, J. K. Ray, and S. Chattopadhyay, 'A low-cost noncontact capacitance-type level transducer for a conducting liquid', *IEEE Trans. Instrum. Meas.*, vol. 55, no. 3, pp. 778–786, Jun. 2006, doi: 10.1109/TIM.2006.873785.
- [41] M. Saleh, G. Oueidat, I. H. Elhadj, and D. Asmar, 'In Situ Measurement of Oil Slick Thickness', *IEEE Trans. Instrum. Meas.*, vol. 68, no. 7, pp. 2635–2647, Jul. 2019, doi: 10.1109/TIM.2018.2866745.
- [42] H. Denkilkian *et al.*, 'Wireless Sensor for Continuous Real-Time Oil Spill Thickness and Location Measurement', *IEEE Trans. Instrum. Meas.*, vol. 58, no. 12, pp. 4001–4011, Dec. 2009, doi: 10.1109/TIM.2009.2021641.
- [43] M. Chaplin, 'Water Structure and Science'. Feb. 19, 2008. [Online]. Available: lsbu.ac.uk

- [44] Z. Otremba, 'Oil droplets as light absorbents in seawater', *Opt. Express*, vol. 15, no. 14, pp. 8592–8597, Jul. 2007, doi: 10.1364/OE.15.008592.
- [45] A. Ishimaru, *Electromagnetic Wave Propagation, Radiation, and Scattering*, 1st ed. John Wiley & Sons, Ltd, 2017. doi: 10.1002/9781119079699.
- [46] Edward Conrad, 'Electromagnetic Waves and Radiating Systems', 1968. <https://khasimgriet.files.wordpress.com/2016/07/edward-conrad-jordan-electromagnetic-waves-and-radiating-systems-prentice-hall-electrical-engineering-series-1968.pdf> (accessed May 01, 2018).
- [47] David Pozar, *Microwave Engineering*, 4th ed. John Wiley & Sons, Inc.
- [48] 'Polar molecules. By P. Debye, Ph.D., Pp. 172. New York: Chemical Catalog Co., Inc., 1929. \$ 3.50', *J. Soc. Chem. Ind.*, vol. 48, no. 43, pp. 1036–1037, Oct. 1929, doi: 10.1002/jctb.5000484320.
- [49] R. Somaraju and J. Trumpf, 'Frequency, Temperature and Salinity Variation of the Permittivity of Seawater', *IEEE Trans. Antennas Propag.*, vol. 54, no. 11, pp. 3441–3448, Nov. 2006, doi: 10.1109/TAP.2006.884290.
- [50] P. Saini, R. P. Singh, and A. Sinha, 'Path loss analysis of RF waves for underwater wireless sensor networks', in *2017 International Conference on Computing and Communication Technologies for Smart Nation (IC3TSN)*, Oct. 2017, pp. 104–108. doi: 10.1109/IC3TSN.2017.8284460.
- [51] F. Daout, A. Khenchaf, and J. Saillard, 'The effect of salinity and temperature on the electromagnetic field scattered by sea water', in *OCEANS '94. 'Oceans Engineering for Today's Technology and Tomorrow's Preservation.' Proceedings*, Sep. 1994, vol. 1, p. I/110-I/115 vol.1. doi: 10.1109/OCEANS.1994.363866.
- [52] MEFEPO, 'North Sea Atlas', 2009. https://www.liverpool.ac.uk/media/livacuk/mefepo/documents/wp1/atlases/N_S_Atlas_English.pdf (accessed May 08, 2018).
- [53] C. Fang, H. Tan, Q. Liu, X. Zhao, and W. Yu, 'Microwave scattering model for two dimensional fractal sea water based on double debye dielectric model', in *2013 5th IEEE International Symposium on Microwave, Antenna, Propagation and EMC Technologies for Wireless Communications*, Oct. 2013, pp. 185–188. doi: 10.1109/MAPE.2013.6689862.
- [54] A. Foudazi and K. M. Donnell, 'Design of a microstrip patch antenna for microwave sensing of petroleum production lines', in *2017 United States National Committee of URSI National Radio Science Meeting (USNC-URSI NRSM)*, Jan. 2017, pp. 1–2. doi: 10.1109/USNC-URSI-NRSM.2017.7878310.
- [55] M. S. R. Bashri, 'Wearable devices for microwave head diagnostic systems', Nov. 2018, Accessed: Jul. 28, 2021. [Online]. Available: <https://era.ed.ac.uk/handle/1842/33243>
- [56] P. Loghmannia and M. Manteghi, 'An Antenna System for Autonomous Underwater Vehicle', in *2019 United States National Committee of URSI National Radio Science Meeting (USNC-URSI NRSM)*, Jan. 2019, pp. 1–2. doi: 10.23919/USNC-URSI-NRSM.2019.8713166.
- [57] I. I. Smolyaninov, Q. Balzano, C. C. Davis, and D. Young, 'Surface Wave Based Underwater Radio Communication', *IEEE Antennas Wirel. Propag. Lett.*, vol. 17, no. 12, pp. 2503–2507, Dec. 2018, doi: 10.1109/LAWP.2018.2880008.

- [58] T. Meissner and F. J. Wentz, 'The complex dielectric constant of pure and sea water from microwave satellite observations', *IEEE Trans. Geosci. Remote Sens.*, vol. 42, no. 9, pp. 1836–1849, Sep. 2004, doi: 10.1109/TGRS.2004.831888.
- [59] I. I. Smolyaninov, 'Communication and sensor techniques for underwater radio communication', U.S. Patent 20180198536, Jul. 12, 2018
- [60] H. Yoshida, 'Underwater electromagnetics and its application to unmanned underwater platforms', in *2013 IEEE International Underwater Technology Symposium (UT)*, Mar. 2013, pp. 1–5. doi: 10.1109/UT.2013.6519886.
- [61] B. Muneer, B. S. Chowdhry, H. Zafar, Z. Ali, and F. K. Shaikh, 'Polarization Agile Antenna for Underwater Communication Using Integrated Power Divider and Phase Shifter', *Wirel. Pers. Commun.*, vol. 116, no. 2, pp. 1137–1149, Jan. 2021, doi: 10.1007/s11277-020-07034-6.
- [62] I. Pasya, H. M. Zali, M. Saat, M. T. Ali, and T. Kobayashi, 'Buffer layer configuration for wideband microstrip patch antenna for underwater applications', in *2016 Loughborough Antennas Propagation Conference (LAPC)*, Nov. 2016, pp. 1–5. doi: 10.1109/LAPC.2016.7807577.
- [63] H. M. Zali, I. Pasya, M. T. Ali, and T. Kobayashi, 'Measurement of wideband microstrip underwater antenna performance with buffer layer structure', in *2017 IEEE 13th Malaysia International Conference on Communications (MICC)*, Johor Bahru, Nov. 2017, pp. 48–52. doi: 10.1109/MICC.2017.8311730.
- [64] Y. Yaozhou, F. Guirong, L. Chen, Y. Hao, and X. Rundong, 'Broadband Circularly Polarized Monopole Antenna with an Open loop', in *2018 International Conference on Microwave and Millimeter Wave Technology (ICMMT)*, May 2018, pp. 1–3. doi: 10.1109/ICMMT.2018.8563333.
- [65] K. P. Ray, 'Design Aspects of Printed Monopole Antennas for Ultra-Wide Band Applications', *Int. J. Antennas Propag.*, p. 713858 (8 pp.), 2008, doi: 10.1155/2008/713858.
- [66] Erli Chen and S. Y. Chou, 'Characteristics of coplanar transmission lines on multilayer substrates: modeling and experiments', *IEEE Trans. Microw. Theory Tech.*, vol. 45, no. 6, pp. 939–945, Jun. 1997, doi: 10.1109/22.588606.
- [67] Qun Li and Yonghong Zhang, 'Analytical Formulas for Conductor-backed Connected-ground Coplanar Waveguide', in *2018 IEEE International Conference on Computational Electromagnetics (ICCEM)*, 26-28 March 2018, Piscataway, NJ, USA, 2018, p. 3 pp. doi: 10.1109/COMPEN.2018.8496585.
- [68] A. A. Qureshi, M. U. Afzal, T. Tauqeer, and M. A. Tarar, 'Performance analysis of FR-4 substrate for high frequency microstrip antennas', in *2011 China-Japan Joint Microwave Conference*, Apr. 2011, pp. 1–4.
- [69] F. Sabath, E. L. Mokole, and S. N. Samaddar, 'Definition and classification of ultra-wideband signals and devices', *URSI Radio Sci. Bull.*, vol. 2005, no. 313, pp. 12–26, Jun. 2005, doi: 10.23919/URSIRSB.2005.7909522.
- [70] H. Jumaat, K. Hong Ping, N. H. Abd Rahman, H. Yon, F. N. Mohd Redzwan, and R. A. Awang, 'A compact modified wideband antenna with CBCPW, stubline and notch-staircase for breast cancer microwave imaging application', *AEU - Int. J. Electron. Commun.*, vol. 129, p. 153492, Feb. 2021, doi: 10.1016/j.aeue.2020.153492.

- [71] A. S. M. Alqadami, N. Nguyen-Trong, B. Mohammed, A. E. Stancombe, M. T. Heitzmann, and A. Abbosh, 'Compact Unidirectional Conformal Antenna Based on Flexible High-Permittivity Custom-Made Substrate for Wearable Wideband Electromagnetic Head Imaging System', *IEEE Trans. Antennas Propag.*, vol. 68, no. 1, pp. 183–194, Jan. 2020, doi: 10.1109/TAP.2019.2938849.
- [72] R. Cicchetti, V. Cicchetti, A. Faraone, L. Foged, and O. Testa, 'A Compact High-Gain Wideband Lens Vivaldi Antenna for Wireless Communications and Through-the-Wall Imaging', *IEEE Trans. Antennas Propag.*, vol. 69, no. 6, pp. 3177–3192, Jun. 2021, doi: 10.1109/TAP.2020.3037777.
- [73] A. Rahman and Yang Hao, 'A novel tapered slot CPW-fed antenna for ultra-wideband applications and its on/off-body performance', in *2007 3rd International Workshop on Antenna Technology: Small and Smart Antennas MetaMaterials and Applications, 21-23 March 2007*, Piscataway, NJ, USA, 2007, pp. 503–6.
- [74] B. Hammache, A. Messai, I. Messaoudene, and T. A. Denidni, 'A compact ultra-wideband antenna with three C-shaped slots for notched band characteristics', *Microw. Opt. Technol. Lett.*, vol. 61, no. 1, pp. 275–279, 2019, doi: 10.1002/mop.31535.
- [75] M. Kumar and V. Nath, 'A high BDR microstrip-line fed antenna with multiple asymmetric elliptical wide-slots for wideband applications', *Int. J. RF Microw. Comput.-Aided Eng.*, vol. 30, no. 7, p. e22202, 2020, doi: 10.1002/mmce.22202.
- [76] S. Modak, T. Khan, and R. H. Laskar, 'Penta-band notched ultra-wideband monopole antenna loaded with electromagnetic bandgap-structures and modified U-shaped slots', *Int. J. RF Microw. Comput.-Aided Eng.*, vol. 29, no. 12, p. e21963, 2019, doi: 10.1002/mmce.21963.
- [77] 'Cross Polar Discrimination (XPD)', *Halberd Bastion*. <https://halberdbastion.com/resources/academic/rf-parameters/cross-polar-discrimination-xpd> (accessed Aug. 13, 2021).
- [78] H. Bahramiabarghouei, E. Porter, A. Santorelli, B. Gosselin, M. Popović, and L. A. Rusch, 'Flexible 16 Antenna Array for Microwave Breast Cancer Detection', *IEEE Trans. Biomed. Eng.*, vol. 62, no. 10, pp. 2516–2525, Oct. 2015, doi: 10.1109/TBME.2015.2434956.
- [79] Y. G. Adhiyoga, S. F. Rahman, C. Apriono, and E. T. Rahardjo, 'Magneto-dielectric properties of PDMS–magnetite composite as a candidate for compact microstrip antennas in the C-band 5G frequency', *J. Mater. Sci. Mater. Electron.*, vol. 32, no. 8, pp. 11312–11325, Apr. 2021, doi: 10.1007/s10854-021-05802-z.
- [80] A. S. Md. Sayem, R. B. V. B. Simorangkir, K. P. Esselle, R. M. Hashmi, and H. Liu, 'A Method to Develop Flexible Robust Optically Transparent Unidirectional Antennas Utilizing Pure Water, PDMS, and Transparent Conductive Mesh', *IEEE Trans. Antennas Propag.*, vol. 68, no. 10, pp. 6943–6952, Oct. 2020, doi: 10.1109/TAP.2020.2996816.
- [81] S. Koulouridis, G. Kiziltas, Y. Zhou, D. J. Hansford, and J. L. Volakis, 'Polymer–Ceramic Composites for Microwave Applications: Fabrication and Performance Assessment', *IEEE Trans. Microw. Theory Tech.*, vol. 54, no. 12, pp. 4202–4208, Dec. 2006, doi: 10.1109/TMTT.2006.885887.

-
- [82] R. B. V. B. Simorangkir, Y. Yang, and K. P. Esselle, 'Robust implementation of flexible wearable antennas with PDMS-embedded conductive fabric', in *12th European Conference on Antennas and Propagation (EuCAP 2018)*, Apr. 2018, pp. 1–5. doi: 10.1049/cp.2018.0846.
- [83] Y. Zhou, Y. Bayram, F. Du, L. Dai, and J. L. Volakis, 'Polymer-Carbon Nanotube Sheets for Conformal Load Bearing Antennas', *IEEE Trans. Antennas Propag.*, vol. 58, no. 7, pp. 2169–2175, Jul. 2010, doi: 10.1109/TAP.2010.2048852.
- [84] T. D. C. Company, 'SYLGARD 184 Silicone Elastomer', no. 11, p. 4, 2017.
- [85] I. Smolyaninov, Q. Balzano, and D. Young, 'Development of Broadband Underwater Radio Communication for Application in Unmanned Underwater Vehicles', *J. Mar. Sci. Eng.*, vol. 8, no. 5, Art. no. 5, May 2020, doi: 10.3390/jmse8050370.
- [86] O. Aboderin, L. M. Pessoa, and H. M. Salgado, 'Performance evaluation of antennas for underwater applications', in *2017 Wireless Days*, Mar. 2017, pp. 194–197. doi: 10.1109/WD.2017.7918142.
- [87] A. R. H. Alhawari *et al.*, 'Compact Elliptical UWB Antenna for Underwater Wireless Communications', *Micromachines*, vol. 12, no. 4, Art. no. 4, Apr. 2021, doi: 10.3390/mi12040411.
- [88] M. Ahmadi, R. Rajamani, and S. Sezen, 'Transparent Flexible Active Faraday Cage Enables In Vivo Capacitance Measurement in Assembled Microsensor', *IEEE Sens. Lett.*, vol. 1, no. 5, pp. 1–4, Oct. 2017, doi: 10.1109/LSENS.2017.2737956.
- [89] J. R. Solin, 'Shielding effectiveness of satellite faraday cages with EMI taped seams and closeouts', *IEEE Electromagn. Compat. Mag.*, vol. 7, no. 2, pp. 40–46, 2018, doi: 10.1109/MEMC.2018.8410660.
- [90] M. Guri, B. Zadov, and Y. Elovici, 'ODINI: Escaping Sensitive Data From Faraday-Caged, Air-Gapped Computers via Magnetic Fields', *IEEE Trans. Inf. Forensics Secur.*, vol. 15, pp. 1190–1203, 2020, doi: 10.1109/TIFS.2019.2938404.
- [91] T. D. Neusitzer *et al.*, 'Examining the Impact of a Crude Oil Spill on the Permittivity Profile and Normalized Radar Cross Section of Young Sea Ice', *IEEE Trans. Geosci. Remote Sens.*, vol. 56, no. 2, pp. 921–936, Feb. 2018, doi: 10.1109/TGRS.2017.2756843.
- [92] H. Liu, W. He, J. Guo, and Q. Huang, 'Risk propagation mechanism: Qingdao Crude Oil Leaking and Explosion case study', *Eng. Fail. Anal.*, vol. 56, pp. 555–561, Oct. 2015, doi: 10.1016/j.engfailanal.2014.10.003.
- [93] J. Li, S. Grzybowski, Y. Sun, and X. Chen, 'Dielectric properties of rapeseed oil paper insulation', in *2007 Annual Report - Conference on Electrical Insulation and Dielectric Phenomena*, Oct. 2007, pp. 500–503. doi: 10.1109/CEIDP.2007.4451582.
- [94] T. Friisø, Y. Schildberg, O. Rambeau, T. Tjomsland, H. Førdedal, and J. Sjøblom, 'COMPLEX PERMITTIVITY OF CRUDE OILS AND SOLUTIONS OF HEAVY CRUDE OIL FRACTIONS', *J. Dispers. Sci. Technol.*, Apr. 2007, doi: 10.1080/01932699808913163.
- [95] S. Sun, X. Zhang, C. Zheng, J. Fu, and C. Zhao, 'Underwater Acoustical Localization of the Black Box Utilizing Single Autonomous Underwater Vehicle Based on the Second-Order Time Difference of Arrival', *IEEE J.*

- Ocean. Eng.*, vol. 45, no. 4, pp. 1268–1279, Oct. 2020, doi: 10.1109/JOE.2019.2950954.
- [96] X. Che, I. Wells, G. Dickers, and P. Kear, ‘TDMA frame design for a prototype underwater RF communication network’, *Ad Hoc Netw.*, vol. 10, no. 3, pp. 317–327, May 2012, doi: 10.1016/j.adhoc.2011.07.002.
- [97] H. Kaushal and G. Kaddoum, ‘Underwater Optical Wireless Communication’, *IEEE Access*, vol. 4, pp. 1518–1547, 2016, doi: 10.1109/ACCESS.2016.2552538.
- [98] J. Guo, R. Zheng, X. Yu, A. Wei, and B. Yang, ‘Autonomous underwater vehicle docking system based on wired transmission’, in *2018 WRC Symposium on Advanced Robotics and Automation (WRC SARA)*, Aug. 2018, pp. 1–6. doi: 10.1109/WRC-SARA.2018.8584153.
- [99] N. Rako-Gospić and M. Picciulin, ‘Chapter 20 - Underwater Noise: Sources and Effects on Marine Life’, in *World Seas: an Environmental Evaluation (Second Edition)*, C. Sheppard, Ed. Academic Press, 2019, pp. 367–389. doi: 10.1016/B978-0-12-805052-1.00023-1.
- [100] ‘Wireless HROV Control with Compressed Visual Feedback Using Acoustic and RF Links | SpringerLink’. <https://link.springer.com/article/10.1007/s10846-020-01157-5> (accessed Jan. 27, 2021).
- [101] S. Han, Y. Noh, U. Lee, and M. Gerla, ‘Optical-acoustic hybrid network toward real-time video streaming for mobile underwater sensors’, *Ad Hoc Netw.*, vol. 83, pp. 1–7, Feb. 2019, doi: 10.1016/j.adhoc.2018.08.020.
- [102] R. Sinha, W. Yiqiao, and S.-H. Hwang, ‘A survey on LPWA technology: LoRa and NB-IoT’, *ICT Express*, vol. 3, Mar. 2017, doi: 10.1016/j.ict.2017.03.004.
- [103] D. Madeo, A. Pozzebon, C. Mocenni, and D. Bertoni, ‘A Low Cost Unmanned Surface Vehicle for Pervasive Water Quality Monitoring’, *IEEE Trans. Instrum. Meas.*, vol. PP, pp. 1–1, Apr. 2020, doi: 10.1109/TIM.2019.2963515.
- [104] J. Cecilio, P. M. Ferreira, and A. Casimiro, ‘Evaluation of LoRa Technology in Flooding Prevention Scenarios’, *Sensors*, vol. 20, no. 14, Art. no. 14, Jan. 2020, doi: 10.3390/s20144034.
- [105] L. Li, J. Ren, and Q. Zhu, ‘On the application of LoRa LPWAN technology in Sailing Monitoring System’, in *2017 13th Annual Conference on Wireless On-demand Network Systems and Services (WONS)*, Feb. 2017, pp. 77–80. doi: 10.1109/WONS.2017.7888762.
- [106] M. E. Sinitsyn, A. S. Podstrigaev, A. V. Smolyakov, and V. V. Davydov, ‘Analysis of the Sea Surface Influence on the Shape of Microwave Spiral Antenna Radiation Pattern’, in *2019 Antennas Design and Measurement International Conference (ADMInC)*, Oct. 2019, pp. 72–74. doi: 10.1109/ADMInC47948.2019.8969319.
- [107] G. L. Gragnani, D. D. Caviglia, and C. Montecucco, ‘A Log-Periodic Antenna for Long Range Communication Within a Wireless Sensor Network System for Sea Water Quality Monitoring’, in *2018 Advances in Wireless and Optical Communications (RTUWO)*, Nov. 2018, pp. 161–166. doi: 10.1109/RTUWO.2018.8587911.
- [108] S. Ryecroft *et al.*, ‘A First Implementation of Underwater Communications in Raw Water Using the 433 MHz Frequency Combined with a Bowtie Antenna’, *Sensors*, vol. 19, no. 8, Art. no. 8, Jan. 2019, doi: 10.3390/s19081813.

- [109] A. A. Abdou *et al.*, ‘A matched Bow-tie antenna at 433MHz for use in underwater wireless sensor networks’, *J. Phys. Conf. Ser.*, vol. 450, p. 012048, Jun. 2013, doi: 10.1088/1742-6596/450/1/012048.
- [110] K. P. Ray, ‘Design Aspects of Printed Monopole Antennas for Ultra-Wide Band Applications’, *Int. J. Antennas Propag.*, vol. 2008, pp. 1–8, 2008, doi: 10.1155/2008/713858.
- [111] P. Purohit, B. K. Shukla, and D. K. Raghuvanshi, ‘A Novel Design of Hybrid Open Slot Antenna with Parasitic Element for Wideband Applications’, *Prog. Electromagn. Res. C*, vol. 90, pp. 95–107, 2019, doi: 10.2528/PIERC18110101.
- [112] ‘HMC849ALP4CE HIGH ISOLATION SPDT NON-REFLECTIVE SWITCH, DC - 6 GHz’, *Analog Devices*, [Online]. Available: <https://www.analog.com/media/en/technical-documentation/data-sheets/hmc849a.pdf>
- [113] ‘HMC245AQS16E GaAs MMIC SP3T Non-REFLECTIVE SWITCH, DC - 3.5 GHz’. *Analog Devices*. [Online]. Available: <https://www.analog.com/media/en/technical-documentation/data-sheets/hmc245aqs16e.pdf>
- [114] ‘Smart | Connected | Secure | Microchip Technology’. <https://aem-origin.microchip.com/> (accessed Oct. 14, 2021).
- [115] S. N. Nafea, ‘Improving Performance of Patch Antenna For IEEE 802.16e Applications Using Multi-layer Antenna Structure with Reflector’, in *2018 Al-Mansour International Conference on New Trends in Computing, Communication, and Information Technology (NTCCIT)*, Nov. 2018, pp. 18–22. doi: 10.1109/NTCCIT.2018.8681183.
- [116] F. C. Gül, K. Karaçuha, and S. Eker, ‘Dual-Band Quasi- Yagi Antenna Gain Enhancement by using a Reflector Plate’, in *2019 Photonics Electromagnetics Research Symposium - Spring (PIERS-Spring)*, Jun. 2019, pp. 3594–3600. doi: 10.1109/PIERS-Spring46901.2019.9017703.
- [117] M. M. Gajibo, M. K. A. Rahim, O. Ayop, N. A. Murad, M. A. Baba, and H. A. Majid, ‘X-Band Directivity improvement using Reflector’, in *2018 International Symposium on Antennas and Propagation (ISAP)*, Oct. 2018, pp. 1–2.
- [118] M. S. R. Bashri, ‘Wearable devices for microwave head diagnostic systems’, Nov. 2018, Accessed: Oct. 14, 2021. [Online]. Available: <https://era.ed.ac.uk/handle/1842/33243>
- [119] ‘ATmega328P Datasheet | Microchip - Datasheetspdf.com’. <https://datasheetspdf.com/datasheet/ATmega328P.html> (accessed Sep. 14, 2021).
- [120] ‘HC-06 Bluetooth Module’, [Online]. Available: <https://www.olimex.com/Products/Components/RF/BLUETOOTH-SERIAL-HC-06/resources/hc06.pdf>
- [121] ‘200 Adafruit Solar Panel 6V 2W| Mouser’, *Mouser Electronics*. <https://www.mouser.co.uk/ProductDetail/485-200> (accessed Sep. 14, 2021).
- [122] ‘3.7V 7000mAh 1S2P Li-Ion Battery Pack - 2447-3033-20’. <https://cpc.farnell.com/ansmann/2447-3033-20/battery-pack-li-ion-1s2p-3-7v/dp/BT06446> (accessed Sep. 14, 2021).

- [123] ‘Universal USB / DC / Solar Lithium Ion/Polymer charger (bq24074)’, *Cool Components*. <https://coolcomponents.co.uk/products/universal-usb-dc-solar-lithium-ion-polymer-charger-bq24074> (accessed Sep. 14, 2021).
- [124] ‘mEZD41503A-X 2.7V - 10V Input, 3A, Step-Up Power Supply’. Monolithic Power Systems. [Online]. Available: https://www.mouser.co.uk/datasheet/2/277/mEZD41503A_B-1384075.pdf
- [125] S. Mercer, ‘Minimizing RF PCB electromagnetic emissions’, p. 4, 1999.
- [126] ‘PCB Prototype & PCB Fabrication Manufacturer - JLCPCB’. https://jlcpcb.com/?_ga=2.68498966.641982531.1631792018-1554734245.1542549401&_gac=1.186927962.1631121705.CjwKCAjwvuGJBhB1EiwACU1AiZfSvxz8EN5ORFATjq_hvGtjonsbOh2wYOhGvt_DELoidNBM6-9g_xoCPRUQAvD_BwE (accessed Sep. 16, 2021).
- [127] ‘CON-SMA-EDGE | RF Solutions 50Ω Straight PCB Mount, SMA Connector , jack | RS Components’. <https://uk.rs-online.com/web/p/products/1258190/> (accessed Sep. 20, 2021).
- [128] G. Wang, Z. Zeng, X. Wu, T. Ren, J. Han, and Q. Xue, ‘Three-dimensional structured sponge with high oil wettability for the clean-up of oil contaminations and separation of oil–water mixtures’, *Polym. Chem.*, vol. 5, no. 20, pp. 5942–5948, 2014, doi: 10.1039/C4PY00552J.
- [129] K. T. Selvan and R. Janaswamy, ‘Fraunhofer and Fresnel Distances : Unified derivation for aperture antennas.’, *IEEE Antennas Propag. Mag.*, vol. 59, no. 4, pp. 12–15, Aug. 2017, doi: 10.1109/MAP.2017.2706648.
- [130] V. Yadav *et al.*, ‘High-Frequency Transmission Characteristics of Inert Coolant Liquids for High-Power Gyrotron Windows’, *IEEE Trans. Plasma Sci.*, vol. 41, no. 3, pp. 450–455, Mar. 2013, doi: 10.1109/TPS.2013.2243473.
- [131] A. V. Goncharenko, V. Z. Lozovski, and E. F. Venger, ‘Lichtenecker’s equation: applicability and limitations’, *Opt. Commun.*, vol. 174, no. 1, pp. 19–32, Jan. 2000, doi: 10.1016/S0030-4018(99)00695-1.
- [132] G. R. Govinda Raju, ‘Dielectric constant of binary mixtures of liquids’, in *1988. Annual Report., Conference on Electrical Insulation and Dielectric Phenomena*, Oct. 1988, pp. 357–363. doi: 10.1109/CEIDP.1988.26358.
- [133] J. Sun and S. Lucyszyn, ‘Extracting Complex Dielectric Properties From Reflection-Transmission Mode Spectroscopy’, *IEEE Access*, vol. 6, pp. 8302–8321, 2018, doi: 10.1109/ACCESS.2018.2797698.
- [134] ‘How Is an Oil Spill in a River Different Than One in the Ocean? | response.restoration.noaa.gov’. <https://response.restoration.noaa.gov/about/media/how-oil-spill-river-different-one-ocean.html> (accessed Oct. 04, 2021).

Appendices

APPENDIX A: OIL SPILL MEASUREMENT WITH RAPESEED OIL

Crude oil is highly combustible [92]. Thus, the experiment began with a non-volatile liquid that is not as inflammable as crude oil to provide a proof of concept for the microwave oil spill detection. Rapeseed oil which has a close dielectric constant with that of crude oil [93] was chosen. Rapeseed oil has a dielectric constant of around 2.93 while crude oil has a relative permittivity of 2.2 to 2.4 [94].

The two antennas were placed in the Faraday cage. A 650 ml volume of water was then poured into the Faraday cage. The S parameters for the unadulterated freshwater and seawater were obtained using KE5FX VNA Utility software on the PC that was connected to the 8753 VNA. Subsequently, 10 ml of the rapeseed oil was added to the water medium and the S Parameters were measured for both the freshwater and seawater. 10 ml of the crude oil were continuously added to the solution until a limit of 100 ml of the rapeseed oil was added to the water medium with the S Parameters continuously measured for each added rapeseed oil inclusion. These was done for all the three antenna setups with antenna spacing of 15 mm, 50 mm and 70 mm.

A.1 Rapeseed Oil Spill

The results obtained during the experiment with rapeseed oil spill shall be discussed in this section. The work shall look at both the reflection and transmission coefficients for the proof of concept validation of the underwater oil spill detection capability of the system before proceeding with crude oil.

A.1.1 Reflection Coefficient

The reflection coefficients obtained at varying volume of the rapeseed oil added to the water medium could be seen in Figure A.1, Figure A.2 and Figure A.3 for 15mm, 50mm and 70mm antenna spacing respectively.

From Figure A.1, noticeable difference could be seen from the water medium starting from around 1000 MHz when it was unadulterated and when 10ml of the rapeseed oil

was continually added to it for the 15 mm antenna spacing. The same behaviour was exhibited by the 50mm antenna spacing from around 900 MHz and at 300 MHz for the 70 mm antenna spacing from Figure A.2 and Figure A.3 respectively.

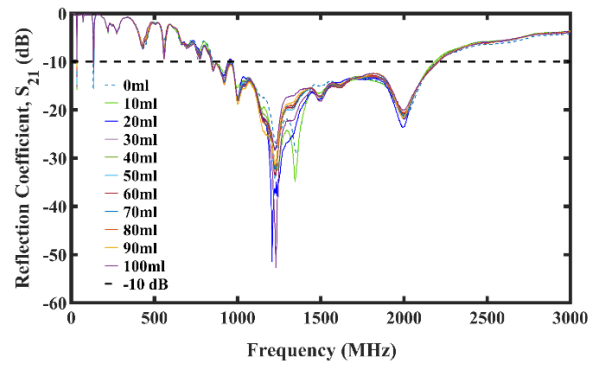


Figure A.1: Plot showing S11 for rapeseed oil spill experiment with 15mm spaced antennas.

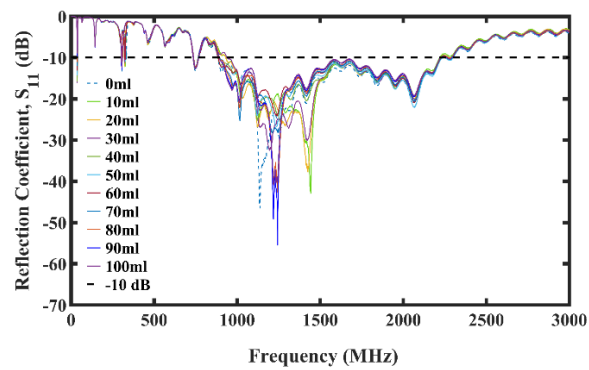


Figure A.2: Plot showing S11 for rapeseed oil spill experiment with 50 mm spaced antennas.

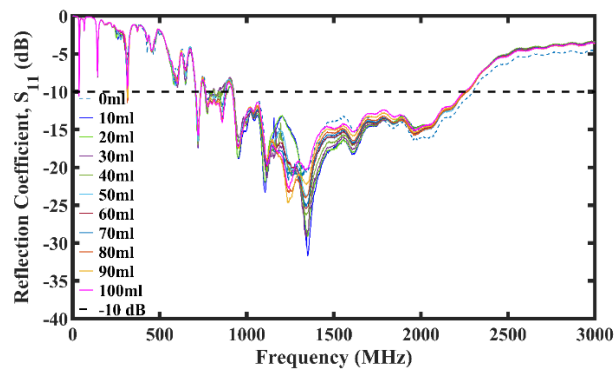


Figure A.3: Plot showing S11 for rapeseed oil spill experiment with 70 mm spaced antennas.

These results satisfactorily prove that the setup could be used to detect changes in the relative permittivity in the water medium using the reflection coefficients for all

setups. The antenna spacing at 70mm had more noticeable difference in the S11 over wider bandwidth.

For brevity, the reflection coefficients of the freshwater and that with rapeseed inclusions at 10ml, 50ml and 100ml were compared as it could be seen in Figure A.4, Figure A.5 and Figure A.6 respectively for the 70 mm antenna spacing setup.

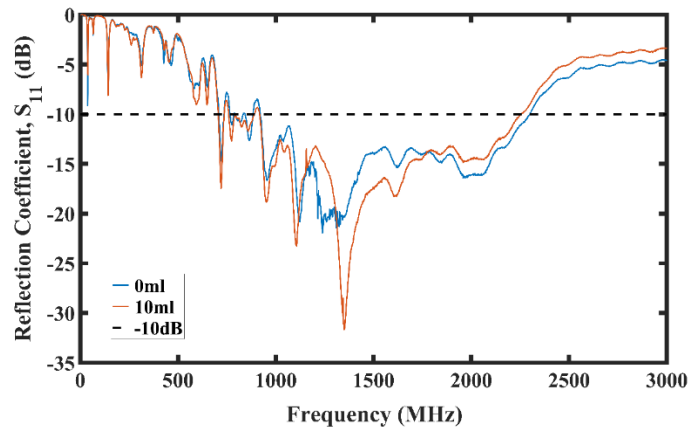


Figure A.4: Plot comparing S11 of freshwater and rapeseed inclusion at 10 ml with 70 mm spaced antennas.

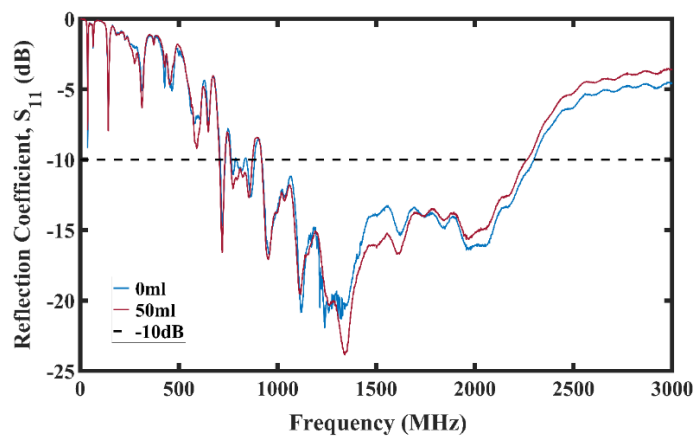


Figure A.5: Plot comparing S11 of freshwater and rapeseed inclusion at 50 ml with 70 mm spaced antennas.

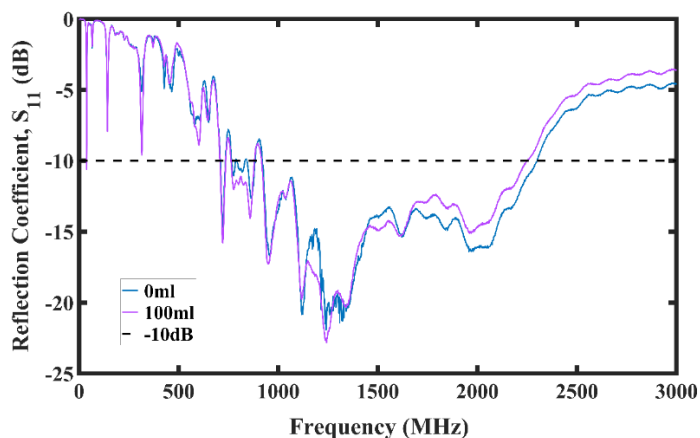


Figure A.6: Plot comparing S_{11} of freshwater and rapeseed inclusion at 100 ml with 70 mm spaced antennas.

It is obvious from the figures that the rapeseed oil was detectable in the water starting from 10 ml and up to 100ml by shift in the reflection coefficient compared to that of the unadulterated water.

A.1.1 Transmission Coefficient

The transmission coefficients for the antenna spacing of 15mm, 50mm and 70 mm could be seen in Figure A.7, Figure A.8 and Figure A.9 respectively. All setups exhibited changes as the rapeseed oil was added. However, the 15mm setup had the minimal changes in the S_{21} while the 70mm and 50mm antenna spacing exhibited good performances with respect to the S_{21} as it could be seen in the figures.

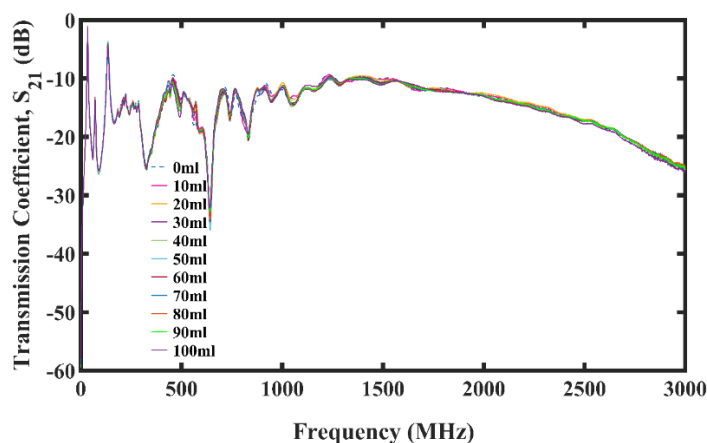


Figure A.7. Plot showing S_{21} for rapeseed oil spill experiment with 15 mm spaced antennas.

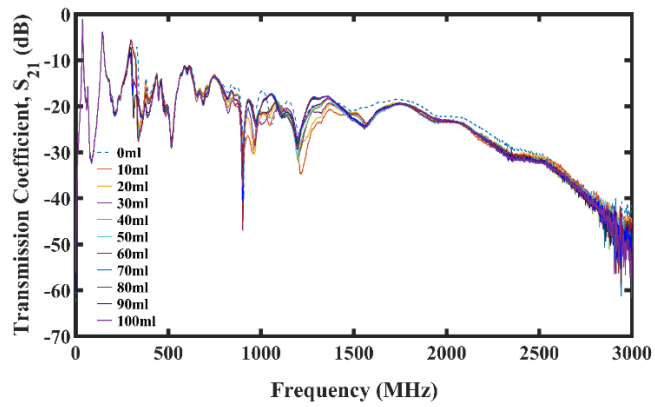


Figure A.8: Plot showing S21 for rapeseed oil spill experiment with 50 mm spaced antennas.

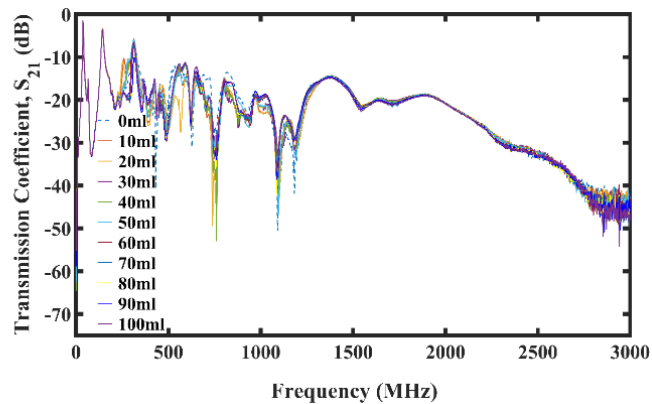


Figure A.9. Plot showing S21 for rapeseed oil spill experiment with 70 mm spaced antennas

For brevity, the transmission coefficients of the freshwater and the new medium with rapeseed inclusions at 10ml, 50ml and 100ml were compared as it could be seen in Figure A.10, Figure A.11 and Figure A.12 respectively for the 70 mm setup.

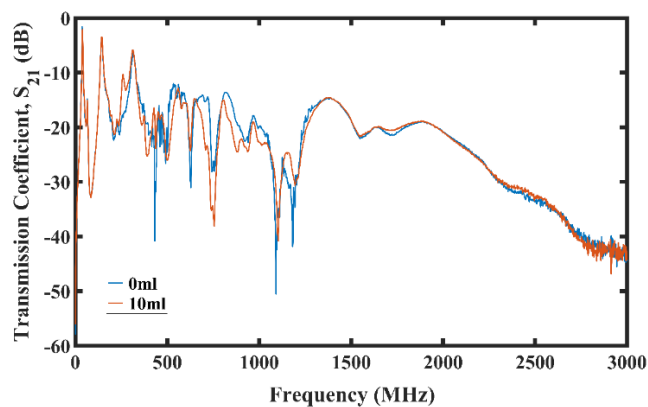


Figure A.10: Plot comparing S21 of freshwater and rapeseed inclusion at 10 ml with 70 mm spaced antennas.

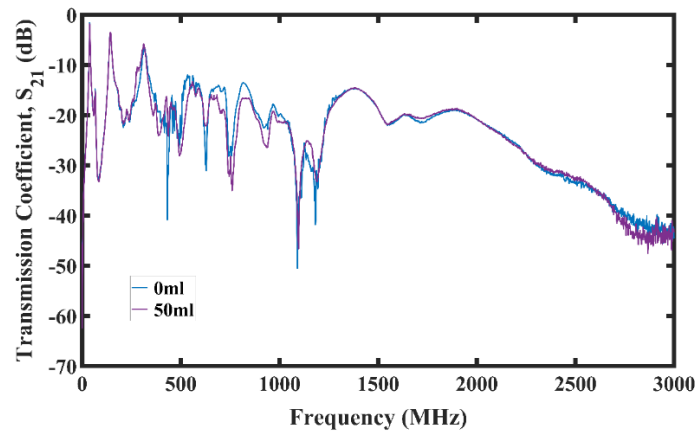


Figure A.11. Plot comparing S_{21} of freshwater and rapeseed inclusion at 50 ml with 70 mm spaced antennas.

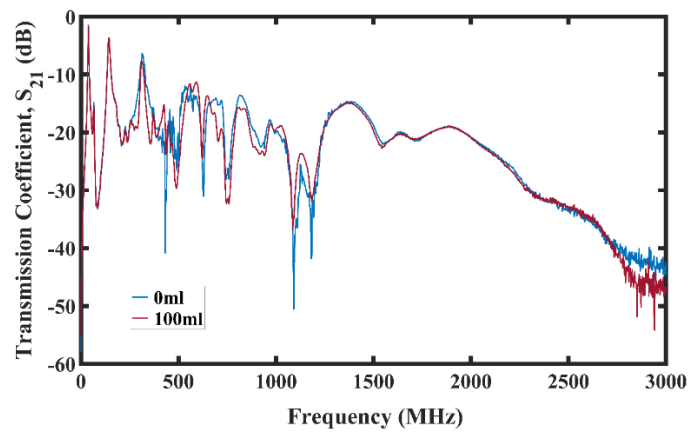


Figure A.12: Plot comparing S_{21} of freshwater and rapeseed inclusion at 100 ml with 70 mm spaced antennas.

APPENDIX B: HANACO Crude Oil Experiment in Freshwater

The measurements of the reflection and forward transmission coefficients undertaken for all three Faraday experimental setup for antenna separations of 70 mm, 50 mm and 15 mm antenna spacing in freshwater medium with crude oil inclusion shall be discussed here.

B.1 Reflection Coefficient

B.1.1 15 mm Antenna Spacing

Variation of the reflection coefficient for the 15mm was from 452 MHz to 2436 MHz which could be seen in Figure B.1. For brevity, the reflection coefficients of the pure freshwater and those at 10ml, 50ml and 100 ml HANACO inclusions for the antenna spacing of 15mm could be seen in Figure B.2, Figure B.3 and Figure B.4 respectively.

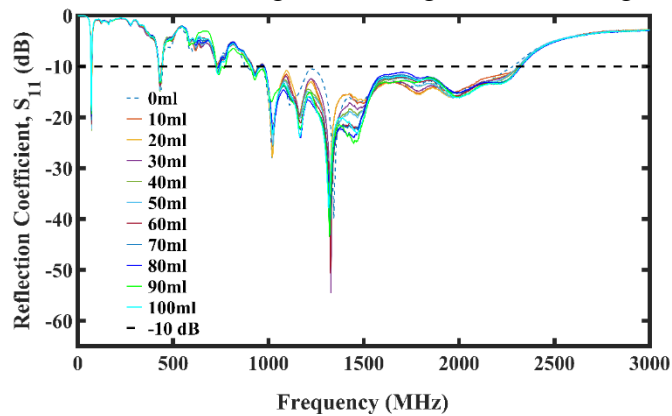


Figure B.1: Plot showing S11 for HANACO crude oil spill experiment with 15 mm spaced antennas in freshwater.

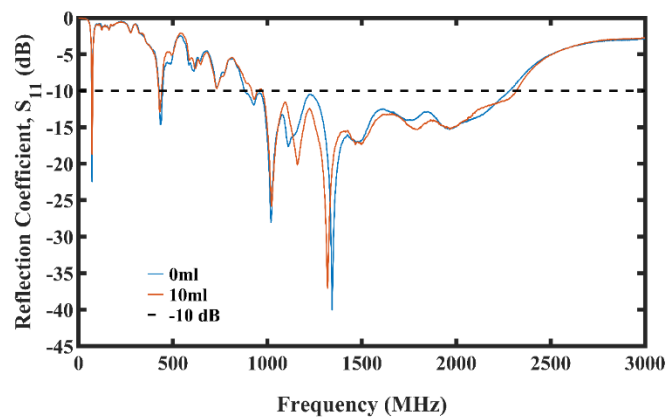


Figure B.2: Plot comparing S11 of freshwater and HANACO crude oil inclusion at 10 ml with 15 mm spaced antennas.

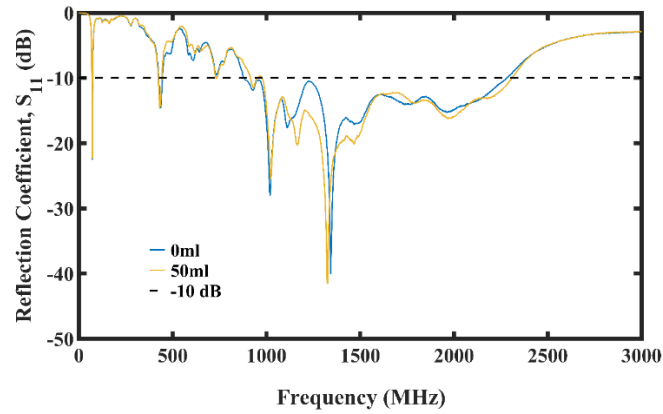


Figure B.3: Plot comparing S_{11} of freshwater and HANACO crude oil inclusion at 50 ml with 15 mm spaced antennas.

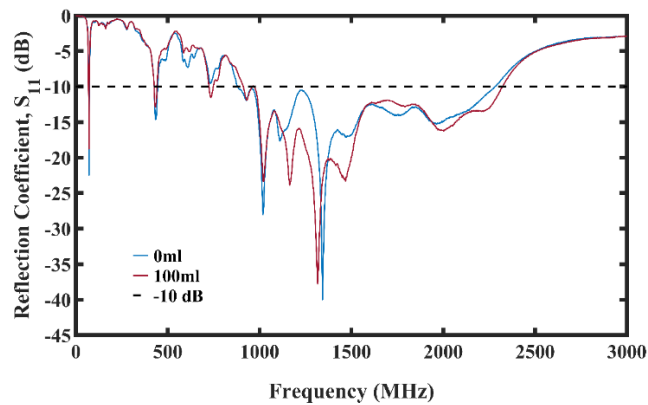


Figure B.4: Plot comparing S_{11} of freshwater and HANACO crude oil inclusion at 100 ml with 15 mm spaced antennas.

B.1.2 50 mm Antenna Spacing

The reflection coefficients for the 50mm antenna spacing in freshwater could be seen in Figure B.5. The observable variation of the reflection coefficient for the 50mm antenna spacing was from 274 MHz to 2199 MHz. For brevity, the reflection coefficients of the pure freshwater and those at 10ml, 50ml and 100 ml inclusion of crude oil are shown in Figure B.6, Figure B.7 and Figure B.8 respectively for the antenna spacing of 50mm.

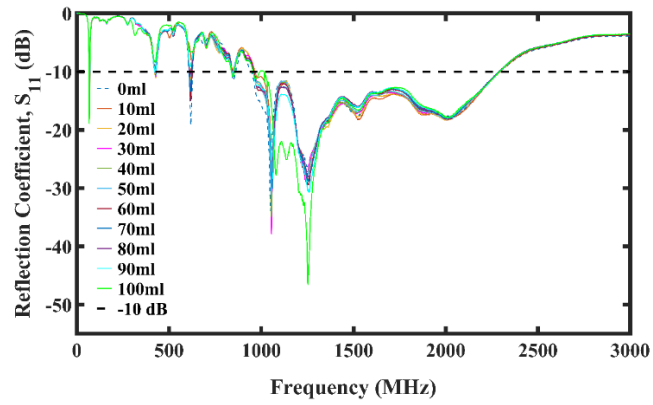


Figure B.5: Plot showing S11 for HANACO crude oil spill experiment with 50 mm spaced antennas in freshwater.

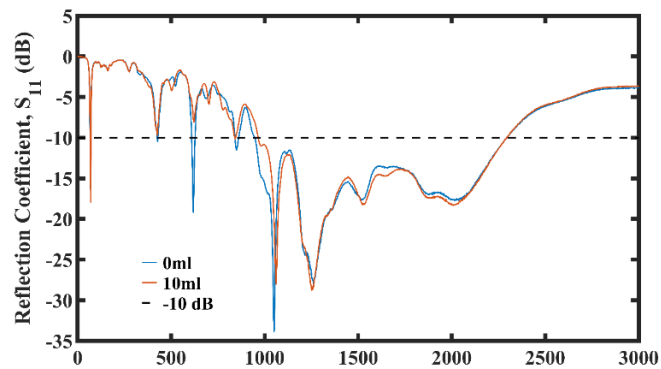


Figure B.6: Plot comparing S11 of freshwater and HANACO crude oil inclusion at 10 ml with 50 mm spaced antennas.

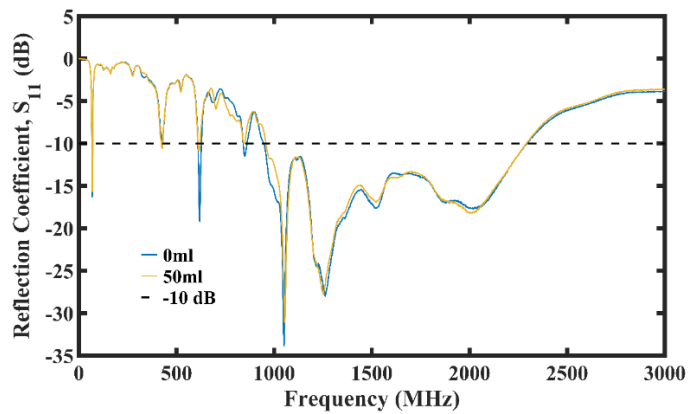


Figure B.7: Plot comparing S11 of freshwater and HANACO crude oil inclusion at 50 ml with 50 mm spaced antennas.

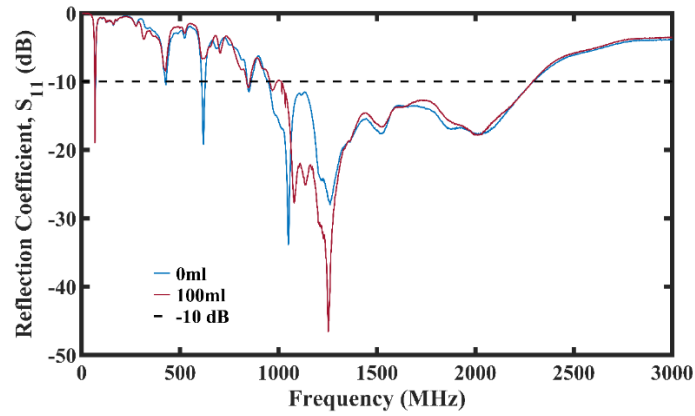


Figure B.8. Plot comparing S_{11} of freshwater and HANACO crude oil inclusion at 100 ml with 50 mm spaced antennas.

B.1.3 70 mm Antenna Spacing

The reflection coefficients for the 70mm antenna spacing in freshwater could be seen in Figure B.9. The observable variation of the reflection coefficient for the 50mm antenna spacing was from around 500 MHz to 2200 MHz. For brevity, the reflection coefficients of the pure freshwater and those at 10ml, 50ml and 100 ml crude oil inclusions are shown in Figure B.10, Figure B.11 and Figure B.12 respectively for the antenna spacing of 70mm.

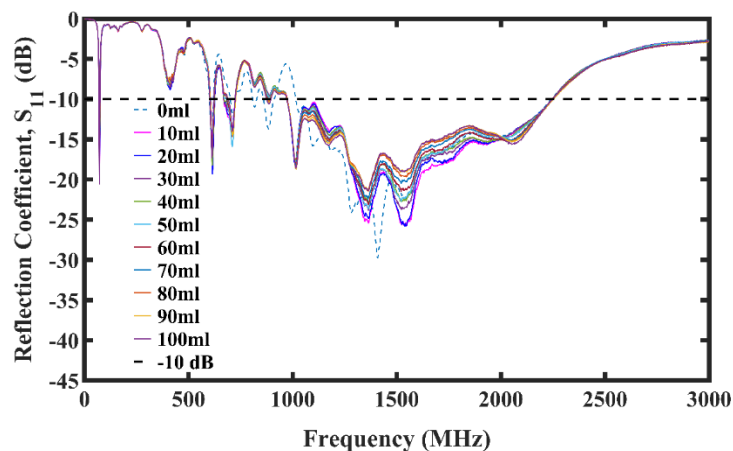


Figure B.9: Plot showing S_{11} for HANACO crude oil spill experiment with 70 mm spaced antennas in freshwater.

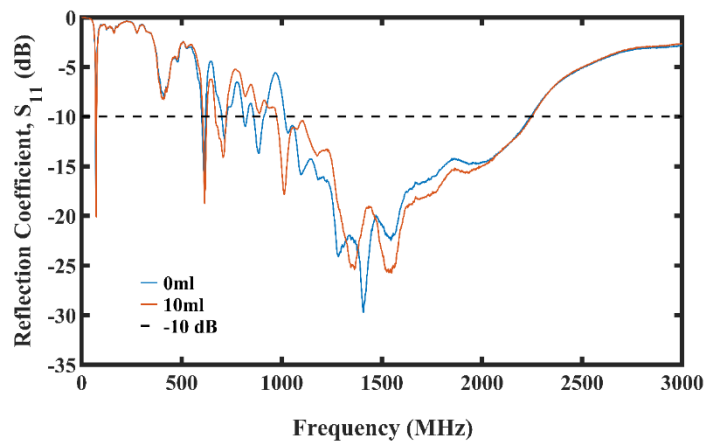


Figure B.10: Plot comparing S_{11} of freshwater and HANACO crude oil inclusion at 10 ml with 70 mm spaced antennas.

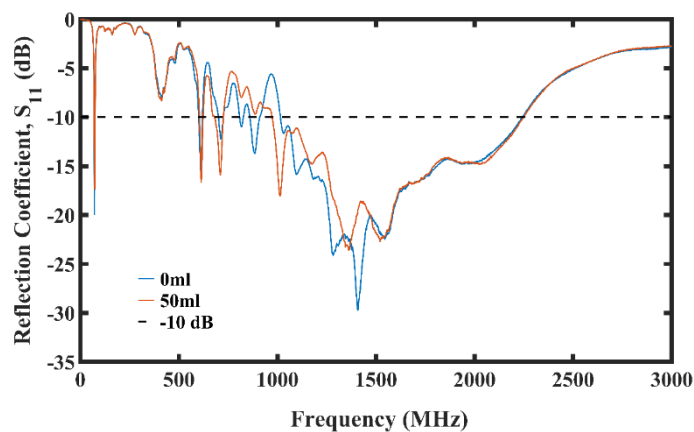


Figure B.11: Plot comparing S_{11} of freshwater and HANACO crude oil inclusion at 50 ml with 70 mm spaced antennas.

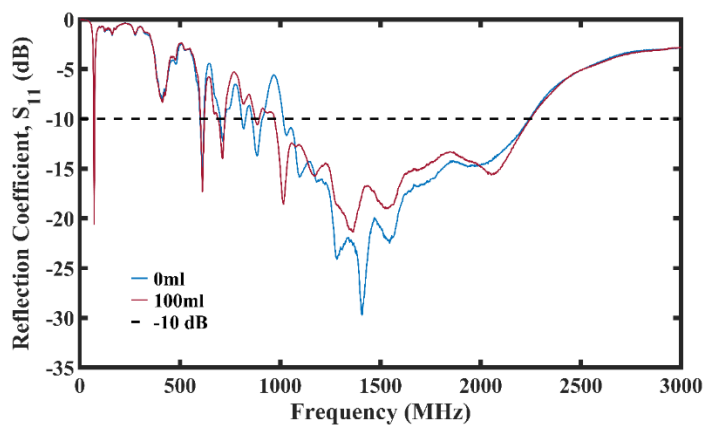


Figure B.12: Plot comparing S_{11} of freshwater and HANACO crude oil inclusion at 100 ml with 70 mm spaced antennas.

B.2 Transmission Coefficient

The transmission coefficient for the three antenna spacing could be seen to reduce with increasing frequency due to the losses incurred at higher frequencies. The S_{21} for the 15mm, 50mm and 70mm antenna spacing could be seen in Figure B.13, Figure B.14 and Figure B.15 respectively. In each setup, the transmission coefficients of unadulterated freshwater was compared with those at 10ml, 50ml and 100ml crude oil inclusions. It could be seen that in all cases the S_{21} of the pure freshwater was changed when the crude oil inclusions were added to it. These results are better than those obtained for the seawater because freshwater has lower salinity and thus lower level of dispersion of the radio frequency signals.

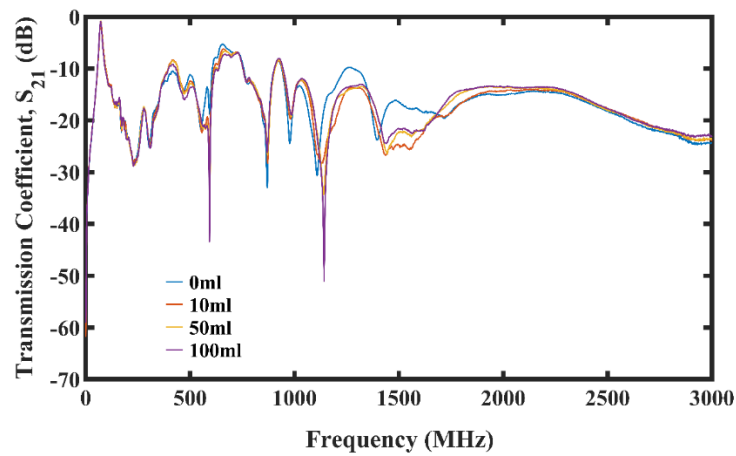


Figure B.13: Plot comparing S_{21} of freshwater and HANACO crude oil inclusion at 10 ml, 50 ml, and 100 ml with 15 mm spaced antennas.

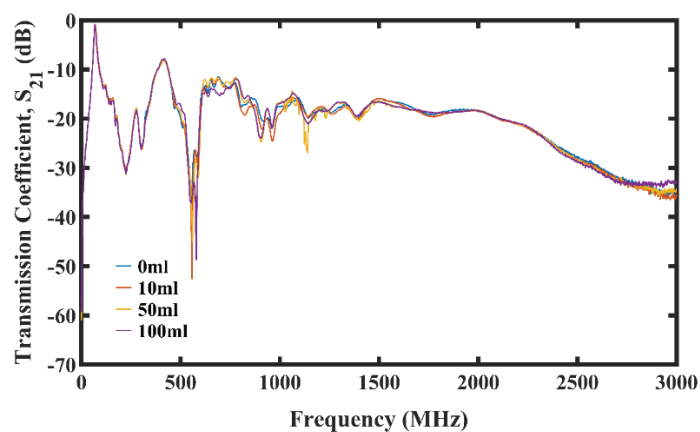


Figure B.14: Plot comparing S_{21} of freshwater and HANACO crude oil inclusion at 10 ml, 50 ml, and 100 ml with 50 mm spaced antennas.

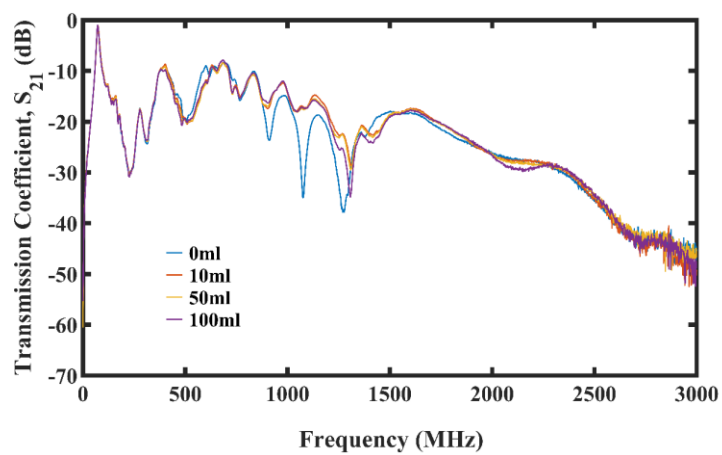


Figure B.15: Plot comparing S_{21} of freshwater and HANACO crude oil inclusion at 10 ml, 50 ml, and 100 ml with 70 mm spaced antennas.